Superresolution applied to optical data storage systems

INFORMATION TO USERS

This manuscript has been reproduced from the microfilm master. UMI films the text directly from the original or copy submitted. Thus, some thesis and dissertation copies are in typewriter face, while others may be from any type of computer printer.

The quality of this reproduction is dependent upon the quality of the copy submitted. Broken or indistinct print, colored or poor quality illustrations and photographs, print bleedthrough, substandard margins, and improper alignment can adversely affect reproduction.

In the unlikely event that the author did not send UMI a complete manuscript and there are missing pages, these will be noted. Also, if unauthorized copyright material had to be removed, a note will indicate the deletion.

Oversize materials (e.g., maps, drawings, charts) are reproduced by sectioning the original, beginning at the upper left-hand corner and continuing from left to right in equal sections with small overlaps.

Photographs included in the original manuscript have been reproduced xerographically in this copy. Higher quality 6" x 9" black and white photographic prints are available for any photographs or illustrations appearing in this copy for an additional charge. Contact UMI directly to order.

Bell & Howell Information and Learning
300 North Zeeb Road, Ann Arbor, MI 48106-1346 USA
800-521-0600

SUPERRESOLUTION APPLIED TO OPTICAL DATA STORAGE SYSTEMS

by

Edwin Parker Walker

A Dissertation Submitted to the Faculty of the

COMMITTEE ON OPTICAL SCIENCES (GRADUATE)

In Partial Fulfillment of the Requirements
For the Degree of

DOCTOR OF PHILOSOPHY

In the Graduate College

THE UNIVERSITY OF ARIZONA

1999

THE UNIVERSITY OF ARIZONA ®
GRADUATE COLLEGE

As members of the Final Examination Committee, we certify that we have read the dissertation prepared by Edwin P. Walker

entitled Superresolution Applied to Optical Data Storage Systems

and recommend that it be accepted as fulfilling the dissertation requirement for the Degree of Doctor of Philosophy

Thomas Milster	**Date** 12/7/98
Glenn Sincerbox	**Date** 12/7/98
Roland Shack	**Date** 12/7/98
	Date
	Date

Final approval and acceptance of this dissertation is contingent upon the candidate's submission of the final copy of the dissertation to the Graduate College.

I hereby certify that I have read this dissertation prepared under my direction and recommend that it be accepted as fulfilling the dissertation requirement.

Thomas Milster **Dissertation Director**	**Date** 12/7/98
Glenn Sincerbox **Co-Director**	12/7/98

STATEMENT BY AUTHOR

This dissertation has been submitted in partial fulfillment of requirements for an advanced degree at the University of Arizona and is deposited in the University Library to be made available to borrowers under rules of the Library.

Brief quotations from this dissertation are allowable without special permission, provided that accurate acknowledgment of source is made. Requests for permission for extended quotation from or reproduction of this manuscript in whole or in part may be granted by the head of the major department or the Dean of the Graduate College when in his or her judgement the proposed use of the material is in the interests of scholarship. In all other instances, however, permission must be obtained from the author.

SIGNED: Edwin Parker Walker

ACKNOWLEDGMENTS

I would like to thank my advisor, Dr. Tom Milster, for the opportunity to work with him. His patience and tolerance will always be remembered. His support and encouragement allowed me to complete this graduate study.

I would like to thank Kevin Erwin and Warren Bletscher as their contribution to this work is inseparable. I am grateful to them for teaching me their knowledge of optics, mechanics, and electronics. I would also like to thank Mark Shi Wang for showing me the ropes of the dynamic magneto-optic data storage tester. Special thanks to the Optical Data Storage Center and all their sponsors who provided financial support and helped make this work a reality. In particular I would like to thank Scott Hamilton for the opportunity to work with him and Apex systems on the green light optical head media tester. Wenbin Jiang, of Motorola, for the opportunity to work with their new VCSEL'S. Gerry Joyce, of Terabank, for the opportunity to work on the TRAAMS project. Dr. C. David Wright of the Universtiy of Manchester, England, for thermal simulations.

I would also like to thank the teachers and researchers of the Optical Sciences Center who contributed to my education through their ability to relate concepts with such clarity that even I could understand. In particular I would like to thank Jack Gaskill, John Greivenkamp, Arvind Marathay, Roland Shack, James Wyant, Angus Macleod, George Lawrence, James Burke, Ewan Wright, Ray Kostuk, Rick Shoemaker, Art Gmitro, Phil Slater, Dennis Howe, Masud Mansuripur, and Glenn Sincerbox.

I would also like to thank everyone who was a part of my life during graduate school. My fellow students contributed greatly to my education and influenced my work in one way or another. Gratitude is extended in particular to Joe Shiefman, Mike Schaub, Kevin Matherson, Mark Eastman, Mark Prusten, Sergio Mendes, Mike Rivera, Matt Chang, Nobuo Mushiake, Craig Curtis, Josh Kann, Fred Froehlich, Wolfgang Schlichting, Rudy Himawan, Zhi-yong Chen, Mike Tuell, Mike Schweisguth, Robert Upton, the Milster research group, Didi Lawson, Pat Gransie, and many others for their kindness and support. My parents and in-laws deserve special thanks as their encouragement and support helped me to complete this work. I would also like to give thanks and praise to my Lord and Savior Jesus Christ who is with me all the time whether I know it or not.

Last but not least, I would like to thank my wife Liza, her love, support, and encouragement enabled me to complete this work, and our sons Santiago, Emiliano, and Alejandro, as their fascination and discovery of life is inspirational.

To my wife Liza,

and our children

TABLE OF CONTENTS

TABLE OF CONTENTS - *Continued*

TABLE OF CONTENTS - *Continued*

TABLE OF CONTENTS - *Continued*

LIST OF ILLUSTRATIONS

LIST OF ILLUSTRATIONS- *Continued*

LIST OF ILLUSTRATIONS - *Continued*

LIST OF ILLUSTRATIONS - *Continued*

LIST OF ILLUSTRATIONS - *Continued*

LIST OF ILLUSTRATIONS - *Continued*

LIST OF ILLUSTRATIONS - *Continued*

LIST OF ILLUSTRATIONS - *Continued*

LIST OF ILLUSTRATIONS - *Continued*

LIST OF ILLUSTRATIONS - *Continued*

LIST OF ILLUSTRATIONS - *Continued*

LIST OF TABLES

ABSTRACT

This dissertation investigates superresolution applications in optical data storage systems. The performance of standard and superresolving magneto-optic data storage system are quantified by scalar diffraction modeling and experiments.

Classical resolution measures are reviewed. Background on superresolution definitions and their conceptual development in scanning optical microscopes, optical data storage, and image processing is presented. Figures of merit for quantifying the performance of the systems are reviewed, such as system transfer function, two-point response, focused spot size, and signal-to-noise ratio.

The description of the scalar diffraction modeling used to simulate an optical data storage system is reviewed. Operation of the magneto-optic data storage system and tradeoffs of superresolving techniques are discussed.

The signal and noise spatial distribution in the pupil of an optical data storage system are shown to be different. For a particular spatial frequency bandwidth, the signal and noise are concentrated in different regions of the pupil. This understanding allows the use of optical filters that partially equalize the system transfer function and increase the signal-to-noise ratio.

The main superresolution techniques investigated are those that increase the transmission of the higher spatial frequencies, or equalize the system transfer function, without changing the system cutoff frequency. The optical methods used to achieve superresolution are amplitude and phase filters placed in strategic system locations. One

location influences the properties of the focused spot such as the irradiance distribution and width of the central core. Another location does not change the focused spot at all, but does change the signal and noise properties of the system. Electronic filtering techniques are also used to increase the transmission of the high spatial frequencies. The amplitude and phase filter sensitivities to aberration are also investigated.

Optical properties of a new laser diode are investigated. The new laser diode has potential superresolving properties that are inherent to the device. Potential application of this device in an optical data storage device is presented.

Another method of increasing the transmission of higher spatial frequencies within the system bandwidth and beyond the system cutoff frequency is to use adaptive optical systems. Adaptive systems for optical data storage are also discussed.

CHAPTER 1 - INTRODUCTION

It has been known for some time that placing amplitude or phase filters in the pupil of scanning optical microscopes can change the system transfer function and influence resolution of the resulting image (Jacquinot and Roizen-Dossier 1964). Influencing resolution in this manner is regarded as a form of *superresolution.*

Optical resolution is interpreted in many ways and is ambiguously defined. The most famous of the definitions is due to Lord Rayleigh who said that two point sources are just resolved if the central maximum of one irradiance pattern coincides with the first zero of the other irradiance pattern. Rayleigh's definition is just one form of many two-point resolution definitions (den Dekker and van den Boss 1997). The goal of *superresolution* techniques is to handle poorly resolved spatial frequencies by using some kind of *a priori* information of the signal and extend the cut-off frequency, v_c, of the system.

A simple reflection-type scanning optical microscope is shown in Figure 1.1. A light beam from the source passes through a beam splitter and is focused onto the sample by an objective lens. The arm of the microscope that delivers the light from the source to the sample is known as the illumination path. The focused spot can be as small as 1μm or less. As the light spot scans across the sample the reflected light is collected by the objective lens and directed by the beam splitter to the detectors. The arm of the microscope that delivers reflected light from the sample to the detectors is known as the return path. Two types of scanning optical microscopes are nonconfocal systems that

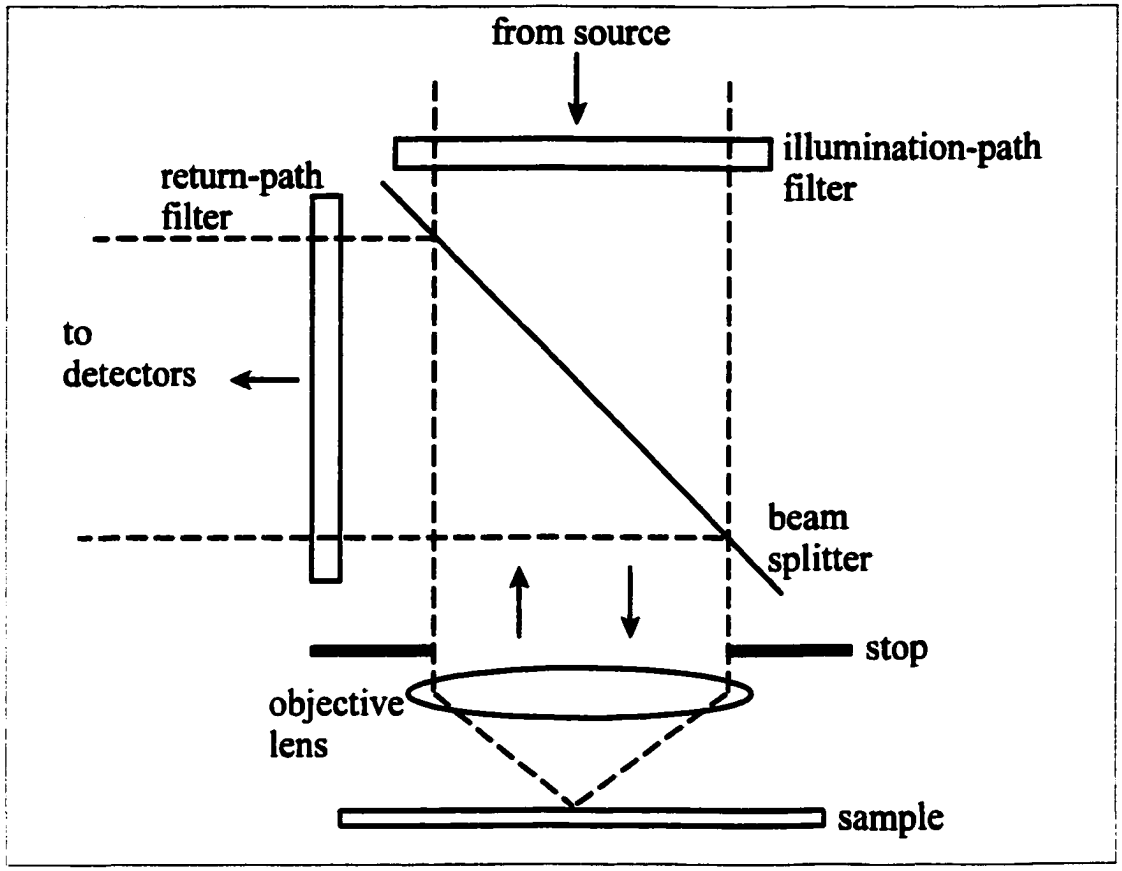

Figure 1.1. Reflection-type scanning optical microscope. Illumination-path filters or return-path filters can be placed in the optical system to change the system transfer function.

collect all of the energy on the detectors, and confocal systems that place pinholes in the detector plane.

A filter placed in the illumination path influences the distribution of focused energy on the sample. By appropriately choosing the amplitude and (or) phase distribution of the filter, the central lobe of the focused spot can be made narrower than the spot without the filter. This concept has been used in optical data storage devices to increase the density of recorded data (Ando, Yokota, and Tanoue 1993). Alternatively, a

filter can be placed in the return path (Walker and Milster 1995). The return-path filter does not influence the spot distribution on the disk, but it does influence the system transfer function.

The system transfer function of a laser scanning optical microscope is neither coherent nor incoherent, even though a coherent laser is used as a source. The effect can be described by observing the diffracted orders from varying spatial frequencies of reflectivity variations on the medium. There are often many diffracted orders observed depending upon the spatial frequency content of the reflectivity variations, but for the present discussion is limited to single tone sinusoidal variations. Two diffracted orders are produced in the return path from each spatial frequency component, as shown in Figure 1.2 for a low and high spatial frequency. The phase difference between the zero-

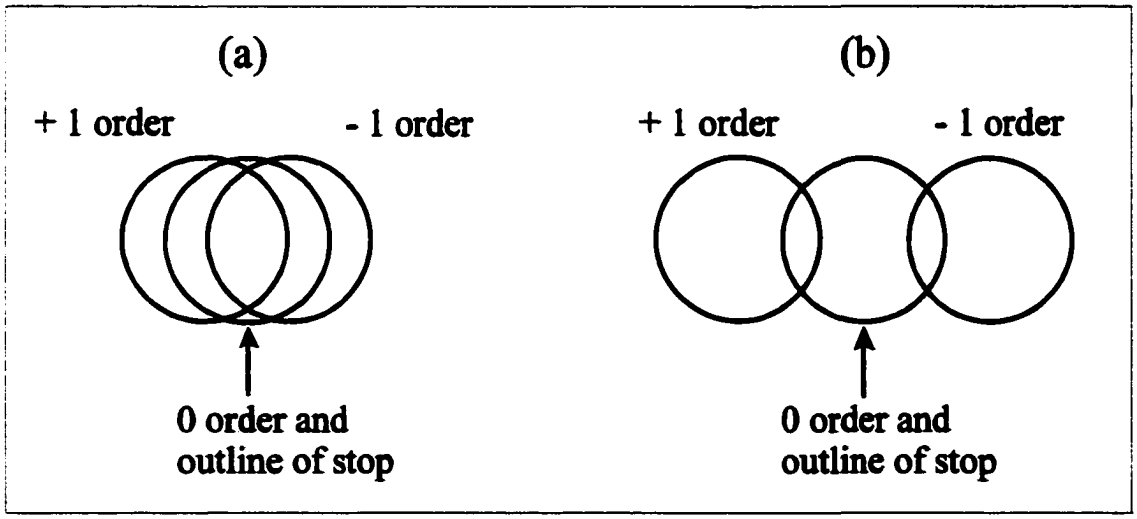

Figure 1.2. Diffracted orders produced in the return path for (a) low spatial frequency, and (b) high spatial frequency. As the object is scanned, a phase shift is introduced between the zero order and the ±1 diffracted orders that produces a modulation in data signal received at the detectors.

order reflected light and the ±1 diffracted orders changes as the object is scanned, which produces a modulation in the data signal received at the detectors. Interference only occurs in the overlap regions of the diffracted orders and the zero order. For low-frequency components there is a large overlap area. For high-frequency components the overlap area is decreased and spreads toward the edges of the pupil.

Consider the confocal detector arrangement of Figure 1.3a with uniform illumination in the pupil. Low spatial frequencies exhibit the first diffraction order overlapping the area of the pinhole, as shown in Figure 1.3a. As spatial frequency increases, the first diffraction orders separate, but the overlap area on the pinhole is not

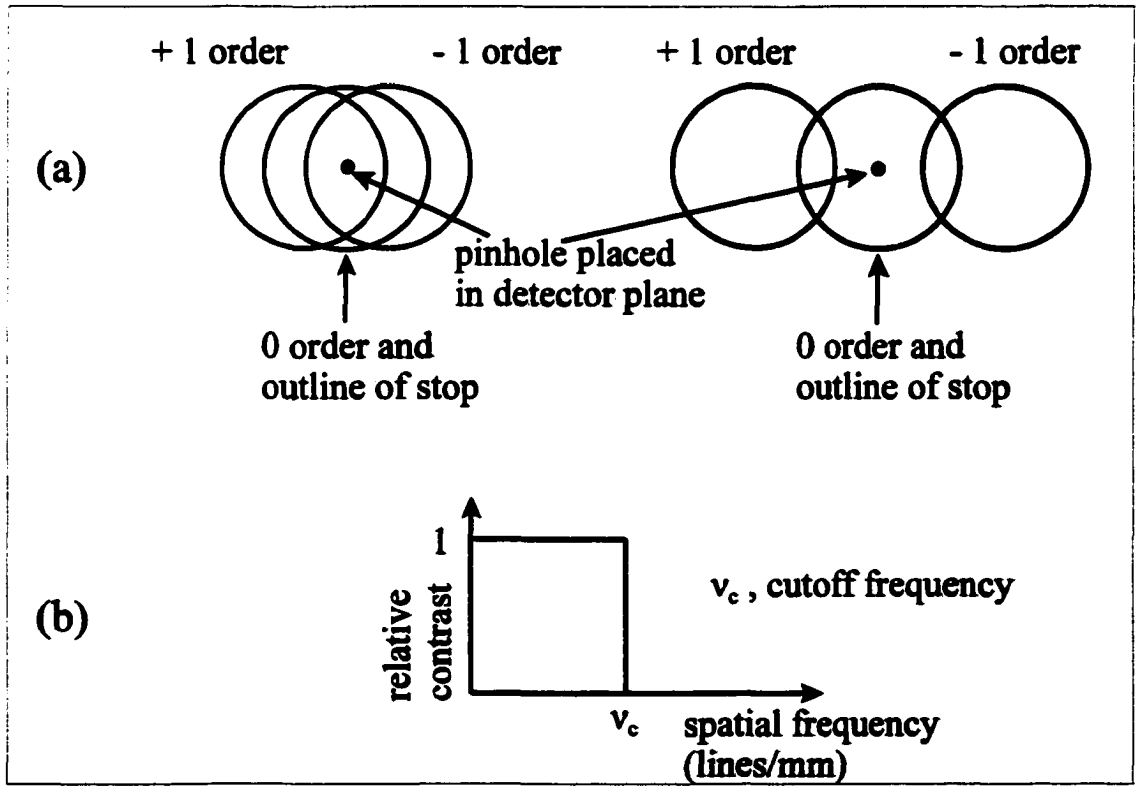

Figure 1.3 confocal detector arrangement, (a) ±1 diffracted order for low and high spatial frequency, (b) transfer function for this detector arrangement.

affected. As spatial frequency increases further, there is a frequency such that none of the light from the first diffraction order overlaps the pinhole area, as shown in Figure 1.3a. The result is a transfer function that has a uniform response out to a cutoff frequency v_c, as shown in Figure 1.3b. This behavior is characteristic of coherent imaging systems.

Now consider the nonconfocal detector arrangement of Figure 1.4a. Low spatial frequencies completely overlap the aperture. As spatial frequency increases, the first diffraction orders no longer completely overlap the aperture, as illustrated in Figure 1.4a. As spatial frequency increases further, the amount of overlap area decreases until there is no overlap. The cutoff frequency is now $2v_c$ as shown in Figure 1.4b. This behavior is

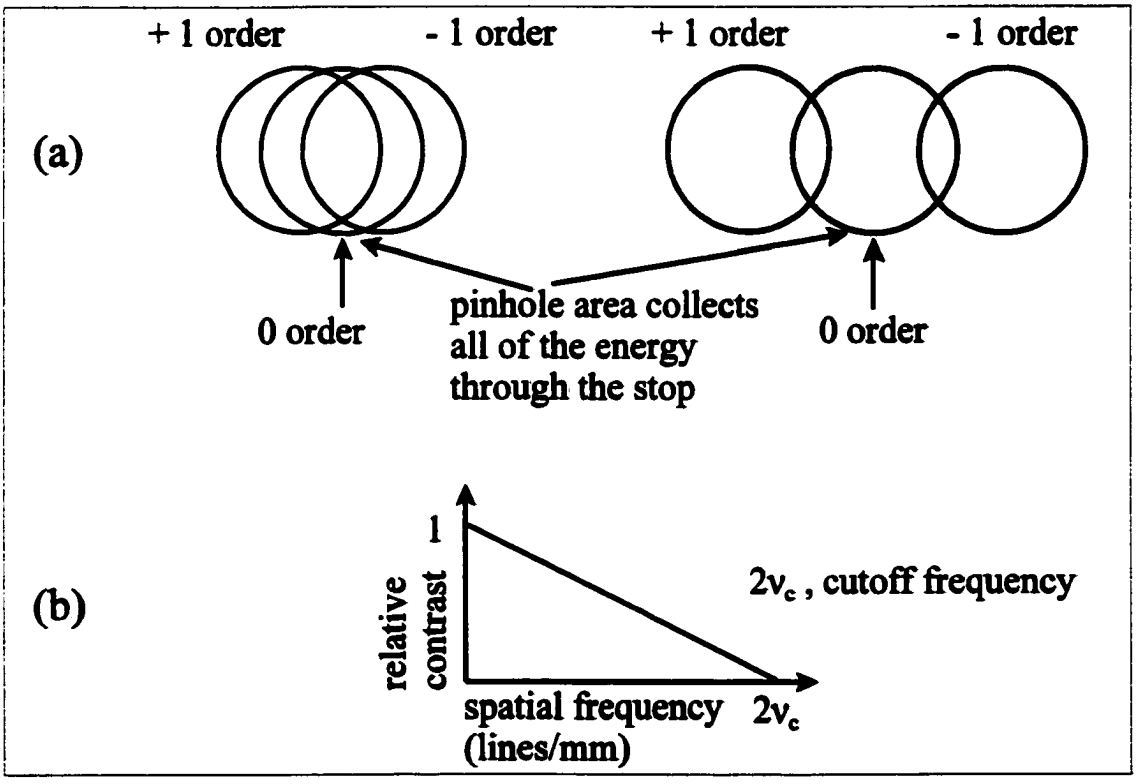

Figure 1.4 nonconfocal detector arrangement, (a) ±1 diffracted order for low and high spatial frequency, (b) transfer function for this detector arrangement.

somewhat characteristic of an incoherent imaging system and assumes that the collection and spot forming lens diameters are equal, which is the usual case in optical data storage.

One application of scanning optical microscopy is data storage. The basic operation of an optical data storage device is as follows. A laser diode is collimated, and the beam is circularized if necessary. Then it is focused down to the recording layer with an objective lens where data are encoded as marks in the in track direction. Grooves are present in the cross-track direction for tracking information. The objective lens is controlled by a voice-coil actuator that keeps the objective lens in focus and on track in accordance with the particular servo technique, such as astigmatic focus, push-pull, differential wax-wane, differential spot size, etc (Wang 1992).

In the same spirit as the description of the system transfer function for the scanning optical microscope, the collection of data marks along a track in the Fourier domain can be thought of as the spatial frequencies from which the diffracted orders reflected from the medium are observed. That is, marks along a data track act like a grating to the focused beam. The reflected light is composed of a zero order and ± 1 diffracted orders. Higher diffraction orders are present for low spatial frequencies of the grating, but we restrict our discussion to relatively high spatial frequencies where the ± 1 diffracted orders are the only significant components that return through the objective lens. The separation angle between the ± 1 diffracted orders depends on the spatial frequency of the grating. High spatial frequencies yield a large separation of the diffracted orders. Light collected by the objective lens contains the zero order and

portions of the ±1 diffracted orders. The signal amplitude received from the detectors depends on the modulation of the interference between the ±1 diffracted orders and the zero order. The amount of modulation depends on the overlap area. At low frequencies, the overlap area is a large percentage of the collection aperture. At high frequencies the overlap area is reduced, so the signal amplitude is reduced proportionally. The reduction of overlap area explains the falloff in the transfer function as the spatial frequency of the data pattern is increased.

Signal quality in an optical storage device depends greatly on the optical system transfer function that is used to write and read data patterns. Equalization of the system transfer function to obtain the desired frequency response is the basis of improved resolution, whether it is accomplished optically, electronically or with a combination of techniques. A typical optical data storage system transfer function exhibits reduced contrast at high frequencies relative to low frequencies, where contrast is defined by the ratio of the signal amplitude at frequency f to the maximum signal amplitude in the frequency range of interest, i.e., $C(f) = I_{sig}(f)/I_{max}$. One way to equalize the system transfer function is to apply *superresolution* methods in an optical storage device as a means to increase data capacity. This dissertation discusses theory, simulations, and practical implementation for several superresolution methods. Experimental results obtained on a magneto-optical data storage system are presented.

This dissertation is organized into several chapters. Definitions of resolution as understood classically, definitions of *superresolution* in the literature and present

conceptual developments of *superresolution* as applied in optical data storage systems, scanning optical microscopy, radar, and astronomy are reviewed in chapter 2. In chapter 3 simulations of a magneto-optic data storage system are presented that include applications of superresolution techniques. Background on diffraction modeling used in simulating a magneto-optic data storage system is also discussed in chapter 3. In chapter 4 experimental results from a magneto-optic data storage system are presented. In chapter 5 a recently developed laser diode is described that has potential superresolving properties. In chapter 6 future work and a summary of this dissertation are presented.

CHAPTER 2 - BACKGROUND

Definitions of resolution and superresolution are reviewed in this chapter. The difference between calculated and detected images is also discussed.

Superresolution is a topic of active research, and much has been published on the subject. There is more than one definition of superresolution, just as there is more than one definition of resolution. Each definition of superresolution is geared toward a particular specialization. Superresolution is defined in the disciplines of scanning optical microscopy, optical data storage, astronomy, radar, image processing, and oceanography. Background is presented in this chapter on superresolution methods presently used in these subject areas.

In Section 2A classical resolution criteria are reviewed. In Section 2B superresolution definitions are reviewed. Chapter 2 is summarized in Section 2C.

2A - Classical resolution

Classical resolution criteria are based on some measure of the system impulse response. The impulse response of an optical system is the image of a point object. For a perfect ideal imaging system the image of a point object is a point image, that is, a delta function. Unfortunately, nature does not allow delta function point images. The diffraction process blurs the image of a point object into a spot that has finite dimensions.

Resolution in scanning optical microscopes and in optical data storage devices depends greatly on the focused spot size. In order to obtain increased resolution, shorter wavelength sources can be used, like blue laser diodes when they become available, or

the numerical aperture of the objective lens can be increased. A higher numerical aperture solution leads to much more complicated servo controls and may involve immersion type objectives. Also, higher NA requires vector diffraction simulations to truly describe the focal plane irradiance. Decreasing λ or increasing NA are direct, classical means of improving resolution.

In order to understand superresolution, resolution in the classical sense is reviewed. In Section 2A.1, two-point resolution and focused spot size are discussed. In Section 2A.2, signal-to-noise ratio is discussed. In Section 2A.3, resolution based on the contrast of single tone patterns is discussed.

2A.1 - 2-point resolution

Consider the simple optical system of Figure 2.1. The complex object amplitude distribution $u_o(\sigma)$ is incident upon a lens and then passes through the transmitting aperture function $p_1(\sigma)$. The ideal thin lens has focal length f, diameter d and numerical aperture

$$NA = n \sin(\theta) \quad , \tag{2-1}$$

where n is the image space refractive index (usually $n \approx 1$) and θ is the marginal ray angle. The stop with diameter d is located in the rear focal plane. The value I_i, is which is proportional to the image irradiance, is defined as

$$I_i = \left|u_i(\mathbf{r}_0)\right|^2 \quad . \tag{2-2}$$

In general the object is located at a distance o from the lens and the image location is at a distance i from the lens. The image

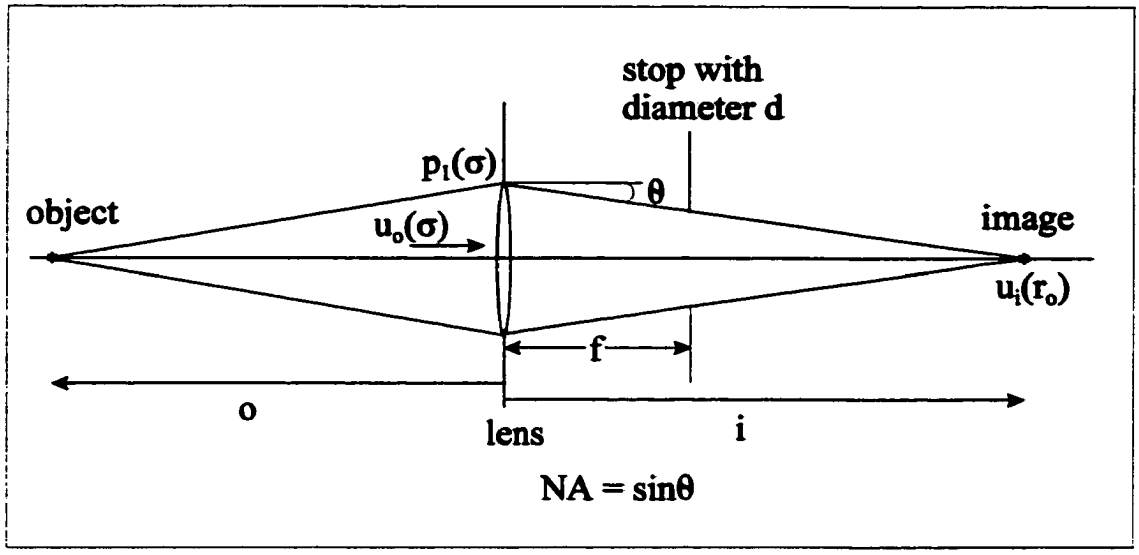

Figure 2.1. Thin lens optical system.

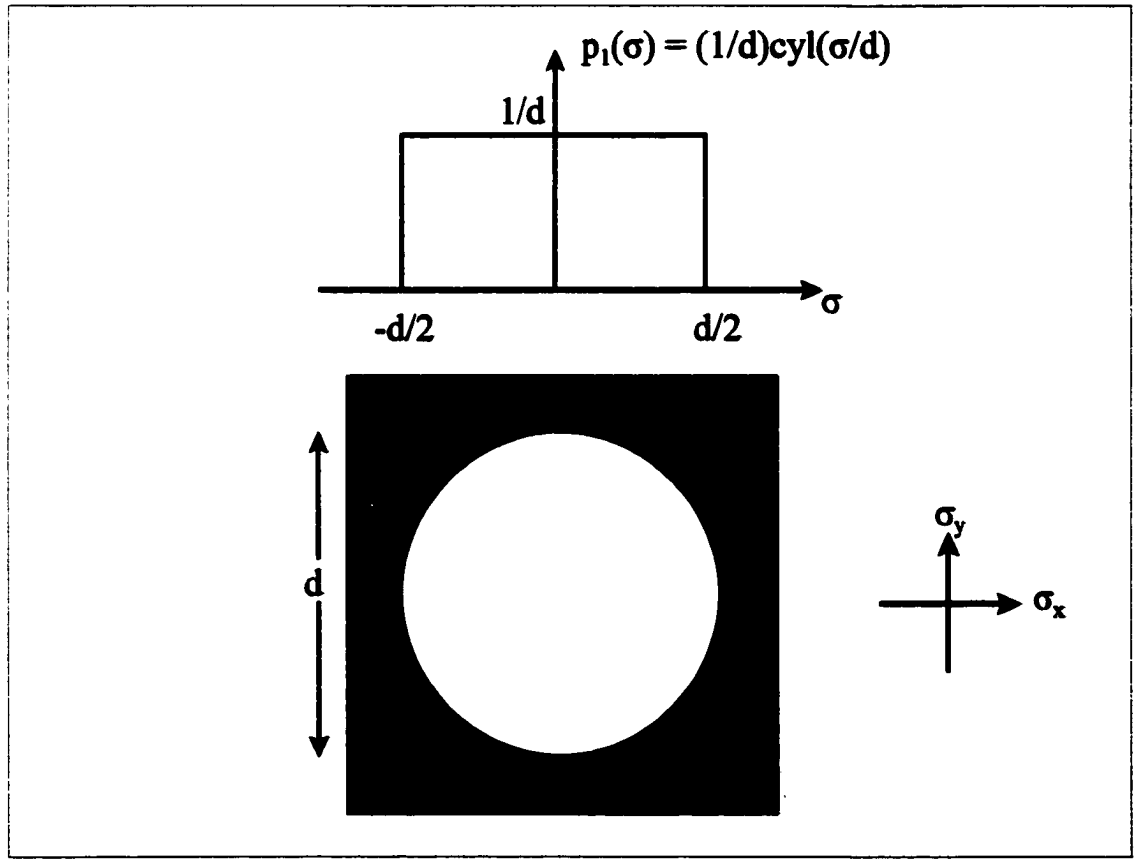

Figure 2.2. Transmittance function of aperture

distance is related to the object distance through the lens formula

$$\frac{1}{i} = \frac{1}{o} + \frac{1}{f} \quad , \tag{2-3}$$

The physical form of $p_1(\sigma)$ is typically a round hole, and is represented by

$$p_1(\sigma) = \frac{1}{d}\mathrm{cyl}\left(\frac{\sigma}{d}\right) \quad , \tag{2-4}$$

(Gaskill 1978), where

$$|\sigma| = \left(\sigma_x^2 + \sigma_y^2\right)^{1/2} \quad , \tag{2-5}$$

and d is the diameter of the circle with a uniform transmittance of 1/d, as shown in Figure 2.2.

For monochromatic uniform plane-wave illumination resulting from an on-axis coherent point source, the coherent impulse response, $h_c(r_o)$ is given by the classic Airy disk, as shown in Figure 2.3a. The incoherent impulse response, $h_i(r_o)$, is proportional to the square magnitude of $h_c(r_o)$, as shown in Figure 2.3b. The Airy disk is given by the Fourier transform of the (1/d)cyl(σ/d) function, which is

$$\Im\left\{\frac{1}{d}\mathrm{cyl}\left(\frac{\sigma}{d}\right)\right\} = \left(\mathrm{somb}\left(dr_0\right)\right) = \frac{2J_1\left(\pi dr_0\right)}{\left(\pi dr_0\right)} \quad . \tag{2-6}$$

$J_1(r_o)$ is a Bessel function of the first kind.

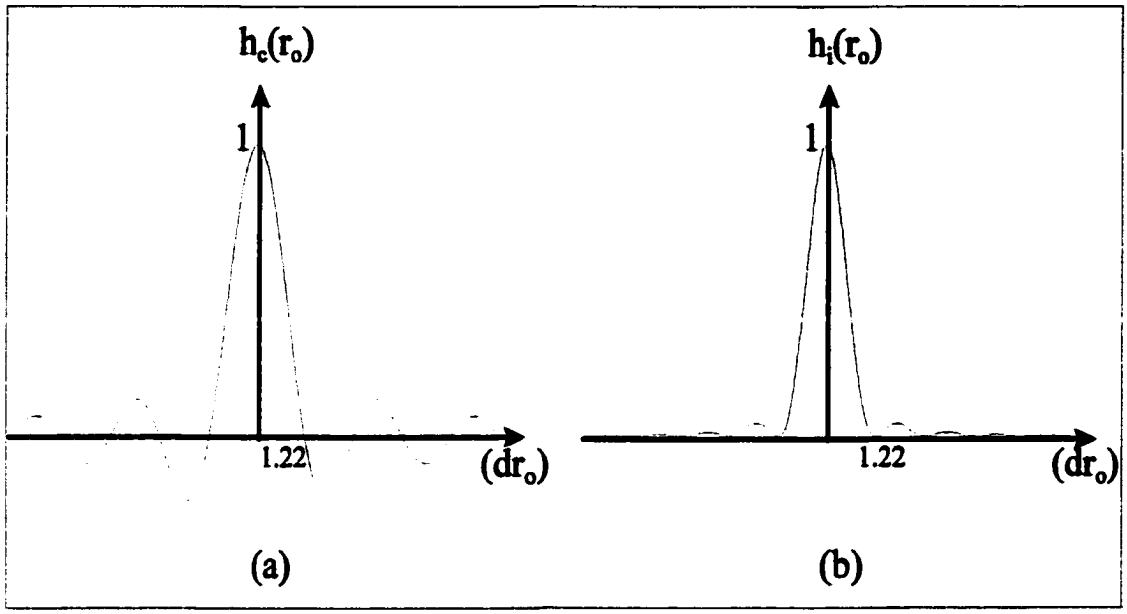

Figure 2.3. (a) $h_c(r_0)$, coherent impulse response, (b) $h_i(r_0)$, incoherent impulse response.

There are some important features to note in Figure 2.3. The first zero location in both the coherent and incoherent patterns occur at the location $dr_o = 1.22$, where r_o is the image plane coordinate. $r_o = 0.61\lambda/NA$ is the radius of the 1st zero, and the diameter of the central core is $1.22\lambda/NA$. The focused spot size is commonly given as λ/NA, which is approximately the $1/e^2$ width of the central lobe in the irradiance pattern.

If there is another point source in the object plane that is slightly displaced from the first point source and incoherent with respect to it, an additional plane wave is incident upon the lens aperture at a small angle. The result in the image plane is two overlapping Airy disk irradiance patterns. Since the objects are incoherent, what is observed in the image plane is the simple addition of the two image irradiance patterns.

Lord Rayleigh's criterion states that two point sources are just resolved if the central maximum of the first irradiance pattern coincides with the first zero of the second

irradiance pattern, as shown in Figure 2.4a. The diameter of the central core is at the heart of Rayleigh's resolution criterion. As the numerical aperture increases, the diameter of the central core decreases, and the cut-off frequency $v_c=2NA/\lambda$ of the system transfer function increases. Thus, as the width of the central core decreases, the optical system resolves finer and finer object detail and provides better resolution.

A second popular resolution definition is the *Sparrow criterion*, which states that two point images are just resolved if the distance between the two point sources is such that the second-order derivative of the composite irradiance distribution at the center of

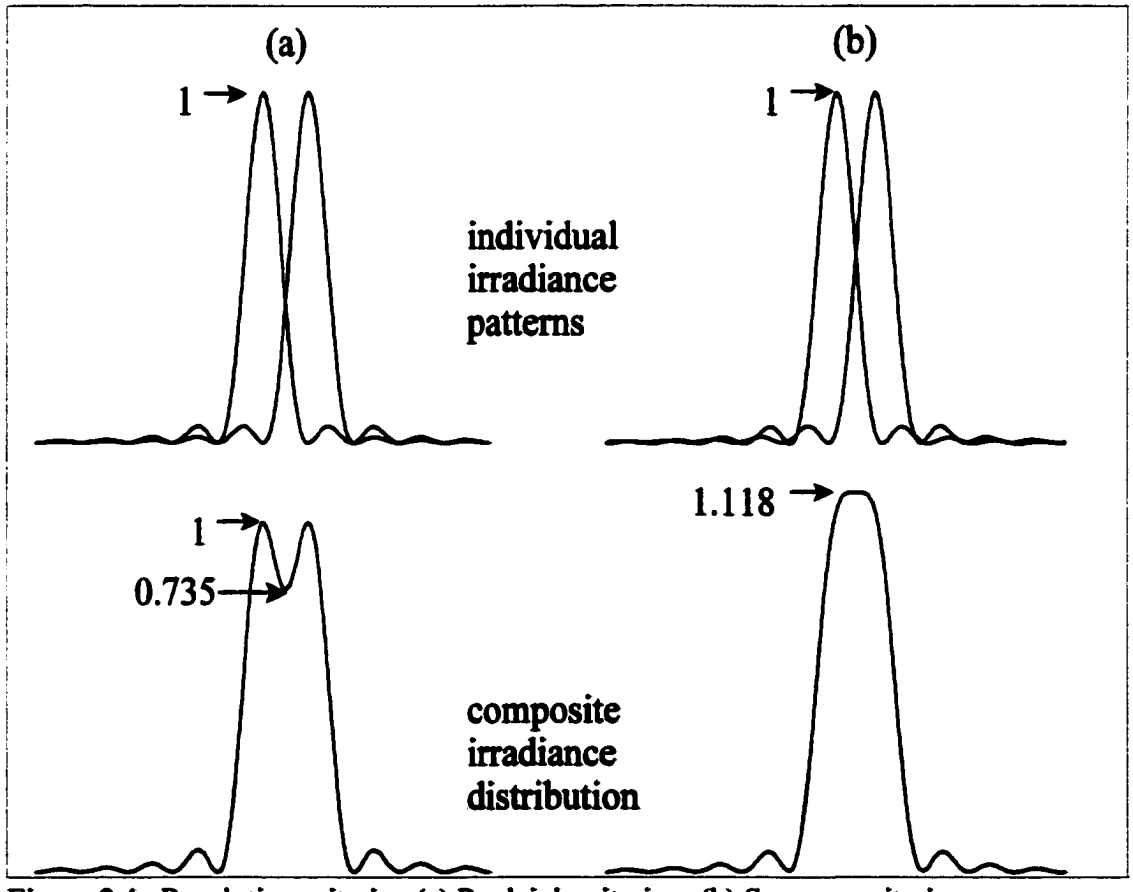

Figure 2.4. Resolution criteria. (a) Rayleigh criterion, (b) Sparrow criterion.

the diffraction image just vanishes, as shown in Figure 2.4b. This criterion is based on placing the sources just close enough so that an irradiance measurement would be just past the point of being able to detect the central dip between the two images.

The Rayleigh and Sparrow performance measures are based on mathematical calculations of system parameters and are very good starting points for expected system performance. If a noise-free, and error-free irradiance measurement existed, the Rayleigh and Sparrow criteria could be realized as perfect indicators of resolution. However, ideal and noise-free images do not exist in the real world. Starting with two image points at

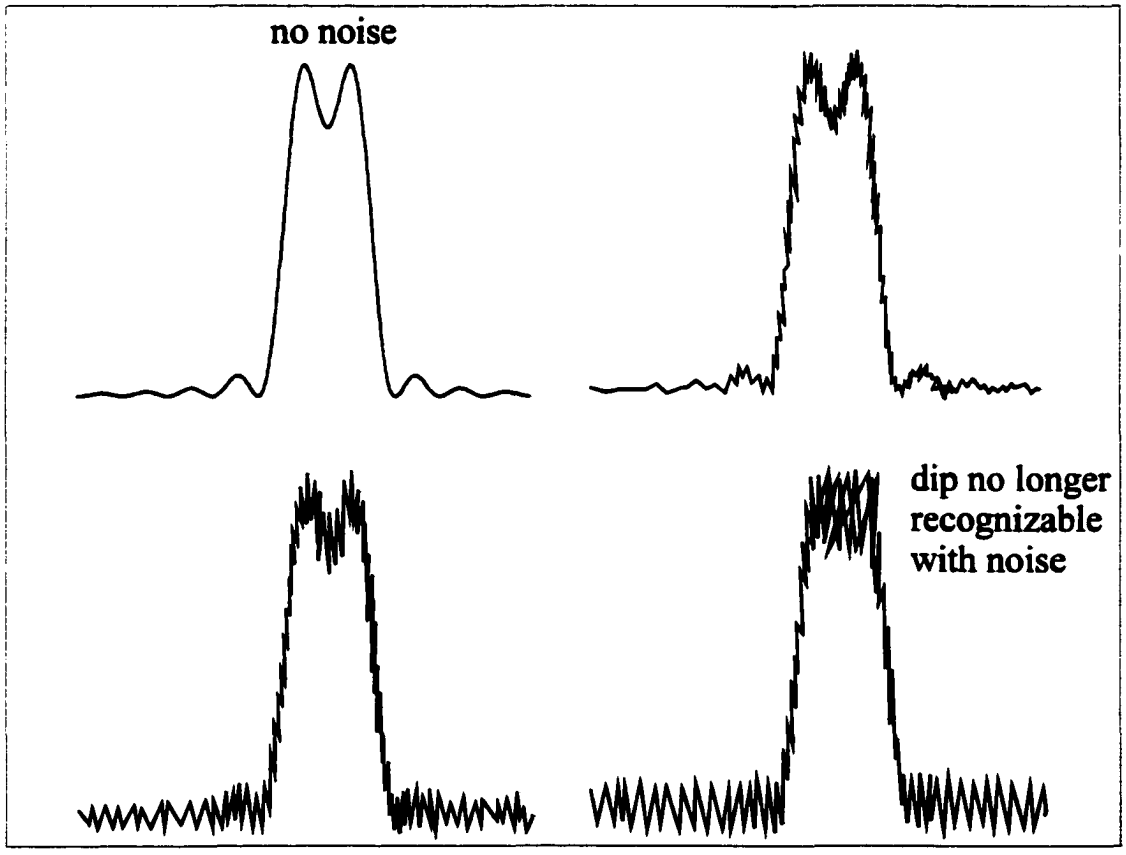

Figure 2.5. progressive amounts of noise added to two point images separated by the Rayleigh criterion.

the *Rayleigh criterion*, which results in a pronounced dip in the center of the image, and adding progressively larger amounts of noise to the measurement a particular amount of noise makes the central dip in the image no longer discernable, as shown in Figure 2.5. At this point the two images are not resolved according to the Rayleigh criterion. Figure 2.5 illustrates that noise can limit the resolution of detected images even though a mathematical calculation based on NA and λ indicates that they are resolvable.

2A.2 - Signal-to-noise ratio

It is pointed out in the literature (den Dekker and van den Bos, 1997) that resolution is limited by systematic and random errors, as illustrated in the example of Figure 2.5. Therefore, the resolution of *detected* images rather than *calculated* images should be the concern. Quantities of interest such as signal power, noise power, and signal-to-noise ratio are now defined in this context. A simple photoconductive circuit is considered, such as a pin photodiode in a transimpedance amplifier configuration. The current generated from each detector element is proportional to the irradiance incident upon it. This theory is equally valid with other detection geometries.

Noise is defined as any detected current modulation other than the desired signal itself. Noise sources are present in the detection electronics and the object/source light distribution. *Signal power* P_{sig} is the electrical power of the desired signal current and may be just a fraction of the current generated from the total light power incident on the detector. *Noise power* P_N is the electrical power of the undesired modulation. *Signal-to-noise-ratio (SNR)* is the ratio of the above quantities,

$$SNR = \frac{P_{sig}}{P_N} \quad , \tag{2-7}$$

and is a figure of merit for the system.

2A.3 - Resolution based on the contrast of single tone patterns

The system transfer function of a scanning optical microscope or an optical data storage system is neither coherent or incoherent, but is partially coherent. The partially coherent transfer function of an optical data storage system has characteristics of both coherent and incoherent systems. The basics of coherent and incoherent image formation are now reviewed.

Since the amplitude and phase of the diffraction image $u_i(\mathbf{r}_o)$ may be regarded as the output of a linear filter (Gaskill, 1978) the *coherent transfer function* $H(\mathbf{v})$ of the image forming system is the normalized Fourier transform of the coherent impulse response $u_i(\mathbf{r}_o)$. For the example optical system shown in Figure 2.1, $H(\mathbf{v})$ is just a scaled version of the aperture function $p_1(\boldsymbol{\sigma})$,

$$H(v) = cyl\left(\frac{v\lambda}{NA}\right) \quad , \tag{2-8}$$

as shown in Figure 2.6a. If the object is considered as a collection of single-tone patterns with on-axis plane wave illumination, Equation (2-8) describes the relative reduction of the amplitude of each object spatial frequency in the image. One important feature to note of the coherent transfer function is the uniform response out to cutoff frequency

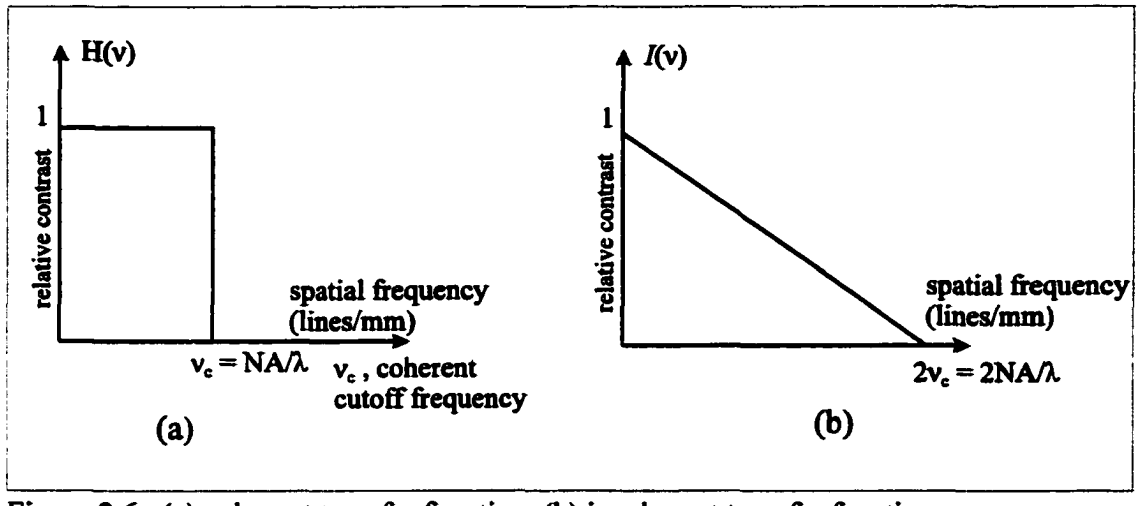

Figure 2.6. (a) coherent transfer function, (b) incoherent transfer function.

v_c=NA/λ where NA is the numerical aperture in image space. After v_c the response of the system is zero.

The *incoherent transfer function*, *I*(v), of this imaging system is given by the Fourier transform of the incoherent impulse response and is the normalized autocorrelation of the aperture function $p_1(\sigma)$,

$$I(v) = \mathrm{cyl}\left(\frac{v\lambda}{NA}\right) * \mathrm{cyl}\left(\frac{v\lambda}{NA}\right) \quad , \qquad (2\text{-}9)$$

as shown in Figure 2.6b. The incoherent object can be considered as a collection of single-tone patterns that are diffusely illuminated. Equation (2-9) describes the relative reduction of the amplitude of each object spatial frequency in the image. Two important features to note are the rolling off of the incoherent system response out to a cutoff frequency of $2v_c$=2NA/λ and after $2v_c$ the response of the system is zero. That is, with

incoherent illumination, the high-frequencies are attenuated relative to the low-frequencies. In practice the theoretical cutoff frequency is not realized due to reduced signal-to-noise-ratio (SNR) at high frequencies. The required SNR and contrast level dictate the useable frequency range. The highest possible frequency passed by the system is $2NA/\lambda$.

2B - Superresolution definitions

Performance measures, such as cutoff frequency of the system transfer function, relative contrast, focused spot size, and SNR are described in section 2A. Superresolution methods that improve these measures beyond what is expected from the calculated system performance with uniform illumination are now reviewed.

Three definitions of superresolution are presented in Table 2.1. Definition #1 is used by researchers in scanning optical microscopy and optical data storage. Definition #2 is used by researchers in astronomy and radar. Definition #3 is recent (Mendlovic,1997) and has many potential applications.

DEFINITION #1:	increase the transmission of high spatial frequencies relative to the low spatial frequencies.
DEFINITION #2:	restore lost frequency information beyond the system cutoff frequency.
DEFINITION #3:	space-bandwidth product(SBP) adaptation, so that the SBP of the object is matched to the SBP of the system.

Table 2.1 Superresolution definitions

Methods to achieve superresolution according to Definition #1 include optical amplitude and phase filtering, noise suppression, and electronic filtering. Image processing algorithms are used in astronomy and radar to achieve superresolution according to Definition #2. To achieve superresolution according to Definition #3 a secondary optical system is used to either adapt the space-bandwidth of the object to the space-bandwidth of the system or adapt the space-bandwidth of the system to the space-bandwidth of the object.

Superresolution Definition #1 is expanded on in Section 2B.1, which also discusses the optical and electronic filtering methods used to increase the transmission of high spatial frequencies relative to low spatial frequencies. Superresolution Definition #2 is expanded on in Section 2B.2, which discusses image processing routines used to restore lost frequency information beyond the system cutoff frequency. Superresolution Definition #3 is expanded on in Section 2B.3, which discusses the space-bandwidth product adaptation of an object to a system.

2B.1- Superresolution definition #1

Superresolution DEFINITION #1: increase the transmission of high spatial frequencies relative to the low spatial frequencies.

Altering the relative transmission of the object low frequencies relative to the transmission of the object's high frequencies can influence the image dramatically. In

systems that are used at or near the limit of resolution, it is desirable to increase the high-frequency content of the image so that small features can be more easily resolved.

The process of making the system transfer function uniform is known as *equalization.* Equalization can be accomplished by cascading a second linear system $H_2(v)$ with the first linear system $H_1(v)$ in order to produce a uniform response out to $v=2v_c$, as shown in Figure 2.7. For example, in a scanning optical microscope (SOM), the cascaded system $H_2(v)$ can be a simple peak gain electronic filter that boosts the high frequencies relative to the low frequencies. This type of electronic filtering has the

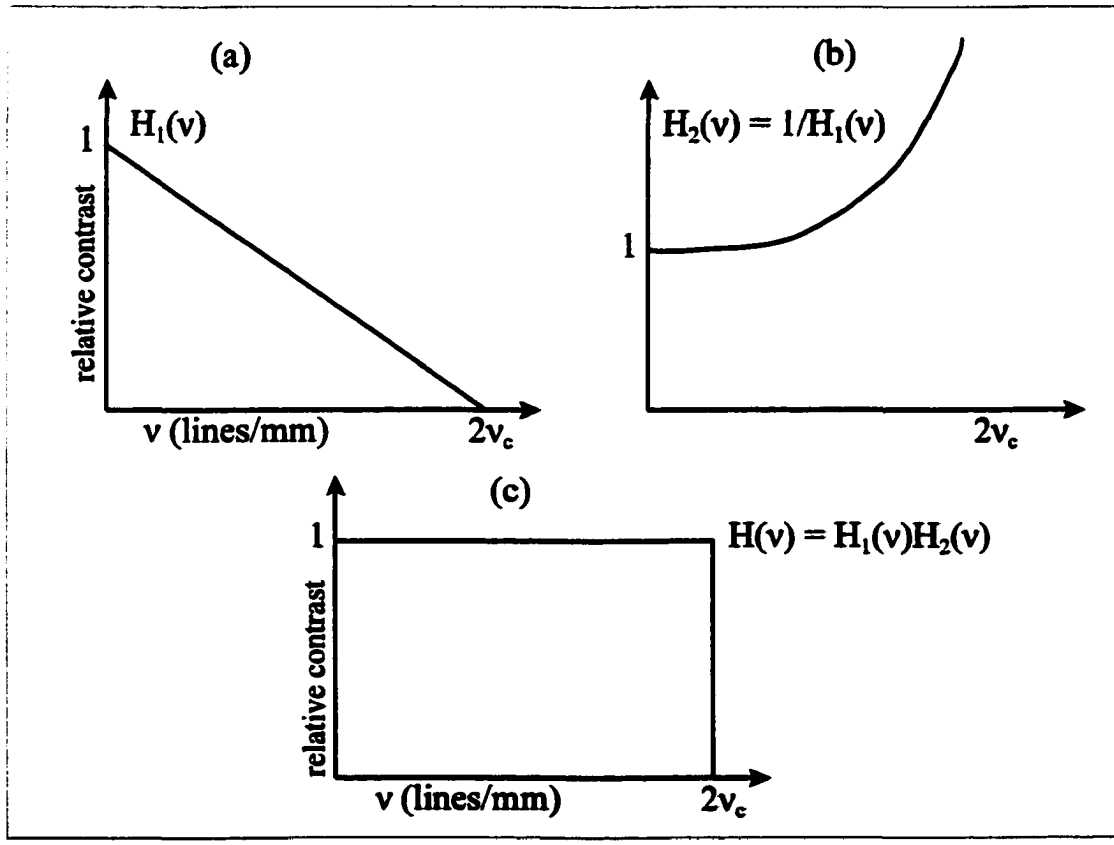

Figure 2.7. Equalization of system transfer function. (a) original system transfer function, (b) equalizing transfer function, (c) combined system transfer function.

desired benefit of increasing the relative amplitude of the high spatial frequencies. However, the noise is increased along with the signal, so the SNR remains unchanged.

Optical filters can also be used to modify the system transfer function. Figure 2.8 shows the unfolded light path for a reflection-type SOM. In the focal plane a target with reflectivity $r(\mathbf{r}_o)$ is located. The field distribution just after reflection is $u_r(\mathbf{r}_o)$ and is given by the product of $u_i(\mathbf{r}_o)$, the image field or focused spot distribution, and $r(\mathbf{r}_o)$, that is $u_r(\mathbf{r}_o) = u_i(\mathbf{r}_o)r(\mathbf{r}_o)$. The light collected by the objective lens in the return-path is $u_c(\sigma)$ and is given by

$$u_c(\sigma) = \left[\Im\{u_r(\mathbf{r}_0)\}\right]P_2(\sigma) \quad . \tag{2-10}$$

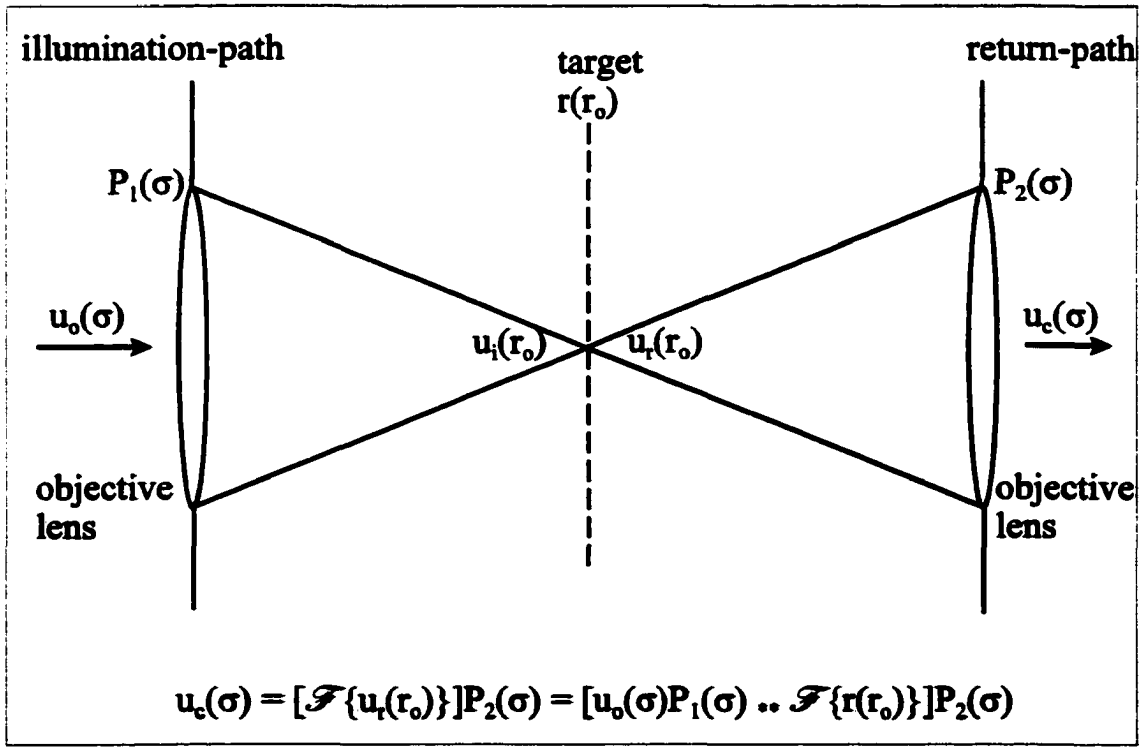

Figure 2.8. Unfolded light path for a reflecting scanning optical microscope SOM.

Usually $P_2(\sigma) = P_1(\sigma)$, but they are kept distinct in order to allow for separate filtering functions in the return path and illumination path.

Section 2B.1.A discusses amplitude filtering. Section 2B.1.B discusses phase filtering. Section 2B.1C discusses the combination of amplitude and phase filtering.

2B.1.A- Amplitude filtering

Amplitude filtering improves the optical data storage system in its ability to write and read smaller marks. They partially equalize the system transfer function and can suppress noise. Amplitude filtering is done in either the illumination path, return path, or both.

One method of amplitude filtering is to place an opaque disk in the middle of the aperture, which creates an annular region of illumination, as shown in Figure 2.9. The mathematical representation of this combination aperture is represented by

$$P_1(\sigma) = \mathrm{cyl}\left(\frac{\sigma}{d2}\right) - \mathrm{cyl}\left(\frac{\sigma}{d1}\right) \quad . \qquad (2\text{-}11)$$

Figure 2.9 also shows the definition of the obscuration ratio, $\varepsilon = d1/d2$, which is the ratio of the inner opaque circle diameter to the outer aperture diameter.

When amplitude filters are placed before the objective lens they generally have the effect of narrowing the central core of the light spot focused on the target. Amplitude filters also lower the peak irradiance and redistribute the energy into the first few rings of the Airy pattern. This redistribution has the desired action of narrowing the central core,

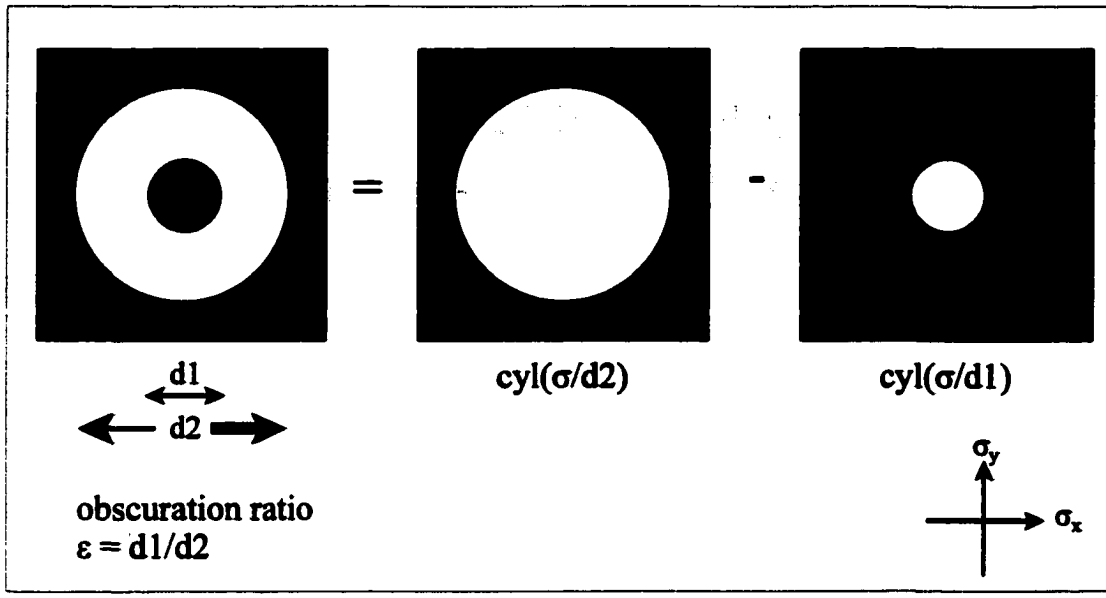

Figure 2.9. Amplitude filtering using a central obscuration.

which increases resolution in the Rayleigh sense, and the undesired consequence of lowering the peak irradiance and increasing sidelobe energy. Even though amplitude filters narrow the central core of the focused spot, the cutoff frequency of the system transfer function remains unchanged. There are a number of papers published on obscured optical systems that describe the effect of the obscuration ratio on the focused spot properties (Mahajan, 1986). More detail on specific design examples using this technique is presented in Chapter 3.

This type of amplitude filtering is also investigated by researchers of scanning optical microscopy and optical data storage. Z. Hegedus (Hegedus, 1985) investigated amplitude filters having multiple annular zones of transmittance applied to a confocal scanning microscope. He found that by using multiple zones the side lobe levels could be decreased from the case of a single opaque annular disk, but at the expense of increasing

the central core width compared to the system using the single opaque annular disk.

Y. Yamanaka (Yamanaka, 1990) investigated amplitude filters having an opaque stripe (rectangle) down the center of the of the objective lens applied to an optical data storage system. Having a rectangular amplitude filter breaks the circular symmetry in the focused spot. The consequence of this type of filter is that the central core reduction occurs in only one dimension while the other dimension remains unchanged. The result of this work was a decrease in the central core width to 80% of the unobscured case resulting in an increase in the linear recording density by a factor of 1.2. The disadvantage of this system is that a more complex optical system must be used where the sidelobes are spatially filtered out of the reflected light by a slit before the signal reaches the detectors in order to provide for acceptable signal quality.

T. Tanabe (Tanabe, 1995) investigated the same amplitude filtering technique as Yamanaka while using an alternative technique to suppress the effects of the sidelobes on the readout signal quality. Rather than using a slit to spatially filter the sidelobes out of the reflected light, an electrical equalizer is used to pass the signal read from the main central core while suppressing the sidelobe signals. This technique of sidelobe elimination has the advantage of no additional optics to readout the signal at the cost of more complicated electronic circuits.

Amplitude filters can also be placed in the return path, where they have no effect on the shape of the focused light spot (stylus). One way to filter in the return path is to place a shading band in the $p_2(\sigma)$ plane to block the central portion of the aperture, as

shown in Figure 2.10. This new aperture with the filter can be mathematically represented by two shifted cyl functions multiplied by a non-shifted cyl function,

$$p_2(\sigma) = \mathrm{cyl}\left(\frac{\sigma}{d}\right)\left[\mathrm{cyl}\left\{\frac{\left((\sigma_x-\sigma_{x0})^2+\sigma_y^2\right)^{1/2}}{d}\right\}+\mathrm{cyl}\left\{\frac{\left((\sigma_x+\sigma_{x0})^2+\sigma_y^2\right)^{1/2}}{d}\right\}\right] . \quad (2\text{-}12)$$

The shading band in the return-path alters the transfer function of the system. This can be qualitatively understood by recognizing that the transfer function of Figure 1.4 can be thought of as a collection of diffracted orders from the data pattern. The amount of contrast, or modulation, depends on the overlap area of the ±1 diffracted order with the zero order. At low spatial frequencies of the data pattern some of the overlap area is blocked, which reduces the signal amplitude at the detectors, as shown in Figure

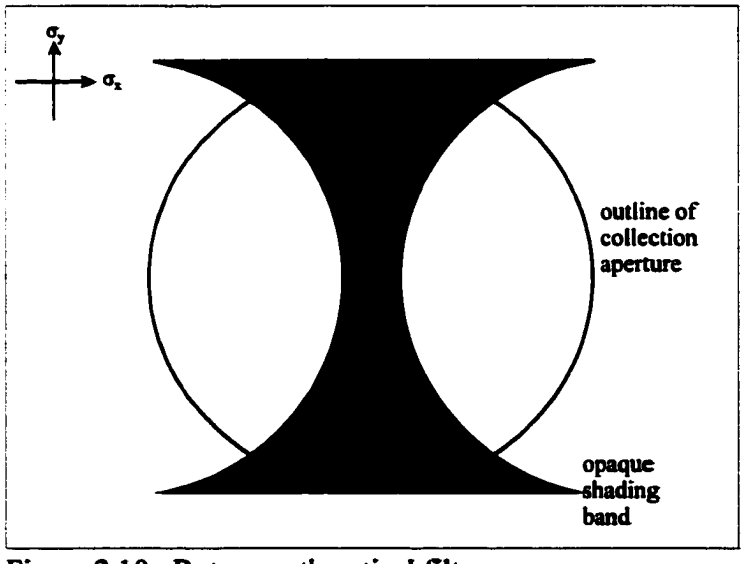

Figure 2.10. Return-path optical filter.

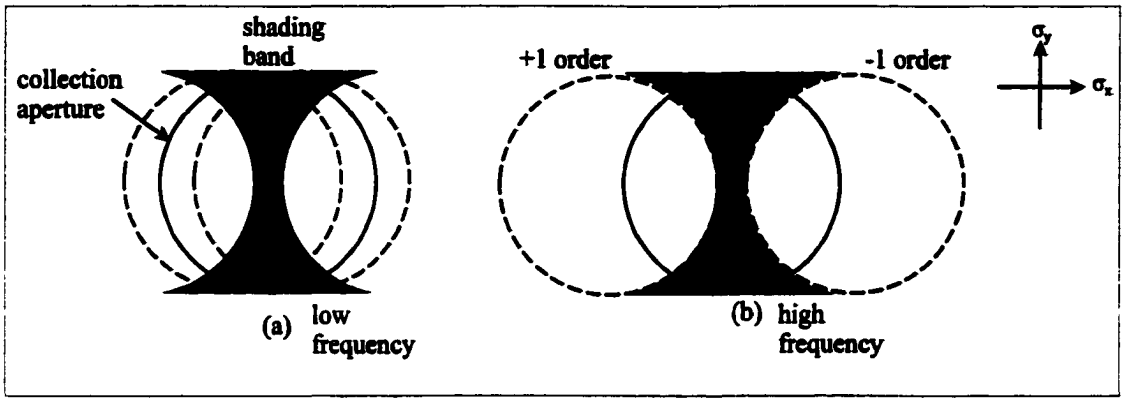

Figure 2.11. Action of the return-path optical filter on the diffracted orders, (a) for low frequency, (b) for high frequency.

2.11(a). At high spatial frequencies the overlap area is unaffected, so the signal amplitude is unchanged, as shown in Figure 2.11(b). When placed in the return-path, amplitude filters have the effect of partially equalizing the system transfer function by attenuating the low frequencies relative to the high frequencies.

The shading band in the return-path also alters the SNR of the system. This can be understood as follows. For low spatial frequencies light is attenuated that contributes to the signal by the nature of the large overlap region of the diffracted orders, so a reduction in signal amplitude in the low frequency region is experienced. The attenuated light also contributes to noise, since most of the noise sources considered follow the irradiance distribution. At low frequencies the signal power P_{sig} is attenuated more than the noise power P_n, and as a consequence there is reduced contrast and reduced SNR at low frequencies. However, a given high spatial frequency experiences no attenuation because the diffracted orders for this frequency do not overlap with the shading band. The shading band is still blocking light that contributes to P_n, so there is the desired

action of increasing the SNR at the high spatial frequencies.

The mathematical representation of the system transfer function for the confocal SOM of Figure 1.4, the mode of optical data storage, has been derived (Milster, 1992). The system transfer function can be separated in two parts. The first part describes the properties of the medium or target, M(v:v′). The second part describes the properties of the optical system. The optical system transfer function is described by the function C(v,v′), and can be written as a function of $p_1(\sigma)$ and $p_2(\sigma)$ and illumination conditions (uniform or Gaussian) and is given by

$$C(\nu;\nu') = \iint_{\infty} h_c(\mathbf{r}_o)h_c^*(\mathbf{r}_o')\times\exp[2\pi j(\nu\cdot\mathbf{r}_o - \nu'\cdot\mathbf{r}_o')]\,d\mathbf{r}_o d\mathbf{r}_o' \qquad (2\text{-}13a)$$

$$= \iint_{\infty} P_2(\sigma)P_2^*(\sigma')P_1(\sigma+\lambda f\nu)P_1^*(\sigma'+\lambda f\nu') \qquad (2\text{-}13b)$$

$$\times\exp[-\frac{|\sigma+\lambda f\nu|^2}{\omega^2}]\times\exp[-\frac{|\sigma+\lambda f\nu'|^2}{\omega^2}]\,d\sigma\,d\sigma' \quad .$$

Equation (2-13a) is in terms of the optical system coherent impulse response, and Equation (2-13b) is for Gaussian illumination with beam width parameter ω. From C(v,v′) the influence of the return-path and illumination-path filters on the amount of change in the optical system transfer function can be predicted.

Ultimately it is the signal current at the data detectors that is of interest. The

expression for the signal current i_{sig} at the detectors is given by,

$$i_{sig}(\mathbf{r}_s) = \iint_{\infty} C(\nu;\nu')M(\nu;\nu')\exp\left[-2\pi j(\nu-\nu')\cdot\mathbf{r}_s\right]d\nu d\nu' \quad , \qquad (2\text{-}14)$$

where M(ν:ν') is a function of the medium. More detail on specific design examples using amplitude filtering is presented in Chapter 3.

2B.1.B- Phase filtering

Phase filtering, as with amplitude filtering, improves the optical data storage system in its ability to write and read smaller marks. Phase filters can also be used to partially equalize the system transfer function.

Phase filtering is accomplished by placing optical path difference (OPD) masks in the optical system. Phase filters are placed before the objective lens. They have the effect of narrowing the central core of the focused spot while lowering the peak irradiance and redistributing the energy into the first few rings of the Airy pattern. This redistribution has the desired action of increasing resolution in the Rayleigh sense and the undesired consequence of lowering the peak irradiance and increasing sidelobe energy. The consequences are very similar to those of amplitude filtering. However, the phase filters have been shown to perform better in the sense that the magnitude of the undesirable consequences are less than for the amplitude filtered source (Sales, 1997). Sales (Sales, 1997) also showed that the least reduction in peak irradiance occurs for phase filters. He also derives a formula to predict the reduction in peak irradiance as a function of the desired reduction in central core width.

H. Ando (Ando, 1992) discusses the optimization of phase filters to achieve focused spot performance criteria that have the desired effects of narrowing the central core and reasonable sidelobe levels. Ando's three-portion phase filter is shown in Figure

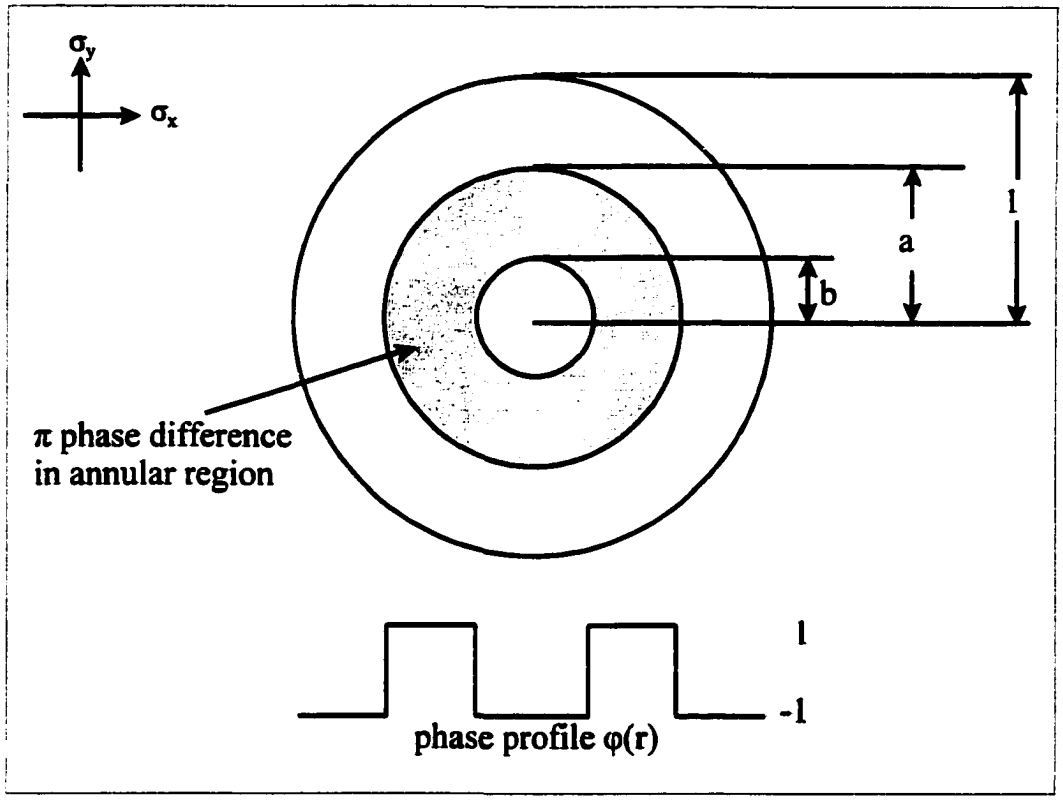

Figure 2.12. Three portion phase filter.

2.12. The filter equation is given by,

$$\phi(r) = \mathrm{cyl}(r) - 2\left\{\mathrm{cyl}\left(\frac{r}{2a}\right)\right\} + 2\mathrm{cyl}\left(\frac{r}{2b}\right) \quad , \qquad (2\text{-}15)$$

where the first term is the normalized exit pupil.

Ando shows that for a given reduction in the central core width, the reduction in the on-axis irradiance is not as much as for the amplitude filters, and the side-lobe level is not as high. Also, the side-lobe level experiences a further reduction by increasing the number of annular regions of phase shift.

2B.1.C- Combination amplitude and phase filtering

Frieden (Frieden, 1969) theoretically showed the possibility of aperture synthesis where a given small aperture may be made to form images as if it were from a larger uniform aperture . The disadvantages of this approach are that the peak irradiance reduces much faster than for either the amplitude or phase filters applied individually and the difficulty in manufacturing the appropriate coating to achieve this pupil distribution.

Frieden derived a pupil function to achieve arbitrarily perfect imagery over a given field of view. His example showed the central core width reducing to 20% of the unfiltered case, with sidelobe levels comparable to the unfiltered focused spot. The derived pupil function has an amplitude variation that behaves as a cosine function with increasing frequency and amplitude at the edges of the pupil. The negative portions of the cosine are interpreted as a phase change in that particular pupil zone.

2B.2- Superresolution definition #2

> *Superresolution* DEFINITION #2: restore lost frequency information beyond the system cutoff frequency.

Superresolution in astronomy implies the restoration of lost frequency information outside the system bandwidth, thereby extending the system cutoff frequency. The conventional means of increasing resolution in astronomy is to use larger diameter primary mirrors. Besides directly increasing the diameter of the primary mirror, a technique using multiple aperture telescopes is used where many smaller diameter mirrors are used together to produce a very large diameter mirror (Meinel, 1983). Image processing is done on the detected images to reduce artifacts from the structure that makes up the dead space between the apertures and the result approaches the image resolution from a mirror with the multiple aperture diameter. This technique overcomes the difficulty to manufacture large diameter mirrors of the potential size of a multiple aperture, and is a direct classical way to increase resolution.

Superresolution in radar, as in astronomy, also implies restoration of lost frequency information. The image processing techniques are the same algorithms used in astronomy. The most direct way to increase resolution in real aperture radar is to use shorter wavelength sources and longer antennas. However, there is a limit to the size of an antenna that can be flown on an aircraft. The antenna length quickly exceeds the length of the aircraft for the desired resolution. A technique called synthetic-aperture radar makes the antenna appear to be much larger than it really is (Cutrona, 1961). The length of the synthetic antenna can be as long as the length of the flight. The receiver collects, and records, a series of amplitude and phase data from positions along the flight path. Then the individual frames can be processed together, summed and phased to

achieve the desired resolution. This is analogous to a linear antenna array where a number of individual antennae are used together to shape the overall radiation pattern.

Figure 2.13 illustrates what is meant by lost object information for a simple one-dimensional object. The object frequency spectrum $O(\nu_x)$ is shown along with the system transfer function $H(\nu_x)$. The lost object information is that part of the object spectrum that lies beyond the cutoff frequency of $H(\nu_x)$. The image $I(\nu_x)$ only contains information from the object up to the cutoff frequency of the system. With superresolution applied to the resultant image, the lost object information is recovered. This technique effectively

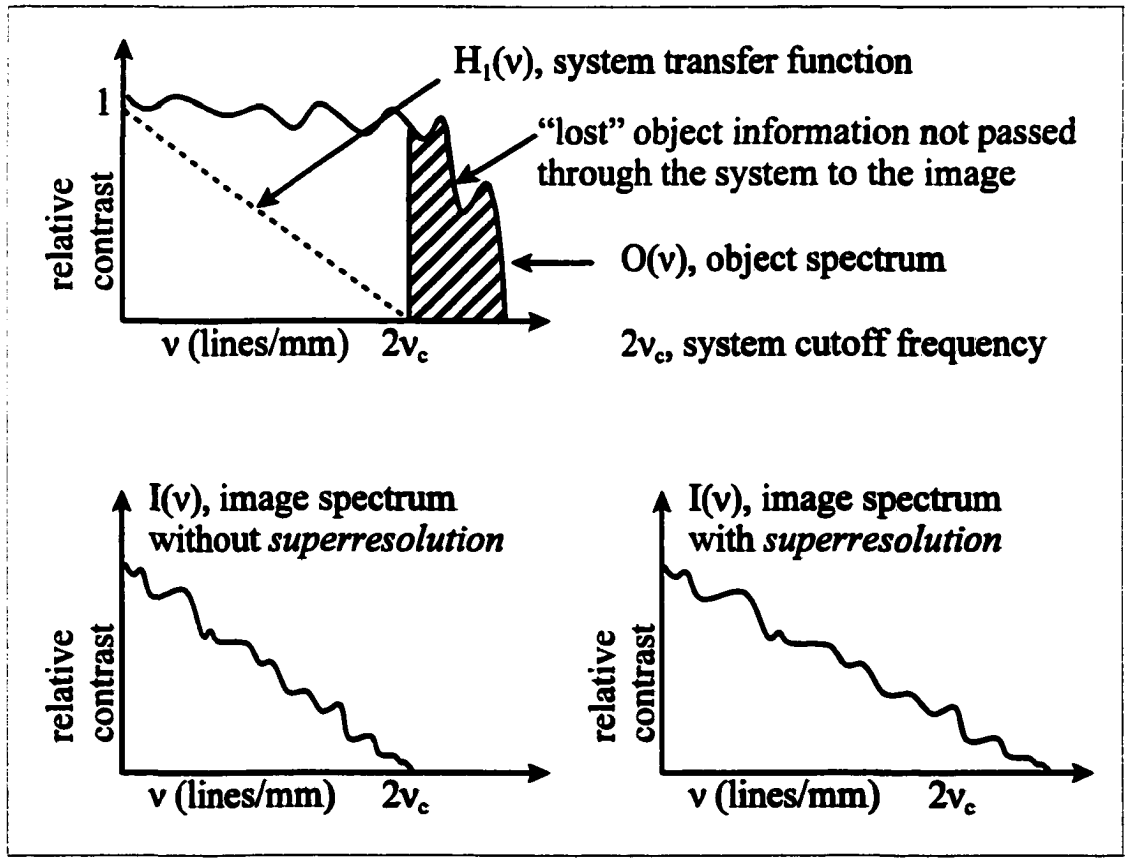

Figure 2.13. Description of lost object information through a band-limited system and the restoration of lost object information in the image spectrum.

increases the theoretical cutoff frequency through the use of image processing algorithms.

Superresolution image processing algorithms extract object information from detected data that exceed the geometrical diffraction resolution limit. Some superresolution algorithms extrapolate beyond the cutoff frequency directly in a one shot calculation (Walsh, 1994) while others use iterative routines (Gerchberg, 1974) (Fienup,1996). Also, there are image processing algorithms that reduce the effects of the impulse response sidelobes on the imagery. Sidelobe level reduction algorithms have traditionally been at the expense of main lobe resolution, but more recent techniques preserve the main lobe resolution while practically eliminating the side lobes (Feinup, 1996). Both astronomy and radar use these image processing techniques to their advantage. Image processing algorithms that may be applicable to optical data storage are now reviewed.

The most popular algorithm is the Gerchberg superresolution algorithm (Gerchberg, 1974). To set up the problem, only a limited object frequency spectrum is given. The spatial extent of the object and the object spectrum are assumed to be known. The object spectrum is reconstructed with the apriori information. For example, the known, true, object shown in Figure 2.14(a) is given by,

$$o(x) = 1000\left\{\text{rect}\left[16\left(x-\frac{3.5}{32}\right)\right]+\text{rect}\left[16\left(x+\frac{3.5}{32}\right)\right]\right\} \quad , \qquad (2\text{-}16)$$

which has known, true, extent given by rect[x/(9/32)]. From equation (2-16) the true

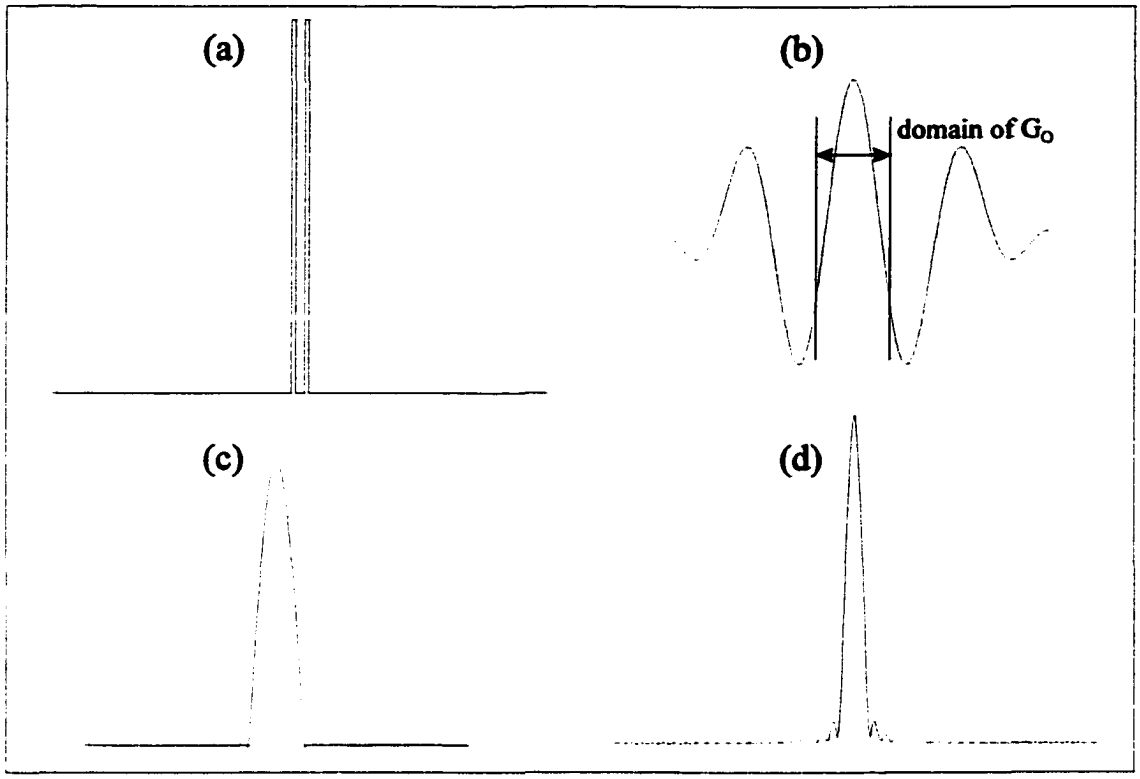

Figure 2.14. Gerchberg superresolution algorithm, (a) known object, (b) true spectrum of known object, (c) given spectrum G_0 of true object as measured from some imperfect system, (d) object estimate from the given spectrum.

spectrum of the object is known, as shown in Figure 2.14b. In this example there is only a finite spectral segment of the true object spectrum given, G_0, as shown in 2.14c. Taking the Fourier transform of G_0, an initial estimate of the object is formed, as shown in Figure 2.14d. The object estimate is then truncated by multiplying by rect[x/(9/32)], which sets the estimate to zero outside the known extent of the true object. Then this truncated object estimate is Fourier transformed to obtain an estimate of the true spectrum. This estimated spectrum is corrected by truncating the bandwidth to that of the true spectrum. These steps are repeated until a satisfactory error energy is reached between the energy in

the true spectrum and the energy in the estimated spectrum.

Another popular superresolution algorithm is the super-SVA (Fienup, 1996) (super-Spatially Variant Apodization). Super-SVA is a modified Gerchberg algorithm. Instead of truncating the estimated object to zero outside the known extent of the object, the SVA sidelobe-elimination operation is performed at this step. Energy is added at the higher spatial frequencies, and as iterations progress improved resolution is achieved. The super-SVA algorithm does not assume any apriori information about the object. If an object is present it will be revealed after a number of iterations.

These methods are iterative and require time and computer memory. There are superresolution algorithms that are noniterative (Walsh, 1994). The noniterative algorithm performs as well as the Gerchberg algorithm in only a fraction of the time required to do so. The noniterative superresolution algorithm could be implemented in a digital signal processing (DSP) chip in the data channel of an optical data storage system. This requires precise knowledge of the written mark and space dimensions obtained from a microscope capable of resolving the spatial frequencies of interest.

2B.3- Superresolution definition #3

> *Superresolution* DEFINITION #3: Space-bandwidth product (SBP) adaptation, so that the SBP of the object is matched to the SBP of the system.

In designing optical systems it is helpful to understand the properties of the object

to be imaged as well as the imaging properties of the optical system. If the object properties such as the object spectrum and spatial extent are sufficiently known, the optical system designer needs to determine which optical systems will transmit an object with a given space-bandwidth without losing any object information. The following discussion is for a one-dimensional object f(x) with corresponding Fourier transform F(v).

The Wigner distribution of a one dimensional object f(x) is given by,

$$W(x,v) = \int_{-\infty}^{\infty} f(x + \frac{x'}{2}) f^*(x - \frac{x'}{2}) \exp(-2\pi j v x') dx' \quad , \qquad (2\text{-}17)$$

and shows the spatial and spectral information simultaneously. In the paper by Mendlovic the space-bandwidth product, $SW = \Delta x \, \Delta v$, is shown to be estimated from the Wigner chart W(x,v) by projecting the chart on the x and v axis to obtain Δx and Δv . Since by definition the Wigner distribution is infinite along one direction the estimation of Δx and Δv is not exact. The space-bandwidth product can be generalized as a function, SW(x,v), by using the Wigner distribution, W(x,v). Generalizing SW(x,v) to a binary function of x and v gives

$$SW_B(x,v) = \begin{cases} 1 & W(x,v) > W_{thresh} \\ 0 & \text{otherwise} \end{cases} \quad . \qquad (2\text{-}18)$$

Where W_{thresh} is a certain threshold value. The total area of W(x,v) has meaning of energy and is incorporated into the definition of SW(x,v)

$$SW(x,\nu) = S_T SW_B(x,\nu) \quad , \tag{2-19}$$

where S_T the total energy is selected such that

$$S_T = \frac{\iint SW_B(x,\nu)W(x,\nu)dxd\nu}{\iint SW_B(x,\nu)dxd\nu} \quad . \tag{2-20}$$

This definition of the total energy neglects the tails of the Wigner function below the threshold W_{thresh}.

A necessary condition for transmitting the object without losing information is the optical system space-bandwidth chart, denoted SWY(x,ν), must contain the object space-bandwidth chart SW(x,ν), (Mendlovic, 1997), as shown in Figure 2.15a. Usually SW(x,ν) is not contained in SWY(x,ν), as shown in Figure 2.15b. Without containment of SW(x,ν) in SWY(x,ν) the system would not transmit all the object information resulting in lost object frequency information. A requirement for the space-bandwidth adaptation algorithm is that the area of SW(x,ν) must be less than or equal to the area of the SWY(x,ν).

The goal of the algorithm is to adapt the object SW(x,ν) to the system SWY(x,ν) using any one or combination of basic optical systems, such as free space propagation, a lens, magnification, Fourier transform, or a fractional Fourier transform (Mendlovic, 1997). Figure 2.16 shows the effect of these optical systems on a given object Wigner

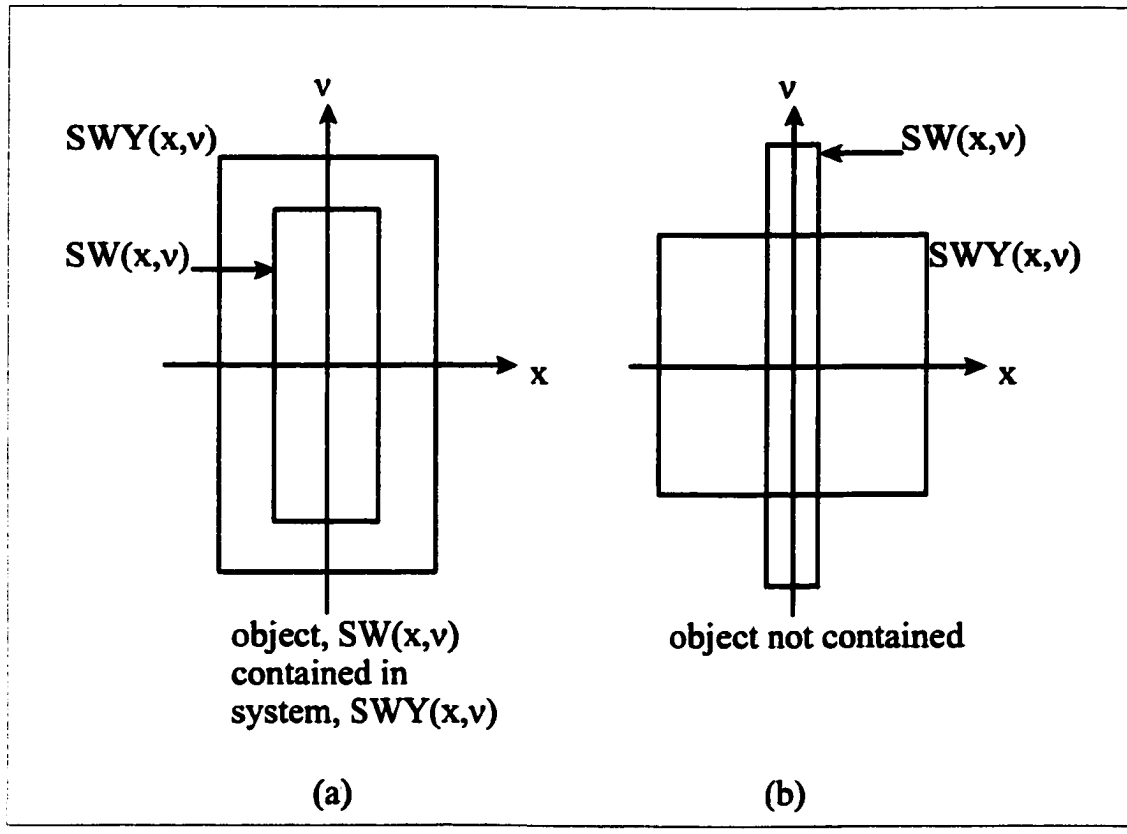

Figure 2.15. Space-bandwidth chart for object and system, (a) object contained within the system, (b) object not entirely contained within system.

Chart (Mendlovic, 1997).

The Wigner distribution (Wigner, 1932) is a useful signal processing tool that allows a signal to be described by both space and frequency variables simultaneously, rather than a single variable (Classen, 1980). This representation links the physical optics description of an optical system with the geometrical description (Bastiaans, 1978). When displayed graphically the Wigner Distribution is a space-bandwidth chart that allows the optical system characteristics to be viewed in both domains simultaneously

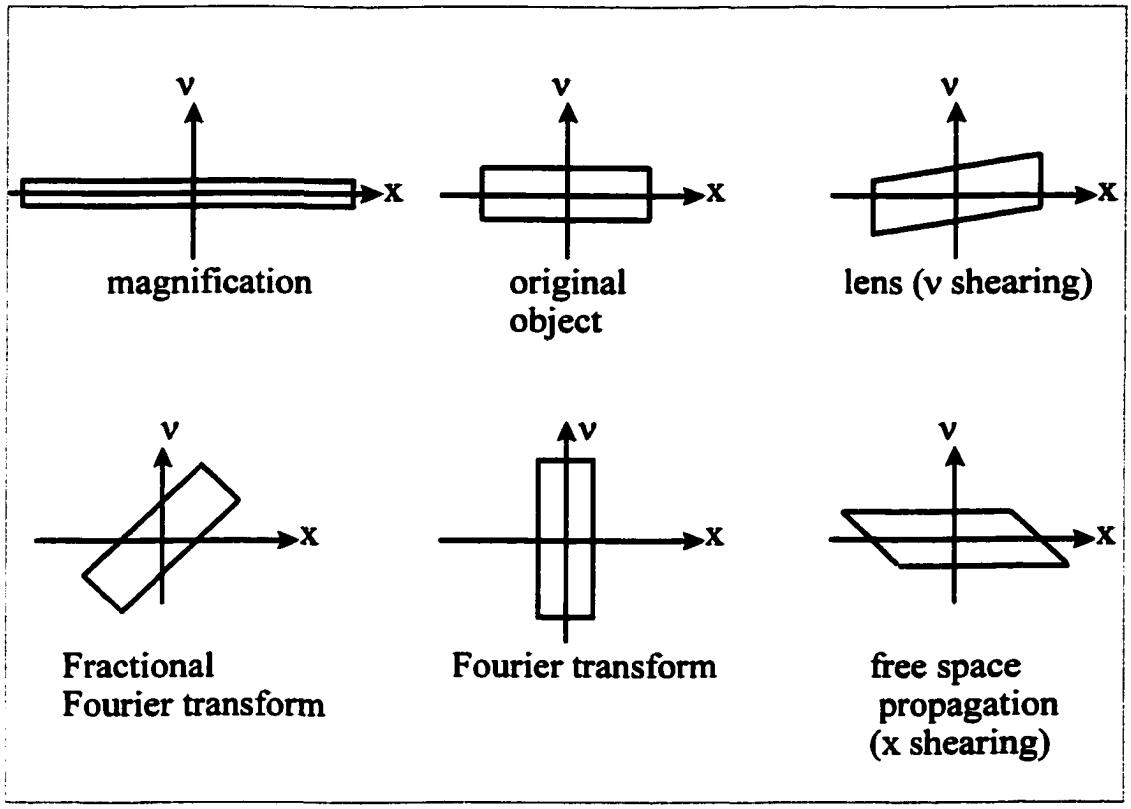

Figure 2.16. Optical systems to adapt the space-bandwidth charts of object and system to each other.

(Mendlovic, 1997). This chart is used as a tool for designing superresolving optical systems.

The space-band width adaptation definition closely resembles the previous definition of restoring lost frequency information. The main difference is that it allows the use of optical systems to adapt the object to the system without the need to use image processing routines. The advantages are the image resulting from an adapted system will not require the image processing routines of an unadapted system. The disadvantages are the additional elements in the optical system that need to be designed, toleranced, and

mounted.

2C - Summary

In Chapter 2, background on resolution and the related concepts of spot size, cutoff frequency of the MTF, and two-point resolution are presented. The influence of noise on classical resolution definitions is shown to influence the decision of whether or not two point sources are resolved, as shown in Figure 2.5. The concept of signal-to-noise ratio(SNR) is defined as a figure of merit to describe the detectability of a signal.

Then the development of superresolution is broken up into three definitions. The first definition of superresolution parallels that used by researchers in optical data storage and scanning optical microscopy, and is sometimes referred to ultra-resolution in the literature(Wilson and Sheppard, 1984). The second definition of superresolution parallels that used by researchers in astronomy and radar where superresolution is achieved through the use of image processing algorithms. The image processing algorithms are not particularly well suited for optical data storage because of the required intermediate storage and mathematical routines required to extrapolate the data. The third definition of superresolution parallels that used by researchers in optical superresolution, where space-bandwidth adaptation is used as a tool for designing superresolving optical systems. This technique if applied to optical data storage has the advantage of no required intermediate computer storage for signal processing. However it has the disadvantage of additional optical elements.

Superresolution Definition #1 methods, presented in Section 2B.1 of Chapter 2,

are used in a magneto-optic data storage system simulation that is discussed in Chapter 3. The simulations in Chapter 3 investigate the influence of superresolution on performance measures of the magneto-optic data storage system, such as system transfer function and two-point system response. In Chapter 4, particular superresolution Definition #1 techniques are utilized in an experimental magneto-optic data storage system, and the influence of the particular superresolution techniques on the performance measures of the system are reported. Chapter 6 introduces adaptive optical systems that may achieve superresolution Definition #3, by adapting the bandwidth of the object to the standard magneto-optic data storage system.

CHAPTER 3 - MODELING AND SIMULATING A MAGNETO-OPTIC DATA STORAGE SYSTEM

The goal of superresolution in optical data storage is to increase data capacity by improving readout signal quality in the high-frequency region of the system transfer function where contrast is poor. Superresolution is realized without using shorter wavelength sources and unreasonably high numerical aperture objective lenses. Superresolution techniques will be complimentary as shorter wavelength sources become realized and objective lenses move toward higher numerical apertures.

In this chapter, the simulated performance of a magneto-optic data storage system data channel is reported. The system transfer function and the two-point response are discussed. The spatial distribution of the data signal current in the pupil of the optical system is presented. Then, the introduction of different superresolution components and their effects on the performance of the system is reported.

In Section 3A diffraction modeling used to simulate a magneto-optic data storage system is described. The propagation of light from object to entrance pupil, between the entrance and exit pupil, and from exit pupil to image is discussed.

In Section 3B the magneto-optic data storage system is described. Parameters associated with the system are discussed. Optical and electronic filters used for realizing superresolution are discussed. Filtering methods used in the simulations are introduced and physical locations of the filters in the system are identified. The reading and writing processes are also described.

In Section 3C the simulated performance of a standard magneto-optic data storage system data channel is illustrated. Simulations are performed in the OPTISCAN work environment. Sampling issues relating to computer modeling are discussed. Implementation of the necessary components of a magneto-optic data storage system within OPTISCAN is presented. Spatial distributions of data signals within the pupil of the optical system are presented. The system transfer function and the two-point response of the system are investigated.

In Section 3D superresolution components are introduced in the system. Their effect on system performance is demonstrated. Specifically, the influence of superresolution filters on the system transfer function and two-point response are observed.

In Section 3E the effects of third order aberrations on system performance is demonstrated. The influence of aberrations on the system transfer function and signal current distributions are observed. Sensitivities of the unfiltered system, the ring-phase filtered system, and a centrally obscured system for a given amount of aberration are investigated.

3A.1 - Description of diffraction model

In order to illustrate the operation of a magneto-optic data storage system, it is essential to discuss diffraction modeling. There are many formulations of the diffraction process, as well as many excellent textbooks on basic diffraction theory in optical systems (e.g., Gaskill, 1978). The goal of diffraction theory is to predict the distribution

of light on a surface some distance away from where the distribution of light is known.

The history of diffraction theory started with Huygen's reconstruction in the 17th century, which is based on purely geometrical arguments. Young performed the famous double slit experiment at the beginning of the 19th century that introduced wave theories. Fresnel then took Huygen's concept, applied Young's principle and had each wavelet interfere with every other wavelet. Fresnel had to ad-hoc some fudge factors, such as an obliquity factor, a (1/4)λ shift relative to the reconstructed wavefront and the wavefront that produced them, in order for the theory to agree with experiment. Kirchoff applied a Green's function approach with an incorrect obliquity factor. Rayleigh-Sommerfeld resolved the ambiguity by using a pair of spherical waves as a Green's function. The reader is referred to some very good references on the history of diffraction theory (Goodman, 1968) (Born and Wolf, 1989) for further details.

An approach based on the direct application of Fourier transform theory was developed in 1979 by Shack and Harvey (Harvey, 1979) and is well suited for computer programming. It is helpful to outline Harvey's method here, since it is one of the propagation options in OPTISCAN, and it is the method that is used in the simulations.

3A.1 - Propagation from exit pupil to image

Referring to Figure 3.1, the two planes of interest are P_0 and P with the coordinate system scaled by λ. Starting out with a scalar monochromatic field amplitude U_o in plane P_0, the Fourier Transform relations are defined

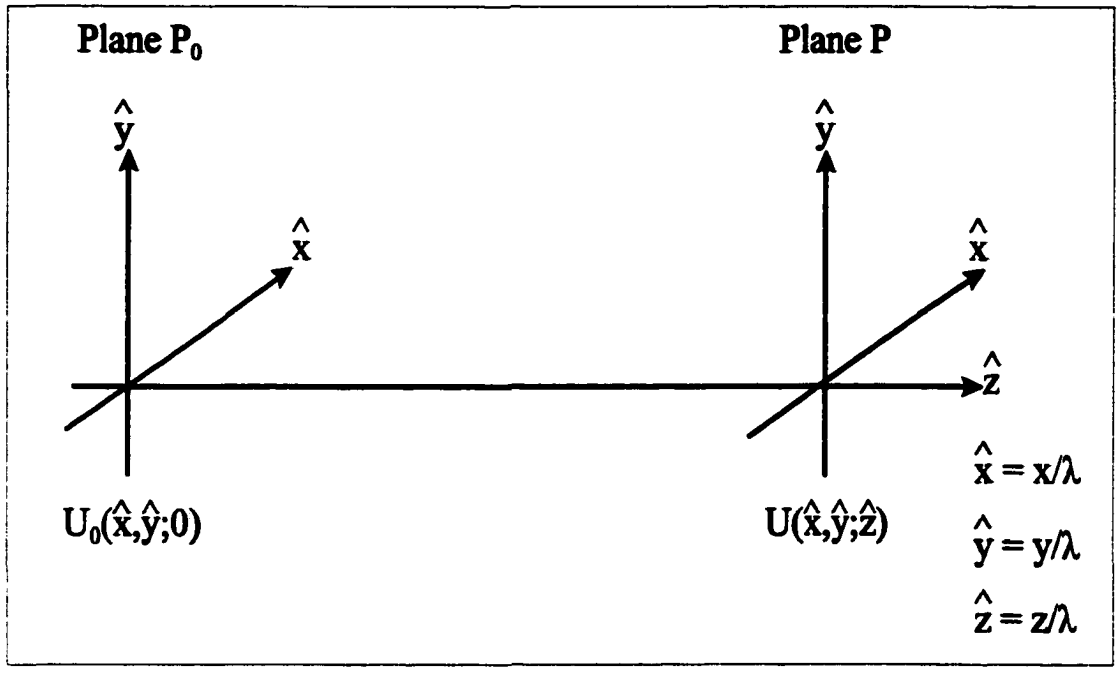

Figure 3.1. Two planes of interest for diffraction process.

$$A_0(\alpha,\beta;0) = \iint_{\infty} U_0(\hat{x},\hat{y};0)e^{-i2\pi(\alpha\hat{x}+\beta\hat{y})}d\hat{x}d\hat{y} \quad , \tag{3-1}$$

$$U_0(\hat{x},\hat{y};0) = \iint_{\infty} A_0(\alpha,\beta;0)e^{i2\pi(\alpha\hat{x}+\beta\hat{y})}d\alpha d\beta \quad , \tag{3-2}$$

and

$$A(\alpha,\beta;\hat{z}) = \iint_{\infty} U(\hat{x},\hat{y};\hat{z})e^{-i2\pi(\alpha\hat{x}+\beta\hat{y})}d\hat{x}d\hat{y} \quad , \tag{3-3}$$

$$U(\hat{x},\hat{y};\hat{z}) = \iint_{\infty} A(\alpha,\beta;\hat{z})e^{i2\pi(\alpha\hat{x}+\beta\hat{y})}d\alpha d\beta \quad , \tag{3-4}$$

where A_0 and A are the direction cosine spectra of plane waves contributing to the fields U_0 and U, respectively, where α, β, and γ are the direction cosines for the x, y, and z

components of the plane-wave propagation vectors. With the requirement that $U_0(x,y;0)$ and $U(x,y,z)$ must satisfy the wave equation, the transfer function of free space is found to be

$$H(\alpha,\beta;\hat{z}) = A(\alpha,\beta;\hat{z}) / A_0(\alpha,\beta;0) = e^{i2\pi\gamma\hat{z}} \quad . \qquad (3\text{-}5)$$

From Eq. (3-5) it is interesting to ask what is the significance of having $\gamma=(1-(\alpha^2+\beta^2))^{0.5}$ real or imaginary? Figure 3.2 shows the unit circle $(\alpha^2 + \beta^2) = 1$. Inside the unit circle the value of γ is real, and outside of the unit circle γ is imaginary. The part of the original disturbance in plane P_0 corresponding to $\gamma \in Re\{\}$ will propagate and contribute to the

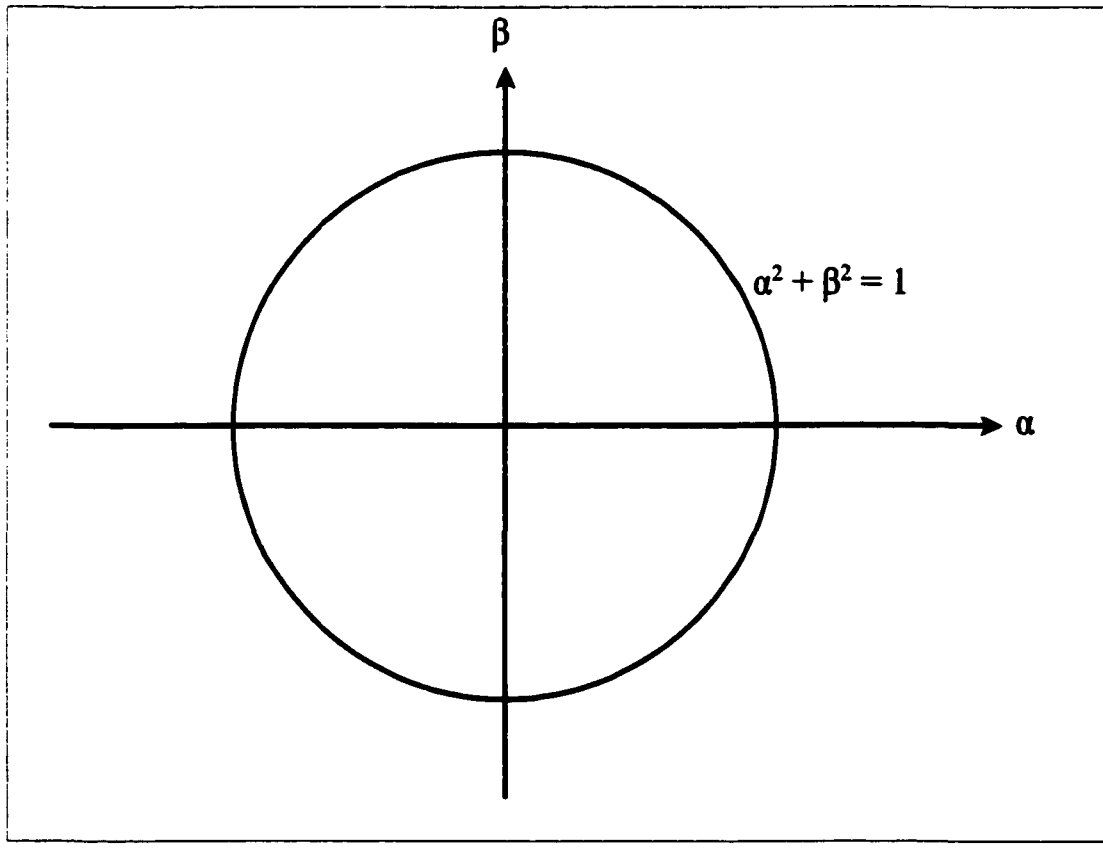

Figure 3.2. Unit circle in direction cosine space

disturbance in plane P. The part of the original disturbance corresponding to $\gamma \in \mathrm{Im}\{\}$ experiences an exponential decay and contributes very little or nothing to the disturbance at plane P if ž is greater than a few wavelengths.

The disturbance U in plane P is determined by first Fourier transforming the original disturbance U_0 in plane P_0 and obtaining the direction cosine spectrum A_0. Then A_0 is multiplied by the transfer function of free space to obtain the direction cosine spectrum A in plane P. Then the inverse Fourier transformation of A is performed to obtain U. This procedure is straightforward and clear, but the procedure does involve two Fourier transformations that may or may not be a problem numerically.

The free space impulse response is given by the Fourier transform of the free space transfer function, and is (Weyl, 1919)

$$h(\hat{x},\hat{y};\hat{z}) = \Im^{-1}\left\{e^{i2\pi\gamma\hat{z}}\right\} = \left(\frac{1}{2\pi\hat{r}} - i\right)\frac{\hat{z}}{\hat{r}}\frac{e^{i2\pi\hat{r}}}{\hat{r}} \quad , \tag{3-6}$$

where

$$\hat{r}^2 = \hat{x}^2 + \hat{y}^2 + \hat{z}^2 \quad . \tag{3-7}$$

Eq. (3-6) is an exact expression for a Huygen's wavelet, which reduces to the familiar spherical wave expression

$$h(\hat{x},\hat{y};\hat{z}) = -i\frac{\hat{z}}{\hat{r}}\frac{e^{i2\pi\hat{r}}}{\hat{r}} = \frac{\hat{z}}{\hat{r}}\frac{e^{i2\pi(\hat{r}-1/4)}}{\hat{r}} \quad , \tag{3-8}$$

when r » 1. By applying the convolution integral for U in plane P, the *general Rayleigh-Sommerfeld diffraction formula* is given by

$$U(\hat{x},\hat{y};\hat{z}) = \iint_{\infty} U_0(\hat{x}',\hat{y}';0)\left(\frac{1}{2\pi\ell} - i\right)\frac{\hat{z}}{\ell}\frac{e^{i2\pi\ell}}{\ell}d\hat{x}'d\hat{y}' \quad , \tag{3-9}$$

where

$$\ell^2 = (\hat{x}-\hat{x}')^2 + (\hat{y}-\hat{y}')^2 + \hat{z}^2 \quad , \tag{3-10a}$$

and,

$$\ell = \hat{z}\left[1 + \left(\frac{(\hat{x}^2+\hat{y}^2)}{\hat{z}^2} + \frac{(\hat{x}'^2+\hat{y}'^2)}{\hat{z}^2} - \frac{2(\hat{x}\hat{x}'+\hat{y}\hat{y}')}{\hat{z}^2}\right)\right]^{1/2} \quad . \tag{3-10b}$$

No approximations are made in the scalar diffraction formula of Eq. (3-8). It is valid throughout the entire space that diffraction occurs. It is clear that Eq. (3-9) is difficult to solve. The binomial expansion may be applied to ℓ in Eq. (3-10b) to obtain the standard Fresnel and Fraunhofer diffraction formulas, but these impose severe restrictions on the region of space where the approximations are valid. So, rather than make any approximations, all of the terms in a binomial expansion of Eq. (3-10b), except for the term that makes up the Fourier kernel, can be grouped into the quantity $\hat{w}$ along with any other phase variations in the incident wavefront,

$$\ell \approx -\frac{\hat{x}\hat{x}' + \hat{y}\hat{y}'}{\hat{z}} + \hat{w} \quad . \tag{3-10}$$

The quantity $\hat{w}$ can be written as a power series that corresponds to the familiar forms of the conventional aberrations. These aberrations are due to the diffraction process itself and not from an imperfect optical system.

If the diffracted wave field is considered on a hemisphere centered on the plane P_0 as illustrated in Figure 3.3 and the aberrations in $\hat{w}$ inherent to the diffraction process are neglected, the general Rayleigh-Sommerfeld diffraction formula, Eq. (3-8), reduces to the Fourier transform of U_0 multiplied by a spherical Huygen's wavelet

$$U(\alpha,\beta;\hat{r}) = \gamma\left(\frac{e^{i2\pi\hat{r}}}{i\hat{r}}\right)\iint_{\infty} U_0(\hat{x}',\hat{y}';0)e^{i2\pi(\alpha\hat{x}'+\beta\hat{y}')}d\hat{x}'d\hat{y}' \quad , \tag{3-12}$$

or

$$U(\alpha,\beta;\hat{r}) = \gamma\left(\frac{e^{i2\pi\hat{r}}}{i\hat{r}}\right)\Im[U_0(\hat{x},\hat{y};0)] \quad . \tag{3-13}$$

Eqs. (3-12) and (3-13) are valid as long as the observation surface is a hemisphere centered on the diffracting aperture in plane P_0, and the incident radiation is a spherical wave with center of curvature lying on the intersection of the observation hemisphere with the z axis. If $\hat{r}$ is large compared to the radius of the diffracting aperture, the Fourier

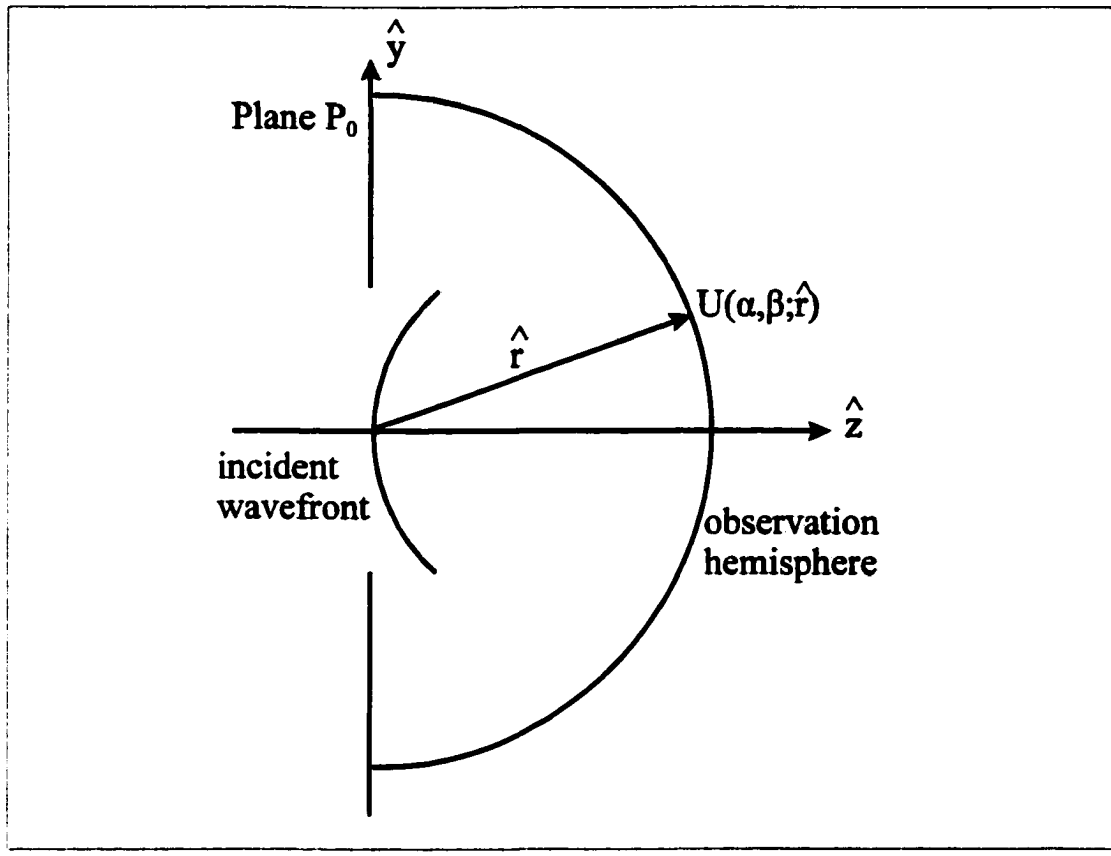

Figure 3.3. Diffraction geometry for spherical wave field observed on hemisphere centered on aperture

transform relationship is accurate over the entire hemisphere.

The relationship of Eq. (3-12) only requires one Fourier transform and is very advantageous to implement in computer code. Eq. (3-12) is a scalar development that works very well compared with experiment. This development has been expanded to include vector diffraction(Flagello, 1996), and included in the capability of OPTISCAN. All simulations in this work are done with the scalar model.

3A.2 - ABCD method of propagation

For propagating light between the entrance and exit pupils of the optical system, the ABCD matrix method is used (Seigman, 1990). The ABCD matrix method is the standard matrix method for paraxial analysis, and it is very convenient to implement in computer code. A review of this method can be found in a number of geometrical optics and optical engineering textbooks (e.g., Smith, 1990). The matrix method consists of representing an optical surface as a refraction matrix and the space between optical surfaces as transfer matrices.

3B - Magneto-optic data storage system layout

A typical magneto-optic data storage system is shown in Figure 3.4(a). Labeled for clarity is the illumination-path, which is that part of the system that delivers light to the

disk, and the return-path, which is that part of the system which delivers light reflected from the disk to the servo and data detectors.

Figure 3.4(b) shows the system layout without the component labels. Instead the optical and electronic filtering locations in the system are identified. A complete description of each filtering technique is described in subsequent sections. The purpose of Figure 3.4(b) is to identify the physical location of the various filters.

Optical filtering in the illumination path is performed with amplitude and phase filters. These concepts are introduced in Section 2B.1. Specific illumination-path phase and amplitude filters used in simulations are presented in Section 3D.1. The specific optical illumination-path filters to be studied are a ring-phase filter and a central pupil

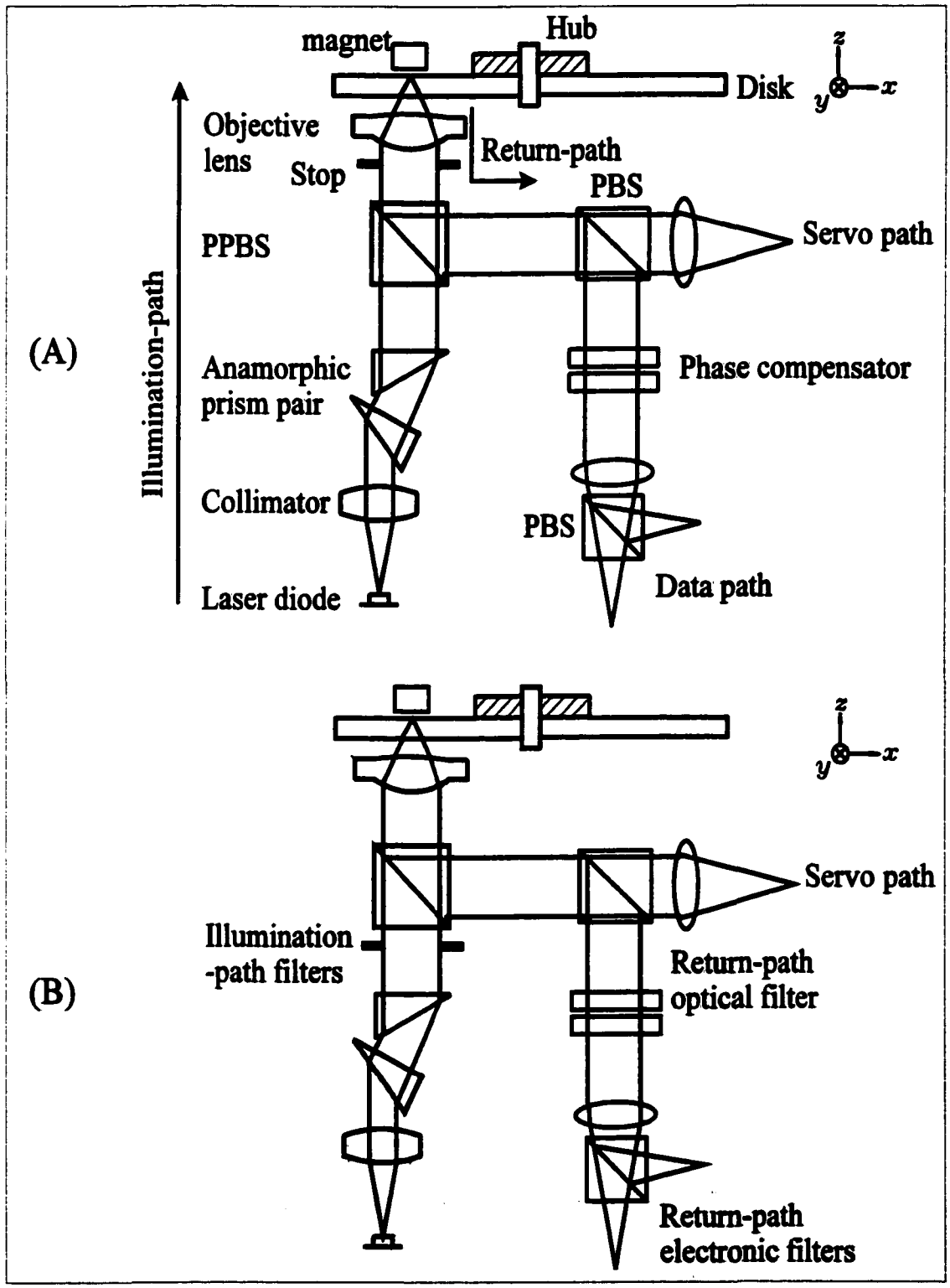

Figure 3.4. Magneto-optic data storage system layout. (A) component description and explanation of illumination-path and return-path. (B) filtering locations in the system.

obscuration filter.

Optical filtering in the return path is performed with the amplitude filters that are introduced in Section 2B.1. Specific return-path optical amplitude filtering used in the simulations are presented in Section 3D.2.A.

Electronic filtering is performed in the return-path of the system with equalizing filters discussed in Section 2B.1. Specific return-path electronic filters are discussed in section 3D.2.B. The electronic filters to be studied are an electronic boost filter that provides a nonlinear gain as a function of frequency and an electronic tapped-delay-line filter used to remove artifacts in the data signals and partially equalize the system transfer function.

3B.1 - Magneto-optic data storage system parameters

The source used is a typical edge emitting laser diode. Details on the solid state physics of these devices can be found in many semiconductor optics books (e.g., Peyghambarian, 1993). Typical performance characteristics of a diode used in this work are λ=780nm, polarization ratio of 20:1 aligned in the x direction, and a maximum output power of 30mW. The light is emitted with different divergence angles in orthogonal directions, which results in an elliptical cross section. For the laser diodes used in data storage, the FWHM divergence in the direction parallel to the junction(x) is typically 10° and the divergence in the direction perpendicular to the junction(y) is typically 30°. The lens immediately following the laser diode in Figure 3.4a functions to collimate the light emitted from the laser diode. The light leaving the lens is collimated but is elliptical in

cross section. This elliptical beam needs to be corrected or there will be problems when the light is focused. For instance, if not corrected, the objective lens is underfilled in one dimension, resulting in a focused spot that is elongated in the underfilled direction. One way to compensate for this effect is to apply an anamorphic prism pair, which is the next element shown in the layout of Figure 3.4a. This prism combination provides magnification in the x direction only, and results in a nearly circular cross section laser beam. Light is then passed through a partially polarizing beam splitter (PPBS) and is focused through the substrate of a spinning disk on to a recording layer. The PPBS reflects 99% of the y-polarized light and 30% of the x-polarized light. Approximately 70% of the x-polarized light is transmitted. The numerical aperture of the objective lens is 0.55. Reflected light, which is modulated by the data pattern, is redirected into the servo and data paths. The servo optics generate tracking error and focus error signals. Focus and tracking correction is performed by moving the objective lens in a voice-coil actuator. The data signal is recovered by sensing a change in the polarization state of the reflected light caused by the magneto-optic Kerr effect. Because of the small signal levels, which are typically on the order of 1μW, a differential arrangement of detectors must be used to limit common-mode noise (Marchant, 1990).

3B.2 - Recording process of magneto-optic data storage system

MO recording is a thermomagnetic recording process. Background on this process can be found textbooks on magneto-optic recording (Mansuripur, 1995). Historically, MO recording has been a two-step process. First, the data track in question

has to be erased, and then it is written with new data. The two-step process requires at least two revolutions of the disk. There are new techniques of writing that allow direct overwriting in one pass, but these techniques require sophisticated laser modulation combined with high frequency magnetic field modulation (Marinero, 1995), and they are not discussed further in this work.

An erased track consists of magnetic domains orientated in one direction, either NS or SN, as shown in Figure 3.5(a). To accomplish erasure, the laser spot is used as a localized point source of heat. The focused laser is brought from a nominal reading power of 1mW to a power level of approximately 6mW for one revolution of the spinning disk. This power level provides heat to the magnetic domains through material absorption. Once the local temperature of the recording layer has reached the Currie

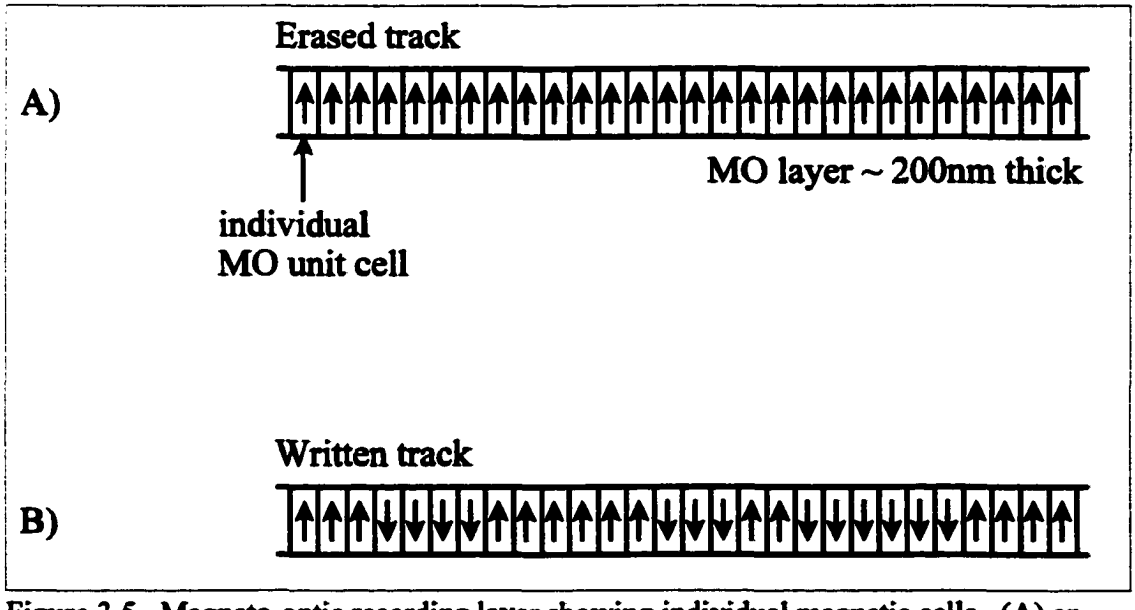

Figure 3.5. Magneto-optic recording layer showing individual magnetic cells. (A) an erased track with magnetic domains all in one orientation, (B) a written track with magnetic domains in both orientations.

temperature (about 200°C), the magnetic domains are no longer rigid but can be aligned by relatively weak external magnetic fields. There is a coil magnet for this purpose located behind the spinning disk, as indicated in Figure 3.4. To erase the track the magnet is turned on, the laser is brought to the erase power level and the magnetic domains of the recording layer align themselves to the external magnetic field. This action produces an erased track with magnetic domains oriented in the same direction. If the external magnetic field was not applied, the track would consist of randomly oriented magnetic domains, resulting in a very noisy background signal when read back through the data channel.

To record(write) on the erased track the magnet is turned on with the polarity of the magnet in the opposite orientation used during erasing. The focused laser is pulsed by electronically modulating the laser diode injection current according to the desired data pattern. The laser is pulsed from a low level which is the nominal read level of 1mW, to a high level of typically 8mW. On the recording layer in those regions where the laser is pulsed to a high level the magnetic domains orient themselves along the applied magnetic field, which is opposite to the orientation in the erased state. So, when the data track is written, there is a series of oppositely oriented magnetic domains along the track as shown in Figure 3.5(b).

3B.3 - Reading process of magneto-optic data storage system

The read-back system uses a differential detection technique. When linearly polarized light is incident onto the magneto-optic storage layer the reflected light is

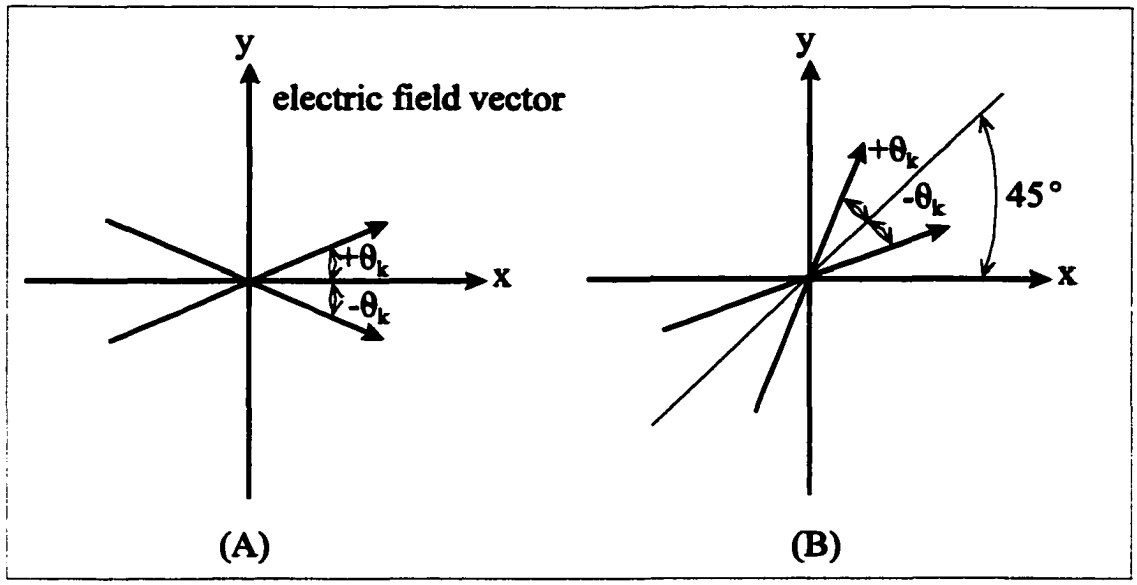

Figure 3.6. Reflected field amplitudes, (A) before the λ/2 plate, (B) after the λ/2 plate.

rotated due to the polar Kerr effect. The rotation is either clockwise or counterclockwise, depending on the data pattern. In addition, the bulk reflectivity of the disk reduces the magnitude of the reflection. If the incident light is x polarized, the Kerr effect introduces a small positive or negative y component corresponding to magnetization out of or into the plane of the disk. The amount of rotation, called the Kerr angle θ_K, is very small, typically 1°.

The reflected x and y components may be out of phase. This phase shift, δ, causes a reduction in signal at the detectors and can be compensated with a quarter-wave plate. However, this effect is ignored in all simulations where $\delta = 0$.

The reflected light is recollimated by the objective lens and is reflected into the read-back optics by the PPBS. Figure 3.6(a) shows the electric field vector after passing through the PPBS. A half-wave plate is used to balance the light on the data detectors

through a polarizing beam splitter. Figure 3.6(b) shows the reflected electric field vector after the half-wave plate. As the disk spins under the focused laser spot, a rotation in the polarization of the reflected light is induced in accordance with the data pattern written on the disk. This polarization rotation causes the detectors to become unbalanced, which generates a signal current when the detectors are connected differentially.

3C - Simulated performance of magneto-optic data storage system

The simulated operation of the data channel of a magneto-optic data storage system is presented in this section. The system is implemented in the OPTISCAN environment. Simulation of the data channel of a magneto-optic data storage device is schematically represented in Figure 3.7, which shows the equivalent unfolded optical

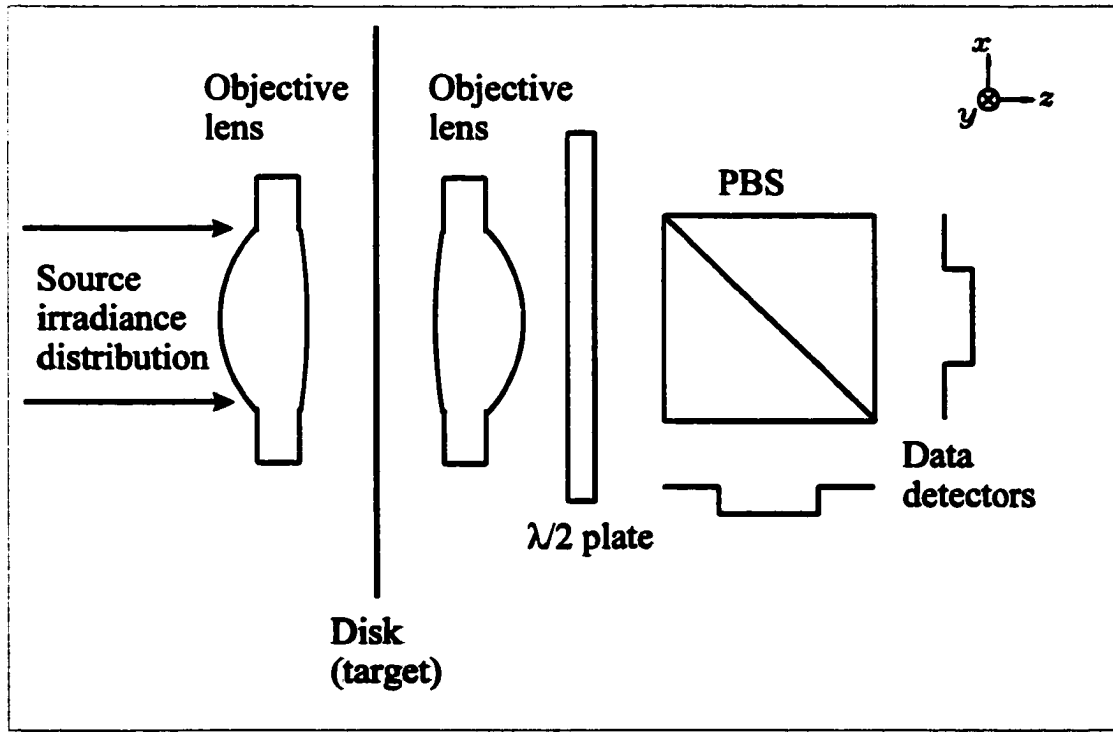

Figure 3.7. Simulated magneto-optic data storage system.

system used in the simulation. All matrices used in the simulation are 512x512 unless noted.

3C.1 - Sampling issues

It is convenient at this point to examine the basics of the DFT (discrete Fourier transform) to provide some clarity on sampling issues involved with modeling optical systems. In Figure 3.8 a continuous non periodic function f(x) is shown accompanied by its Fourier transform $g(\xi)=\Im[f(x)]$. The variable x is a real coordinate not scaled by wavelength. In a computer environment it is necessary to digitize f(x) in order to represent it numerically. Knowing that the function f(x) has a finite dimension, say X,

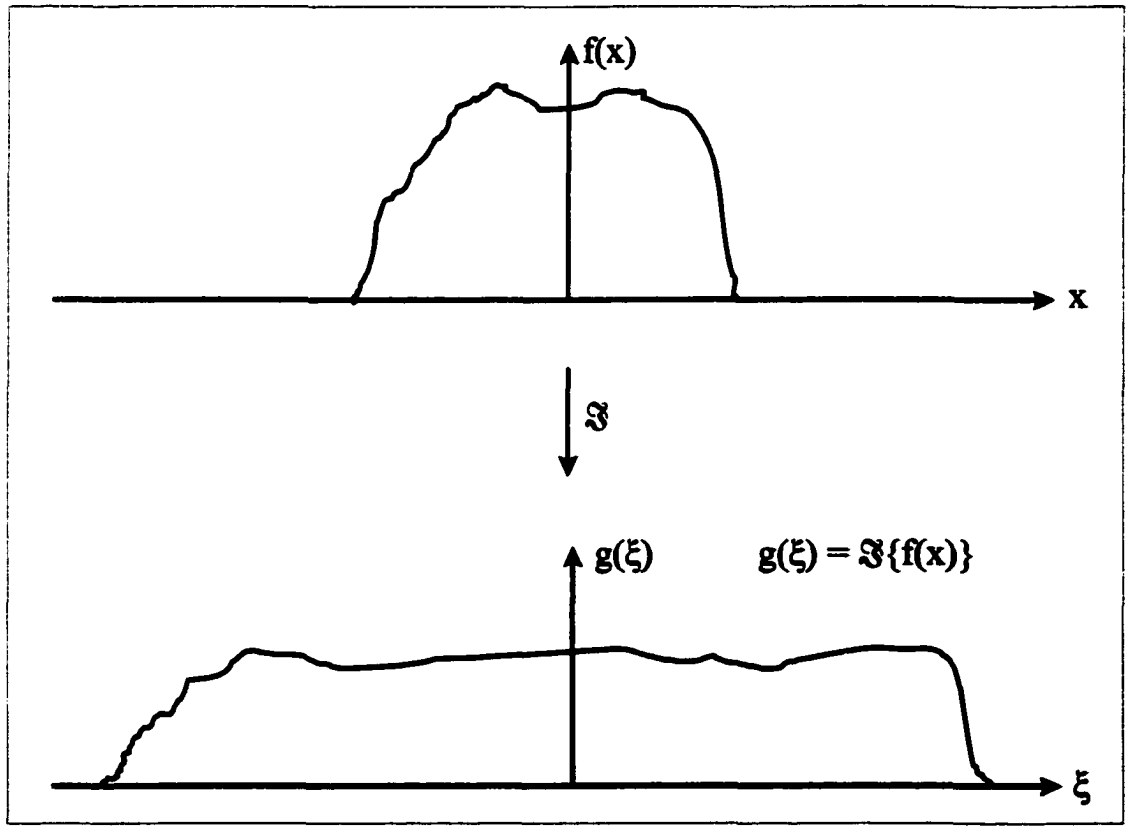

Figure 3.8. Continuous non periodic function f(x) having Fourier transform g(ξ).

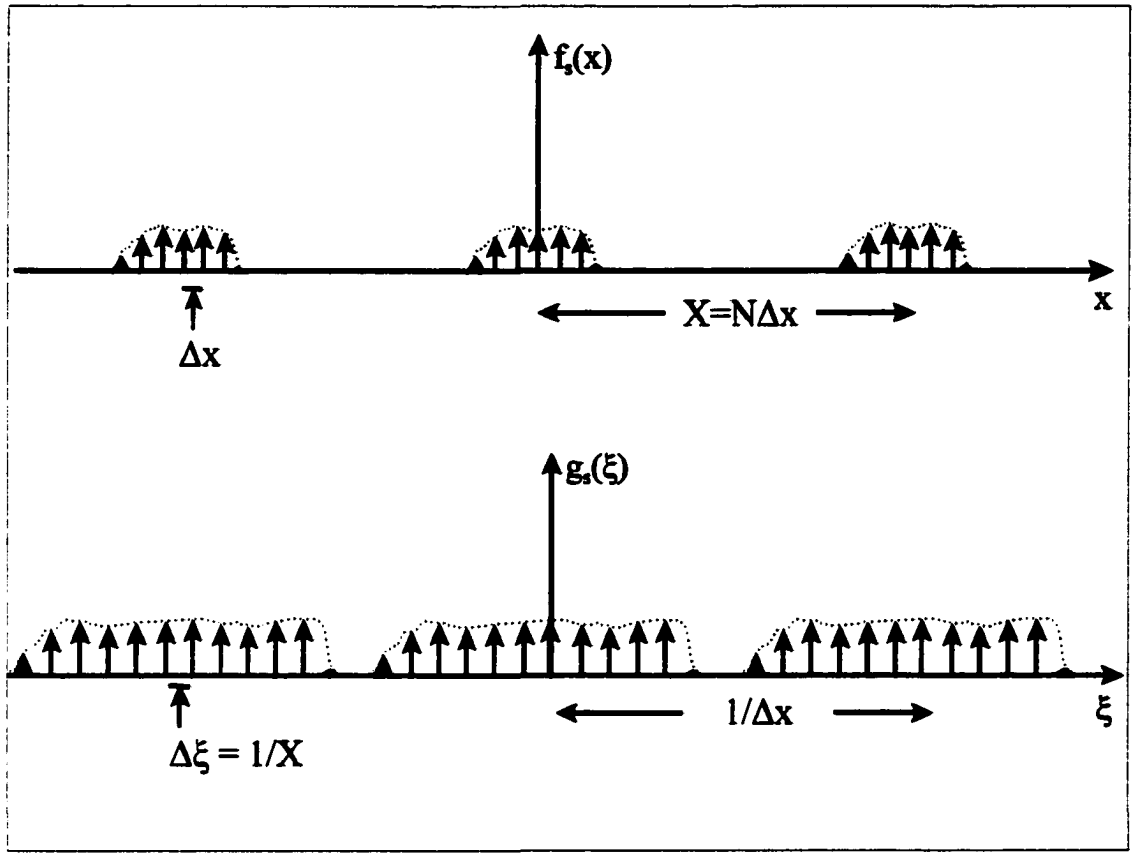

Figure 3.9. Sampled versions of f(x) and g(ξ).

within which it is known, it is sampled at a rate Δx=X/N, where N is a fixed number, like N=512. Also, this function is made to be periodic by convolving f(x) with a comb function such that the sampled function $f_s(x)$ is given by

$$f_s(x) = \left[f(x) * \frac{1}{X} \mathrm{comb}\left(\frac{x}{X}\right) \right] \mathrm{comb}\left(\frac{x}{\Delta x}\right) \quad , \qquad (3\text{-}14)$$

which has a Fourier transform given by

$$g_s(\xi) = \left[g(\xi)\mathrm{comb}(X\xi)\right] * \mathrm{comb}(\Delta x\xi) \quad . \tag{3-15}$$

Both $f_s(x)$ and $g_s(x)$ are plotted in Figure 3.9. There exist some tradeoffs that need to be considered. First consider the situation where N is fixed at N=512. $\Delta x = X/N$ represents the sampling in the focal plane of an optical system. The sampling interval in the frequency domain is related to X by the relation $\Delta\xi = 1/X$. $\Delta\xi$ is proportional to the sampling in the entrance pupil of the optical system. $\Delta\xi$ can be related to some parameters of an optical system by

$$\Delta\xi = \frac{1}{X} = \frac{1}{N\Delta x} = \frac{\Delta x_{pupil}}{\lambda f} = \frac{2NA}{\lambda N_{pupil}} \quad , \tag{3-16}$$

where Δx_{pupil} is the sample interval in the pupil. N_{pupil} is the number of sample points within the entrance pupil diameter of the optical system. From relation (3-16) it is clear that care must be exercised when choosing the sampling in one domain in light of the consequence this choice has on the sampling in the other domain. For instance, a fine sampling in the focal plane results in a coarse sampling in the pupil and vice versa.

3C.2 - Description of the simulated system.

The first step in modeling the system is to decide on a desired source distribution in the entrance pupil of the objective lens. This is accomplished in OPTISCAN where sources are defined with specific dimensions and user defined profiles, such as Gaussian or Hermite-Gaussian, with a chosen wavelength. When designing the source there is the

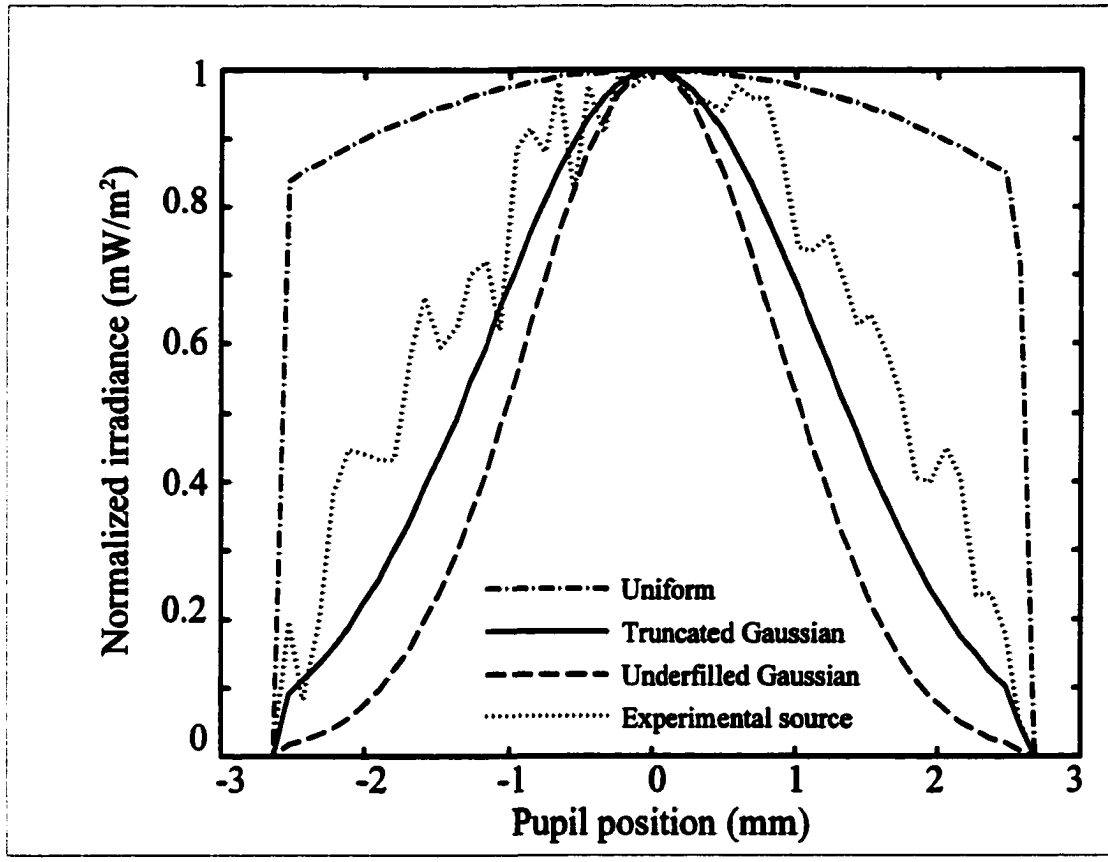

Figure 3.10. Irradiance profiles of the four source distributions used in the simulation.

question of truncation of the Gaussian beam. Truncation is the ratio of the peak irradiance in the center of the beam to the irradiance at the edge of the entrance pupil. To start with, a truncation factor of approximately 0.9 (Haskal, 1979) is chosen for a symmetrical Gaussian beam with λ=780nm. This truncation maximizes the on-axis peak irradiance of the focused spot, and is widely used in optical recording. The effect of an underfilled Gaussian beam and a uniformly filled or extremely overfilled Gaussian beam on the system performance is also considered with separate source distributions. The source distribution from the experimental system is saved with a CCD camera and frame

grabber. This is imported into OPTISCAN and the system is also simulated using the experimental source distribution. Profiles of the four entrance pupil source distributions are shown in Figure 3.10. The experimental source distribution closely follows that of the truncated Gaussian. The uniform distribution is slightly curved on top because it is mapped on to a spherical reference pupil.

The second step is to decide what objective lens to use. OPTISCAN allows the use of real or paraxial ZEMAX lenses in the simulation environment. A paraxial lens with typical data storage parameters of NA=0.55, focal length f = 3.89mm, and diameter d = 5mm is chosen. These paraxial values are based on the GELTECH 30080, which is a commercially available data storage objective lens.

The third step is to define the desired MO data pattern. The magneto-optic recording layer is a high performance thin film multilayer on the order of 200nm thick. The optical properties of a typical CoPd MO layer are $R=|r|^2 = 0.2$, and $\theta_K = 0.5°$. Also, there is a 1.2mm thick polycarbonate protective layer on top of the storage layer to prevent damage to the recording layer and to allow the disk to be removable. The cover layer is not necessary to include in the model when a paraxial lens is used, but is necessary when a real lens prescription is used that is designed to compensate for aberrations introduced by the cover plate.

The MO layer is characterized by its bulk reflectivity r and by its Kerr angle θ_K. In the OPTISCAN program environment MO layers properties are easily modeled. A reflective target is created to which is assigned the physical dimensions of width and

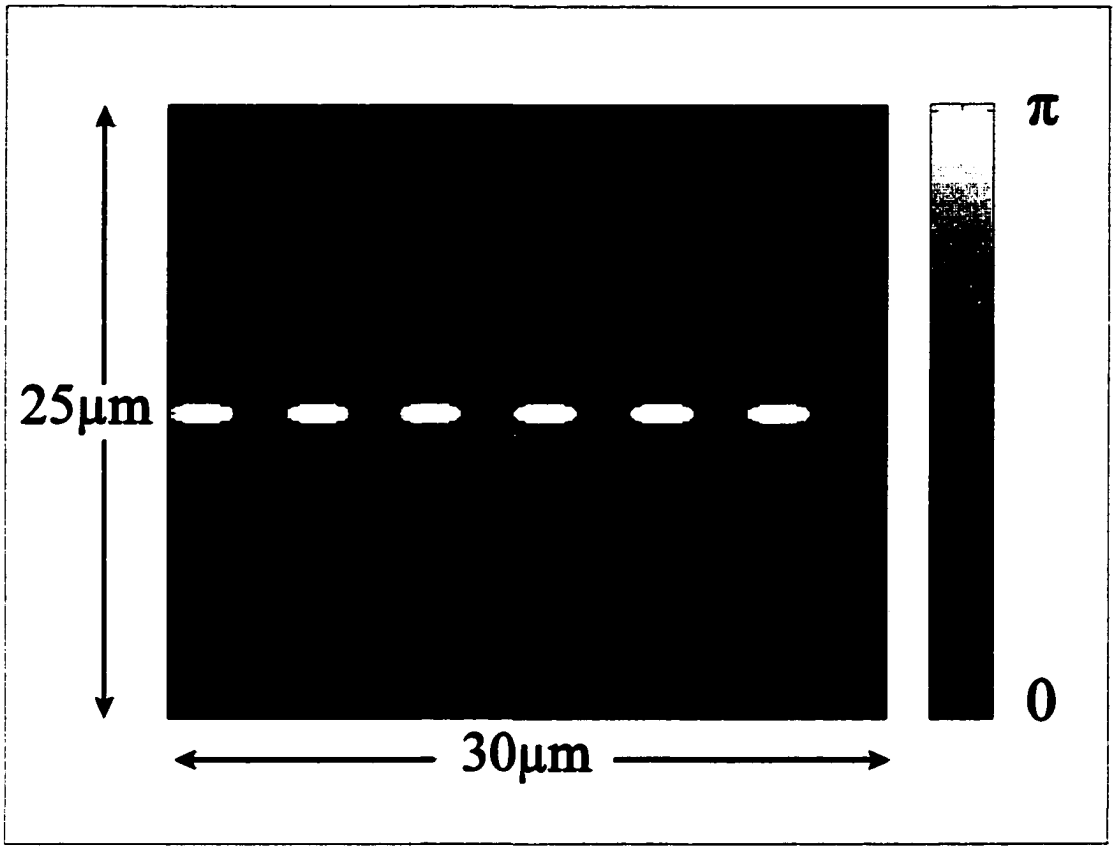

Figure 3.11. Data pattern representing the $\pm\theta_k$ of the magneto-optic recording layer.

length, the matrix size of the target, and the bulk reflectivity. The Kerr properties of the base layer are easily modified. This modification is accomplished by creating a realistic binary data pattern in a bitmap editor that ultimately represents $\pm\theta_K$. Figure 3.11 shows a typical data pattern used in the following simulations where the white regions represent $+\theta_K$ and the black region represents $-\theta_K$.

Eleven single-tone patterns are generated in order to build up the system transfer function from the amplitudes of the detector signals. The patterns range in pitch from 200 lines/mm to 1300 lines/mm and are chosen to include typical commercial mark sizes.

The smallest mark size used is 0.4μm. This is also a logical point to decide N_{pupil}, the number of sample points within the exit pupil of the optical system. N_{pupil} determines Δx, the spatial sampling of the optical system in the target plane. $N_{pupil} = 50$ is chosen, providing a Δx of 0.07μm with approximately 5 of these samples across the smallest feature size. Another important point is to decide on the fidelity of the target. The target matrix size should be large enough so that an individual target pixel is about the same size as Δx. A target length and width of 30μm x 30μm interpolated on a 900 x 900 matrix is used. This provides a target sampling, or grain size of 0.035μm per sample(or grain) giving 2 individual target grains for one optical system sample Δx in the target plane.

To simulate the spinning of the disk, the target has a window with length and width less than the total target dimensions. The target window is centered on the data pattern in the starting position for the scan. The function of this window is to provide a centering location for the interaction of the incident field with the target. By shifting the center of the window, the scanning action along the shift direction is simulated. The action of spinning the disk transforms a spatial frequency into a temporal one. The velocity v of the spinning disk is given by $v = r\omega$, where $\omega = 2\pi f$, and f is the temporal frequency. For a given mark pitch ℓ the corresponding temporal frequency is given by $f = v/\ell$ Spatial frequencies $v = 1/\ell$ are used in the following discussions, because the simple relation $f = vv$ exists for conversion to a temporal frequency.

Polarization elements are implemented in OPTISCAN through the use of a

polarization object. The object may describe a general polarization element characterized by its material dielectric tensor directly, or a simple uniaxial crystal characterized by rotation and phase retardation values. For instance, a simple half-wave plate may be modeled as a uniaxial crystal with a phase difference of 180° between the x and y polarizations. With the crystal principal axis at 22.5°, provides a 45° rotation for the output electric field when an x- or y-polarized electric field is used as input.

Detectors are implemented in OPTISCAN through the use of the detector object where a simple photoconductive detector is modeled. The detector active area is

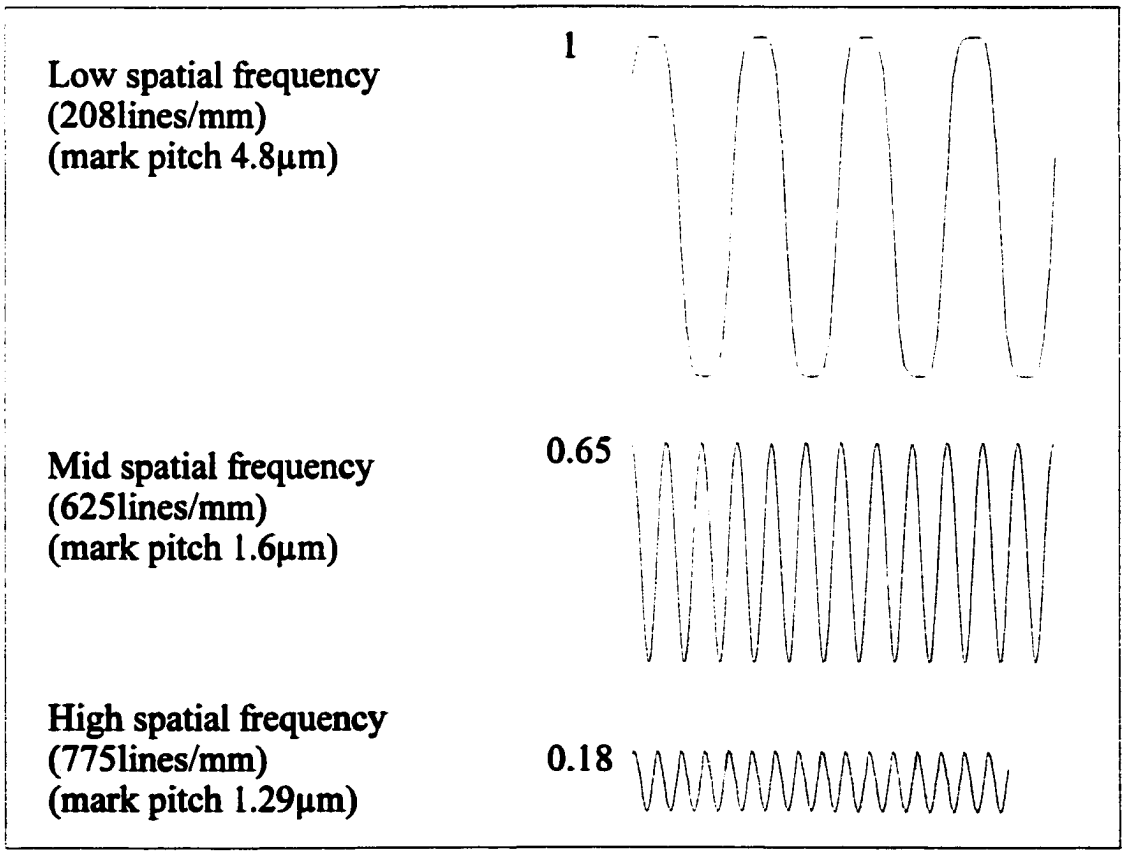

Figure 3.12. Data current signals for low, medium, and high spatial frequencies for the truncated Gaussian source distribution.

simulated through the use of graphical interfaces where information on the detector size and shape and responsivity are assigned. Single cell and segmented detectors are modeled using a bitmap editor. The basic operation of the detector is to convert the incident radiation to an electrical current. Since detectors respond to optical power, it is necessary to calculate the power. Once the optical power is calculated it is multiplied by the responsivity of the detector to obtain the detector output current. The optical power is calculated from the magnitude of the Poynting vector. The conversion from electric field amplitude to detector output current is accomplished internally in the OPTISCAN

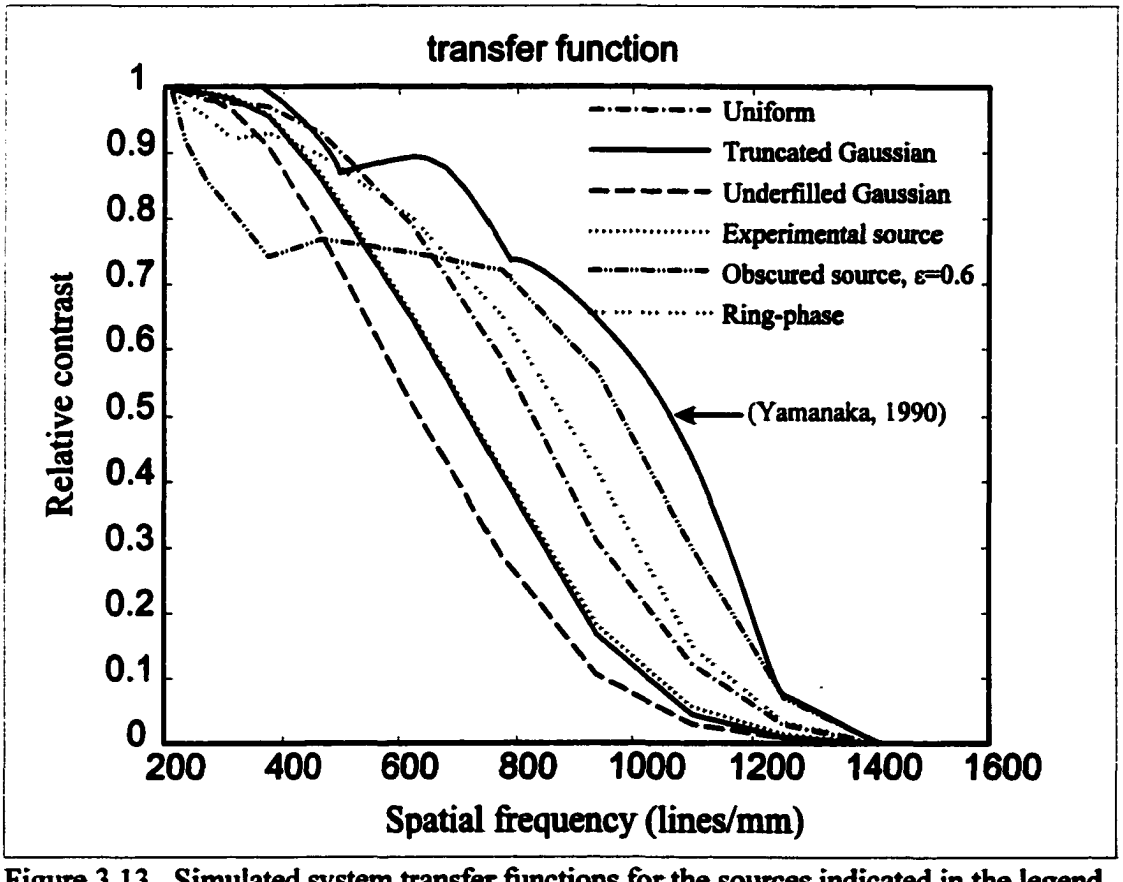

Figure 3.13. Simulated system transfer functions for the sources indicated in the legend.

program.

3C.3 - Simulation results

This section presents the simulation results. Figure 3.12 shows data current signals for low (208 lines/mm), mid (625 lines/mm), and a high (775 lines/mm) spatial frequencies observed with the truncated Gaussian source distribution. The system transfer function is obtained by taking the peak-to-peak amplitudes of the signals and plotting them versus spatial frequency. Figure 3.13 shows the transfer functions for the 4 different sources of Figure 3.10 as well as other transfer functions that are discussed in

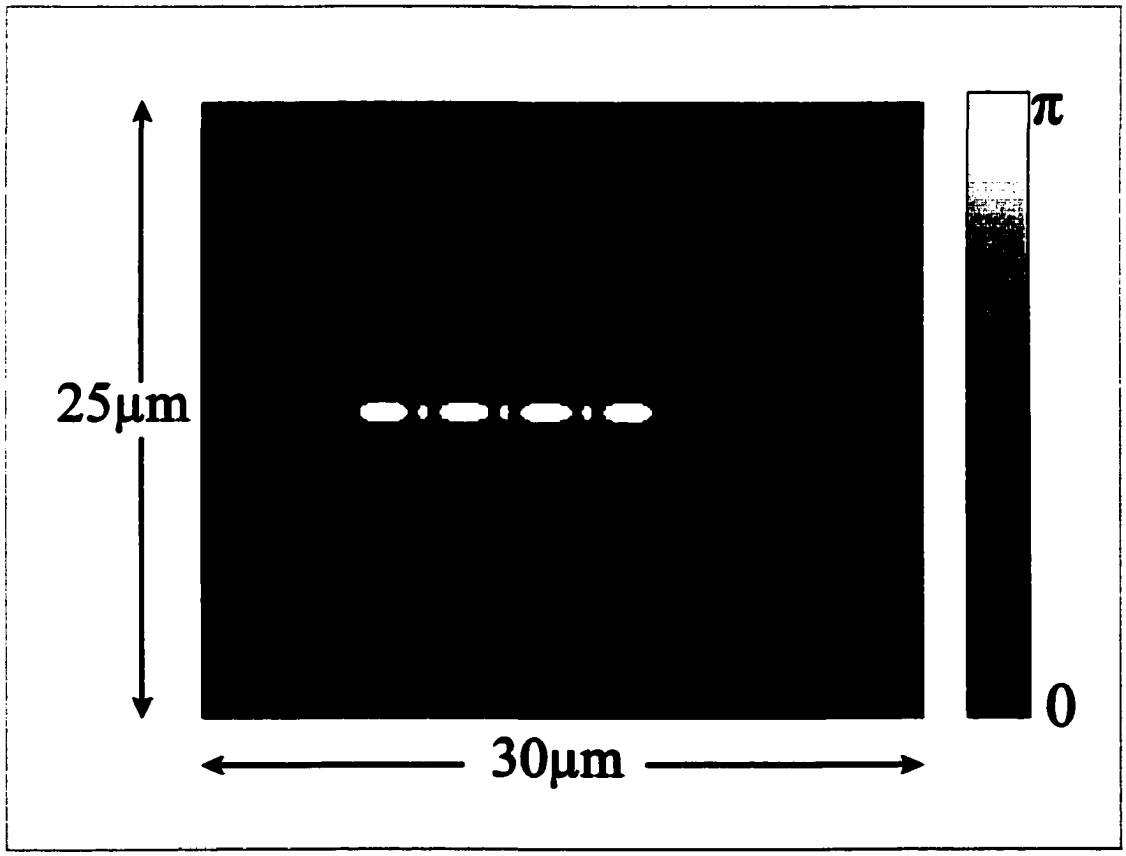

Figure 3.14. Worst case scenario data pattern where the long mark is 2.7μm long and the short mark is 0.6μm long.

subsequent sections. As expected, the roll off at high frequencies of the system transfer function for the 4 sources is observed. A notable difference is that the uniform source has the slowest roll off due to the fact that the central core of the focused spot is the smallest of the four illuminations. Also, the underfilled Gaussian source has the fastest roll off due to the fact that it has the largest focused spot diameter of the 3 distributions. The system transfer function of the experimental source distribution follows very closely the system transfer function of the truncated Gaussian.

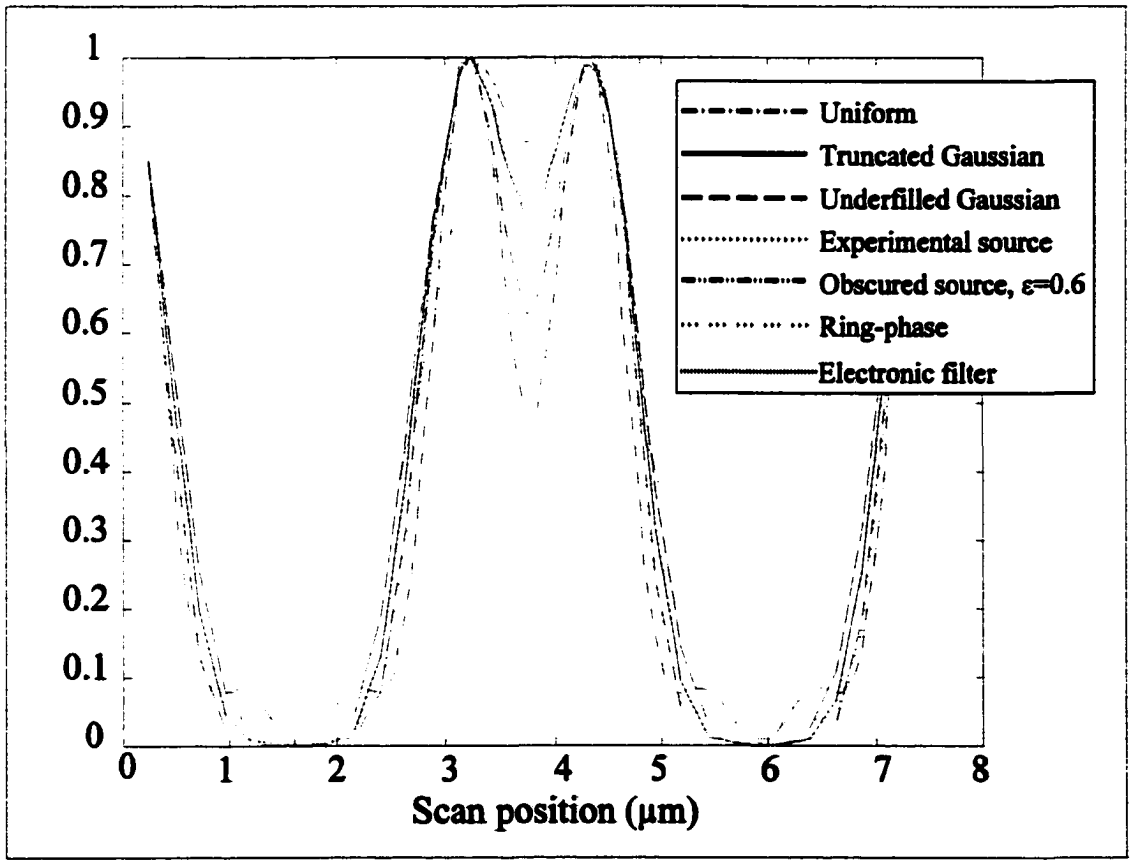

Figure 3.15. Data signal current(ma), for the worst-case scenario data pattern of Figure 3.14 for indicated sources and filters. Each signal is normalized to the signals maximum.

Another data pattern of interest in data storage is the so called "worst case" scenario pattern, as shown in Figure 3.14. This pattern consists of the longest mark in a given data channel code followed by the shortest space, shortest mark, shortest space, and longest mark again. This is a worst case pattern because it is one that is most likely to cause a detection error. This type of pattern produces a signal response that is very much like a two-point response for the system. Figure 3.15 shows the detector current signal for this pattern as a function of scan position for the different sources as well as other current signals that are discussed in subsequent sections. Detection errors are produced when electronic threshold circuits misread the edge positions of the small dip in the center of the pattern. It is interesting to note that the underfilled source barely resolves the short mark as shown by the shallow dip in the center of the signal. The deepest dip of the four sources examined so far is due to uniform source.

3C.3.A - Signal current distributions of a standard system

It is necessary to understand how signal energy is distributed in the pupil in order to design effective return-path optical amplitude filters. In this section the simulated signal current distributions in the pupil are presented.

The description of the procedure to simulate the signal current distribution in the pupil is as follows: first, the matrix corresponding to the mean signal current distribution is calculated by summing the individual signal current distribution matrices for each scan location and then dividing this matrix sum by the number of scan positions. Then, the signal current distribution matrices are subtracted individually from the mean signal

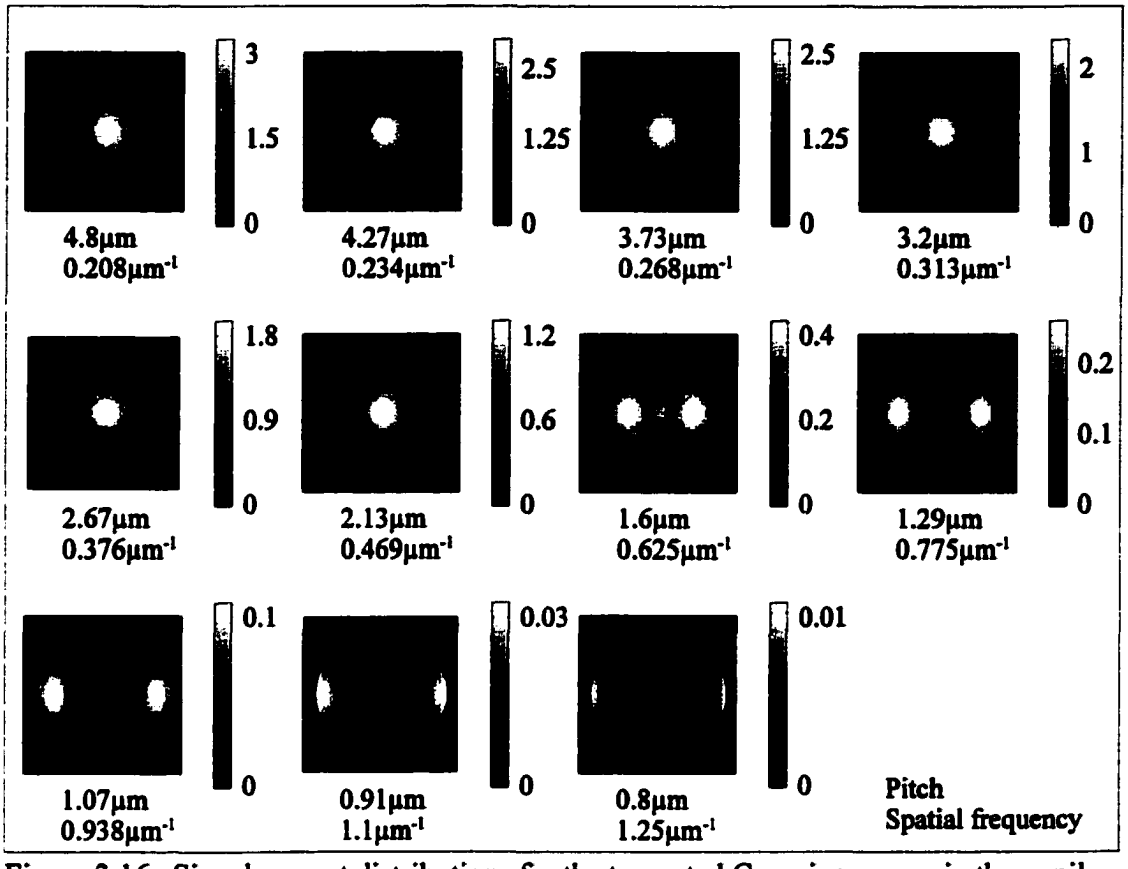

Figure 3.16. Signal current distributions for the truncated Gaussian source in the pupil of the objective lens after reflection from the disk, in units of mA. Decreasing mark pitch, Increasing frequency left to right, top to bottom.

distribution matrix, and each resultant matrix is squared. These resultant matrices are then summed and divided by the number of scan locations to obtain the signal current distribution in the pupil.

Figure 3.16 displays signal distributions for the Gaussian source with 0.9 truncation. Each subplot is normalized to its own peak value, as shown on the scale bar, in order to bring out the qualities of the distribution. From the peak values indicated on the scale bar, a reduction in signal strength as frequency is increased is observed, which

corresponds to the transfer function roll off of Figure 3.13. The other interesting feature to note is the shape of the distribution as frequency is increased. At low frequency the signal distribution is concentrated in the center of the pupil, and at high frequency the overlap area of the diffracted orders separates resulting in the signal being concentrated at the edge of the pupil, as predicted in Chapter 1. These distributions are an aid in designing return-path optical amplitude filters that partially equalize the system transfer function, as will be shown in Section 3D.2.A.

3C.4 - Summary of magneto-optic data storage system performance

In summary of this section, performance of the data channel of a magneto-optic data storage system is demonstrated. The system transfer function is shown to roll off at high frequencies as predicted from the scanning optical microscope description of Chapter1.

The effect of an underfilled Gaussian beam on the transfer function is faster roll off at high frequencies. The effect of an underfilled Gaussian beam on two-point resolution is to have a very small dip, only 12% modulation, in the center of the data signal. The effect of a uniform source on the transfer function is fast roll off at high frequencies, only not as fast as the underfilled Gaussian source. The effect of a uniform source on two-point resolution is to have a very noticeable dip, 37% modulation, in the center of the data signal. The truncated Gaussian source and the experimental source have a 23% modulation in the center of the two-point resolution data signal of Figure 3.15.

The signal current distributions in the pupil are shown to be concentrated in the center of the pupil for low-frequency data patterns. At spatial frequencies near $NA/\lambda=0.7\mu m^{-1}$, which is the cutoff frequency for an equivalent coherent uniformly illuminated plane-wave system, the signal current distribution becomes bimodal and is concentrated toward the edges of the pupil. The separation of the lobes increases with increasing frequency.

3D - Introduction of superresolution components in a magneto-optic data storage system

The physical location of the optical and electronic filters to be studied are shown in Section 3B Figure 3.4b. Superresolution techniques include optical filtering in both the illumination path and the return path, and electronic filtering in the return path, as discussed in Section 3B.

In order to implement an illumination-path filter in OPTISCAN, a reflective target with the appropriate amplitude and/or phase distribution is applied to the source distribution before it is used in the entrance pupil of the objective lens. For a return-path filter, a reflective target with the appropriate amplitude and/or phase distribution may be used after the light is recollimated by the objective lens. Figure 3.17 shows an OPTISCAN project window for the magneto-optic data storage system. The icons in Figure 3.17 represent the different elements in the MO data storage system and tools for manipulation of data. The OPTISCAN website "http://www.opt-

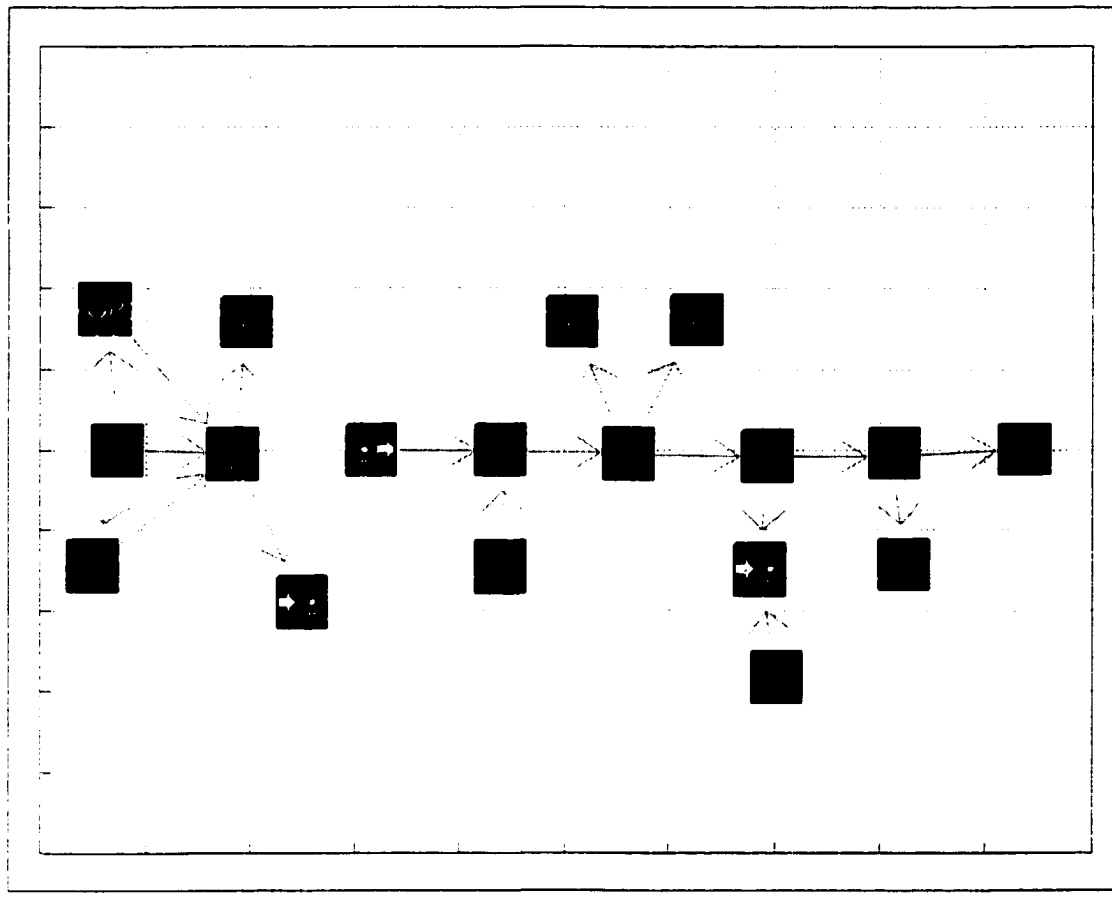

Figure 3.17. Optiscan project window of a magneto-optic data storage system showing icons representing sources, lenses, targets, wave-plate, beam splitter, detectors, save and load data, mathematical operation, and graphical data output. For more information visit the Optiscan homepage at "http://www.opt-sci.arizona.edu/milster/optiscan/help/main.html "

sci.arizona.edu/milster/optiscan/help/main.html" has help information and tutorials.

Another type of return-path filter is an electronic boost filter. This filter is modeled using the electronic filter transfer function characteristics. The action of the electronic boost filter is simulated by multiplying the Fourier transform of the detector current signals by the corresponding electronic boost filter value to obtain the electronically filtered data signals. One other electronic filter considered is a tapped-

delay-line filter. The delay-line filter is used to reduce artifacts in the data signals that are a result of sidelobes introduced to the focused spot from the illumination-path filters.

3D.1 - Illumination-path filtering

Two different illumination-path filtering techniques are discussed in this section. The first illumination-path filter is the ring-phase filter (Ando, 1993) described in Section 2B.1B. The other type of illumination-path filter is a circularly symmetric amplitude filter that blocks the central portion of the pupil described in Section 2B.1A. This type of filter has been studied extensively (Mahajan, 1983), and it is instructive to analyze its effects in the magneto-optic system.

3D.1.A - Ring-phase illumination-path filtering

Figure 3.18 displays the signal current distribution for the ring-phase filtered source. Each subplot is normalized to its own peak value, as shown on the scale bar, in order to bring out the qualities of the distribution. From the peak values indicated on the scale bar, a reduction in signal strength as frequency is increased is observed that corresponds with the transfer function roll off in Figure 3.13. An interesting feature of the distribution is the increased structure around the edge of the filter boundary. This structure is observed in the experimental distributions also, as discussed in Chapter 4. The trend of low frequency signal distributions is to concentrate signal power in the center of the pupil. For high frequency signal distributions, signal current is concentrated at the edge of the pupil.

There are some interesting comparisons to be made between the signal current

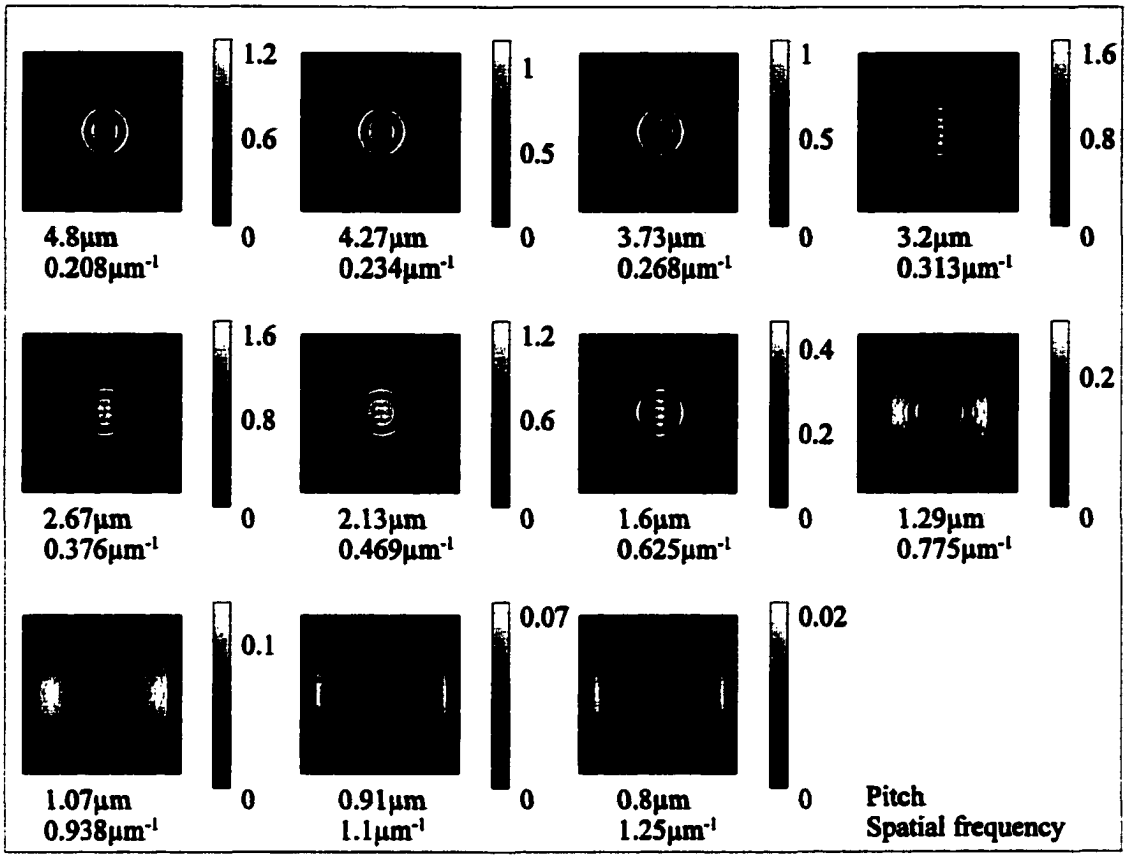

Figure 3.18. Signal current distributions for the ring-phase illumination-path filtered source in the pupil of the objective lens after reflection from the disk, in units of mA. Decreasing mark pitch, Increasing frequency left to right, top to bottom.

distributions in Figure 3.18 for this ring-phase filter source and those of the conventional unfiltered truncated Gaussian source of Figure 3.16. In Figure 3.18 the scales range in value from 1.6 to 0.02, while in Figure 3.16 the scales range in value from 3 to 0.01. The variation in total signal current from low to high frequency with the ring-phase filtered source is less than the variation in signal current with the conventional unfiltered source. This indicates the action that the ring-phase filter has on equalization for the system. The ring-phase filter accomplishes equalization by lowering the low frequency response and

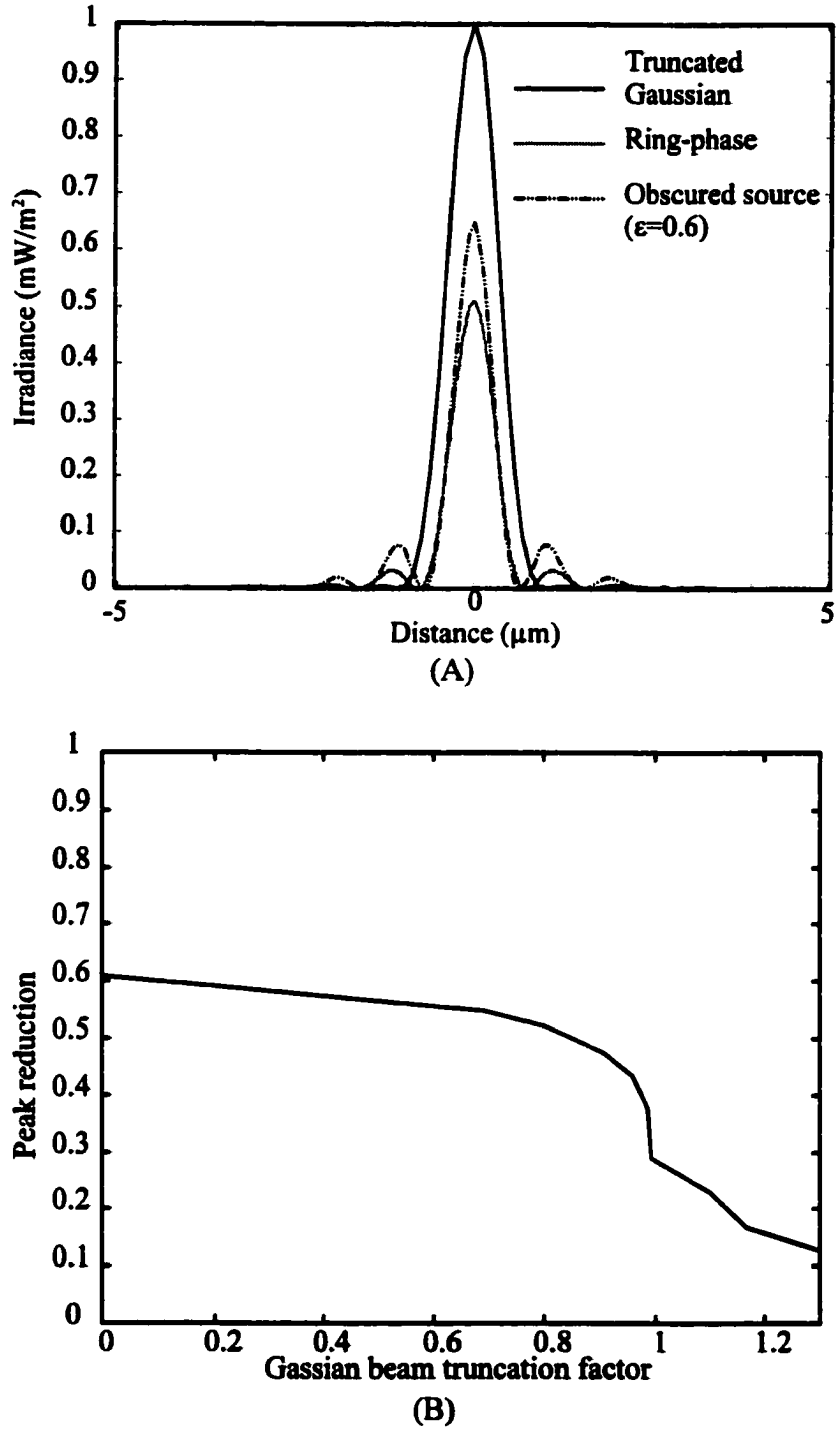

Figure 3.19. (A) irradiance profiles of focused spots, (B) ratio of peak irradiance with ring-phase filter to peak of unfiltered irradiance as a function of Gaussian beam truncation.

by increasing the high frequency response. For example, the peak for the unfiltered system at a low spatial frequency of $0.208\mu m^{-1}$ is 3mA while that of the ring-phase filtered system is 1.2mA at the same frequency. At a high spatial frequency of $1.1\mu m^{-1}$ the peak for the unfiltered system is 0.03mA while that of the ring-phase filtered system is 0.07mA.

The focused spot profile for the ring-phase filtered source is shown in Figure 3.19(a) along with the focused spot profile for the unfiltered system and a centrally obscured source that is discussed in section 3D.1B. The Gaussian truncation factor used for Figure 3.19(a) is 0.7, which is the same used by Ando. The filter produces a peak irradiance reduction of approximately 50% and a side-lobe level at 6% of the peak value, as shown in Figure 3.19. The peak reduction is understood from the central ordinate theorem of Fourier optics. That is, the area of a function is equal to the value of the Fourier transform at the origin in the Fourier domain.

It is worth while to discuss this peak reduction a little further. The peak reduction is a function of the radii of the phase annulus and also a function of the Gaussian truncation. Figure 3.19(b) shows the ratio of peak irradiance with the ring-phase filter to peak irradiance of the unfiltered focused spot as a function of Gaussian beam truncation. The simulation holds the ring parameters constant, as well as the total power in the pupil. The peak reduction is slow and gradual from uniform illumination to a truncation factor

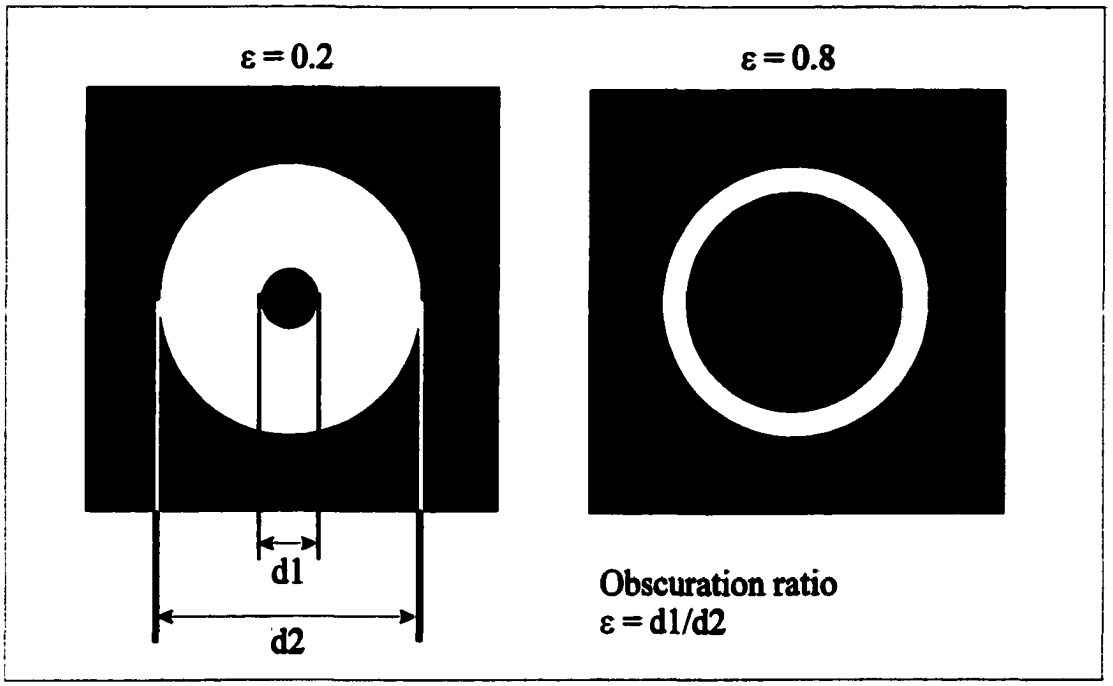

Figure 3.20. Definition of obscuration ratio, ε. Amplitude filtering in the illumination-path with a circular obstruction.

of 0.9, varying from 0.61 to 0.45. After the truncation factor of 0.9 the peak reduction becomes steep quickly. The truncation factors >1 are when the lens is underfilled. As the lens becomes underfilled the peak reduction becomes severe. For instance, when this same ring-phase filter is used with a Gaussian truncation factor of 0.9, a 45% reduction in peak irradiance occurs. This 45% reduction is not significantly different than the 55% reduction at 0.7, as predicted by this simulation. A favorable aspect of the filter is that the diameter of the central core is reduced by about 12%, which results in better contrast for the high spatial frequencies.

Figure 3.13 shows the transfer function curve for the ring-phase filtered system. Contrast is indeed improved at high frequency, even beyond that of the uniformly

illuminated pupil. For instance, at 900 lines/mm the contrast is 0.4 for the uniformly illuminated filter and 0.5 with the phase-ring filtered source, which is an improvement of 25% in contrast level.

In Figure 3.15 the two-point response curve of the ring-phase filtered system is shown. There is a pronounced central dip observed for the ring-phase source, which is deeper than that of the uniformly illuminated source. The modulation level of the central dip is 43% for the ring-phase filtered source compared to 37% for uniform illumination.

3D.1.B - Central obscured pupil illumination-path filtering

The other filter that is used in the illumination path is a circularly symmetric amplitude filter that obstructs the central portion of the pupil. Figure 3.19 depicts the

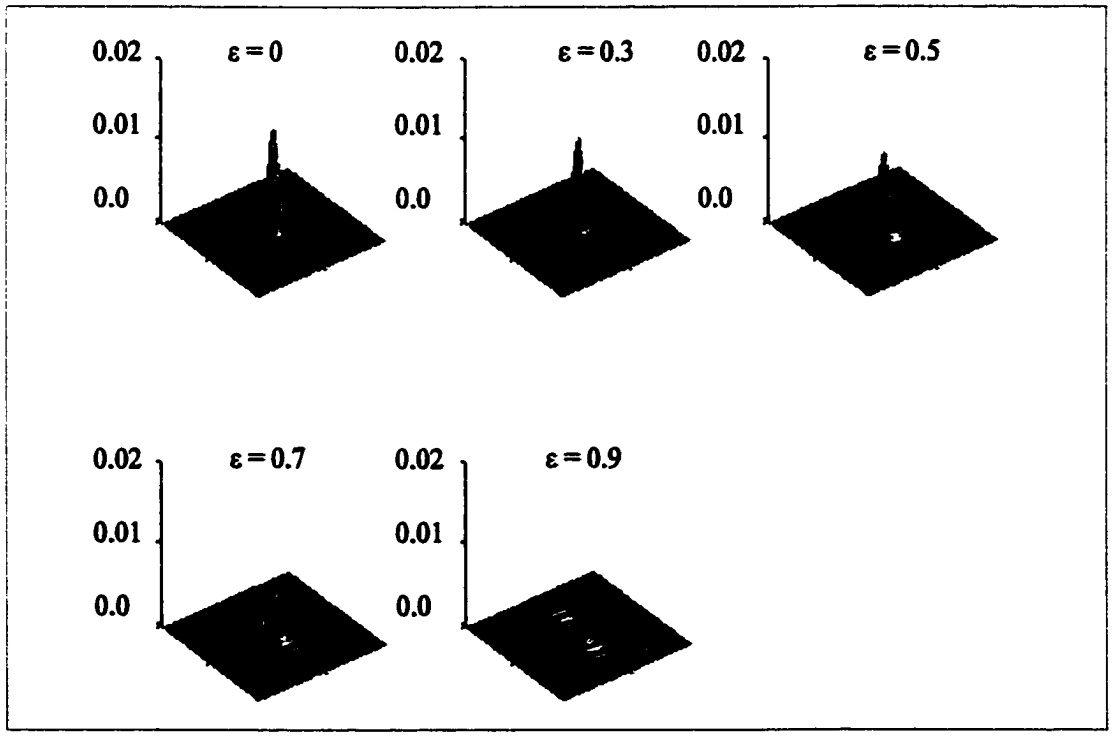

Figure 3.21. Focused spot irradiance distributions as a function of obscuration ratio, ε.

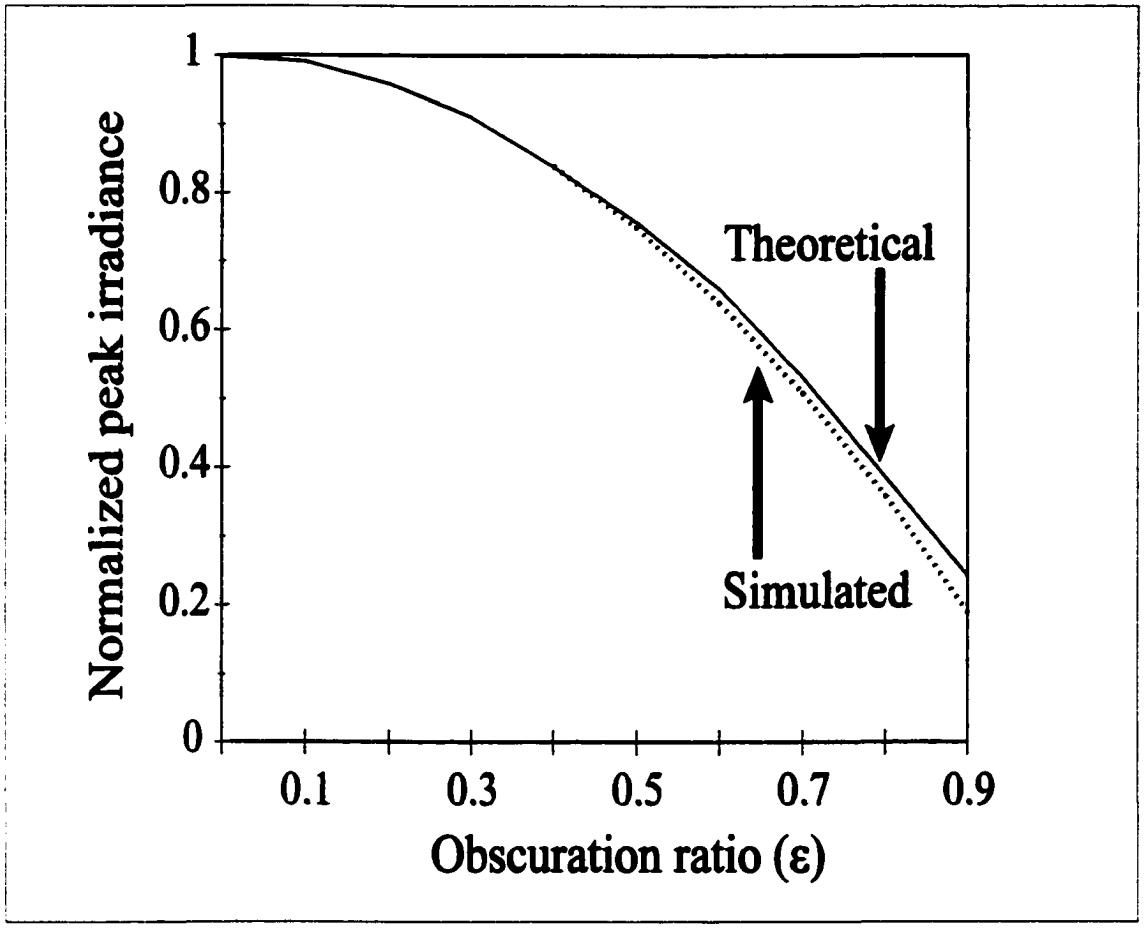

Figure 3.22. On axis peak irradiance as a function of obscuration for the focused spot distributions of Figure 3.20, showing the simulated and the theoretical curve.

central obscuration in the pupil and the definition of the obscuration ratio ε, where ε is the ratio of the central obscuration diameter to the pupil diameter, that is $\varepsilon = d1/d2$.

The motivation for considering this type of amplitude filtering is due to new laser diodes that are different than traditional edge emitters. The new lasers are Vertical Cavity Surface Emitting Lasers that emit radiation in a circularly symmetric ring structure by purposely exciting a higher order mode (Milster, 1998). This source can be thought of as

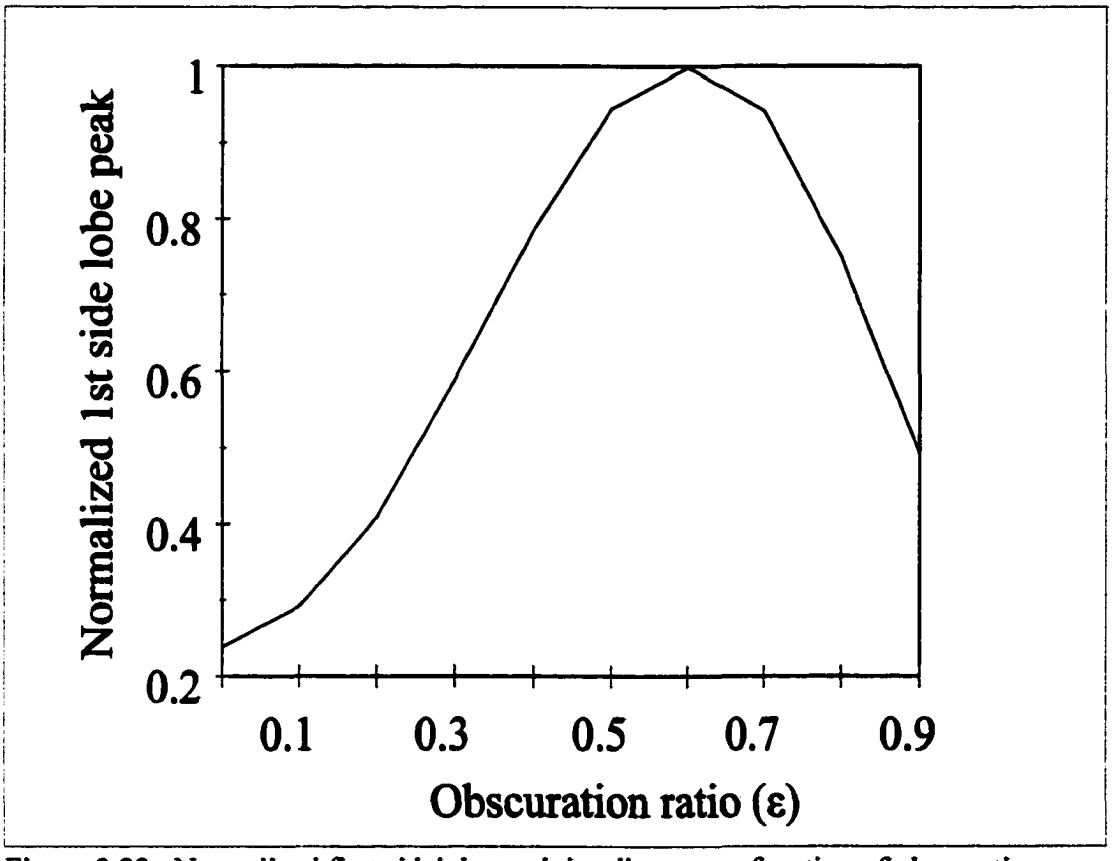

Figure 3.23. Normalized first sidelobe peak irradiance as a function of obscuration ratio.

a highly obscured circularly symmetric source for data storage applications. More details on this source is given in Chapter 5.

A design example characterizing the effects of this type of amplitude filter on the focused spot is now presented. The focused spot parameters, such as on-axis peak irradiance, first side-lobe behavior, full-width-at-half maximum (FWHM), and encircled energy, for a fixed total power P_0 transmitted by the aperture are investigated as a function of ε. The Optiscan system consists of a source, lens, and observation plane.

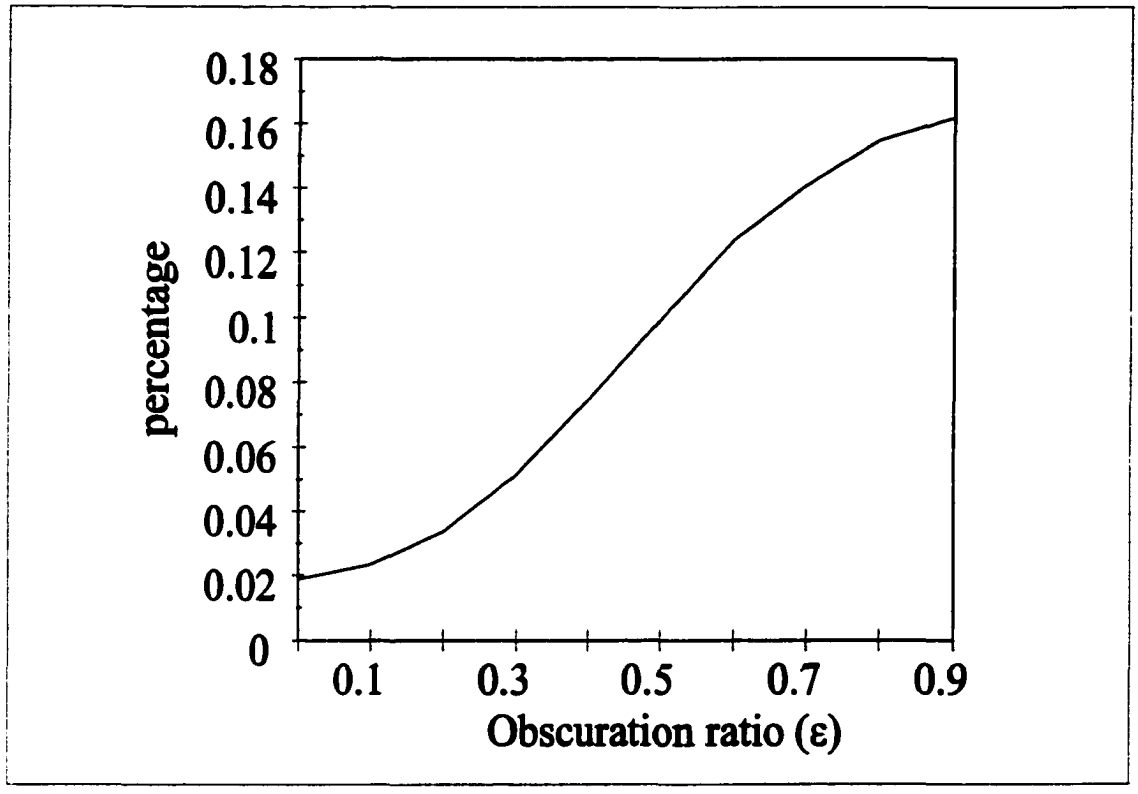

Figure 3.24. Ratio of the first side lobe irradiance to the central maximum value of the focused spot as a function of obscuration ratio.

The source is the obscured source that is directly inserted into the entrance pupil of the lens. The lens is a Zeemax paraxial lens with a focal length of 3.89mm, entrance and exit pupil diameters of 5mm, and a numerical aperture of 0.55. The observation plane where the focused spot distributions are observed is the back focal plane of the lens.

Figure 3.21 shows the focused spot distributions as a function of ε. Qualitatively, as ε increases, the peak irradiance decreases and the sidelobes increase. The theoretical on-axis peak irradiance follows the expression $I_{peak} = (1 - \varepsilon^2)$. Figure 3.22 shows how the on-axis peak irradiance falls off with increasing ε for both the simulation and theory.

The plots in Figure 3.22 are normalized to the on-axis peak irradiance for the unobscured system, $\varepsilon = 0$. The simulation and theory agree very well with slight differences at high ε's. The differences at the high ε's may be due to high NA effects or sampling effects.

Figure 3.23 shows how the first side-lobe peak irradiance changes with obscuration ratio. The plot is normalized with respect to its maximum. A gradual increase in the first side-lobe irradiance occurs until about $\varepsilon = 0.6$, where a maximum is reached. The irradiance decreases after this point. This trend is observed in Figure 3.21, where for $\varepsilon = 0.7$ and $\varepsilon = 0.9$ the central maximum is visibly reduced, but there is more

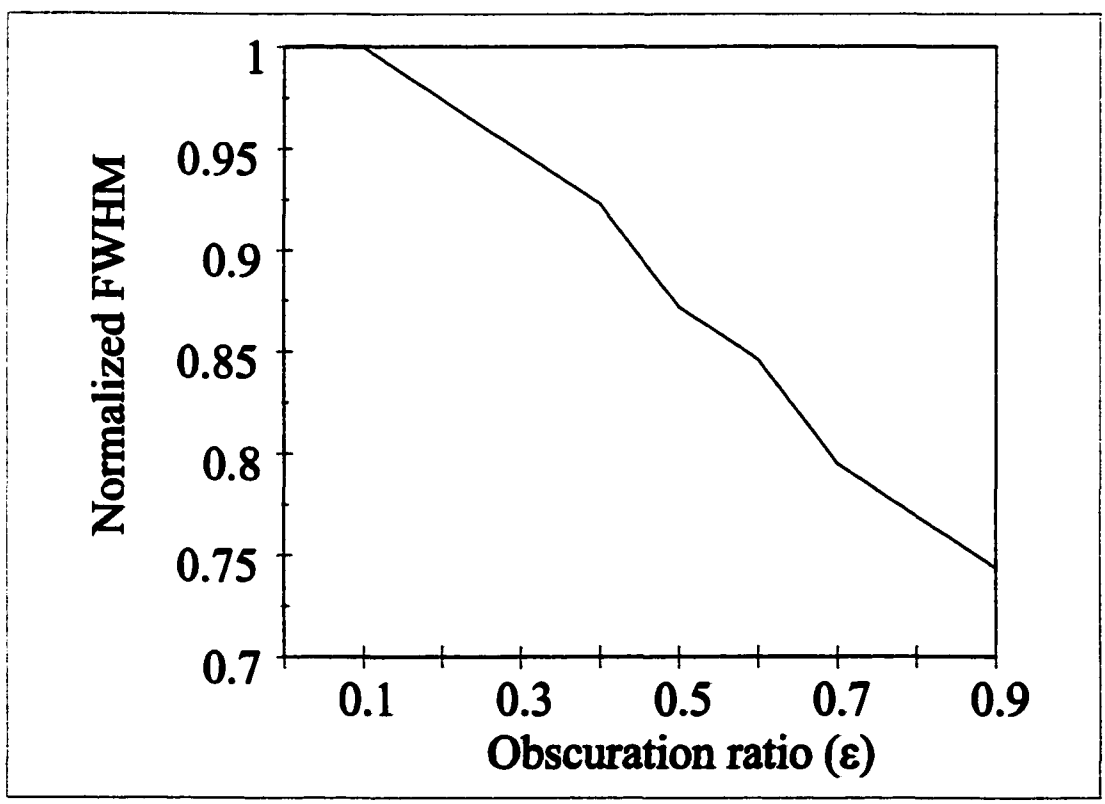

Figure 3.25. Full width at half maximum (FWHM) of the focused spot as a function of obscuration ratio.

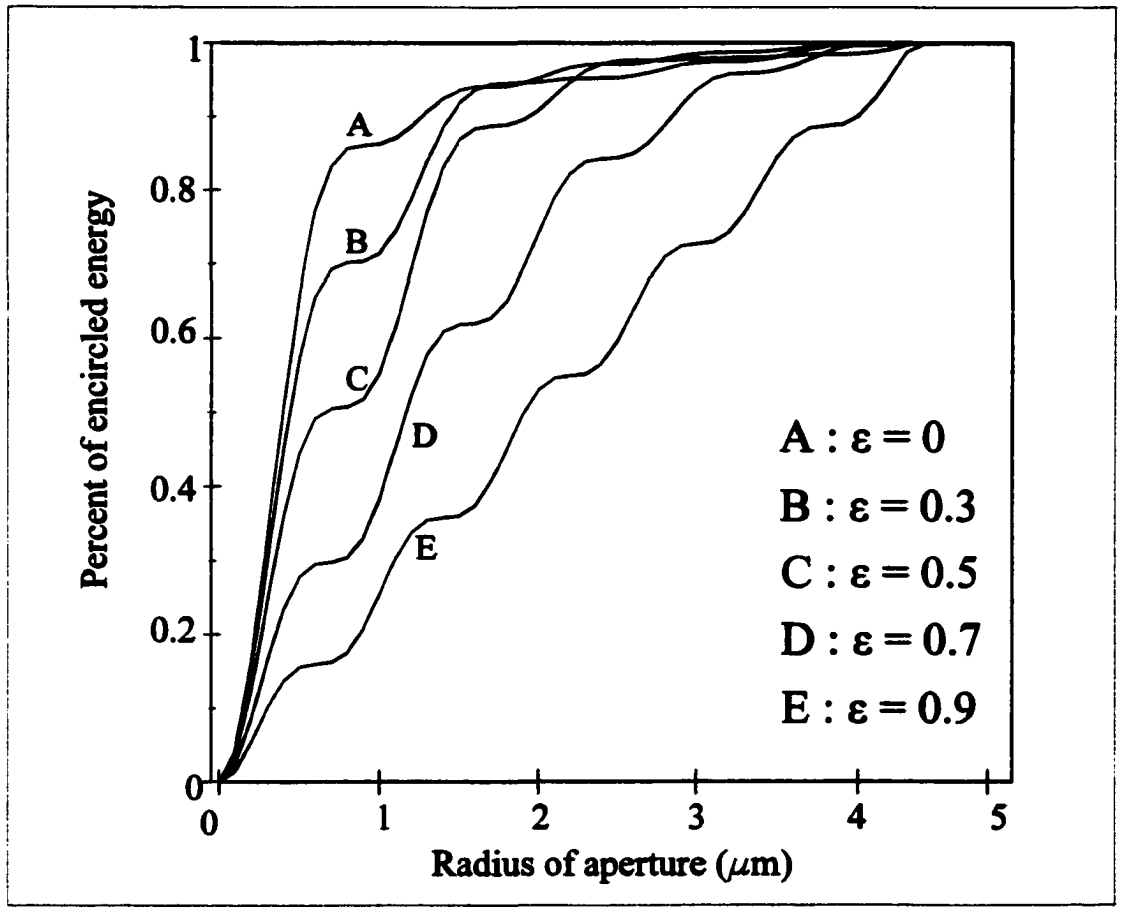

Figure 3.26. Encircled energy of the focused spots for different obscurations

sidelobe level becomes larger relative to the on-axis peak irradiance. In the limit as $\varepsilon \to 1$, an infinitely thin ring, the focused spot irradiance follows a squared J_0 Bessel function with a theoretical sidelobe-to-peak ratio of about 0.1621.

Figure 3.25 shows how the full-width-at-half maximum (FWHM) changes as a function of ε. The plot is normalized to the FWHM of the unobscured system with $\varepsilon = 0$. The FWHM decreases as ε increases, which is a desirable feature because contrast at high spatial frequencies will be increased with a reduced FWHM. However, the tradeoff for reduced FWHM is shown in Figures 3.22-3.24 with reduced peak irradiance and higher

side-lobe levels.

Figure 3.26 shows the encircled energy diagrams for different obscurations. Encircled energy is calculated by varying the radius of a pinhole in the focus plane from zero to 5μm, and the corresponding energy that is passed through the pinhole at each radius step is recorded. The plots are normalized by the maximum amount of light passing through the completely open pinhole. For obscurations of about $\varepsilon \leq 0.5$, the energy stays well confined within a radius of 1μm. For $\varepsilon > 0.5$ the energy spreads out rather quickly into a larger radius.

For a fixed amount of source power, the on-axis peak irradiance of the focused spot decreases with increasing ε. The FWHM of the focused spot decreases with increasing ε, which improves resolution in the Rayleigh sense. However, the increased resolution is achieved at the price of reduced peak irradiance, higher side lobe levels, and a spread of energy into the outer lobes of the diffraction pattern.

Now consider an amplitude filtered source with an obscuration ratio of $\varepsilon = 0.6$ in the previously described MO data storage system. Figure 3.13 shows the transfer function curve for this source. The contrast is improved at high frequency relative to the unfiltered source. The shape of the ε=0.6 transfer function is significantly different than the other sources due to the illumination conditions in the pupil. This is understood by the amplitude filter blocking the central portion of the pupil resulting in low spatial frequency attenuation. The nearly flat response in the mid-frequency region indicates that the system is well equalized in this region. Figure 3.15 shows the two-point response of

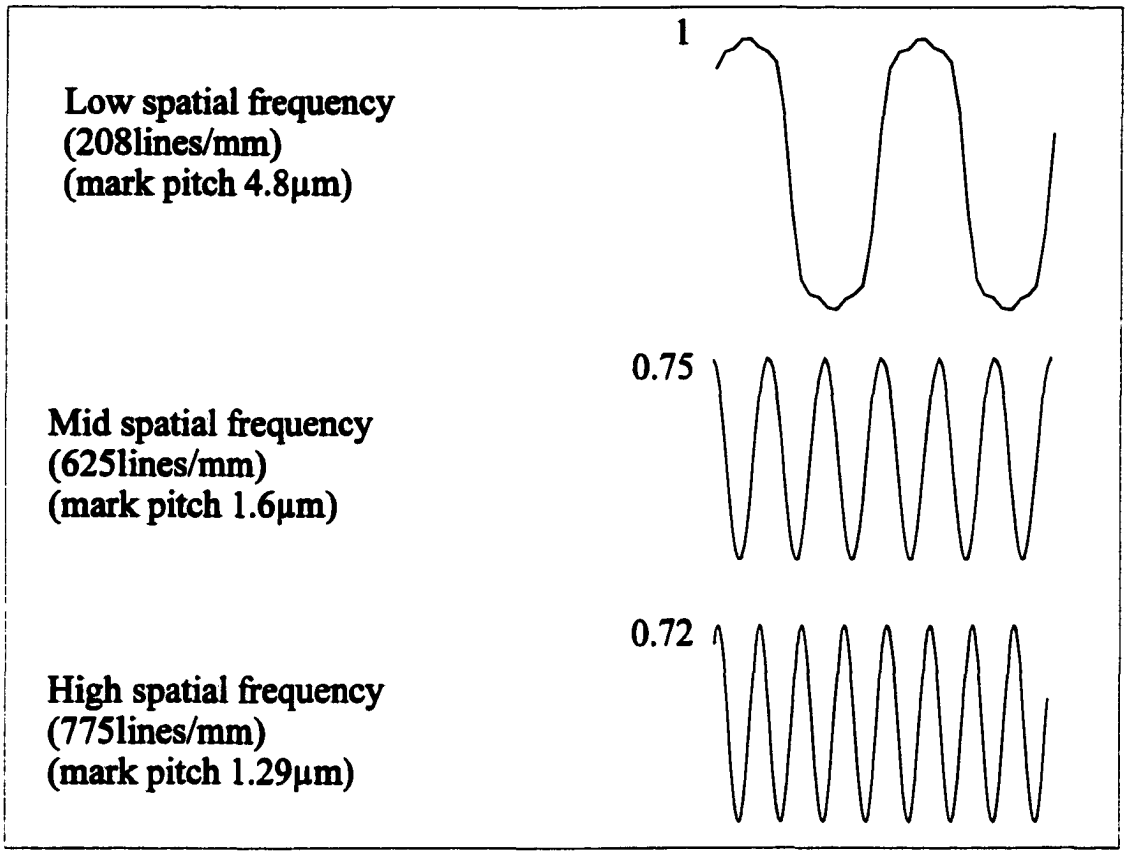

Figure 3.27. Data current signals for low, medium, and high spatial frequencies for an amplitude filtered source with central obscuration ratio $\varepsilon = 0.6$.

the ε=0.6 source. There is a pronounced central dip observed for this source, a 53% modulation, which is the largest of the filters studied in this report. It is tempting to say that there is no problem here, and to try an even higher obscuration ratio. However, the effects of sidelobes must first be determined. Figure 3.27 shows the data current signals for a low (208 lines/mm), mid (625 lines/mm), and a high (775 lines/mm) spatial frequency for this obscured source distribution. From these signals the artifacts from the sidelobes are evident. The undulations in the signals from the sidelobes are easily observed in the flat portions of the low frequency signal. The influence of the sidelobes

in the high frequency signal are not as obvious. Any corruption of the data signal reduces the system's ability to reliably interpret the data signal.

One way to deal with the corruption of the data signal due to the sidelobes is to use an electronic filter called a tapped-delay-line filter. This aids in reducing the effect of the sidelobes on the data signal (Tanabe, 1995). Strictly speaking, the tapped-delay-line filter is a return-path filter and will be discussed in section 3D.2.C.

Figure 3.28 displays the signal current distribution for the centrally obscured

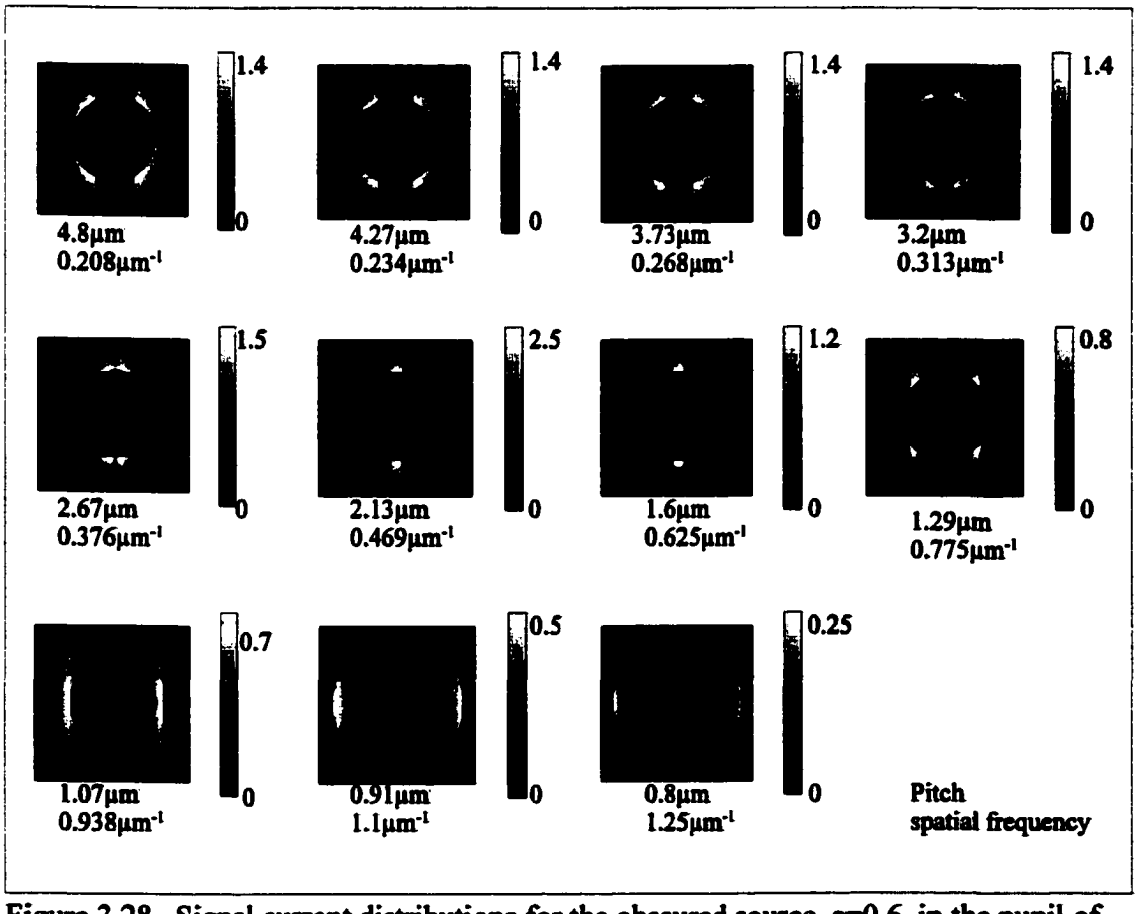

Figure 3.28. Signal current distributions for the obscured source, ε=0.6, in the pupil of the objective lens after reflection from the disk, in units of mA. Decreasing mark pitch, increasing frequency left to right, top to bottom.

source with $\varepsilon = 0.6$.. Each subplot is normalized to its own peak value, as shown on the scale bar, in order to bring out the qualities of the distribution. From the peak values indicated on the scale bar, a reduction in signal strength as frequency is increased is observed that corresponds with the transfer function roll off in Figure 3.13. An interesting feature to note is that there is no signal power in the center of the pupil even though the pupil is not physically obscured upon collection. The trend of low frequency signal distributions is to distribute signal power throughout the illuminating ring. For high frequency signal distributions, signal current is concentrated at the edge of the pupil.

There are some interesting comparisons to be made between the signal current distributions in Figure 3.28 for this centrally obscured source and those of the conventional unfiltered truncated Gaussian source of Figure 3.16. In Figure 3.28 the scales range in value from 2.5 to 0.25, while in Figure 3.16 the scales range in value from 3 to 0.01. The variation in total signal current from low to high frequency with the centrally obscured source is less than the variation in signal current with the conventional unfiltered source. This indicates the action that the centrally obscuration has on equalization for the system. The centrally obscuration accomplishes equalization by lowering the low frequency response and by increasing the high frequency response. For example, the peak for the unfiltered system at a low spatial frequency of $0.208\mu m^{-1}$ is 3mA while that of the centrally obscured system is 1.4mA at the same frequency. At a high spatial frequency of $1.1\mu m^{-1}$ the peak for the unfiltered system is 0.03mA while that of the centrally obscured system is 0.5mA.

3D.1.C - Writing with illumination-path filtering

Another issue of illumination-path filtered sources is concerned with the writing process of various data patterns. The main issue in writing centers on the heating effects caused by the sidelobes. The question is: "How does the preheating of the sidelobes affect the formation of the recorded marks?" This preheating in the recording layer due to the sidelobe energy can result in magnetic domain boundaries that are not clearly defined, which results in additional noise introduced into the system and a degradation of system performance.

An outline of a thermal simulation performed by Dr. C. D. Wright is presented in this section. The recording layer investigated is a phase-change recording layer. The thermal properties of the phase-change recording layer are compared to the thermal properties of a magneto-optic recording layer. Thermal simulations are presented for the phase-change recording layer for an unfiltered source, and for a circularly apertured source with obscuration ratio ε=0.9.

The temperature distribution in the recording layer is broken up into two parts(Wright, 1998)

$$T(x,y,z,t) = T_{PAL}(x,y,z,t) + T_{BHF}(x,y,z,t) \quad . \qquad (3\text{-}17)$$

$T_{PAL}(x,y,z,t)$ describes the temperature change due to heat absorbed by the layer from the laser source, that is, power absorbed from laser(PAL). $T_{BHF}(x,y,z,t)$ describes the temperature change due to heat flow across the layer boundaries, that is, boundary heat flow(BHF). Table 3.1 describes the optical and thermal constants for the 6-layer phase-

change structure used in the thermal simulation (Hirota, 1997). For a standard unfiltered focused spot, most of the heat generated in the recording layer is by the absorption of laser power that flows out through the layer boundary into the reflective layer below, rather than staying within the recording layer and acting as an additional heat source. The heat flowing down through the layers rather than accumulating in the recording layer means that

$$T_{BHF}(x,y,z,t) \approx - T_{PAL}(x,y,z,t) \quad . \quad (3\text{-}18)$$

Description of the layer	Thickness (nm)	Refractive index	Thermal Conductivity J/(m s °C)	Heat Capacity MJ/(m^3 °C)
polycarbonate substrate	0.6mm semi-infinite	1.585	0.22	1.5
ZnS-SiO_2	90	2.1 - 0.005j	0.66	2.05
Phase-change layer	20	4.1 - 4.1j	0.58	1.29
ZnS-SiO_2	15	2.1 - 0.005j	0.66	2.05
Al alloy	150	1.2 - 5.7j	50	2.4
Overcoat PMMA	100	1.5	0.2	1.7

Table 3.1. 6-layer phase-change medium, listing optical and thermal properties.

The phase-change layer, described in Table 3.1, has low thermal conductivity. The low thermal conductivity means that there is very little lateral heat flow along the

recording layer. The thin dielectric layer between the phase change layer and the reflective layer does not present much of a barrier to heat flow perpendicularly downward. The thick, high thermal conductivity reflective layer is acting as a very efficient heat sink. This means that, for the phase change recording layer structure studied, the heat is well confined to the region of high laser power. The simulation shows that for a source with a central obscuration of ε=0.9 the focused spot side lobes are insignificant as heat sources, and the heat is well confined to the regions directly heated by the central core of the focused laser spot.

Description of the layer	Thickness (nm)	Refractive index	Thermal Conductivity J/(m s °C)	Heat Capacity MJ/(m^3 °C)
glass substrate	1.2mm semi-infinite	1.5	1.5	2.0
SiO	60	2.0	0.66	2.05
Magnetic film	20	3.67 + 3.85j	40	3.2
SiO	100	2.0	0.66	2.05
Al	100	2 + 7.1j	240	2.7
Overcoat PMMA	100	1.5	0.2	1.7

Table 3.2. 5-layer magneto-optic medium, listing optical and thermal properties.

The fact that $T_{PAL}(x,y,z,t) \approx - T_{BHF}(x,y,z,t)$ for this phase change recording structure is unlike many magneto-optic multilayer media where the MO recording layer has a high thermal conductivity. Typically $T_{PAL}(x,y,z,t) \gg T_{BHF}(x,y,z,t)$ for MO media.

The high thermal conductivity of MO media means that heat moves laterally along the MO layer rather than down into the reflective/heat sink layer. This gives rise to the pre-heating and post-heating effects when recording. Typical MO multilayer media optical and thermal properties are given in Table 3.2 (Mansuripur, 1983). The magnetic layer has a thermal conductivity of 40 compared to the phase-change layer that has a thermal conductivity of 0.58.

When a focused spot that has significant sidelobes interacts with an MO layer structure the side-lobes act as significant heat sources. The heat is no longer well-confined to the regions directly heated by the central core of the focused laser spot, but the distribution is influenced by the presence of the side-lobes.

A focused laser spot with significant side lobes may be used for writing with certain phase change data storage systems, since the heating effects of the side lobes do not contribute significantly in the mark formation process. A focused laser spot with significant side lobes may encounter problems when used in MO storage, as the side lobes contribute significantly to the heating in the magnetic recording layer and will influence the formation of marks.

Figure 3.29 shows thermal modeling results for the phase change structure in Table 3.1 with an unfiltered source. Figure 3.29a shows the conventional focused spot profile from a truncated Gaussian source, and the 50% duty cycle write current modulation waveform. The 50% duty cycle waveform is actually rather large and rarely used in a real recording system. A more typical value for the duty cycle is ~20%.

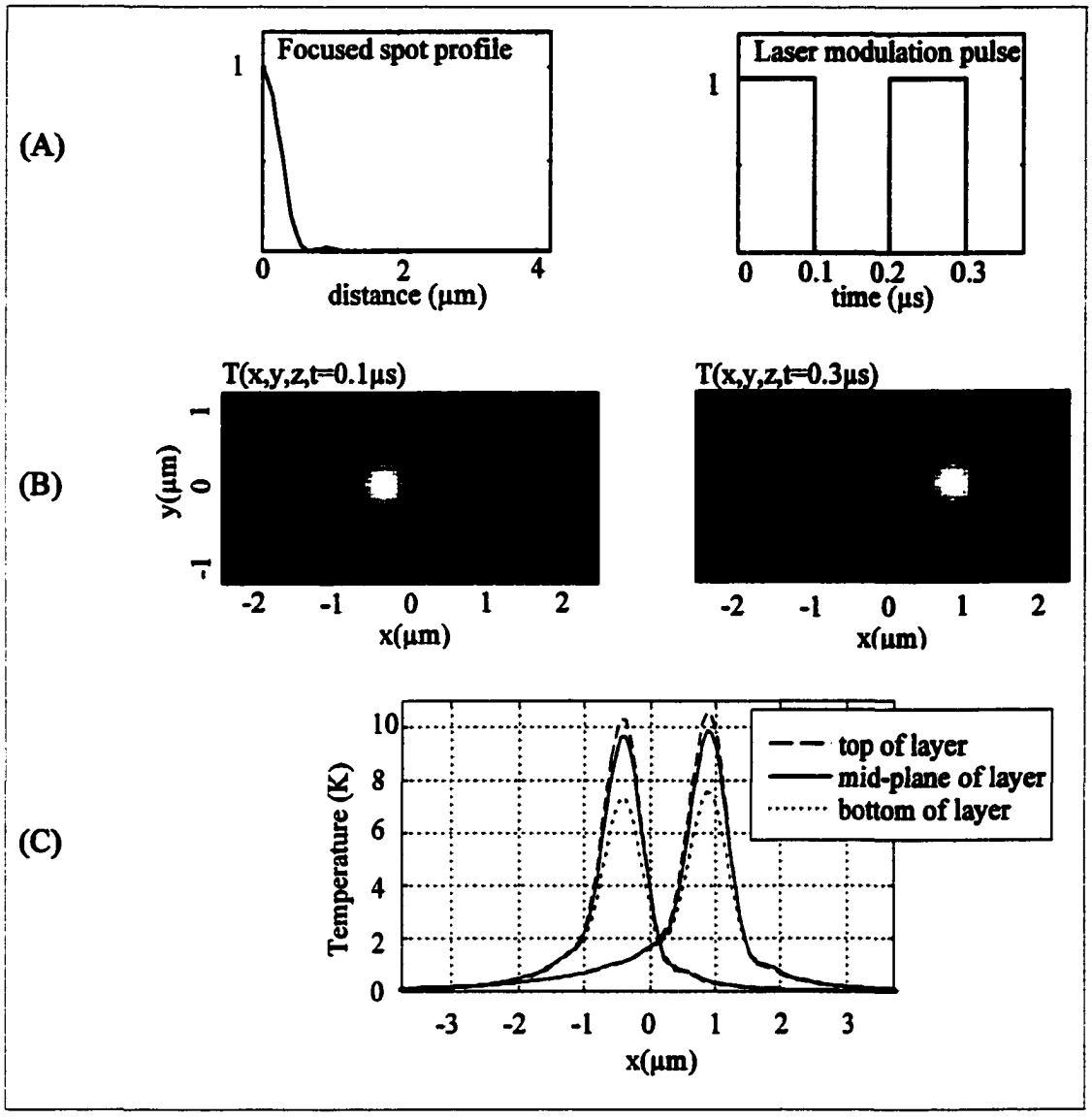

Figure 3.29. Thermal modeling results for the phase-change structure in Table 3.1. (A) Irradiance profile of focused laser spot from a conventional truncated Gaussian source, and write current modulation waveform. (B) Temperature distributions, T(x,y,z,t), at the recording layer mid-plane at the ends of the two write modulation pulses. (C) Profiles of T(x,y,z,t) vs. x at the ends of the two write modulation pulses at the top, mid-plane, and bottom of the phase change recording layer.

used in a real recording system. A more typical value for the duty cycle is ~20%.

However, using this large write current modulation duty cycle shows the effect of thermal

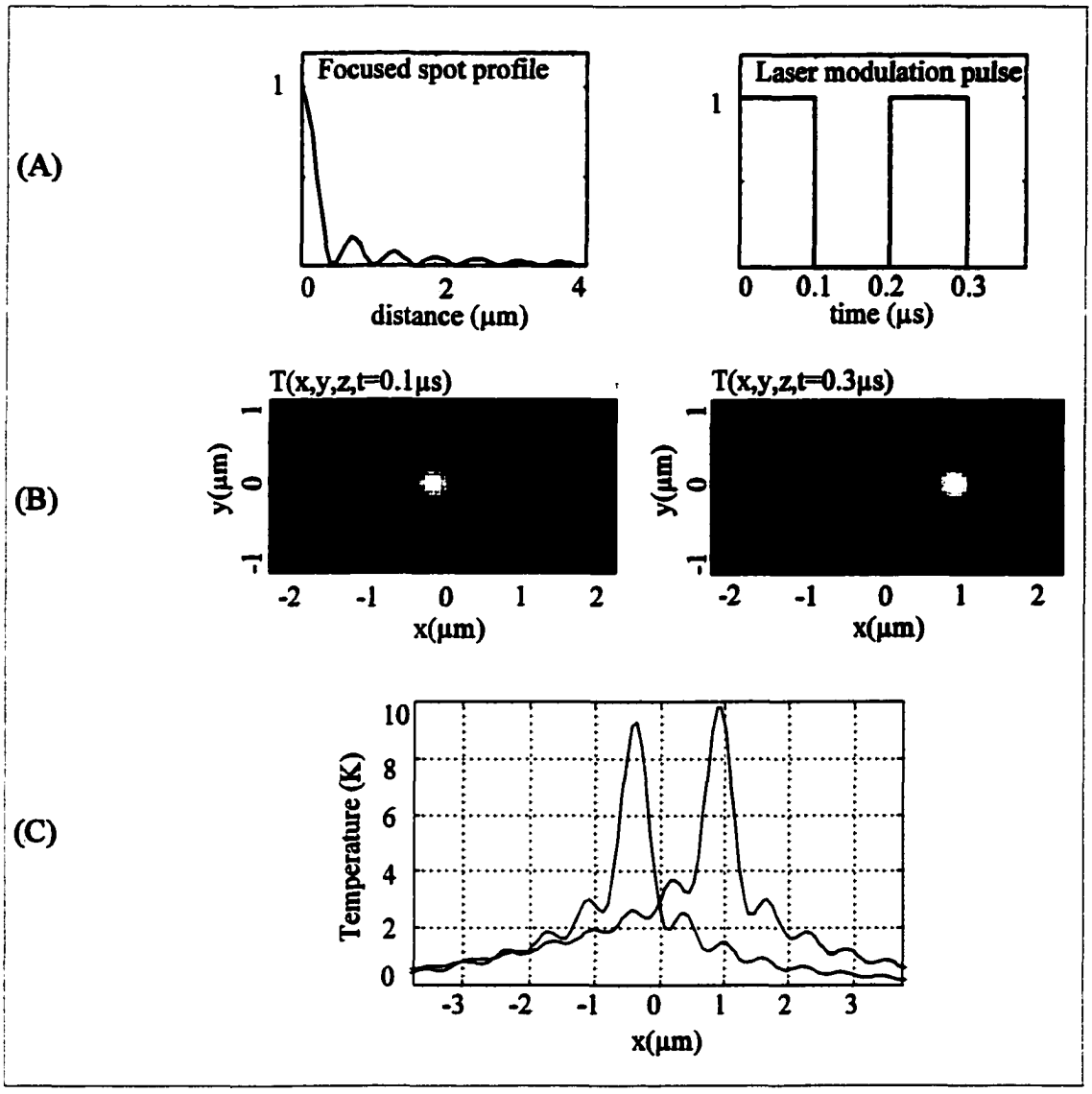

Figure 3.30. Thermal modeling results for the phase-change structure in Table 3.1. (A) Irradiance profile of focused laser spot from a source with an obscuration ratio of ε=0.9, and write current modulation waveform. (B) Temperature distributions, T(x,y,z,t), at the recording layer mid-plane at the ends of the two write modulation pulses. (C) Profiles of T(x,y,z,t) vs. x at the ends of the two write modulation pulses at the mid-plane of the phase change recording layer.

intersymbol interference more clearly. Figure 3.29b shows the 2-dimensional temperature distributions, T(x,y,z,t), in the mid-plane of the phase change recording layer

T(x,y,z,t) vs. x at the ends of the two write modulation pulses at the top, mid-plane, and bottom of the phase change recording layer. This shows that the heat stays confined to the central core of the focused spot.

Figure 3.30 shows thermal modeling results for the phase change structure in Table 3.1 with a circularly apertured source. Figure 3.30a shows the focused spot profile from a source that has an illumination-path amplitude filter with an obscuration ratio of ε=0.9, from Section 3D.1.B, and the 50% duty cycle write current modulation waveform. Figure 3.30b shows the 2-dimensional temperature distributions, T(x,y,z,t), in the mid-plane of the phase change recording layer at the ends of the two write current modulation pulses. T(x,y,z,t) is affected by the sidelobes as indicated in Figure 3.30b. Figure 3.30c shows a profile of T(x,y,z,t) vs. x at the ends of the two write modulation pulses mid-plane of the phase change recording layer. This shows that the heat stays confined to the central core of the focused spot even with the presence of the sidelobes. The increase in thermal intersysmbol interference in Figure 3.30 is due to the duty cycle of the write current modulation waveform and can be minimized by optimizing the duty cycle of the modulation waveform (Wright, 1998).

The laser profiles in Figure 3.29a and Figure 3.30a are normalized to unity and scaled by $P_0/(\pi r^2)$ where P_0 is the laser power of 1mW and r is the radius of 1μm. The temperature values for Figure 3.29 and Figure 3.30 are scaled to the peak power density of a Gaussian beam of power 1mW and 1/e radius of 1μm. To obtain temperature values, T_{actual} for laser powers other than 1mW use the following formula

$$T_{actual} = T_{1mW}\left(\frac{\pi}{10^9}\right)P_{actual} \quad , \qquad (3\text{-}19)$$

where P_{actual} is the focused laser spot irradiance in W/m^2. As an example, a 5mW laser with a 1μm radius has an irradiance of $P_{actual} = 1.6 \times 10^9$ W/m^2, requiring the temperature values in the profiles of Figure 3.29c and Figure 3.30c to be multiplied by a factor of 5.

3D.1.D - Servo system considerations with Illumination-path filtering

The effect of the illumination-path filter on the servo system that controls the position of the objective lens is discussed in this section. The circularly symmetric illumination-path filter alters the shape of the focused spot in both the in-track direction and the across-track direction. The depth of focus actually improves with the use of circularly symmetric filters (Mahajan, 1986). However, the redistribution of energy in the across track direction degrades the tracking performance (Wang, 1993).

The effects on the tracking servo system may be avoided if a different geometry of illumination-path filters is used, as done by both Yamanaka (Yamanaka, 1990) and Tanabe (Tanabe, 1995). Their geometry is to use a rectangular shading band filter that results in a focused spot distribution lacking circular symmetry. Rather than using a rectangular piece of metal in the illumination-path, a double rhomb prism is used to provide the central rectangular shading region without initially throwing away light. The sidelobes and central core reduction occur in the along track direction, but the spot size remains practically unchanged in the across track direction. In order to reduce the corruption in the data signal from the in track sidelobes Yamanaka spatially filters the

sidelobes with a slit just before the data detector, and Tanabe uses a tapped-delay-line electronic filter. Yamanaka's transfer function curve is displayed in Figure 3.13 along with other system transfer function curves for comparison. The Yamanaka type of filter achieves an increase in contrast without the need for drastic servo considerations.

3D.1.E - Summary of illumination-path filtering

The ring-phase filter and the central obscuration pupil filter increase the relative contrast of the high frequencies, as shown in Figure 3.13. The two-point response improves with these filters as shown by the increased modulation of the high frequency portion of the data signal in Figure 3.15.

It is clear that the issues of system performance with illumination-path filters are complex. When writing data patterns, caution must be used due to the thermal effects of the sidelobes, and a thermal simulation to determine the energy threshold of a particular material's susceptibility to the increased sidelobe energy should be performed. In Section 3D.2.D, it is shown that the artifacts in the data signal due to the increased sidelobes may be eliminated or reduced by the introduction of an electronic tapped-delay-line-filter.

3D.2 - Return-path filtering

The main return-path filter is discussed in Chapter 2. This filter is simulated in OPTISCAN by using a bitmap editor to create an amplitude filter shape. The specific return-path optical amplitude filter chosen is discussed in Section 2B.1.A. In Section 3D.2.A the effects of the return-path optical amplitude filter on the system transfer

function and on the system two-point response are shown.

Two types of electronic filters are also simulated. An analog electronic boost filter that has nonlinear gain frequency characteristics is modeled from the experimental filter described in Chapter 4. The effects of the electronic boost filter on the system transfer function and on the system's two-point response are shown in Section 3D.2.B. In Section 3D.2.C different filter combinations are studied, such as the combination of the return-path optical amplitude filter, electronic boost filter and the illumination-path ring-phase filter.

The final type of electronic filter modeled is a tap-delay-line filter. This filter is a digital electronic filter used to reduce artifacts in the data signal from sidelobes and equalize the system transfer function. The effects of the electronic tap-delay-line filter on the system transfer function and data signals are shown in section 3D.2.D.

3D.2.A - Return-path optical filter

Figure 3.31(a) shows the x-band amplitude filter used in the simulation with the unfiltered source distribution. The parameter varied in the simulation is the center width of the band. The x-shape of the filter is selected based on the signal current distribution in the pupil in Figure 3.16. In the experiments of Chapter 4, an 18% x-band is used for the conventional unfiltered illumination, and a simple16% rectangle, shown in Figure 31(b), is used for the ring-phase filtered illumination. The simple bar for the ring-phase filter system is based on the signal current distributions for this source, shown in Figure 3.18, where at low frequencies there is a dark rectangular region where signal strength is

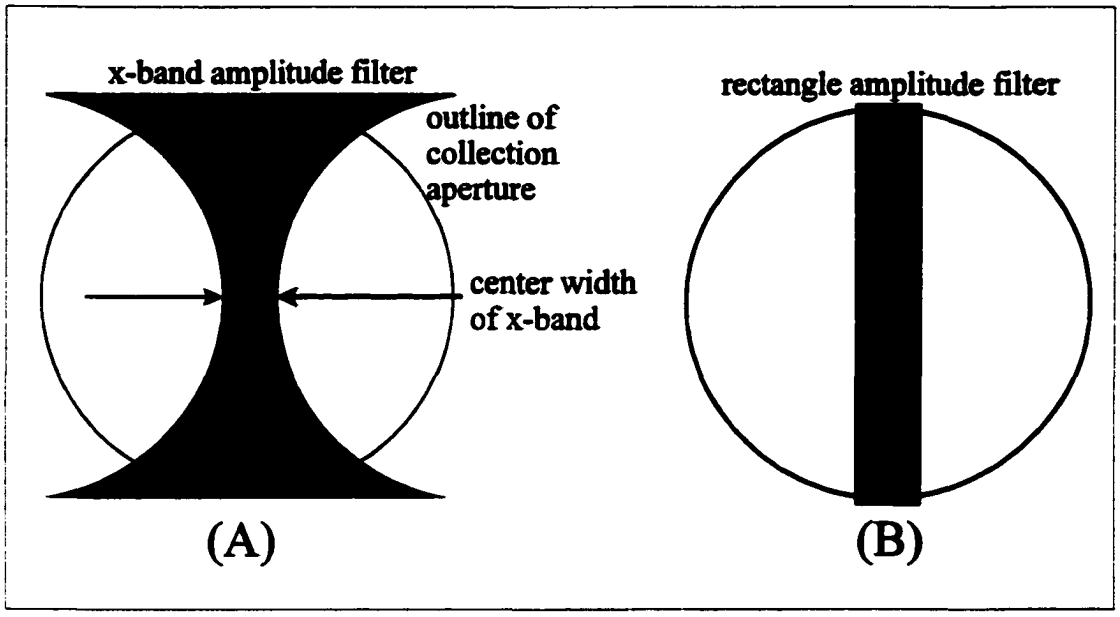

Figure 3.31. Return-path optical amplitude filters. (A) x-band used with conventional truncated Gaussian illumination, (B) rectangle (bar) filter used with the ring-phase illumination-path filtered source.

3.18, where at low frequencies there is a dark rectangular region where signal strength is low. At high frequencies when the signal current distribution becomes bimodal the same dark rectangular region is observed. The filter is oriented to cover the dark region in the signal current distribution. With the filter oriented as shown in Figure 3.31, the light contributing to the high frequency signal current distribution is not affected. However, this filter does affect light that contributes to the low frequency current distribution and has the effect of attenuating the low frequencies relative to the high frequencies. In addition to affecting light that contributes to the low frequency current distribution, it also affects light that contributes to the noise current distribution in the pupil as well, more will be said on this in chapter 4.

The source used in the simulation is the conventional unfiltered Gaussian beam

with truncation factor 0.9. In Figure 3.32 the transfer function curves for x-band center widths ranging in size from 5% - 50% of the width of the objective lens diameter are shown. Increase in contrast at high frequencies is observed, and this increase is dramatic for the larger center widths of the x-band. In the limit, if the center width approaches the edge where two pinholes pass a minimum of signal energy. In this case a uniform response out to the cutoff frequency of the system is observed(Wilson, 1991). This is a desirable characteristic, but the tradeoff for the uniform response is reduction in signal amplitude for low and moderate frequency. In actual practice the signal-to-noise ratio

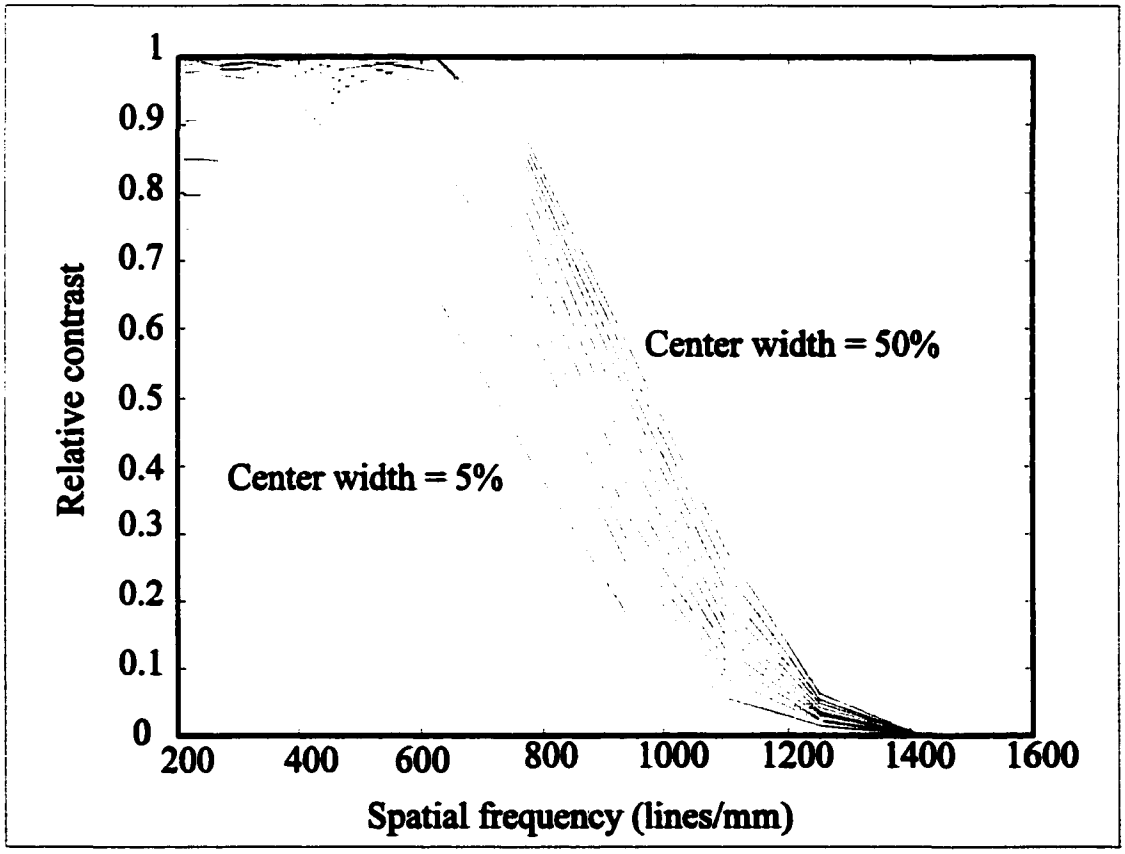

Figure 3.32. Transfer function curves for center widths of the x-band return-path filter ranging from 0%-50% in steps of 5%.

must also be considered as a requirement in addition to the signal contrast.

In Figure 3.33 the two-point response is shown for the unfiltered system and for the x-band return path filter. Observe the reduction in amplitude of the low frequency portion of the signal, relative to the unfiltered case, as the center width of the x-band is increased. Notice that the high frequency response remains unchanged, as expected. This confirms that the x-band return-path filter is equalizing the system transfer function by attenuating the low frequencies and leaving the high frequencies unchanged. Also, the return-path optical amplitude filters introduces no phase distortion into the signal unlike electronic filters that usually have residual phase distortion.

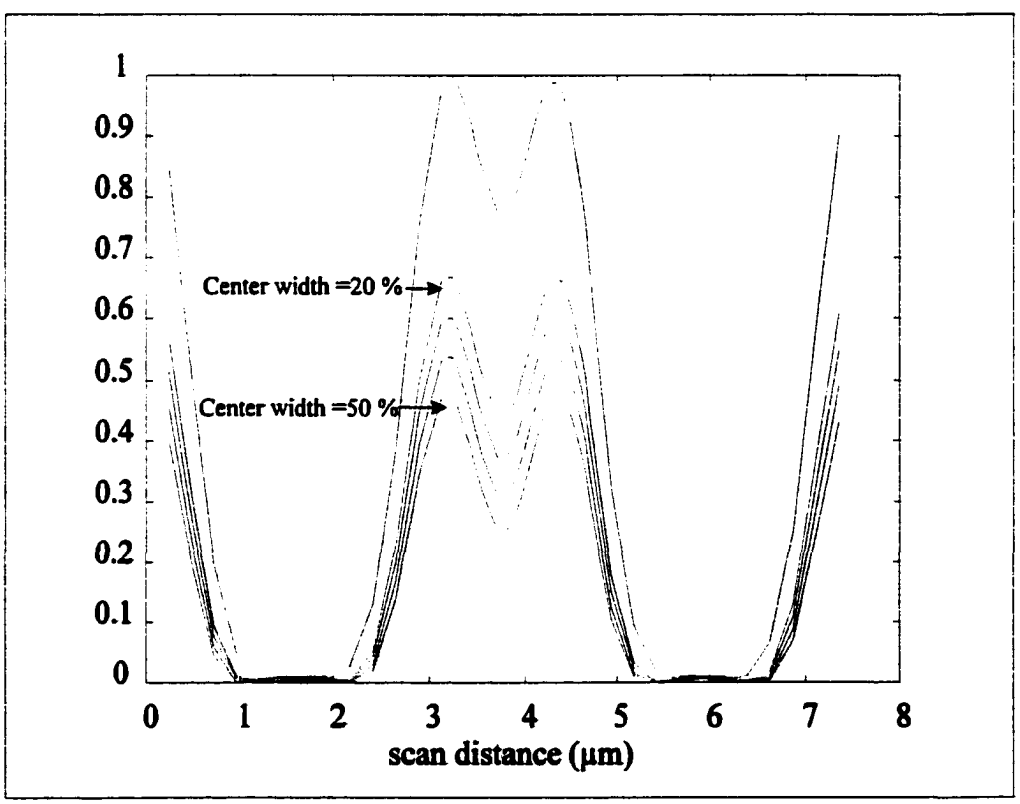

Figure 3.33. Data signal of the worst-case data pattern, of Figure 3.15, for different center widths of the x-band return-path filter.

3D.2.B return-path electronic boost filter

Another return path filter of interest is the electronic boost filter. It is used to boost the high frequency response of the system relative to the low frequency response. This is the opposite action of the x-band amplitude filter discussed previously. The electronic filter used in practice is an analog based filter (Silicon Systems 32f8020a). This has a variable gain and a variable peak gain frequency. The electronic filter transfer function is modeled in MATLAB. Figure 3.34 shows the transfer function of the electronic filter as well as the measured transfer function of our electronic circuit, and the

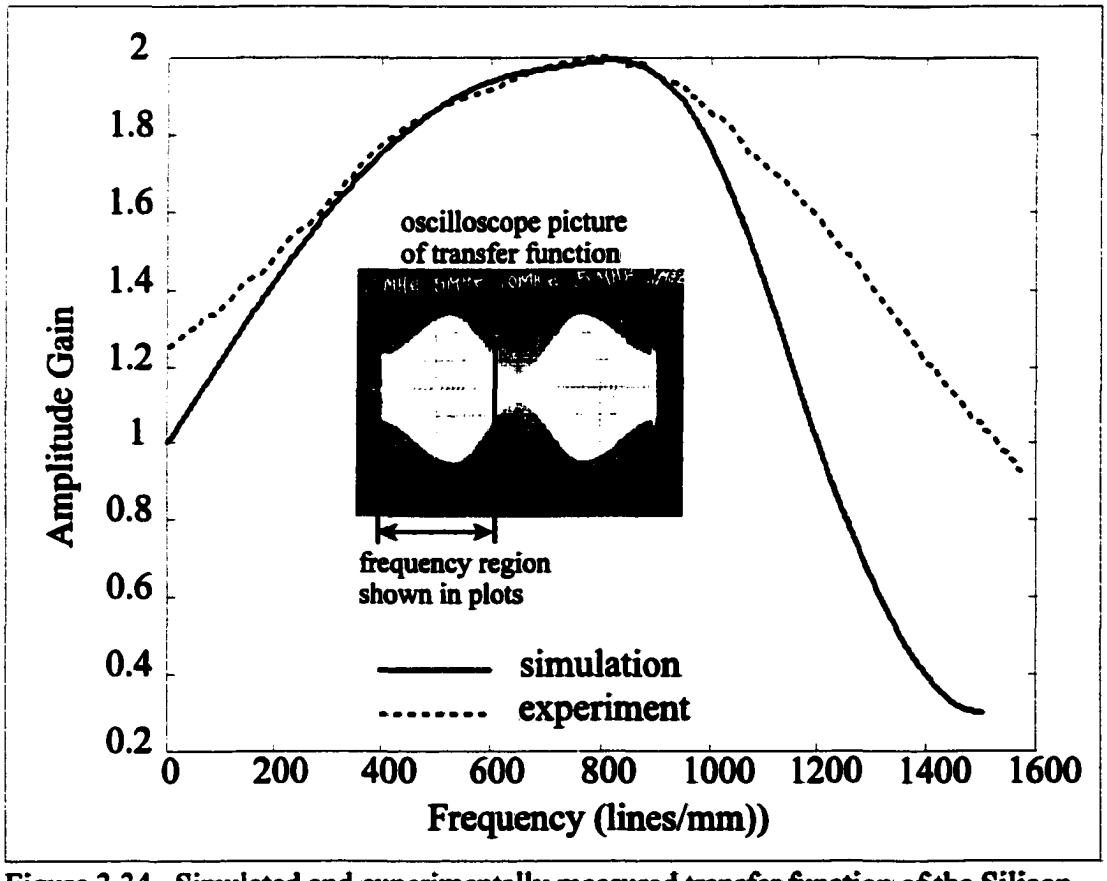

Figure 3.34. Simulated and experimentally measured transfer function of the Silicon Systems 32F8020A electronic boost filter.

two agree reasonably well. The inset of Figure 3.34 shows the oscilloscope display of the measured transfer function as the filter is swept in frequency by a function generator. The modeled electronic filter can be used to predict the response of the system. Figure 3.15 shows the two-point response for the electronic filtered signal. A boost in amplitude of the high frequency portion to a 32% modulation of the signal compared to the 23% modulation of the unfiltered case is observed.

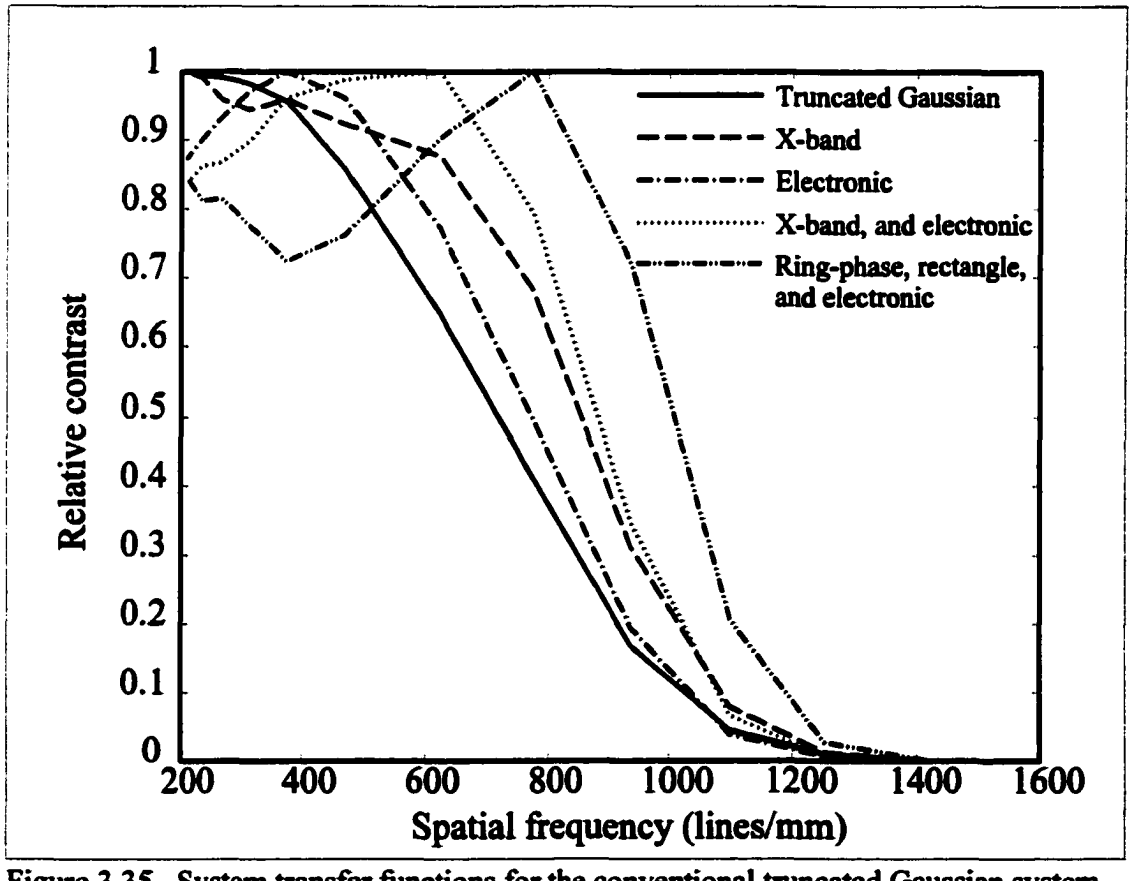

Figure 3.35. System transfer functions for the conventional truncated Gaussian system, for the x-band return-path filtered only system, for the electronic boost filter only system, for the combination of the x-band return-path and the electronic boost filter, and for the combination of the ring-phase illumination-path filter with the rectangle(bar) return-path filter and the electronic boost filter.

The electronic boost filter only has 0.5° of phase distortion. Since the phase distortion is very small the timing of the edges on the data signals are essentially unchanged.

3D.2.C Filter combinations

In Figure 3.35 the system transfer functions for five cases are shown. The unfiltered system, electronic boost filtered system, x-band of 15%, the combination of the 15% x-band with the electronic boost filter, and the combination of the 15% rectangle band(bar) with the electronic boost filter and the ring-phase illumination-path filter are simulated. For the unfiltered system the classic roll off of the system transfer function is observed. For the electronic boost filtered system the transfer function exhibits improved contrast at high frequencies, and the frequency at which the maximum contrast occurs is shifted from dc to 375 lines/mm or a mark pitch of 2.75μm. For the 15% x-band the system transfer function also exhibits improved contrast at high frequencies, which is better than that of the electronic filter. For the combination of the optical and electronic filter the contrast improvement is greater than that of either filter alone, and the frequency of maximum contrast is shifted to 625 lines/mm or 1.6μm mark pitch. It is interesting to note that in the simulation the 15% x-band gives better performance individually than the electronic filter alone. The combination of the ring-phase, rectangle, and electronic boost filter provides the most dramatic increase in contrast at high frequencies. The frequency of maximum contrast shifts to 770lines/mm in this case.

It is clear that the two-point response for the combination of filters behaves in the

following manner. The low frequency portion is reduced when the return-path optical filter is used. The high frequency portion is increased when the ring-phase illumination-path filter or the electronic boost filter is used. The percent modulation of the two-point response for the filter combinations can be predicted from the transfer functions for the filter combinations by looking at the spatial frequency of $940mm^{-1}$, which corresponds to the small mark of the two-point mark pattern in Figure 3.14.

3D.2.D - Tapped-delay-line electronic filter

The tapped-delay-line electronic filter used to reduce distortion in data signals due to large sidelobes is now considered. The design philosophy is reviewed from the work of Tanabe (Tanabe,1995). The filter is simulated in Matlab™. Results from the previous section are used to demonstrate the filter's effectiveness. Specifically, the source studied is the centrally obscured source with ε=0.6, which is studied in 3D.1.B.

The block diagram for a tapped-delay-line filter with three taps is shown in Figure 3.36(a). Each tap has a gain coefficient associated with it. Each tap is also separated by a delay. The delay is usually expressed in units of time T, but the delay can be converted to units of length l, through the relation l=vT where v is the velocity of the disk. The choice for the coefficients of the taps is based on properties of the focused spot. Specifically, the center tap gain C_0= 1, is the normalized peak irradiance of the focused spot. The outer taps C_1=C_{-1}= -K_0, where K_0 is the ratio of the sidelobe peak level to the central core peak level. For this system K_0 = 0.122. The choice for the tap spacing is based on the distance between the two sidelobe peaks. For this system, T = 1.02μm.

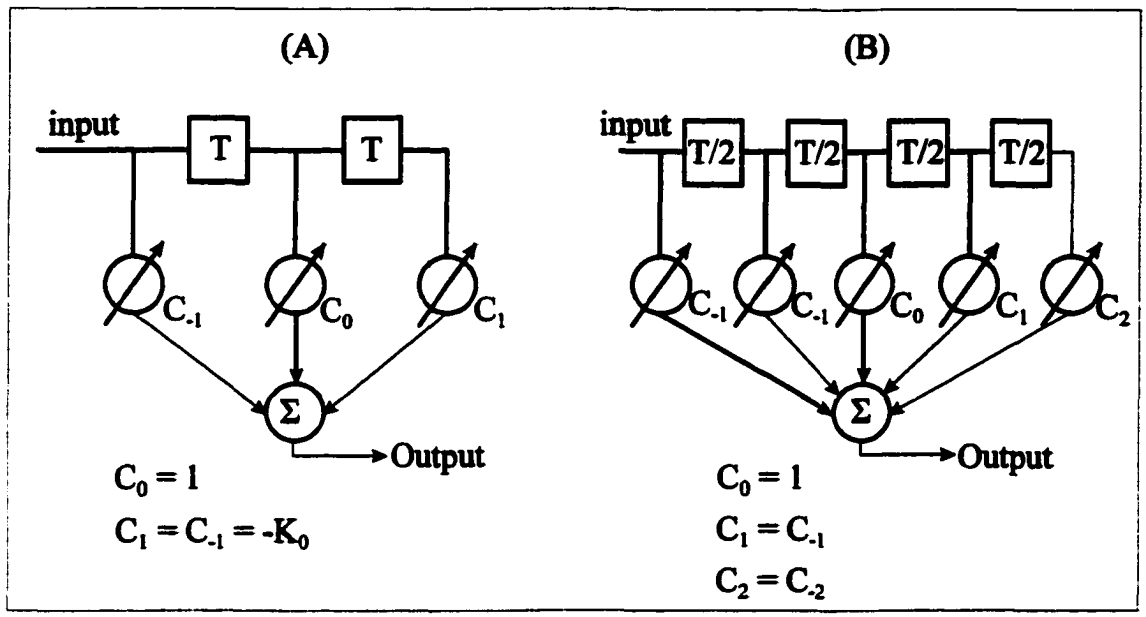

Figure 3.36. tapped-delay-line electronic filter. (A) 3 tap filter, (B) 5 tap filter, the delay of the 5 tap filter is half the delay of the three tap filter.

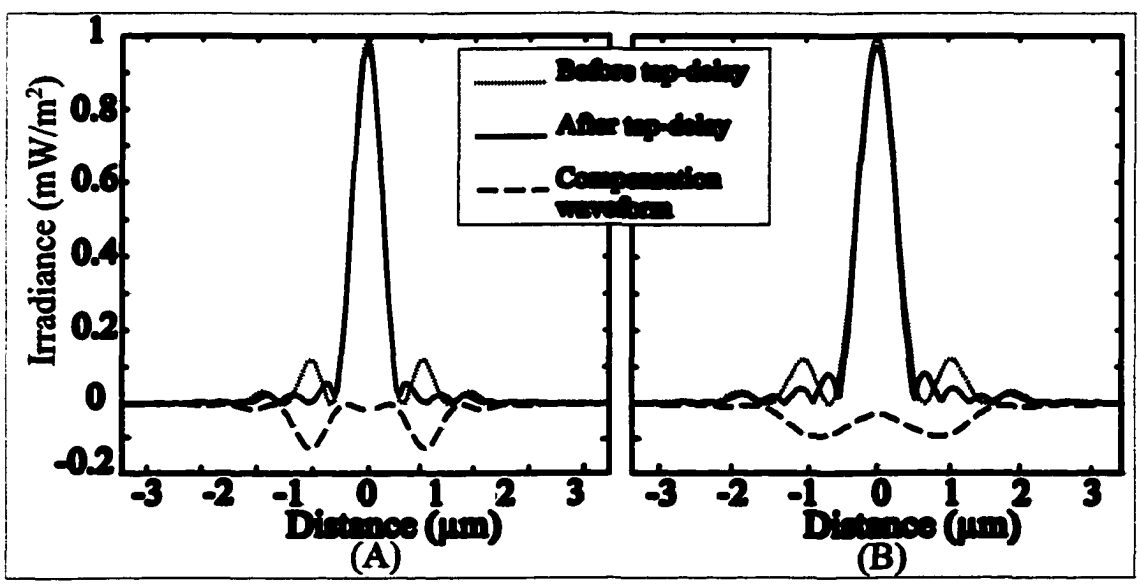

Figure 3.37. (A) signal representing the focused spot before and after the application of the 3 tap filter, (B) signal representing the focused spot before and after the application of the 5 tap filter.

Figure 3.37(a) shows a signal representing the profile of the focused spot before and after the application of the 3 tap filter, and the corresponding compensation waveform of the filter. The sidelobe levels are reduced, but not completely. This is understood by observing the compensation waveform used to cancel the sidelobes. The compensation waveform is thought of as summed shifted replicas of the central core. Here it is evident that the central core width is not the same as the first sidelobe width; in fact, the central core is a little larger in this case. Tanabe did not use a centrally obscured source, but rather the same rectangular shading band that Yamanaka used mentioned in section 3D.1.D. Tanabe's rectangular shading band width is chosen to provide a central core width very nearly equal to the sidelobe width, thus having better sidelobe reduction performance than indicated by Figure 3.37.

Figure 3.38(a) shows the standard unfiltered low frequency signal of 208(lines/mm). Figure 3.38(b)-(c) show data signals before and after application of this filter. The ringing in the signals from the sidelobes is about the same for each case. Figure 3.38 shows the transfer function for the 3 tap delay-line filtered signals. The benefit of the 3 tap filter is to equalize the transfer function.

The next step in the tap-delay-line filter design is to investigate wether or not going to a 5 tap delay-line filter improves the system further. The block diagram for a tapped-delay-line filter with five taps is shown in Figure 3.36(b). Each tap has a gain coefficient associated with it. Each tap is also separated by a delay. The delay for the five tap filter is half that of the three tap filter, or T=0.501μm. The choice for the

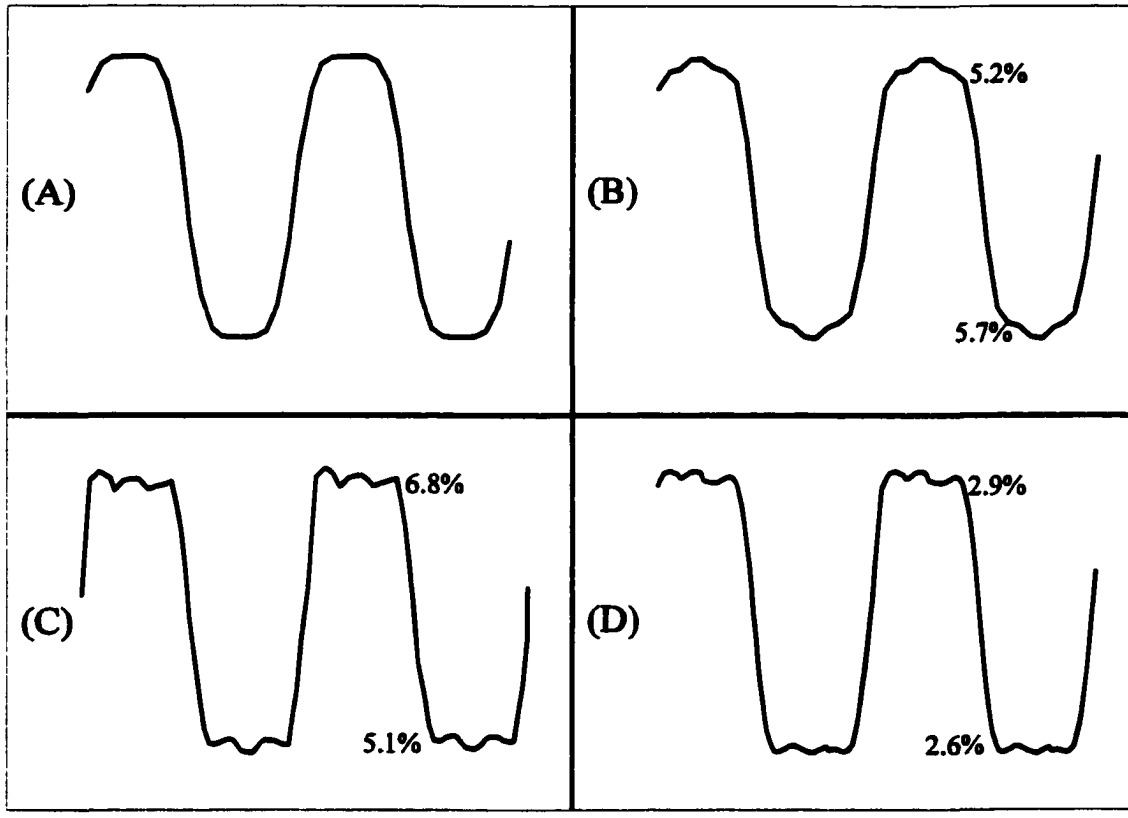

Figure 3.38. Low frequency(208 lines/mm) data signals. (A) unfiltered signal, (B) signal with amplitude filtered source with obscuration ratio of $\varepsilon = 0.6$, (C) signal in (B) after the 3 tap electronic filter, (D) signal in (B) after the 5 tap electronic filter.

coefficients of the taps is based on properties of the focused spot. Specifically, the center tap gain $C_0 = 1$, the normalized peak irradiance of the focused spot. The outer taps $C_1 = C_{-1}$, and $C_2 = C_{-2}$, are designed by iterating until ringing in the data signal is reduced, and good equalization of the system transfer function is achieved. Figure 3.37(b) shows a signal representing the profile of the focused spot before and after the application of the 5 tap filter, and the corresponding compensation waveform of the filter. The sidelobe levels are reduced, but not completely.

Figure 3.38(b)&(d) show the data signal before and after application of this filter. The ringing in the signals from the sidelobes is reduced by a factor of two. Figure 3.39 shows the transfer function for the 5 tap delay-line filtered signals. The benefit of the 5 tap filter is to equalize the transfer function and reduce the ringing in the data signal. This is very desirable since for purposes of reading back data the illumination-path filtered source is a good candidate as long as the tapped-delay-line filter is used in the electronic processing of the data signal. More taps may be used in the filter, which leads into filter structures that are FIR(finite impulse response) digital filters. This leads to

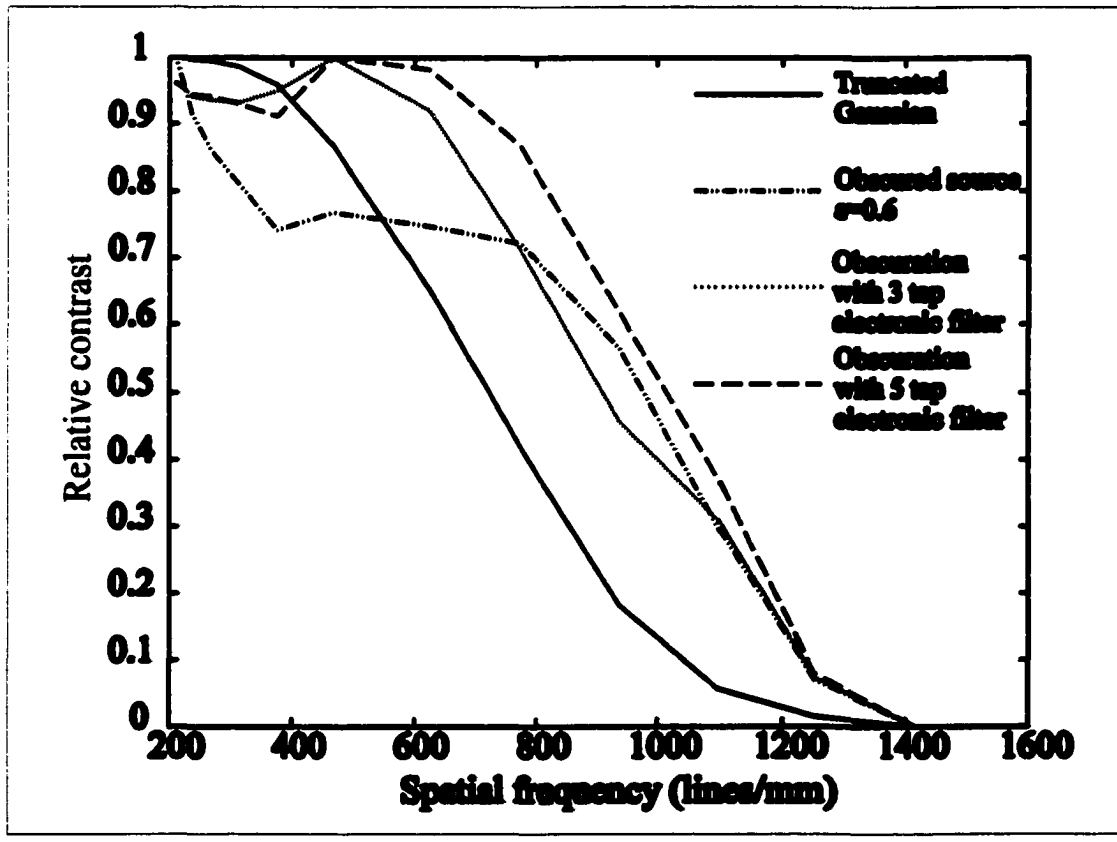

Figure 3.39. Transfer functions for the conventional system, the amplitude filtered obscured source, and the amplitude filtered obscured source filtered by the 3 tap-delay-line filter and the 5 tap-delay-line filter.

more complex electronic filter designs that are usually implemented in a digital signal processor, (DSP), chip. DSP's are an attractive option, but do lead to an increased cost in the data channel.

3D.2.E - Summary of return-path filtering

System performance with return-path filters are illustrated. The return-path optical amplitude filter equalizes the system transfer function by attenuating the low frequencies relative to the high frequencies. The electronic boost filter equalizes the system transfer function by providing a boost(gain) in the high frequency portion of the system transfer function without affecting the low frequencies. For reading data patterns it is shown that the artifacts due to the increased sidelobes may be eliminated or reduced by the introduction of an electronic tapped-delay-line-filter. Return-path filters have no effect on writing the data pattern since they do not affect the focused spot.

3E - Effect of aberrations on system performance

Effects of aberrations on system performance are investigated in this section. Sources of aberration include the laser and collimation optics (source aberrations), the objective lens and disk (disk aberrations), and the detection optics (detection aberrations) (Wang, 1993). The source aberration is typically residual astigmatism from the laser diode. Since the source aberrations and the detection aberrations result from a single pass through the optical components the total aberration does not double (even aberrations) or cancel (odd aberrations) after reflection from the disk. Since the disk aberrations are double pass through the disk and objective lens, the even aberrations such as defocus,

spherical, and astigmatism double after reflection from the disk while the odd aberrations like tilt and coma cancel after reflection from the disk.

In this section, third order disk aberrations are investigated in the unfiltered system, the ring-phase filtered system, and the centrally obscured ε=0.6 system. In section 3E.1 the wavefront aberrations used in the simulations are presented. In Section 3E.2 the aberrated focused spot irradiance distributions are presented. In Section 3E.3 the aberrated system transfer functions and signal power spectra are presented. In Section 3E.4 signal current distributions are presented.

3E.1 - Wavefront aberrations

The wavefront aberration is added to the system in the exit pupil of the objective lens by multiplying the electric field by the appropriate phase distribution (Wang, 1993). The aberrations investigated are defocus W_{020}, spherical W_{040}, coma W_{131}, and astigmatism W_{222}. Spherical is balanced with the appropriate amount of defocus to minimize the rms wavefront error. Coma is balanced with the appropriate amount of tilt W_{111} to minimize the rms wavefront error. Astigmatism is also balanced with the appropriate amount of defocus to minimize the rms wavefront error.

In Figure 3.40 the wavefront aberration in the exit pupil of the objective lens is shown as three dimensional surfaces that represent phase in the exit pupil. Also shown in Figure 3.40 is the corresponding two dimensional projection of the phase surface. Figure 3.40A shows the parabolic surface for $W_{020} = 0.25\lambda$. Figure 3.40B shows the surface for $W_{040} = 1\lambda$ balanced by $W_{020} = -1\lambda$. Figure 3.40C shows the surface for $W_{131} = 0.5\lambda$

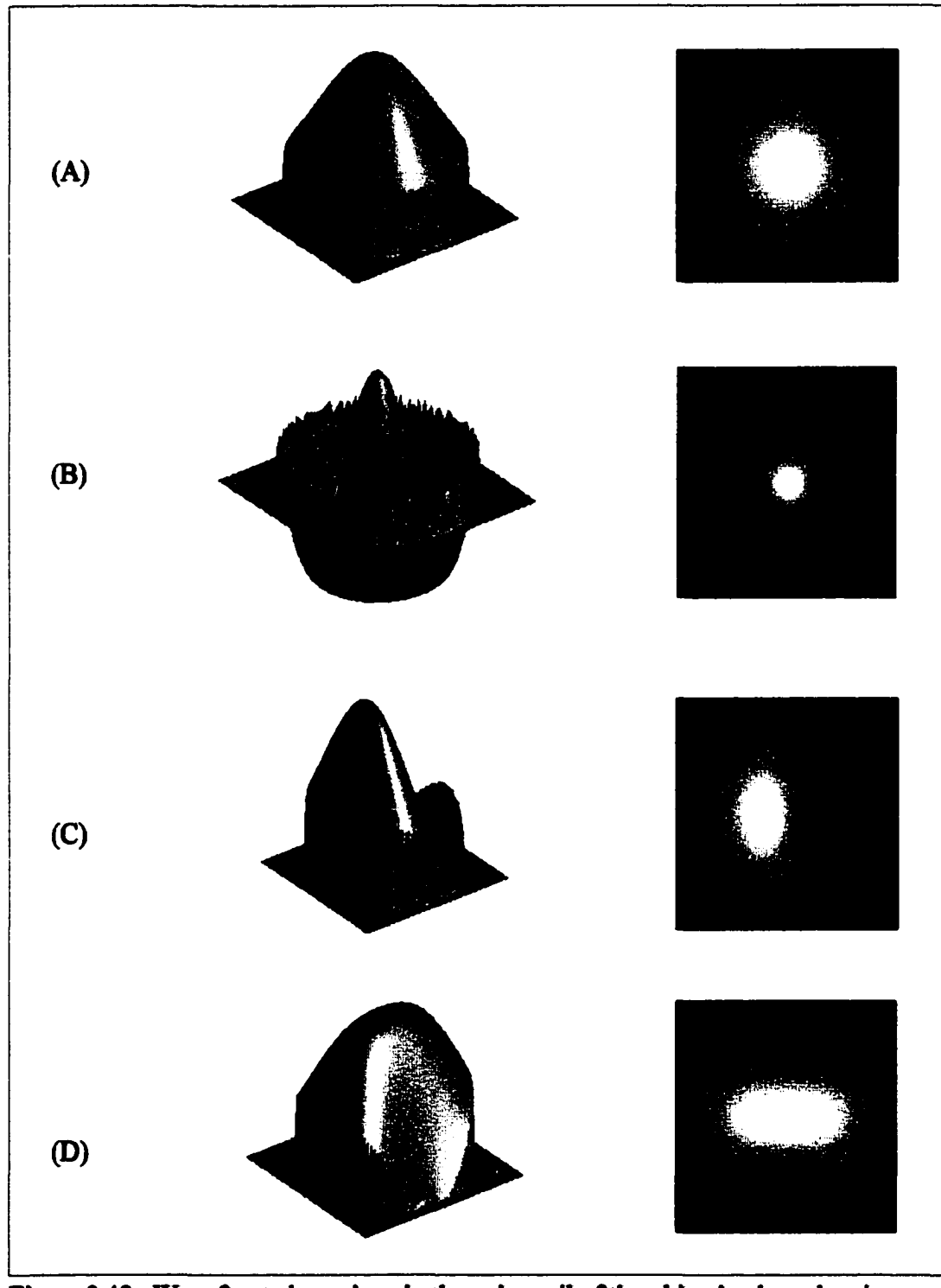

Figure 3.40. Wavefront aberrations in the exit pupil of the objective lens showing three dimensional surface and 2-dimension projection for (A) $W_{020} = 0.25\lambda$, (B) $W_{040} = 1\lambda, W_{020} = -1\lambda$, (C) $W_{131} = 0.5\lambda$, $W_{111} = 0.33\lambda$, and (D) $W_{222} = 0.25\lambda$, $W_{020} = -0.125\lambda$.

balanced by $W_{111} = -0.33\lambda$. Figure 3.40D shows the surface for $W_{222} = 0.25\lambda$ balanced by $W_{020} = -0.125\lambda$.

These aberrations are used for the unfiltered system, the ring-phase system, and the centrally obscured system ε=0.6. The sensitivities of these systems to the aberration values given are investigated in Sections 3E.2 through 3E.4.

3E.2 - Focused spot irradiance distributions with aberrations

The focused spot distributions are an aid in understanding the influence of aberrations for a particular filtering technique. In this section the focused spot irradiance distributions for the unfiltered system, the ring-phase system, and the obscured system ε=0.6 are presented for the aberration values given in Section 3E.1.

Figure 3.41 shows the focused spot irradiance distributions for $W_{020} = 0.25\lambda$, $W_{040} = 1\lambda$ balanced by $W_{020} = -1\lambda$, $W_{131} = 0.5\lambda$ balanced by $W_{111} = -0.33\lambda$, and $W_{222} = 0.25\lambda$ balanced by $W_{020} = -0.125\lambda$. Figure 3.41A shows the unfiltered system focused spot distributions. Figure 3.41B shows the ring-phase system focused spot distributions. Figure 3.41C shows the obscured system focused spot distributions. The unaberrated focused spots are normalized to have equal peak irradiance across different systems; e.g. the power of the source is doubled for the ring-phase filtered system in order to have equal peak irradiances. The distributions shown in each column are normalized by the peak unaberrated value.

Figure 3.41 provides valuable qualitative information. For instance, the unfiltered source is more sensitive to defocus than either the ring-phase source or the obscured

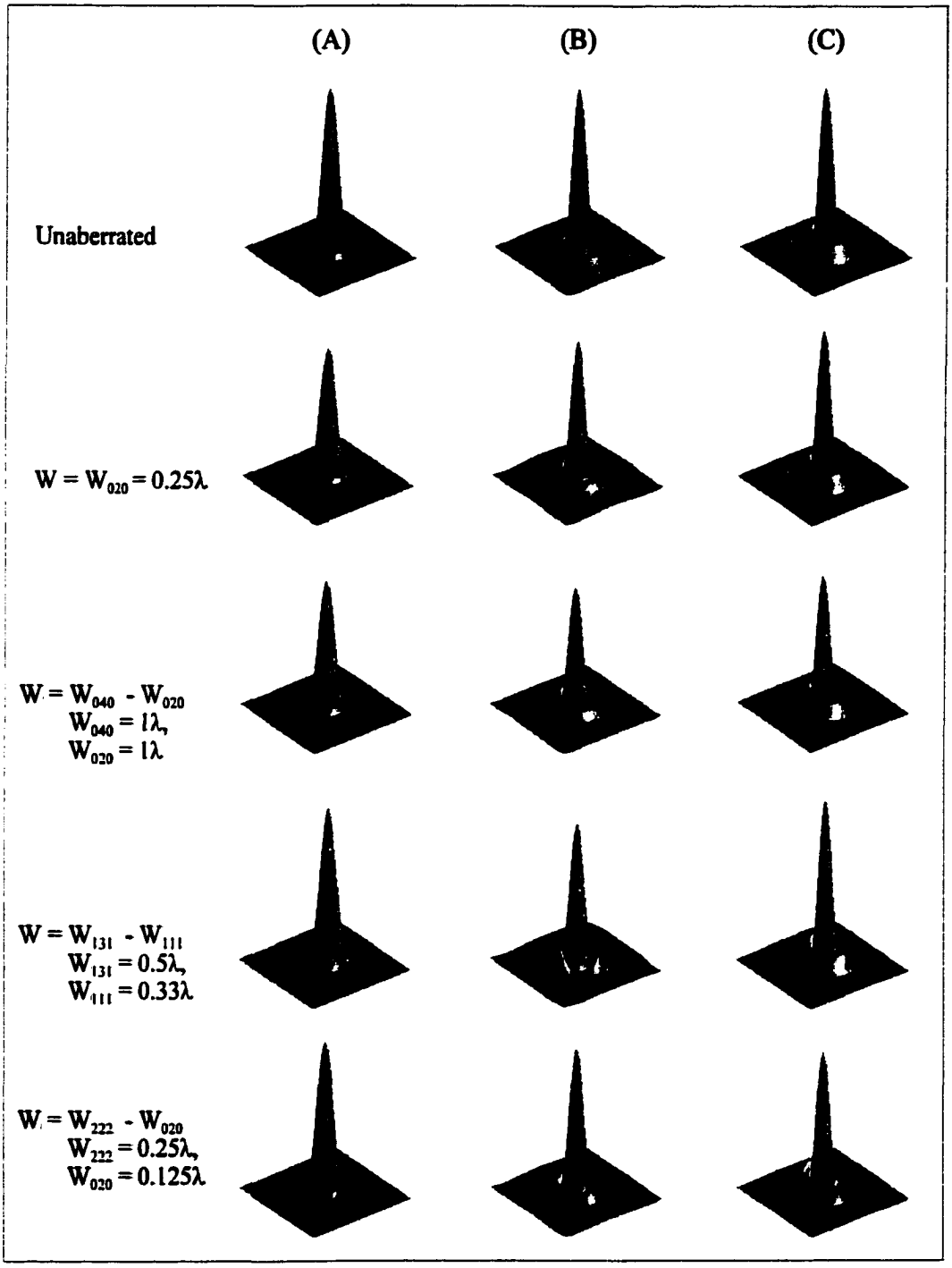

Figure 3.41. Focused spot irradiance distributions for $W_{020} = 0.25\lambda$, $W_{040} = 1\lambda$ balanced with $W_{020} = -1\lambda$, $W_{131} = 0.5\lambda$ balanced with $W_{111} = 0.33\lambda$, and $W_{222} = 0.25\lambda$ balanced with $W_{020} = -0.125\lambda$ (A) unfiltered, (B) ring-phase filter, (C) central obscuration $\varepsilon = 0.6$.

source as shown by the visible reduction in peak irradiance. All of the sources are sensitive to the balanced spherical aberration as shown by the visible reduction in peak irradiance. The ring-phase source is more sensitive to balanced coma than either the unfiltered source or the obscured source as shown by the large sidelobe and reduced peak irradiance. The obscured source is more sensitive to astigmatism than either the unfiltered source or the ring-phase source as indicated by increased sidelobe structure and reduced peak irradiance.

3E.3 - Transfer function and signal power spectra with aberrations

In this section the system transfer function with aberration is presented. Also shown are the corresponding signal power spectra with and without aberrations. The power spectra provide additional information about signal strength and signal contrast.

Figure 3.42A shows the system transfer function for the unfiltered system, the ring-phase filter system, and the obscured system. Figure 3.42B shows the system transfer function for the three systems with no aberrations and with a 0.25 wave of defocus, $W_{020} = 0.25\lambda$. The unfiltered system experiences the greatest reduction in contrast at the low and mid spatial frequencies. The ring-phase and obscured system do not experience significant reduction in contrast. This result indicates the well-known fact that annular beams have a larger depth of focus (Mahajan, 1986). The contrast at high frequencies is unaffected for all three systems with a 1/4 wave of defocus.

Figure 3.42C shows the system transfer function for the three systems with no aberrations and with a wave of spherical aberration, $W_{040} = 1\lambda$, balanced by 1.0 wave of

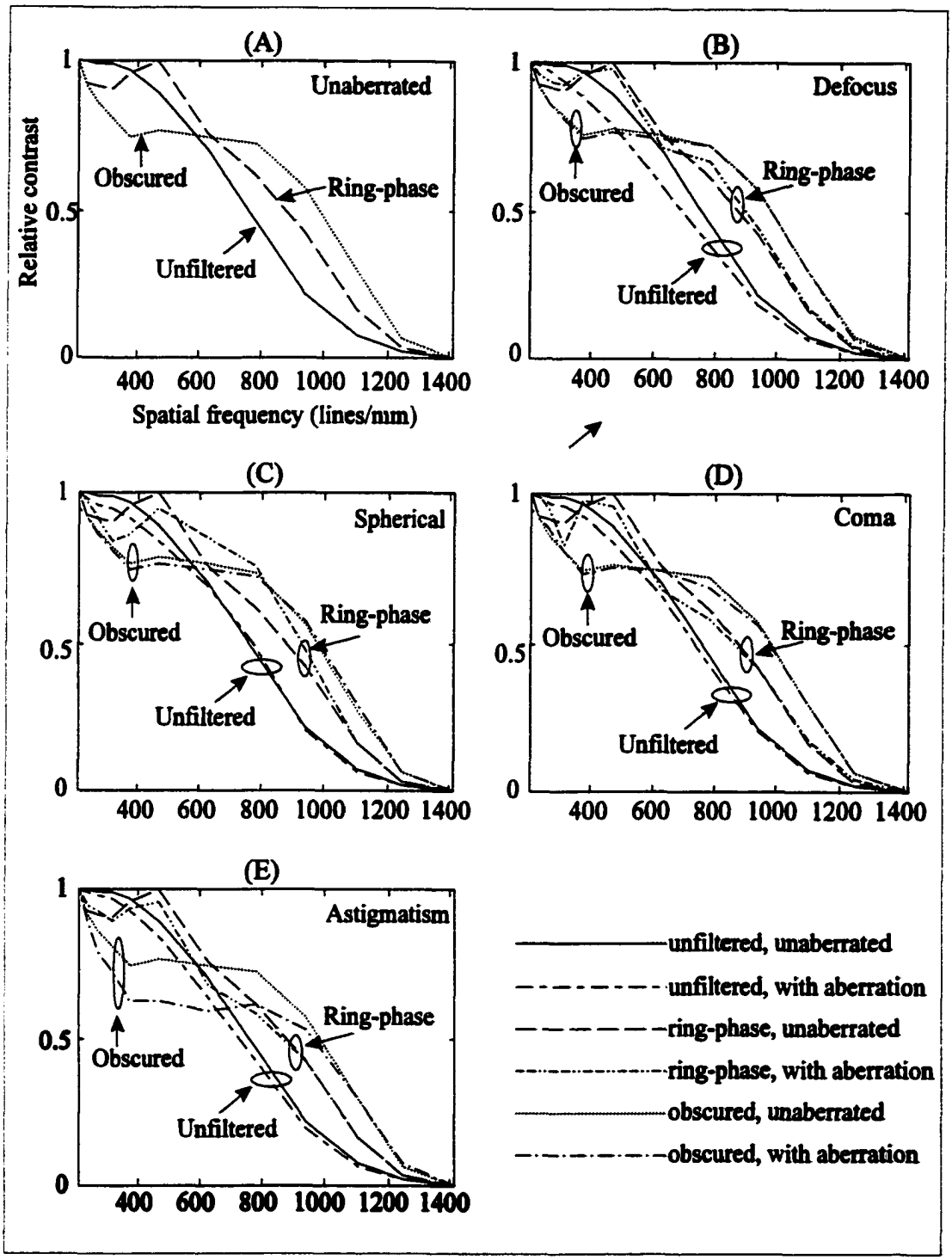

Figure 3.42. System transfer functions for (A) no aberrations, (B) $W_{020} = 0.25\lambda$, (C) $W_{040} = 1\lambda$ balanced with $W_{020} = -1\lambda$, (D) $W_{131} = 0.5\lambda$ balanced with $W_{111} = 0.33\lambda$, and (E) $W_{222} = 0.25\lambda$ balanced with $W_{020} = -0.125\lambda$.

defocus, $W_{020} = -1\lambda$. The unfiltered system experiences reduction in low-frequency contrast. The ring-phase system experiences reduction in contrast at the low spatial frequencies and shows an increase in contrast at mid spatial frequencies. The obscured system experiences only a slight reduction in contrast at low and mid spatial frequencies. For all three systems the contrast at high frequencies is not significantly altered with one wave of W_{040}.

Figure 3.42D shows the system transfer function for the three systems with no aberrations and with a half wave of coma, $W_{131} = 0.5\lambda$, balanced by a third wave of tilt, $W_{111} = -0.33\lambda$. The unfiltered system experiences a small reduction in contrast at the low and mid spatial frequencies. The ring-phase system experiences reduction in contrast at the low and mid spatial frequencies. The obscured system does not experience a significant reduction in contrast. The contrast at high frequencies is essentially unchanged for all three systems.

Figure 3.42E shows the system transfer function for the three systems with no aberrations and with a quarter wave of astigmatism, $W_{222} = 0.25\lambda$, balanced by an eighth wave of defocus, $W_{020} = -0.125$. The unfiltered system experiences reduction in contrast at the low and mid spatial frequencies. The ring-phase system experiences a small reduction in contrast primarily at the low spatial frequencies and some at the mid spatial frequencies. The obscured system experiences a dramatic reduction in contrast at low and mid spatial frequencies. The contrast at high frequencies is essentially unaffected for all three systems.

Table 3.3 shows the integrated system transfer function of Figure 3.42 for the low-frequency region 200-375 lines/mm, mid-frequency region 375-940 lines/mm, and high-frequency region 940-1400 lines/mm. Integrated system transfer function of Figure 3.42 normalized to the unaberrated spatial frequency band for each system.

	low 200-375 lines/mm	mid 375-940 lines/mm	high 940-1400 lines/mm
unaberrated			
- unfiltered	1	1	1
- ring-phase	1	1	1
- obscured	1	1	1
defocus			
- unfiltered	0.964	0.853	0.974
- ring-phase	1.03	1.004	1.073
- obscured	0.996	0.994	0.999
spherical			
- unfiltered	0.969	0.973	0.869
- ring-phase	0.987	1.091	1.018
- obscured	0.990	0.988	1.091
coma			
- unfiltered	0.975	0.939	0.981
- ring-phase	1.021	0.948	1.072
- obscured	1.003	0.975	0.986
astigmatism			
- unfiltered	0.983	0.918	0.965
- ring-phase	1.011	0.949	1.051
- obscured	0.934	0.850	1.007

Table 3.3. Integrated system transfer function of Figure 3.42 normalized to the unaberrated spatial frequency band for each system.

From Table 3.3 the spatial frequency bands that are influenced by aberration are identified. The high frequency band, 940-1400 lines/mm, is least affected by aberrations for all three systems with the exception of spherical aberration where the unfiltered and the obscured system have reduced contrast. The mid frequency band, 375-940 lines/mm, is affected the most where all three systems are observed to have reduced contrast. The low frequency band, 200-375 lines/mm, is also affected where all three systems are observed to have reduced contrast.

Defocus mainly alters the unfiltered system and is most significant in the mid frequency band where integrated system transfer function is reduced by 15% and 3.5% and 2.5% in the low and high frequency bands respectively. The ring-phase and obscured system integrated transfer function are insensitive to the defocus due to their increased depth of focus.

Spherical aberration affects all three systems mainly in the low and mid frequency bands. The low and mid frequencies of the integrated system transfer function for the unfiltered system are reduced by 3% and the high frequency band is reduced by 13%. The obscured system integrated transfer function is insensitive to the spherical aberration. The ring-phase system integrated transfer function improves with the spherical aberration in the mid spatial frequency band by 9%, however this improvement in contrast is misleading as will be shown in the power spectra of Figure 3.43C. The obscured system is the most insensitive to the spherical aberration.

Coma affects all three systems mainly in the mid frequency band. The high

frequency integrated system transfer function is relatively unaffected. At the mid spatial frequency band the obscured system is the least sensitive to the coma with the integrated transfer function only changing by 2.5% while the unfiltered and ring-phase system change by 6% and 5% respectively.

Astigmatism also affects all three systems in the mid frequency band. At the mid spatial frequency band the obscured system is the most sensitive to the astigmatism with the integrated transfer function changing by 15% while the unfiltered and ring-phase system change by 8% and 5% respectively.

Figure 3.43A shows the signal power spectra for the unfiltered system, the ring-phase system, and the obscured system. Figure 3.43B shows the signal power spectra for the three systems with no aberrations and with a 0.25 wave of defocus, $W_{020} = 0.25\lambda$. The unfiltered system experiences the greatest reduction in power level, 2-4 dBm, at the low and mid spatial frequencies. The ring-phase and obscured system also experience a reduction in power level of 1-2 dBm at the low and mid spatial frequencies. The power level at high frequencies is only slightly affected for all three systems being reduced by 1dBm or less for the obscured and ring-phase system and 1-2dBm for the unfiltered system..

Figure 3.43C shows the signal power spectra for the three systems with no aberrations and with1.0 wave of spherical aberration, $W_{040} = 1\lambda$, balanced by 1.0 wave of

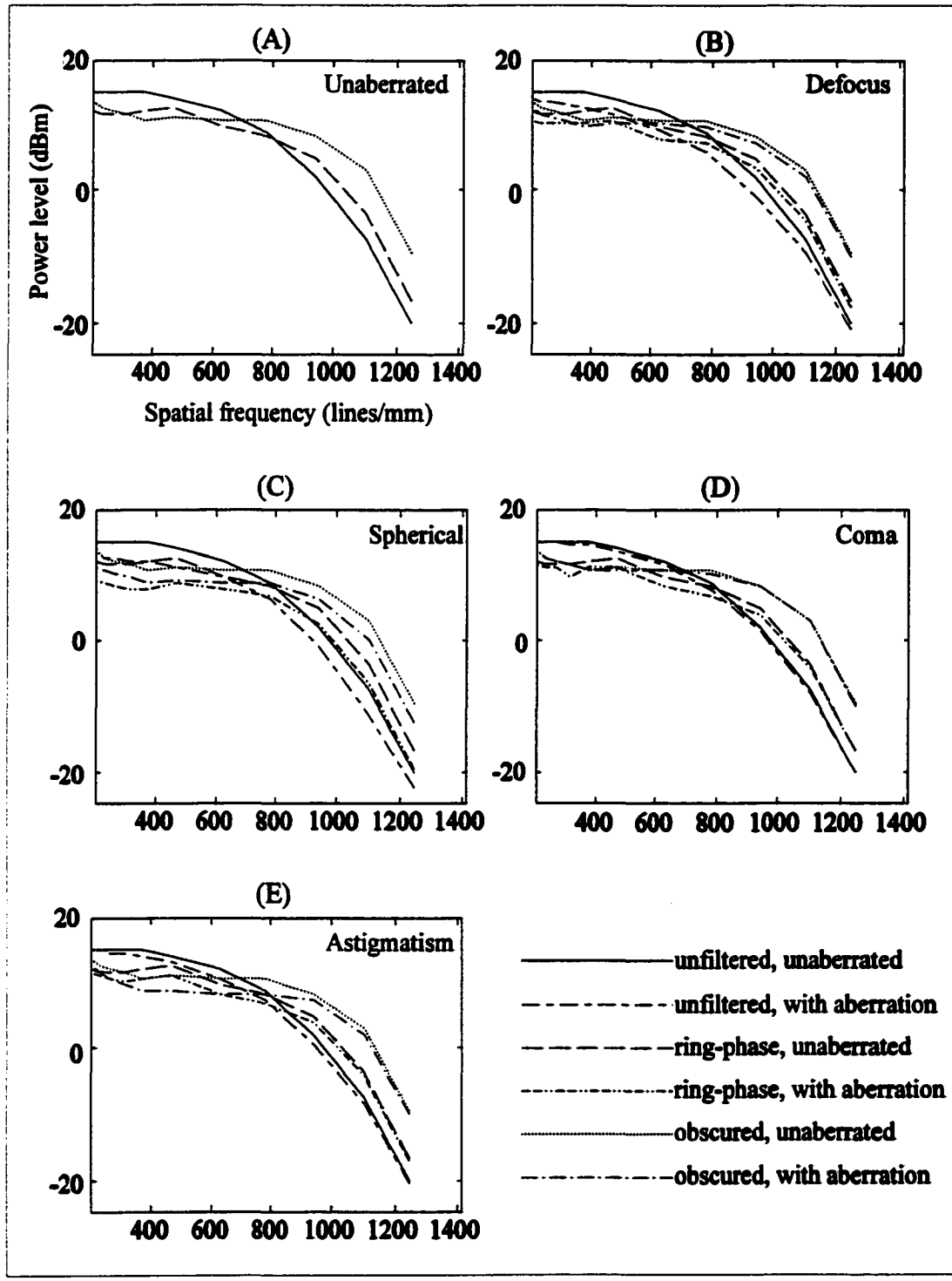

Figure 3.43. Signal power spectra for (A) no aberrations, (B) $W_{020} = 0.25\lambda$, (C) $W_{040} = 1\lambda$ balanced with $W_{020} = -1\lambda$, (D) $W_{131} = 0.5\lambda$ balanced with $W_{111} = 0.33\lambda$, and (E) $W_{222} = 0.25\lambda$ balanced with $W_{020} = -0.125\lambda$.

defocus, $W_{020} = -1\lambda$. The unfiltered system experiences a reduction in power level of 3-6 dBm at low and mid spatial frequencies. The ring-phase and obscured system also experience reduction in power level of 3-6 dBm at low and mid spatial frequencies. The reduced power level of the ring-phase system at the mid spatial frequencies shows the tradeoff of increased contrast in Figure 3.42C. The power level at high frequencies is affected in all three systems where a reduction in power level of 2-4dBm is observed.

Figure 3.43D shows the signal power spectra for the three systems with no aberrations and with 0.5 wave of coma, $W_{131} = 0.5\lambda$, balanced by 0.33 wave of tilt, $W_{111} = -0.33\lambda$. The unfiltered system and obscured system do not experience any significant reduction in signal strength, about 1dBm in the mid spatial frequency band. The ring-phase system experiences a reduction in power level of 1-3 dBm at low and mid spatial frequencies. The power level at high frequencies is unaffected for all three systems.

Figure 3.43E shows the signal power spectra for the three systems with no aberrations and with 0.25 wave of astigmatism, $W_{222} = 0.25\lambda$, balanced by 0.125 wave of defocus, $W_{020} = -0.125\lambda$. The unfiltered system and the ring-phase system experience a reduction in power level of 1-2 dBm at low and mid spatial frequencies. The obscured system experiences a reduction in power level of 1-4 dBm at low and mid spatial frequencies. The power level at high frequencies is reduced by less than 1dBm for all three systems.

Figure 3.42 and Figure 3.43 show that the unfiltered system is more sensitive to defocus than the ring-phase or obscured system. All three systems are sensitive to

spherical aberration. The ring-phase system is more sensitive to coma than the unfiltered or obscured system. The obscured system is more sensitive to astigmatism than the unfiltered or ring-phase system.

3E.4 - Signal current distributions with aberrations

The description of the procedure to simulate the signal current distributions is given in Section 3C.3.A. In this section the simulated signal distributions with spherical aberration is presented.

The unfiltered system with balanced spherical aberration and the ring-phase filter system with balanced spherical aberration both show additional structure in the signal current distributions compared to the unaberrated signal current distributions. The remaining ten signal current distributions did not change significantly when compared to the unaberrated distributions. In order for aberrations to introduce structure in the signal current distributions large values of aberration, $\Delta W > 1\lambda$, are needed.

Figure 3.44 displays signal current distributions for the unfiltered source with 1.0 wave of spherical aberration, $W_{040} = 1\lambda$, balanced by 1.0 wave of defocus, $W_{020} = -1\lambda$. Each subplot gray scale is normalized to its own peak value, as shown on the scale bar, in order to bring out the qualities of the distribution. From the peaks indicated on the scale bar, a reduction in signal strength as frequency is increased is observed, which corresponds to the transfer function rolloff of Figure 3.42C. An interesting feature to note is the hole, which is a reduction of signal strength in the center of the pupil at low frequencies. This reduction of signal strength in the center of the pupil can be understood

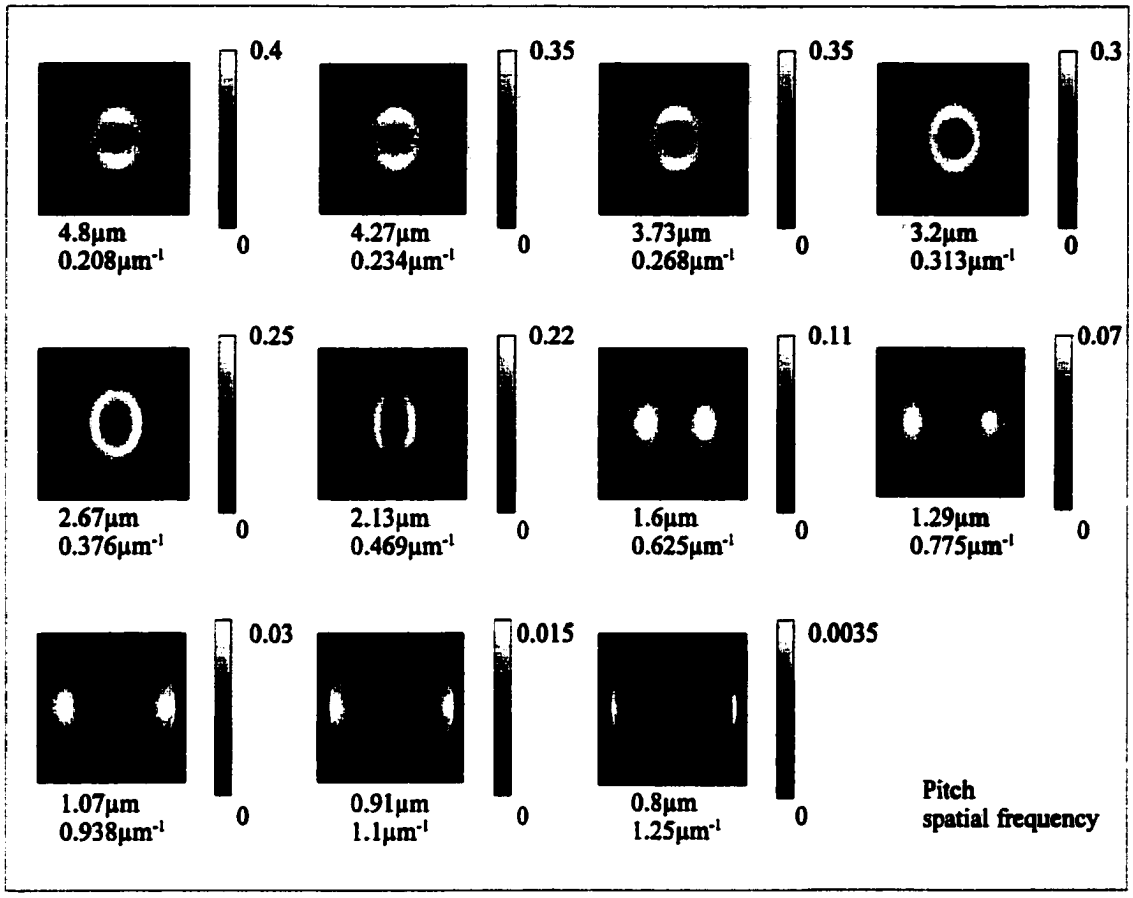

Figure 3.44. Signal current distributions in the pupil of the objective lens after reflection from the disk, in units of mA. $W_{040} = 1\lambda$ balanced with $W_{020} = -1\lambda$ for the unfiltered system. Decreasing mark pitch, increasing frequency left to right, top to bottom.

from the central ordinate theorem of Fourier optics and the use of equation (2-14). At high spatial frequencies the signal is concentrated at the edge of the pupil as in Figure 3.16, and there is no additional structure introduced.

Figure 3.45 displays signal current distributions for the ring-phase source with 1.0 wave of spherical aberration, $W_{040} = 1\lambda$, balanced by 1.0 wave of defocus, $W_{020} = -1\lambda$. Each subplot grayscale is normalized to its own peak value, as shown on the scale bar, in

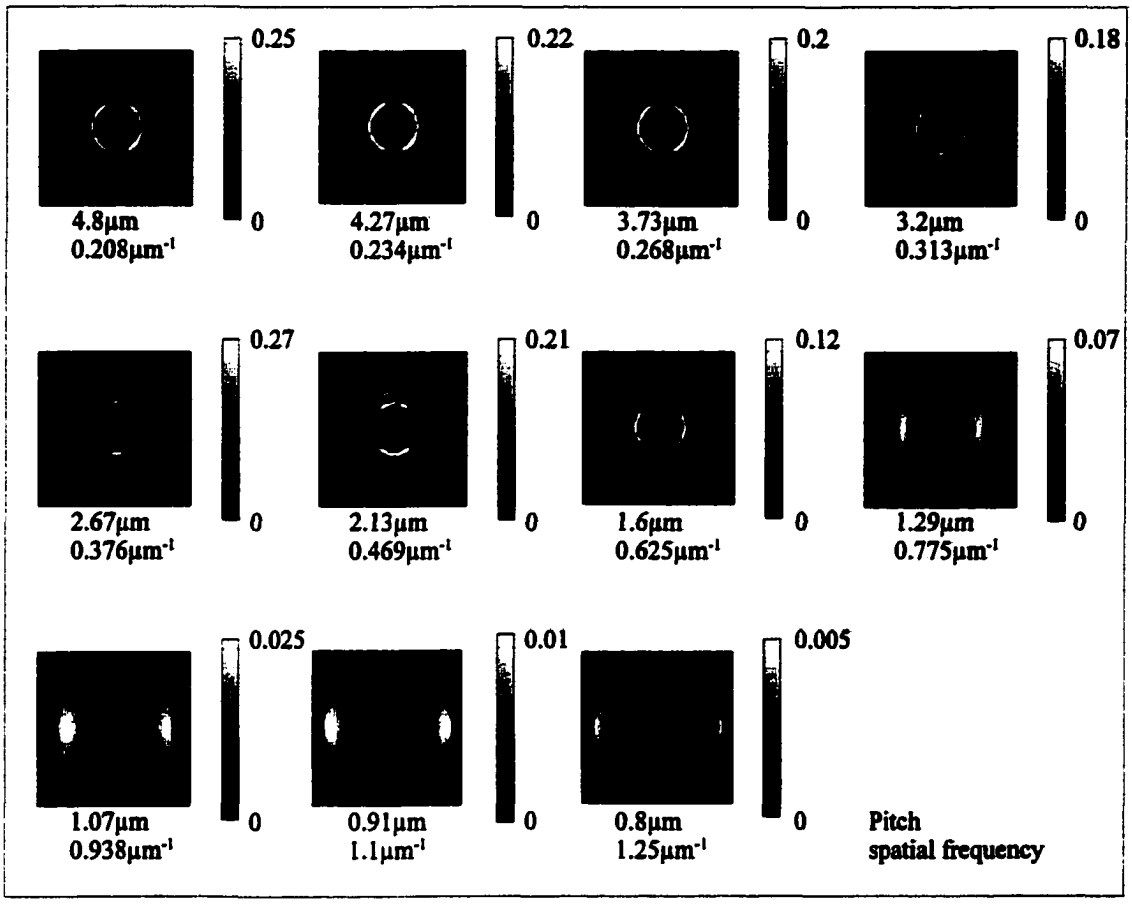

Figure 3.45. Signal current distributions in the pupil of the objective lens after reflection from the disk, in units of mA. $W_{040} = 1\lambda$ balanced with $W_{020} = -1\lambda$ for the ring-phase filtered system. Decreasing mark pitch, increasing frequency left to right, top to bottom.

order to bring out the qualities of the distribution. From the peaks indicated on the scale bar, a reduction in signal strength as frequency is increased is observed, which corresponds to the transfer function rolloff of Figure 3.42C. As in Figure 3.44, an interesting feature to note is the hole in the center of the pupil at the mid spatial frequencies $0.313\mu m^{-1}$ to $0.469\mu m^{-1}$. The low and high spatial frequency signal distributions retain the same shape as observed in Figure 3.18. At high spatial frequencies the signal is concentrated at the edge of the pupil as in Figure 3.18, and there

is no additional structure introduced.

3E.5 - Summary of aberration effects

Figure 3.41 qualitatively shows the change in the focused spot irradiance distributions when aberration is included in the system. The peak irradiance is observed to decrease with aberration, as expected. The redistribution of the energy from the central core to the sidelobes is observed.

For a 0.25λ of defocus, the unfiltered system is more sensitive than the ring-phase or obscured system as observed in Figure 3.42-3.43 and Table 3.3. Defocus reduces contrast in the system transfer function mainly in the low and mid spatial frequency bands and reduces the signal power across the spectrum as shown in Figure 3.42B and Figure 3.43B.

For 1.0λ of spherical aberration balanced with 1.0λ defocus all three systems experience reduced performance as observed in Figure 3.42C-3.43C and Table 3.3. Spherical aberration only slightly alters the contrast of the system transfer function as shown in Figure 3.42C and Table 3.3, however spherical aberration reduces the signal power across the spectrum as shown in Figure 3.43C for all three systems. Spherical aberration also introduces a hole, which is a reduction in signal strength in the center of the pupil at low frequencies that can be understood from the central ordinate theorem of Fourier optics and the use of equation (2-14). This additional structure is observed in the unfiltered and ring-phase systems.

For 0.5λ of coma balanced with 0.33λ tilt the ring-phase system is more sensitive

than the unfiltered or obscured system as observed in Figure 3.42D-3.43D and Table 3.3. Coma mainly influences the low and mid spatial frequency bands of the unfiltered and ring-phase system while the obscured system is the least sensitive to coma.

For 0.25λ astigmatism balanced by 0.125λ defocus the obscured system is more sensitive than the unfiltered or the ring-phase system as observed in Figure 3.42E-3.43E and Table 3.3. Astigmatism mainly influences the low and mid spatial frequency bands of all three systems with the obscured system being the most sensitive of the three systems to astigmatism. The sensitivity of the obscured system to astigmatism agrees with the work of Strand (Strand, 1994). The general result of aberrations on the system is reduced performance relative to the unaberrated system.

3F - Summary

Diffraction modeling for simulating a magneto-optic data storage system is presented. The desired source field distribution is input directly into the entrance pupil of the optical system. The light propagation between the entrance and exit pupil is described by the ABCD matrix method. Light propagation from the exit pupil to the image is described by Eq. (3-13), a Fourier transform of the exit pupil field distribution multiplied by a spherical Huygen's wavelet.

The simulated performance of a standard magneto-optic data storage system is illustrated. The signal current distribution in the pupil is shown to be concentrated in the center of the pupil for spatial frequencies $< NA/\lambda = 0.64\mu m^{-1}$ (the equivalent cutoff frequency of a coherent plane-wave illumination system) and concentrated toward the

edges of the pupil for spatial frequencies > $NA/\lambda=0.64\mu m^{-1}$. The system transfer function is shown to roll off at high frequencies, just as in the scanning optical microscope configuration of Figure 1.4. The system transfer function is shown to depend on the Gaussian illumination conditions in the pupil. The underfilled Gaussian source has the effect of greater contrast reduction at high frequencies, rolling off quickly at high frequencies. The effect of increasing the Gaussian beam truncation on the system transfer function is to increase the contrast at high frequencies until the limit of a uniform pupil is reached where the roll off of the system transfer function is the slowest. The system two-point response is investigated for the data pattern of Figure 3.14. The modulation of the high frequency portion of the two-point response data signal of Figure 3.16 is shown to increase with increasing overfill of the Gaussian beam.

The introduction of different superresolution components and their effect on the performance of the system is documented. The signal current distribution in the pupil for the ring-phase illumination-path filter is also shown to be concentrated in the center of the pupil for low spatial frequencies and concentrated toward the edges of the pupil for high spatial frequencies. The peak current in the signal current distributions with the ring-phase illumination-path filter, Figure 3.17, occurs at a mid spatial frequency around 350 lines/mm rather than the lowest frequency of 208 lines/mm for the conventional unfiltered system, Figure 3.16. Comparing Figure 3.16 and 3.18, the variation in signal current from low to high frequency with the ring-phase filtered source is less than the variation in signal current with the conventional unfiltered source. This indicates the

action of equalization that the ring-phase filter has on the system. The ring-phase filter accomplishes equalization by lowering the low frequency response and increasing the high frequency response, which makes the ring-phase filter a superresolving filter according to definition #1 by boosting the transmission of the high frequencies.

Illumination-path filters are observed to increase the response of the high frequencies as shown in the transfer function curves for the ring-phase filtered system and the amplitude filtered system using a central pupil obscuration($\varepsilon = 0.6$). The tradeoff of the high frequency response increase for the amplitude and phase illumination-path filters is to reduce the response of the low frequencies, as shown in Figure 3.13. Writing data with the illumination-path filters is discussed and a summary of a thermal simulation presented that investigates the accumulation of heat in the recording layer for a phase-change recording layer structure and a magneto-optic recording layer structure. The simulation shows how important the thermal properties of the medium are in determining if the large side-lobes of a focused spot from an illumination-path filtered source act as significant secondary heat sources to the main heat source of the central core. The thermal simulation concludes that the significant side-lobes do not present an obstacle in writing with the phase-change recording layer structure, but would be an impediment with the magneto-optic recording layer structure. The servo system would need to be simulated and appropriate changes made to the control system for implementation in a real system. The through focus irradiance distribution needs to be modeled for the different filters for the focus servo. The across track irradiance distribution needs to be

modeled for the tracking servo. The servo adjustments are necessary due to the different irradiance distribution when the filters are used.

Return-path filters are observed to increase the high frequency response of both the system transfer function and the system two-point response. The action of the return-path optical amplitude filter is to decrease the low frequency response while not affecting the high frequencies, except by increasing their signal-to-noise ratio, as described in chapter 4. The action of the return-path electronic boost filter is to increase the high frequency response relative to low frequency response by providing a nonlinear gain as a function of frequency. The highlight of the improvement is when the filtering techniques are used together. When the return-path filters, the optical amplitude filter, and the electronic boost filter are combined the greatest increase in contrast is observed in the system transfer function and two-point response. When the illumination-path filter is applied with the return-path filters, even more improvement in high frequency system transfer function contrast is observed. The illumination-path amplitude filtered system using a central pupil obscuration($\varepsilon = 0.6$) introduces artifacts into the data signals that are shown to reduce at the expense of a tapped-delay-line electronic filter. The tapped-delay-line electronic filter is also shown to equalize the system transfer function.

The sensitivities of the unfiltered, ring-phase, and obscured system are shown. All three systems are shown to be sensitive to spherical aberration. The unfiltered system is sensitive to defocus while the ring-phase and obscured system have increased tolerance to defocus. The ring-phase system is more sensitive to coma than the unfiltered or

obscured system. The obscured system is more sensitive to astigmatism than the unfiltered or obscured source.

The performance improvements demonstrated did not take into account noise that is present in a real experimental system. The improvements of Chapter 3 are based on mathematical calculations, and are a very good starting point for expectations of system performance. To truly characterize the system, performance measures that take into account noise must be considered as well. The quantities of signal-to-noise ratio and timing jitter are demonstrated next in Chapter 4, which describes the experimental performance of a magneto-optic data storage system.

CHAPTER 4 - EXPERIMENTAL RESULTS FOR A MAGNETO-OPTIC DATA STORAGE SYSTEM

The simulations of Chapter 3 show that significant improvement in contrast of the system transfer function at high frequencies is attained by application of optical and electronic filters. The goal of this chapter is to show that this result is observed experimentally as well.

In this chapter, the experimental performance of a specific magneto-optic data storage system data channel is reported. The system transfer function and the two-point response of the system are discussed. Then, the introduction of different superresolution components and their effects on the performance of the system is demonstrated.

The previous chapter did not discuss the influence that the filters have on noise present in the system or on how noise influences detection of the resulting images. In this chapter, the performance of the system is characterized by measuring the signal current distribution in the pupil, the noise current distribution in the pupil, the transfer function, the carrier-to noise ratio (CNR), and jitter. The measures of CNR and jitter are also defined.

In Section 4A the layout and description of the experimental system is discussed. In Section 4B the alignment, testing, optimization, and component fabrication is discussed. Section 4C discusses the noise characteristics of the system by presenting definitions and system measurements. Section 4D presents the experimental performance of the system, including the signal current distribution in the pupil for both conventional

illumination and ring-phase filter illumination, the transfer function for the ring-phase illumination-path filter and return-path filters, CNR for the ring-phase illumination-path filter and return-path filters, and jitter for the return-path filter.

4A.1 - layout and description of experimental system

The experimental layout of the magneto-optic data storage system is very similar to the layout of Figure 3.4 except for the addition of relay lenses, as shown in Figure 4.1(a). The relay system produces an image of the stop at the aperture plane. The purpose of the relay system is to provide an image location of the stop, that is, a pupil location. In this pupil location an automated scanning pinhole is inserted to map out signal and noise distributions as a function of position in the pupil. This pupil location is also where return-path optical filters are inserted. The measured signal distributions are used for comparison to simulated signal distributions. The noise distributions give insight into the spatial distribution of noise in the pupil and how optical filters influence the noise.

An x-polarized laser diode ($\lambda = 785$nm) is collimated and circularized. Light is passed through a partially polarizing beam splitter (PPBS) and is focused through the substrate of a spinning disk onto the recording layer. The PPBS reflects 99% of the y-polarized light and 30% of the x-polarized light. Approximately 70% of the x-polarized light is transmitted. The numerical aperture of the objective lens is 0.5. The magneto-optic disk is a cobalt pallidum (CoPd) disk with center-to-center track spacing of 1.6μm. Light reflected from the disk is partially modulated by the data pattern, and the reflected

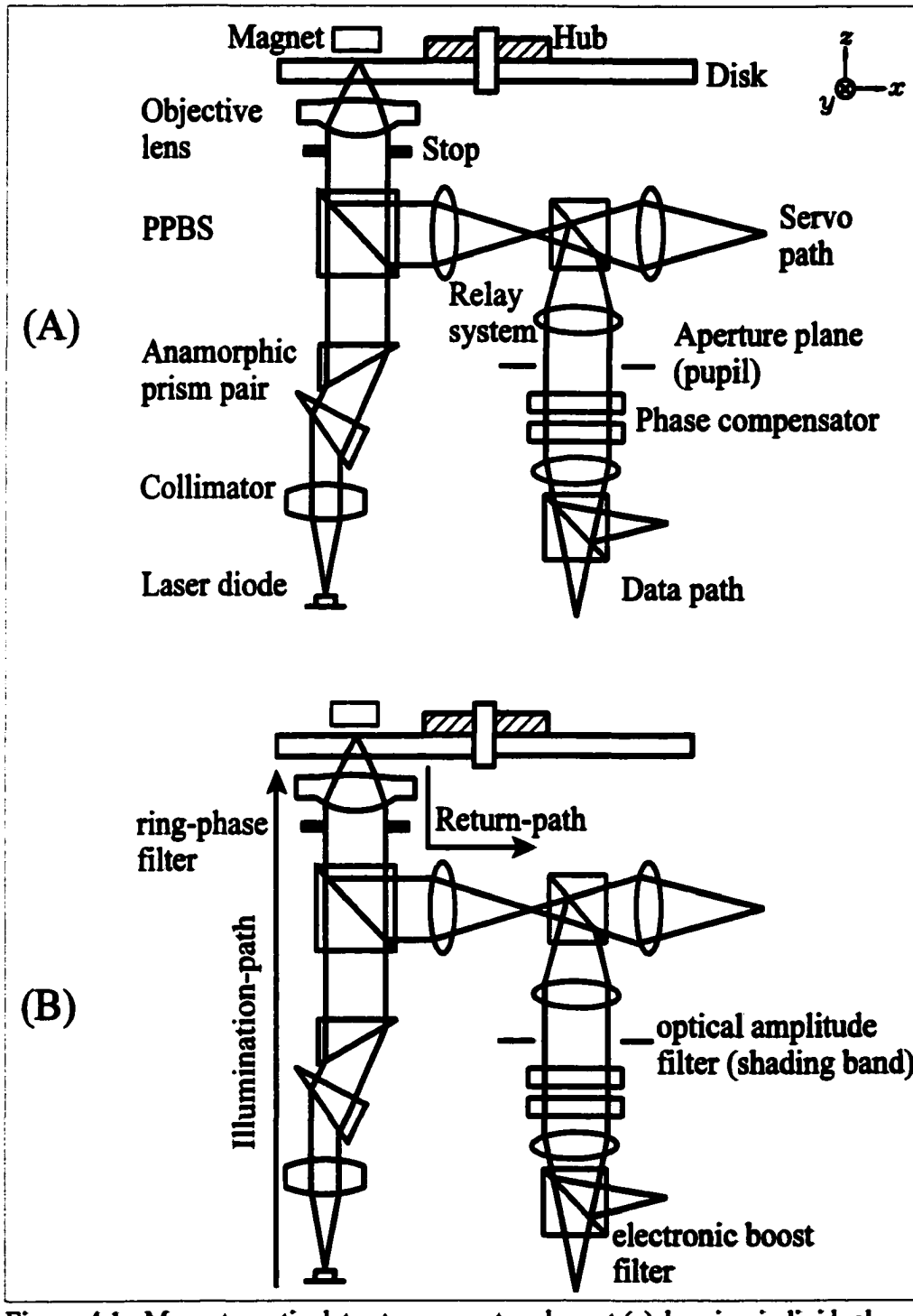

Figure 4.1. Magneto-optic data storage system layout (a)showing individual optical components, (b)clarifying the illumination-path and return-path, and showing the location of the filters to be investigated.

light is redirected into the servo path and the data path.

The servo and data paths are separated in order to simplify operation of the servo system.[1] The servo optics generate tracking error and focus error signals from the servo detectors. Focus and tracking correction is performed by moving the objective lens in a voice-coil actuator. In the data path, the high-frequency data signal is recovered by sensing a change in the polarization state of the reflected light caused by the magneto-optic Kerr effect. Because of the small signal levels, which are typically 2% of the background reflection, a differential arrangement of detectors are used to limit common-mode noise (Marchant, 1990). In the experiments, the velocity between the recording layer and the focused spot is 6.6m/s.

Three filters are investigated experimentally. The ring-phase illumination-path filter described in Section 3D.1.A and Section 2B.1.B, the return-path optical amplitude filter described in Section 3D.2.A and Section 2B.1.B, and the return-path electronic boost filter described in Section 3D.2.B and Section 2B.1. Figure 4.1(b) shows the experimental layout of the magneto-optic data storage system indicating the illumination path and the return path. The illumination path is the part of the system that delivers the light to the disk. The return-path is the part of the system that delivers the light to the detectors. Also labeled are locations of the specific filters that are investigated. The ring-phase illumination-path filter is placed between the partially polarizing beam splitter

---

1

In most commercial devices the servo and data paths are not separated, because servo and data information are derived from the same detectors.

(PPBS) and the prism pair. The return-path optical amplitude filter is placed in the pupil location just before the data detectors. The electronic boost filter used in experiments is described in Section 3D.2.B.

4B - Construction and testing of the experimental system

Great care must be taken when building an optical data storage system. Good design followed by sound optical system construction is essential to obtain satisfactory performance, because diffraction limited micron size focused spots are required. To obtain the performance needed for reliable playback of optical disks, the wavefront quality of the light incident upon the objective lens must be of high quality and the objective lens must also be of high quality and well aligned. Typical requirements of the wavefront quality are 0.02λ rms wavefront error.

In Section 4B.1 optical system alignment, and testing are discussed. In Section 4B.2 system optimization techniques are discussed. In Section 4B.3 system considerations with the ring-phase illumination-path filter are discussed. In Section 4B.4 superresolution component fabrication is discussed.

4B.1 - Optical system alignment and testing

There are a number of methods for alignment of optical systems. A good starting point is the method for the simultaneous alignment and collimation of a laser diode (Froehlich, 1991). An alignment telescope is used for establishing an optical axis. The first step is to establish a system axis by some mechanical means, such as two pinholes mounted on stages at a predetermined height above the optical table. The alignment

telescope is aligned to the pinholes looking into a HeNe laser that is shining light through the two pinholes. Then the anamorphic prism pair is inserted between the HeNe laser and pinholes. The prisms shift the optical axis. The HeNe is translated so that it is centered on the entrance of the prism pair while the laser light exiting the prism pair illuminates both pinholes, thus reestablishing the optical axis with the deviation of the anamorphic prism pair included. The next step is to align the illumination-path elements and collimate the laser diode. Collimation is adjusted with the objective lens removed. The PPBS is inserted between the laser and the telescope and centered on the axis of the alignment telescope. The next step is to use the reflection arm of the PPBS in a WYKO Ladite interferometer for testing wavefront quality. By using the alignment telescope together with the Ladite, the required wavefront quality and alignment to the system axis is achieved. Caution is used when interpreting wavefront data from the Ladite in the reflected arm of the PPBS, as this is not always a true indication of the transmitted wavefront. As a final step, the alignment telescope is replaced by the Ladite to check that the wavefront in the illumination-path is good as well, and fine adjustments are made if necessary.

The next step is to align the objective lens. The proper alignment configuration is to have the alignment telescope in place and aligned to the system axis. Then the objective lens is centered around the axis of the alignment telescope. The lens tip and tilt is adjusted by refocusing the alignment telescope at the focus of each surface of the objective lens so that the reflected crosshair coincides with the telescope crosshair. This

is a very difficult task due to the small diameter of the objective lens and the low reflectivity of its surfaces. Alternately, the objective lens may be aligned by eye so that a nice clean circular diverging beam is exiting the objective when viewed upon a simple screen. Then, fine adjustments can be made when the system is up and running while observing data and servo signals.

The return-path optics can be aligned visually, making sure that the elements are centered around the light, and the tip/tilt is adjusted for back reflections. The lenses used in the return path are commercially available achromats, and they are mounted with the stronger curvature toward the collimated beam. The spacing between the relay system elements is adjusted by checking with a shear plate interferometer so that a collimated beam emerges from the second relay lens. The image plane of the stop, or auxiliary pupil location formed by relay system, is found by using a standard shop method of placing lens tissue against the front surface of the lens, illuminating the tissue with a lamp and physically looking for the image of the tissue behind the second relay lens. This locates where the scanning pinhole is placed for signal and noise distribution measurements, and where the return-path optical amplitude filter is placed. Avalanche photodiodes are used in lieu of standard PN junction photodiodes as data detectors by virtue of their high gain and the small signal levels transmitted by the pinhole when mapping signal and noise distributions.

4B.2 - System optimization methods

There are some fine tuning methods that are particularly helpful when the system

is operating well enough so that the servo system can lock the focus and tracking of the objective lens to the recording layer on a single data track.

While observing a low frequency data pattern on an oscilloscope, the in-track tilt of the objective lens can be adjusted to sharpen the rise and fall times of the signal. If it is found that the edges improve on the data signal, the servo system should be checked to see if it is at optimum performance. The procedure is repeated until maximum performance is achieved.

The across-track tilt can be adjusted by observing residual data signals on adjacent erased tracks. The tilt may be adjusted until the residual signals are equal in amplitude. Care should be made to be sure that there is no tracking offset in the servo channel when performing this adjustment. Another method of adjusting the across track tilt is to write a track of data on grooveless media and then step the optical head in the across track direction and adjust the tilt to provide a symmetrical signal distribution across the track.

4B.3 - System considerations when ring-phase illumination-path filter is used

A few considerations about the use of the ring-phase illumination-path filter in the system is required. Measurements associated with the phase filter for writing data are not presented in this work. The servo would unlock when attempting to write. The reason for the servo unlocking during writing is due to the higher light levels required for writing that in turn saturate the servo detector amplifiers. This is partly due to the 50% reduction in the peak irradiance of the focused spot, as shown in Figure 3.18. To make up for the reduced peak irradiance, the laser driver required modifications. Although the laser is

capable of being driven at higher output powers, the laser driver is not easily modified. A second difficulty is associated with the different irradiance distribution incident on the servo when the ring-phase filter is used.

The phase filter is used in read-only mode, where data are written conventionally and the data signal is read back with the filter in the system. When reading back with the phase filter in place, the conventional read laser power is increased from 1.5mW to 3.5mW in order to make up for the 50% reduction in peak irradiance.

The servo performed well while reading. The servo system is robust enough to stay locked much longer than the six hours needed to obtain signal current distributions with the ring-phase filter illumination for each frequency.

4B.4 - Superresolution component fabrication

Measurements are obtained using the ring-phase illumination-path filter, as shown in Figure 2.12. Implementation of this filter as a component in the optical system is straight forward. The first step is to make a mechanical drawing of the annulus with appropriate ratio of inner to outer diameter at a scale much larger than actual scale. A dark ring is drawn between the two boundaries on a white sheet of paper. The next step is to setup a camera system with a zoom lens and make a series of exposures, being careful to step slowly through the magnification region where the appropriate dimensions will be given to the image of the ring in the film plane. Then the standard photographic film is developed. The series of negatives is examined. The negatives are dark with a transparent ring. From the series of exposures taken, the exposure that matches the

required dimensions is identified by measurement and set aside. The required dimensions are outer diameter, o.d. = 1.935mm, and inner diameter, i.d. = 1.250mm. The next step is to spin coat photoresist on a fused silica glass slide. Then the negative with the transparent ring is placed over the coated side of the slide. This configuration is exposed to a UV lamp. After exposure and development, the glass slide is left with the photoresist coated on one side with a ring lifted away due to the exposure to the UV lamp. The slide is then placed in an ion mill for etching the glass in the ring region. The ion mill etches the glass only from the region of the slide that is not covered by photoresist. The depth of the etch is determined by the etching rate of the ion mill, and how long a time period the mill is left on. For instance, a 180° phase depth, $d=\lambda/(2(n-1))$, at λ=780nm in fused silica having refractive index n=1.45 is 0.87μm. An etch rate of 0.087μm/min means that the sample should stay in the mill for 10 minutes. The finished sample is characterized with a RST profiler[2]. The measured depth of 0.98μm is very close to the desired depth of 0.87μm. The difference represents a 22° phase error that has surprisingly little effect on the focused spot. The simulation of this error shows a peak irradiance change of 3% and very little noticeable change in the sidelobe levels and central core width. The inner and outer diameter measurements are o.d =1.91mm, and i.d.=1.21mm. These dimensions are within 1% of the desired values.

Fabrication of the return-path optical amplitude filter shown in Figure 3.27(a)&(b) is straight forward. The desired pattern can be laid out on thin aluminum stock and then

---

[2] The RST profiler is a WYKO instrument

milled accordingly. Alternately, the desired pattern can be laid out in a drawing package and then used as a template on the thin aluminum stock to be milled. The pattern used in the experiments is an 18% center width x-band filter and a 15% width rectangular filter.

Electronic filtering is achieved by a simple electronic circuit that has a variable gain and a variable peak gain frequency. The chip at the heart of this filter is the Silicon Systems 32f8020a. The settings chosen for the experiments are a peak gain frequency of 5MHz, a peak gain of 6dB, and a high-frequency cutoff of 9MHz.

4C - Noise characteristics of system

For low-contrast objects, the noise properties of the optical system are as important as the signal properties. The low contrast objects in a MO data storage system are in the high frequency region of the transfer function. This region coincides with the shortest pulse widths where operation is desired in order to maximize the capacity of the disk.

Section 4C.1 discusses the definitions of signal-to-noise ratio (SNR) and carrier-to-noise ratio (CNR). Section 4C.2 discusses time interval analysis of waveforms and the definition of jitter. Section 4C.3 reviews sources of noise in a magneto-optic data storage system. Section 4C.4 presents experimental data of the noise spectra in the system data channel. Section 4C.5 presents experimentally measured spatial distribution of noise current in the pupil.

4C.1 - Signal-to-noise ratio/carrier-to-noise ratio (SNR, CNR)

The signal-to-noise ratio (SNR) is not an easily measured quantity of the data

channel (Marchant, 1990, p.247). SNR is defined in Section 2A.2. The signal power is derived from a pseudo-random data pattern, where a track of data is measured that contains all mark lengths and spaces that make up a particular code for the channel. Figure 4.2 shows a data signal for a pseudo-random sequence of data, where the oscilloscope is set to trigger multiple traces of the data detector output during the exposure time of the camera used to take the picture. The data signal displayed in Figure 4.2 is one example of an eye pattern, which is a diagnostic that is frequently encountered in communication systems engineering. It is called an eye pattern because the openings in the center of the waveform resemble the outline of an eye. A good quality signal is indicated by open "eyes".

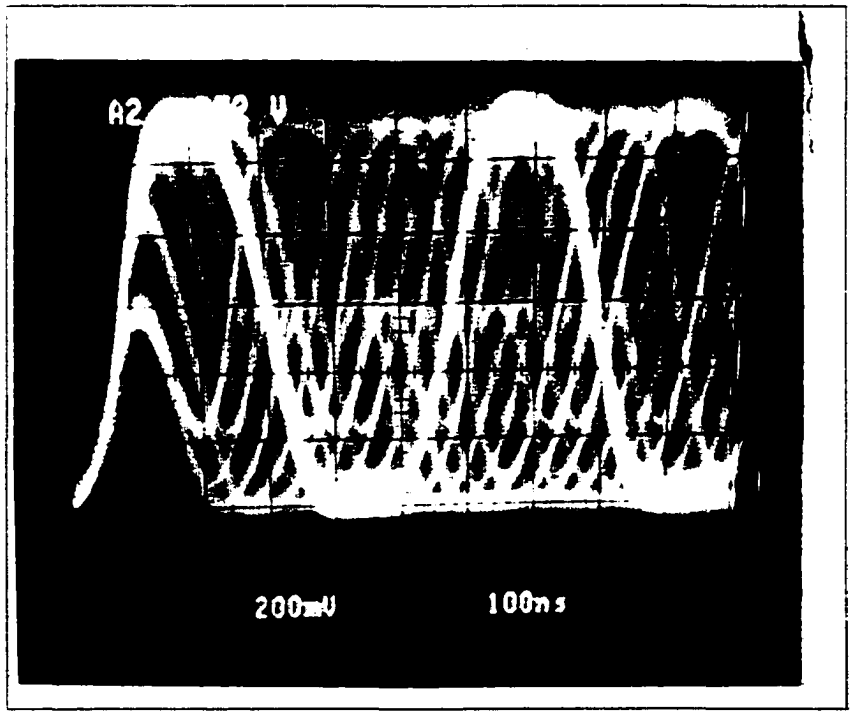

Figure 4.2. Eye pattern, a qualitative tool for signal analysis

Another quantity of measure that is more quantitative is the carrier-to-noise ratio (CNR). It is measured by reading a single-tone pattern on a track using a spectrum analyzer. The convention for measurement bandwidth Δf of the spectrum analyzer is 30kHz. $\Delta f = 30$kHz is chosen because this is usually much wider than the signal peak but is relatively narrow in comparison to the bandwidth of the electronics. The peak of the trace then corresponds to the total signal power P_{sig} measured in dBm units. The spectrum analyzer sweeps through the frequency range containing the data signal. A typical trace is shown in Figure 4.3. The expression relating the equivalent rms signal current amplitude i_{sig} and P_{sig} is given by,

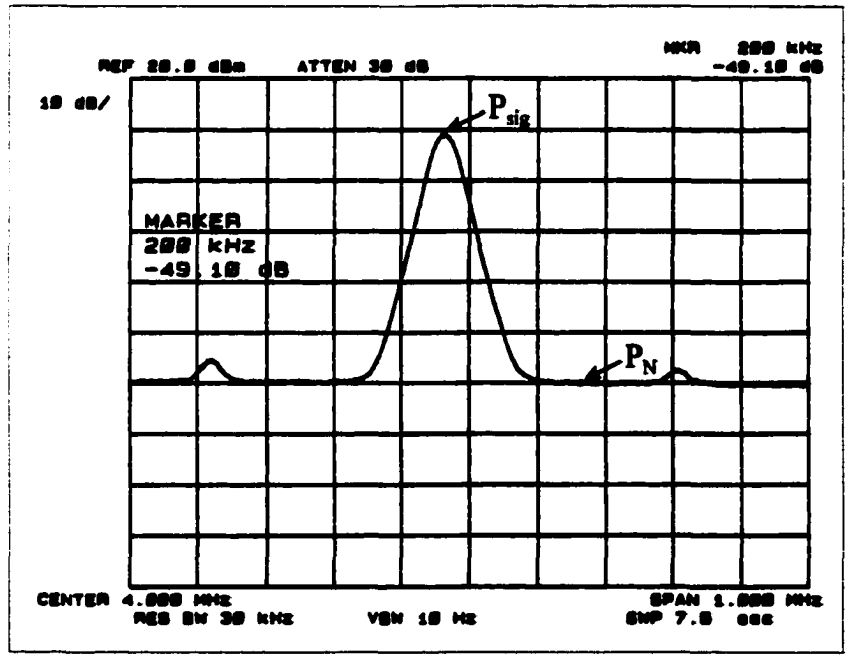

Figure 4.3. Spectrum analyzer trace of the data signal for measuring the carrier-to-noise ratio(CNR)

$$10\log_{10}\left(Ri_{sig}^2\right) = P_{sig} \quad , \tag{4-1}$$

where R=50Ω is the electrical resistance of the spectrum analyzer input port.

The noise power, P_N, is measured at a frequency 200kHz to one side of the peak and is also measured in units of dBm. The expression relating the equivalent noise current amplitude i_N and P_N is given by,

$$10\log_{10}\left(Ri_N^2\Delta f\right) = P_N \quad , \tag{4-2}$$

where R=50Ω is the resistance of the spectrum analyzer. The current i_N represents the equivalent noise current amplitude per unit $(Hz)^{1/2}$. P_N is the noise power delivered to a load R within a bandwidth Δf measured in units of dBm or dBw.

The CNR is expressed in units of dB and is the difference between these two measurements when the two measurements are expressed in dBm, that is,

$$CNR = P_{sig} - P_N \quad . \tag{4-3}$$

Equation (4-3) can be expressed in terms of rms current amplitude through the relation

$$CNR = 20\log_{10}\left(\frac{i_{sig}}{i_N(\Delta f)^{1/2}}\right) \quad , \tag{4-4}$$

where i_{sig}, and i_N are the equivalent rms signal current and noise current amplitudes, respectively.

The CNR is a very good measure for signal quality. It is a widely used

performance measure for optical data storage systems. However, by itself it is not a complete characterization of system performance. Another method called time interval analysis is discussed next.

4C.2 - time interval analysis of waveform

A problem results when measuring pulse transitions with a simple threshold detector. Figure 4.4(a) shows the ideal time response along with the noise-free response

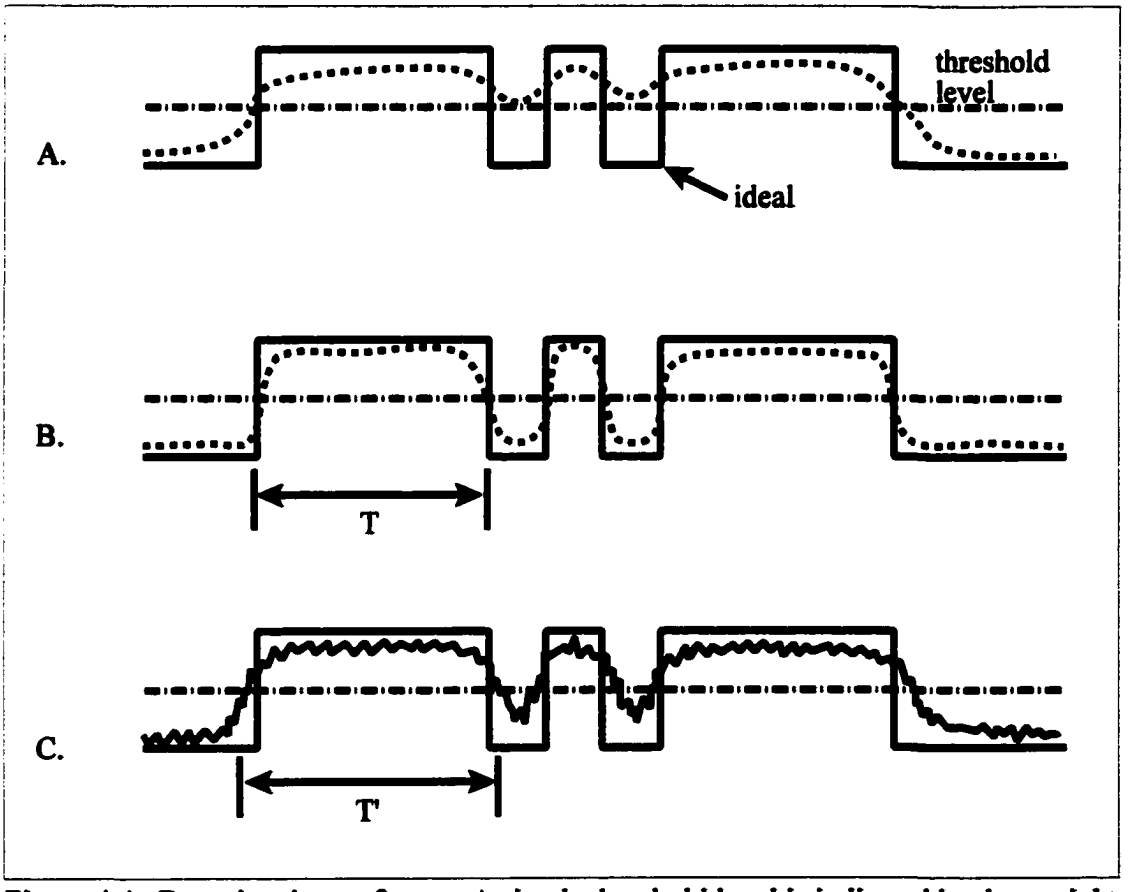

Figure 4.4. Data signal waveforms. A simple threshold level is indicated by the straight line through the waveforms. (A) ideal response together with noise-free response for an unfiltered system, (B) ideal response together with a noise-free response for an equalized system, (C) ideal response together with noisy response for an equalized system.

for an unfiltered system. Depending upon where the threshold is placed, some of the high-frequency transitions can be missed. If the transfer function is equalized, it is less likely that the threshold detector will miss high-frequency transitions. In Figure 4.4(b) a hypothetical readout with an equalized transfer function where the low-frequency response and the high-frequency responses are more nearly equal is shown. An improvement in confidence for detecting the transitions is observed. The noiseless pulsewidth T is now an accurate representation of the data. In Figure 4.4(c) noise is added, and the detection of transitions becomes a stochastic process. The detected pulse width T′ can be slightly larger or smaller than T.

A measurement of quality is the jitter, which is defined as the standard deviation, σ, of T′. Figure 4.5(a) shows a magnified region around the intersection of the waveform with the detector threshold. The standard deviation, σ, is shown to be related to waveform parameters through the relation $\sigma=w/m$ where w is the voltage or current fluctuations of the waveform and m is the slope of the waveform.

Figure 4.5(b) shows the transition location probability distribution associated with the threshold detection process of a waveform with noise. The distribution shown is Gaussian with standard deviation σ. The ideal probability distribution is a delta function. However, due to the presence of noise, this is never achieved in practice. Also, every data channel has a data clock that runs synchronously with the data signal. The timing window, which is defined as one half a period of the data clock, defines the smallest increment in time into which transitions can be counted. A rule of thumb for the jitter σ

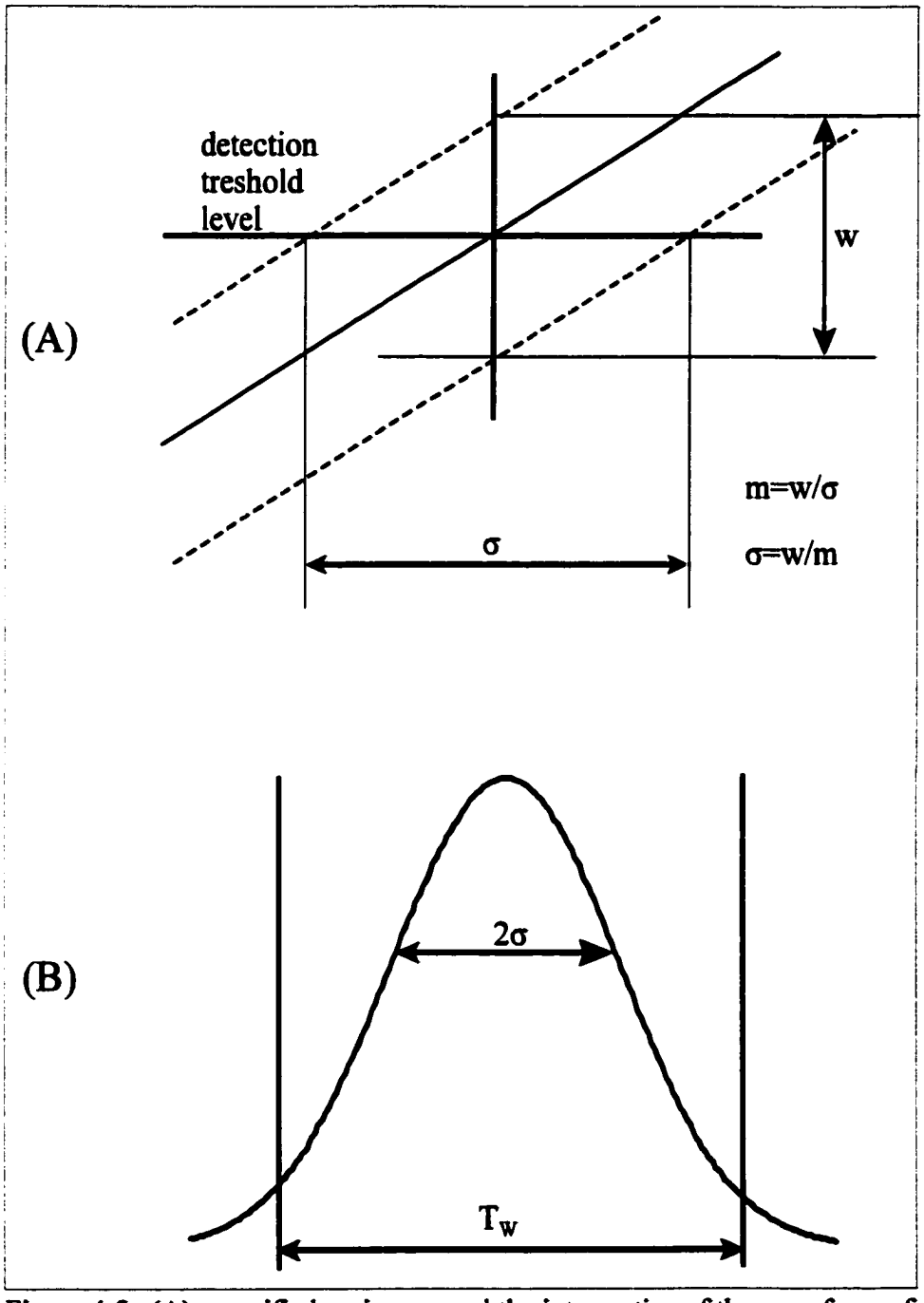

Figure 4.5. (A) magnified region around the intersection of the waveform of Figure 4.4(c) with the threshold detector, (B) Gaussian transition location probability distribution associated with the threshold detection process. The ideal probability distribution is a delta function.

is to be 35% of the timing window in order to allow for other mechanical tolerances(Howe, 1983).

Jitter is an important measure of quality because it used in calculating the error rate of a data channel (Howe,1983). The experimental results of jitter measurements are presented in Section 4D.5. Jitter measurements for the return-path filtering schemes are investigated in detail.

4C.3 - Sources of noise

The noise sources in a magneto-optic data storage system include shot noise, media or disk reflectivity noise, laser noise, and electronic noise. The different noise sources have different spatial distributions in the pupil. For example, shot noise is proportional to the square root of the optical power incident on the detector. Laser noise is proportional to the optical power. Media noise results from what can be thought of as a random distribution of gratings on the recording layer. Therefore, media noise has a spatial distribution in the pupil that depends on the frequency range of interest. For example, low-frequency media noise is concentrated in the central portion of the pupil, and high-frequency media noise is distributed such that more noise energy is near the edge of the pupil. The data detectors are avalanche photodiodes, as mentioned previously. They have high gain and an extra noise factor that is independent of the optical power (Mansuripur, 1982), and multiplies both the signal and the noise.

The noise sources have different dependencies on optical power. For instance, the shot-noise goes as the square root of the optical power. An expression for the equivalent

shot-noise current amplitude i_{shot} is given by,

$$i_{shot} = (2qR\Phi f)^{1/2} \quad , \tag{4-5}$$

where q = 1.6022 x 10^{-19} coulomb is the electronic charge, *R* in units of amps/watt is the responsivity of the detector, Φ is the total optical power incident on the detector, and f is the bandwidth of the measurement electronics. From Equation (4-5) and the fact that Φ is a function of position, it is observed that the shot-noise current amplitude has a spatial distribution that follows the square root of the irradiance distribution.

Laser noise is proportional to the optical power. An expression for the laser noise is given by,

$$i_{laser} = 2\Phi\Delta_e \quad , \tag{4-6}$$

where Δ_e is a dimensionless quantity that is related to time varying amplitude fluctuations of the laser output caused by instabilities of the laser cavity resulting in mode hopping and mode competition. Laser noise is reduced to a tolerable level through differential detection and by modulating the laser at a frequency of a few hundred megahertz. The modulation frequency is typically well outside the 10-20MHz bandwidth of a typical data channel, insuring that the laser looks like a dc source for all practical purposes to the servo and data detectors. The exact modulation frequency is based on the optical path length from the laser to the disk(Call and Finkelstein, 1989). The laser noise is a strong function of the length of the external cavity and is characterized by the phase delay of the reflected pulse

$$\text{phase delay} = f\frac{2L}{c}(360^\circ) \quad , \qquad (4\text{-}7)$$

where f is the modulation frequency, L is the optical path length between the laser and the disk, and c is the speed of light. A minimum noise level occurs every 360° at 90°, 450°, etc. The basic principle is that when reflected light returns to the laser cavity the laser is actually turned off, which results in more stable operation. Also, because the objective lens is constantly moving while the disk is spinning, the modulating frequency is chosen so that the laser noise remains low over the range that the objective lens moves. Equation (4-6) shows that the spatial distribution of laser noise in the pupil is expected to follow the irradiance distribution in the pupil.

Media noise is proportional to Φ and is a dominant noise source that is a function of spatial/temporal frequency. Media noise results from spatial variations of disk reflectivity, depolarization of the incident x-polarized light not due to the MO Kerr effect and other sources such as disk birefringence. The spatial distribution of media noise i_{media} in the pupil is expected to depend on the spatial frequency content of the reflectivity variations and the birefringence.

The electronic noise, also known as Johnson noise, does not depend on the optical power and can be made negligible by using low noise electronics. An expression for the equivalent electronic noise current amplitude is given by,

$$i_{th} = \left(4k_b Tf / R\right)^{1/2} \quad , \qquad (4\text{-}8)$$

where $k_b = 1.38 \times 10^{-23}$ (joule/K) is the Boltzmann constant, T is absolute temperature in degrees Kelvin, f is the bandwidth of the measurement electronics, and R is the resistance in ohms.

The total noise current amplitude i_N is given by

$$i_N^2 = i_{shot}^2 + i_{laser}^2 + i_{media}^2 + i_{th}^2 \quad . \tag{4-9}$$

Some sources of noise are more dominant than others. A method to determine which one is most dominant is to measure them on a spectrum analyzer and separate them out as individually as possible, then estimate relative contributions using the above equations. Spectrum analyzer traces of noise spectra are presented in the next section.

4C.4 - Noise spectra in data channel

Noise distributions are obtained by scanning the laser beam over an erased data track. A region of approximately 10 adjacent tracks is erased to eliminate undesired crosstalk from adjacent tracks. After erasing the laser power is reduced to a constant level of 1.5mW for reading.

Figure 4.6(a) shows the data channel noise spectra when the disk is spinning at 6.6m/s, when the disk is stationary, and the electronic noise with a laser read power of 1.5mW. The velocity of 6.6m/s is not magical; it is on the order of commercial devices and the velocity at which signals are investigated in the next section. The electronic noise is well below any of the other noise sources, indicating well designed low-noise electronics. When the disk is spinning, all sources of noise are present in the data

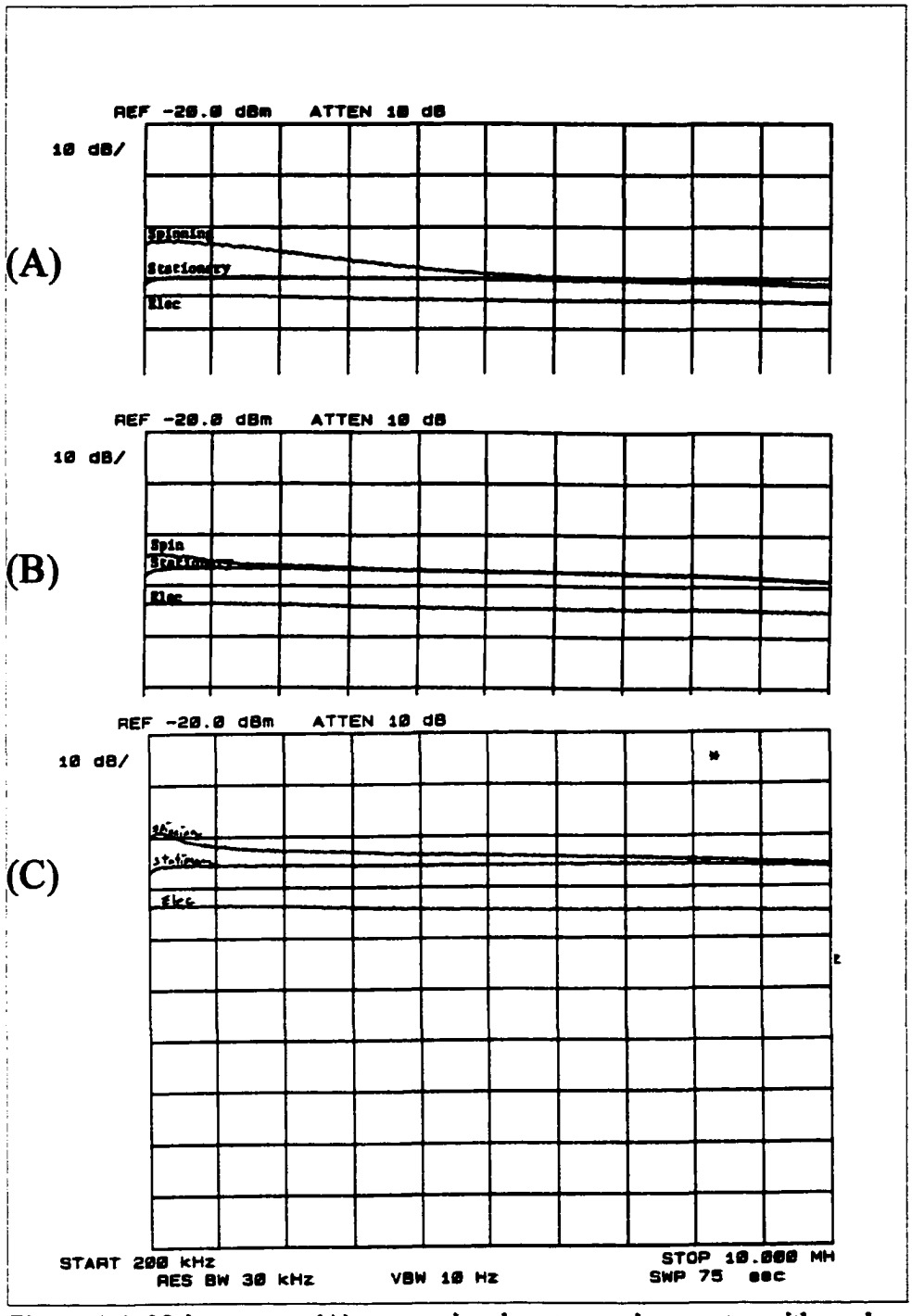

Figure 4.6. Noise spectra (A) conventional system noise spectra with read power of 1.5mW, (B) ring-phase illumination-path filtered system noise spectra with read power of 1.5mW, (C) ring-phase illumination-path filtered system noise spectra with read power of 2.5mW.

channel. When the disk is stationary, the source of noise not present is the media noise. The media-noise contribution is calculated by subtracting the stationary spectra from the spinning spectra.

Figure 4.6(b) shows the data channel noise spectra with the ring-phase illumination-path filter in the system with the same laser read power of 1.5mW. The electronic noise spectrum of the two systems is the same. The stationary noise spectrum for the filtered system is about 3dB higher than the unfiltered system. The spinning noise spectrum, or media noise, for the unfiltered system is higher than the filtered system at frequencies below 3MHz, and lower for frequencies greater than 3MHz.

Figure 4.6(c) shows the data channel noise spectra with the ring-phase filter and a laser read power of 2.5 mW. Both the stationary and spinning noise spectra are increased as a consequence of increased laser power. Also, the spinning noise spectra, or media noise, has a wider bandwidth than the unfiltered system's media noise.

4C.5 - Experimentally measured spatial distribution of noise current in the pupil

The noise current distributions are measured as a function of position in the pupil. The noise distribution measurements are made by scanning a pinhole in the pupil formed in the return path and reading the noise current power on a Hewlett-Packard RF spectrum analyzer. The pinhole location is controlled by stepper motors. The stepper motors and spectrum analyzer are controlled by computer interface using the commercial package LabView™. At each scan position noise spectrum data are collected and stored in the computer.

When the pinhole is placed in the system the optical noise spectra must be above the electronic noise floor in order to measure the spatial dependence of noise. Also, the noise spectra when the disk is spinning must be above the noise spectra when the disk is stationary in order to measure the spatial dependence of the media noise. Several ways are available to have the spinning noise rise above the stationary noise. One is to increase the laser read power, but this is not a good idea because the erased track will slowly become randomized due to heating of the layer. Another way is to increase the size of the pinhole used for scanning the distributions, but this is not a good idea either because good sampling in the scan plane is desired. The best method is to slow the disk down causing the media noise contribution to compress within a smaller bandwidth, which results in greater strength in this bandwidth. In these experiments, the disk is slowed down by a factor of 2 to a velocity of 3.3 m/s when making noise measurements in order to have more media noise power per unit frequency.

The pinhole diameter is 400μm, and the pupil diameter is 4.3mm. By sampling at 100μm intervals, the noise current distributions are measured as a function of position in the pupil. The bandwidth of the spectrum analyzer is 30kHz. The size of the plane to be mapped is 5mm x 5mm to provide easy centering of the scanning pinhole. The noise is measured with the disk spinning and with the disk stationary. Power data in dBm collected from the spectrum analyzer are converted to rms current with units of $mA/(Hz)^{1/2}$. By subtracting the spinning and stationary data sets, the media noise contribution is obtained. Signal processing is used to remove the effect of the pinhole on

the collected data by deconvolution.

Figure 4.7(a) displays the measured laser beam irradiance distribution in the pupil after reflection from the disk. Figure 4.7(b) displays the total noise distribution in the pupil with the disk stopped. The noise follows the Gaussian shape of the illumination, and it contains shot-noise and laser-noise components. Figure 4.7(c) displays the total noise for a spatial frequency of $0.3\mu m^{-1}$. The noise is concentrated near the center of the pupil, like the corresponding simulated signal distribution of Figure 3.16, which is also concentrated near the center of the pupil. Figure 4.7(d) displays the total noise for a higher spatial frequency of $0.6\mu m^{-1}$. The significance of this spatial frequency is that it is very close to the cutoff frequency $0.64\mu m^{-1}$ of a coherent optical system, and is where the $\pm$ 1diffracted orders begin to not overlap each other. Again, the noise is mostly concentrated in the center of the pupil, unlike the corresponding simulated signal distribution in Figure 3.16 and experimental signal distribution in Figure 4.9, which are bimodal and concentrated toward the edge of the pupil. The difference between Figure 4.7(c) and Figure 4.7(d) is that the noise is more spread out in the pupil for higher spatial frequencies. Figure 4.7(e) shows the media-noise contribution, at the spatial frequency of $0.3\mu m^{-1}$, to the total noise, which is obtained by subtracting the data of Figure 4.7(b) from the data of Figure 4.7(c). The media noise is more randomly distributed than the total noise, although most of the media noise is concentrated near the center of the pupil. It is tempting to suspect that the media-noise distribution is smoother than what is observed. However, the distribution shown in Figure 4.7(c) represents one sample of an ensemble

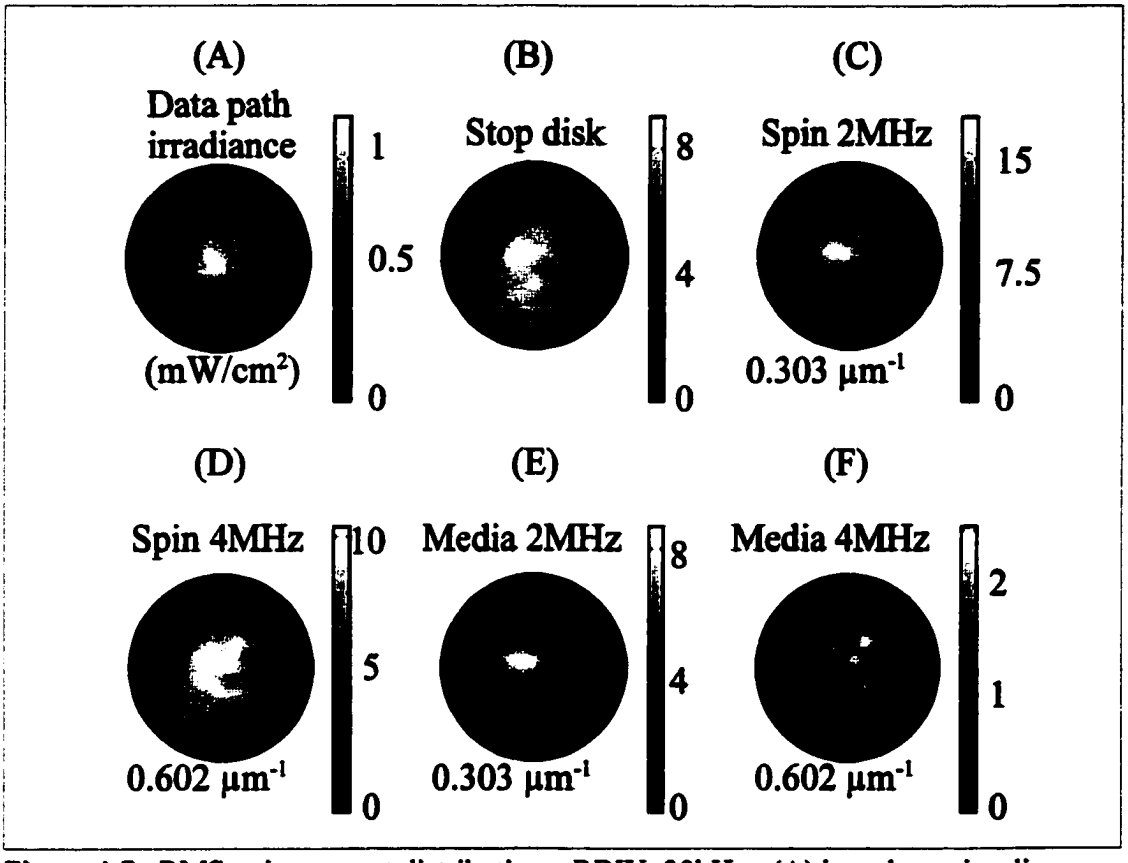

Figure 4.7. RMS noise current distributions, RBW=30kHz. (A) laser beam irradiance distribution in the aperture plane(pupil) of the data path. Units of normalized irradiance (mW/cm^2). The units for B-F are current/ root Hz ($ma/Hz^{1/2}$). (B) Noise distribution when the disk is stationary. (C) Noise distribution at 303lines/mm when the disk is spinning. (D) Noise distribution at 602lines/mm when the disk is spinning. (E) Media noise distribution at 303lines/mm. (F) Media noise distribution at 606lines/mm.

across the disk, for which the ensemble average is a relatively smooth distribution. Figure 4.7(f) shows the media-noise contribution at the spatial frequency of $0.6\mu m^{-1}$, which is obtained by subtracting the data of Figure 4.7(a) from the data of Figure 4.7(d). The difference between Figure 4.7(e) and Figure 4.7(f) is that the media noise is more spread out in the pupil for higher spatial frequencies.

The noise current distribution as a function of position in the stop is shown to be

concentrated within a radius equal to half of the radius of the pupil. The media-noise distribution spreads out toward the edge of the pupil at higher spatial frequencies and diminishes in strength.

4D.1 - experimental performance of magneto-optic data storage system

The measured performance of a data channel in the experimental magneto-optic data storage system is presented. The performance of the system is characterized by measurements of the signal current distributions in the pupil, system transfer function, CNR, two-point response, and jitter.

Section 4D.1 presents spatial distributions of signals in the pupil for the conventional system and the ring-phase illumination and verifies the concept of the data pattern acting as a grating to the focused beam. Section 4D.2 presents transfer functions for the three filters and combinations of them with grooved and groovless media. Section 4D.3 presents CNR measurement for the three filters and combinations of them with grooved and grooveless media. Section 4D.4 presents the two-point response of the system for return-path filtering combinations only. Section 4D.5 presents jitter measurements for return-path filtering combinations only.

4D.1 - Spatial distributions of signal current in pupil

Signal distributions are obtained by writing a single-tone data pattern at the frequency of interest. After writing, the laser power is reduced to a constant read power of 1.5mW. The disk velocity is 6.6m/s. The scanning pinhole is used to obtain the signal power in a 30kHz bandwidth as a function of position in the stop. Data are then erased,

and then a different frequency is written.

In Figure 4.8 the signal current distributions for several different spatial frequencies are displayed. At low frequencies the signal current is concentrated in the center of the pupil, as predicted in Chapters 1 and 3. At high spatial frequencies the signal current is concentrated near the edges of the pupil. Notice the result for the spatial frequency near $NA/\lambda = 0.64$ lines/μm^{-1}, which is the cutoff frequency for a coherent plane-wave illumination system using the same NA and λ. As illustrated in Figure 1.3, the overlap of the diffracted orders begins to separate. As the spatial frequency increases

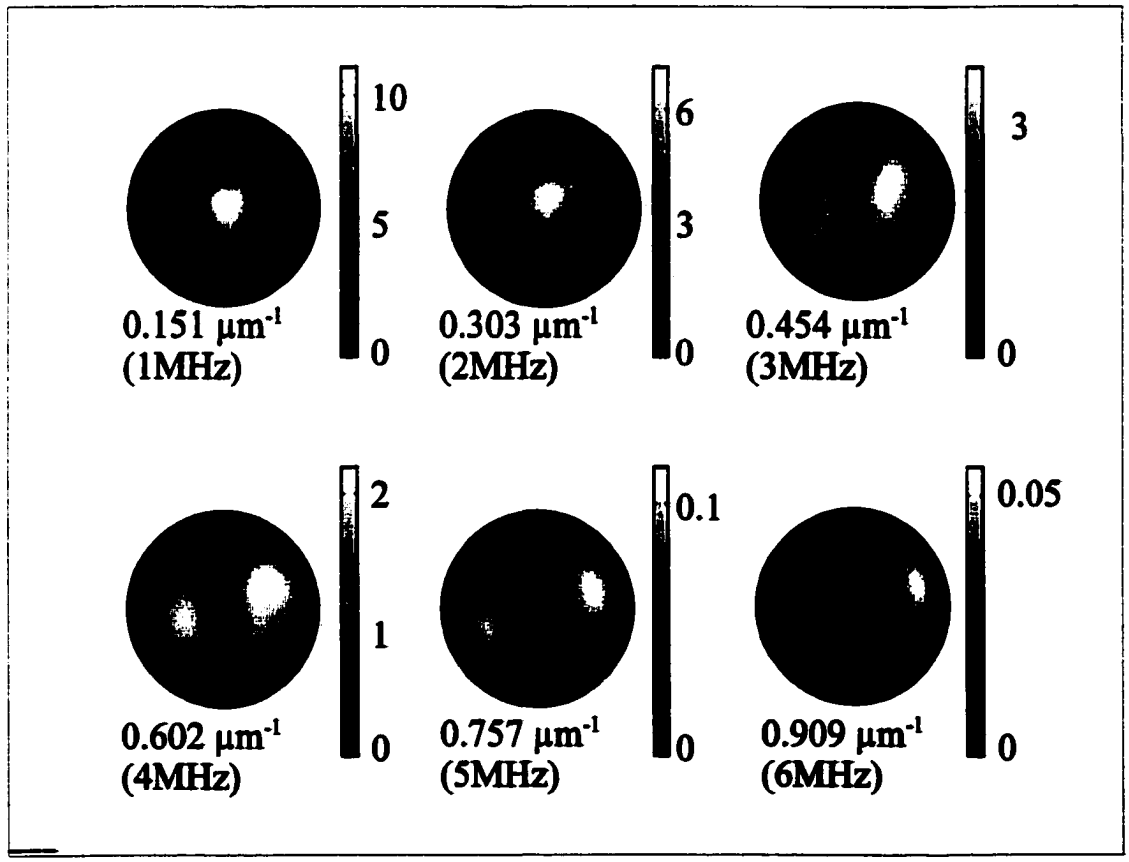

Figure 4.8. Signal current distributions in the pupil, for conventional illumination, after reflection from the disk. Increasing frequency left to right, top to bottom.

toward 1.28μm^{-1}, the cutoff frequency for this type of optical system, the overlap area is significantly reduced. The measured signal distributions are in excellent agreement with the simulated signal distributions shown in Figure 3.16.

Figure 4.9 displays the signal current distributions for the ring-phase illumination-path filtered system. Comparison of the distributions in Figure 4.9 to the simulation in Figure 3.18 shows that the predictions of the distribution are accurate. The additional structure in the distribution is shown to exist in experiments as well. The additional structure is due to the presence of the phase filter. The dark bands occur at the edges of

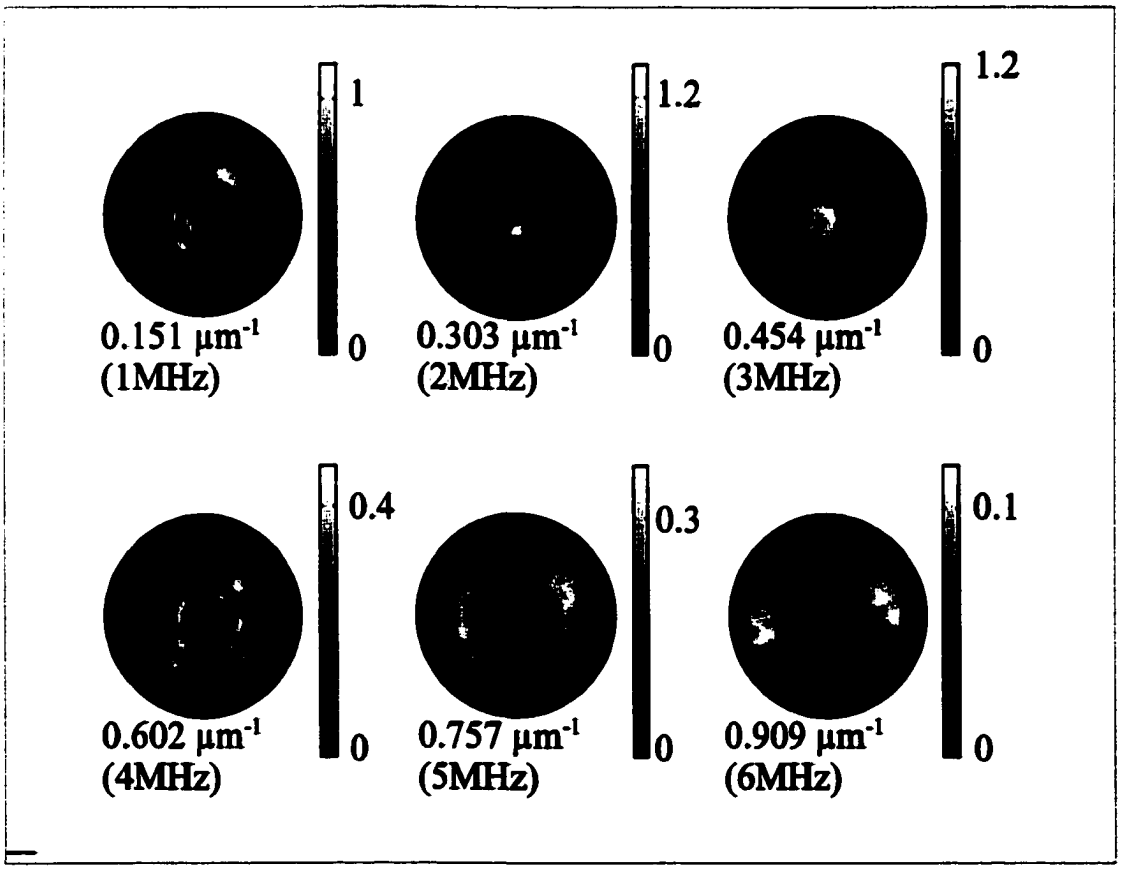

Figure 4.9. Signal current distributions in the pupil with the ring-phase illumination-path filtered source. Increasing frequency left to right, top to bottom.

the phase filter, and they closely follow the outline of the annulus. These are observed in the irradiance of the reflected light from an erased track in the return-path as well. This leads to the conclusion that the dark bands are due to scattering from the imperfect edges of the phase plate. In the simulation it is also observed that the irradiance of the reflected light from an erased track in the return-path contained dark bands. In the simulation these bands are due to the sampling of the bitmap chosen to represent the phase filter in the simulation, that fortuitously "modeled" the imperfect edges of the phase plate.

From the experimental signal distributions observed in Figure 4.9 and in the simulation Figure 3.17, the shape of the dark region when the distribution becomes bimodal is no longer 'x' shaped as with the conventional illumination shown in Figures 4.8 and 3.16. The shape of the dark region is more rectangular in form than the 'x'. Using an x-band filter with this signal distribution will attenuate the low frequencies more than if a simple rectangle shape filter. From Figure 4.9 and 3.18 it was decided not to use the x-band return-path filter, as used in the conventional illumination, but rather a simpler rectangle amplitude filter that has a width of 15% of the pupil. This is an example of a benefit of understanding the signal distributions when designing a return-path filter shape.

4D.2 - Transfer function

The transfer function is measured for the conventional system, for individual filtering techniques and for combinations of filtering techniques. The transfer function is measured for two different types of media: media with grooves (with tracks) and

grooveless media (no tracks).

4D.2.A - Transfer function with grooved media

Media with tracks are investigated first. In Figure 4.10(a) the measured system transfer function is shown for the conventional system, the system with electronic filtering only, an 18% x-band return-path optical filter, and the combination of the two techniques. With no filtering the classic roll off of the system transfer function is observed. For electronic filtering only, the system transfer function exhibits improved contrast at high frequencies and the frequency at which the maximum contrast occurs has shifted from dc to 1.5MHz. For optical filtering only, the system transfer function exhibits improved contrast at high frequencies, but not as much as for the electronic filter only. This is only slightly different from what the simulation indicated, as shown in Figure 3.31. The experiment agrees well with the simulation. For the combination of the two filters, the contrast improvement is greater than either of the three previous cases, and the frequency of maximum contrast has shifted to 3.5MHz. As an example, at 5MHz we see poor contrast H(5)=0.1 for the system with no filtering, but the use of either filtering scheme alone results in an increase in contrast to H(5)=0.2. However, with the combination of the two filters, an increase to H(5)=0.4 in the contrast is observed. It is shown that the best relative contrast improvement is realized when both filters are used.

Figure 4.10(b) shows the system transfer functions for the ring-phase illumination-path filter only, in combination with the return-path optical filter, in combination with the

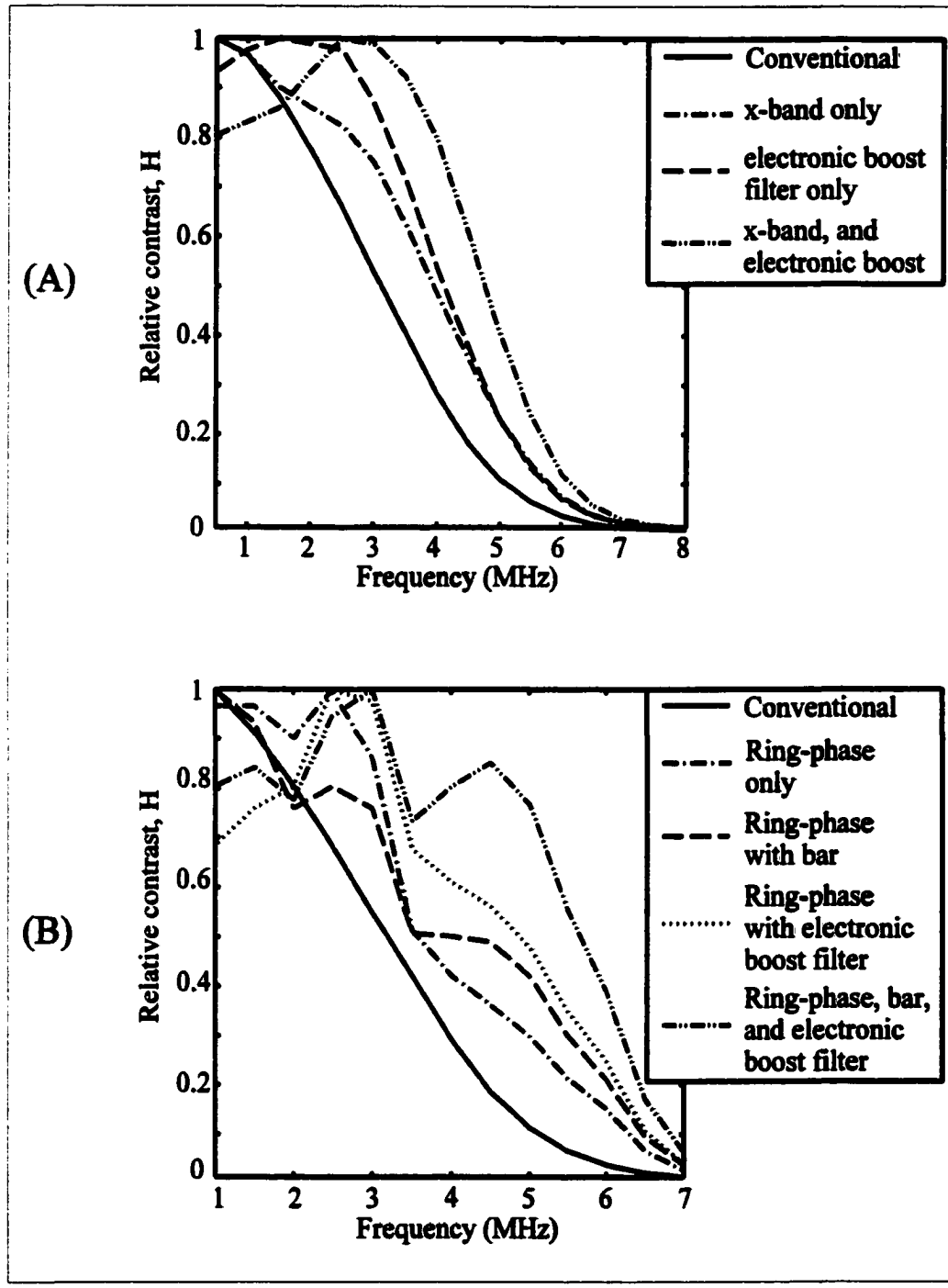

Figure 4.10. System transfer functions for grooved media (A) system transfer functions for the unfiltered system, return-path optical filter, electronic filter, and combination of the two. (B) system transfer functions for the ring-phase illumination-path filter and combinations with the return-path filters.

electronic filter, with both the bar and electronic filter, and the conventional unfiltered system. The contrast at 5MHz improves from H(5)=0.4 in Figure 4.10(a) to H(5)=0.75 with the combination of the three filters. This improvement is almost a factor of two better than the system without the ring-phase filter. It is a factor of seven better than the system without any filtering.

4D.2.B - Transfer function with groovless media

Grooveless media are investigated next. Grooveless media are investigated because they are easier to replicate, but more complicated tracking servos are required. While performing this part of the experiment the focus loop is closed, and the tracking loop is open since the servo used does not track on data.

Figure 4.11(a) shows the system transfer function for the conventional system, the system with electronic filtering only, an 18% x-band return-path optical filter, and the combination of the two techniques. The same trends are observed as for Figure 4.10(a). Figure 4.11(b) shows the system transfer functions for the ring-phase illumination-path filter only, in combination with the return-path optical filter, in combination with the electronic filter, with both the bar and electronic filter, and the conventional unfiltered system. The same trends are observed as for Figure 4.10(b).

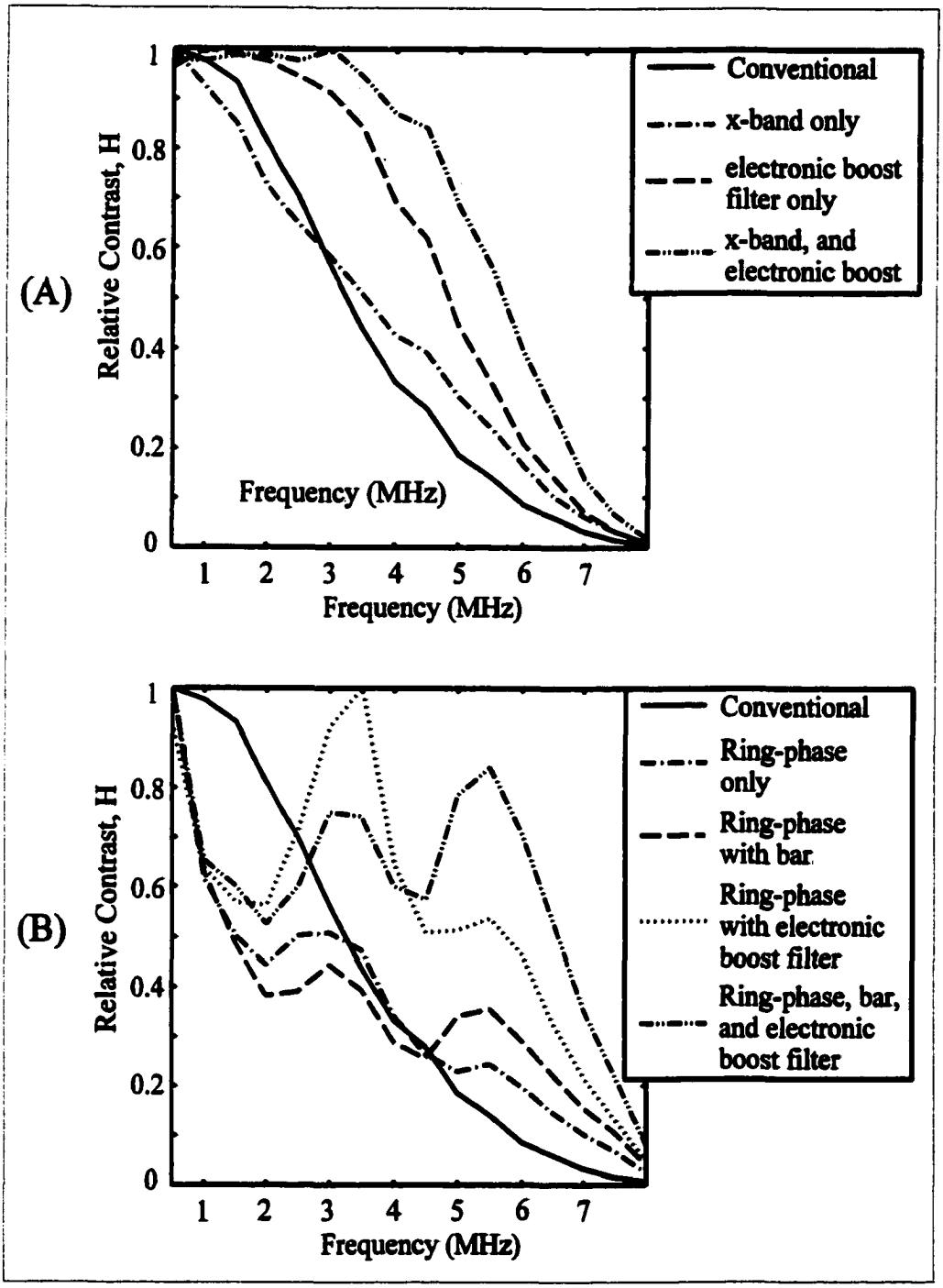

Figure 4.11. System transfer function for grooveless media. (A) system transfer functions for the unfiltered system, return-path optical filter, electronic boost filter, and combination of the two. (B) system transfer functions for the ring-phase illumination-path filter and combinations with the return-path filters.

4D.2.C - Transfer function Summary

The predictions made in Chapter 3 on the influence of the different filtering techniques on the system transfer function are verified experimentally. Both the illumination-path filters and the return-path filters, when used individually, are shown to increase the relative contrast of the high spatial frequencies. The best overall experimental improvement in relative contrast is achieved when the illumination-path and return-path filters are used together.

4D.3 - CNR

CNR is measured for the conventional system, for individual filtering techniques, for combinations of filtering techniques. The transfer function is measured for two different types of media: media with grooves (with tracks) and grooveless media (no tracks).

4D.3.A - CNR with grooved media

In Figure 4.12(a) measured CNR as a function of frequency for the return-path filtering schemes is shown. At frequencies less than 4MHz, the CNR for any of the filtering combinations is 1-4dB less than the CNR of the conventional unfiltered system. However, the reduction is not significant enough to cause unacceptable signal quality. The CNR is comfortably above the 45dB line, which is a rule of thumb for indicating a threshold for reliable recording (Marchant, 1990). For frequencies above 4MHz, the CNR increases by 1-3dB when optical filtering is used alone or in combination with the electronic filter. The electronic filter alone does not increase the CNR, because the

electronic amplification increases the noise as well as the signal.

The increase in CNR when optical filtering is used arises from the way in which the signal and noise are distributed in the pupil of the optical system and from the shape of the return-path optical filter. For frequencies less than 4MHZ, the filter blocks some of signal light and some noise. For frequencies greater than 4MHz, the filter does not block any signal light, but it blocks light in the central portion of the pupil that contributes to noise.

Figure 4.12(b) shows the measured CNR for the ring-phase illumination-path filter along with combinations of the different return-path filters. At frequencies less than 4.5MHz, the CNR for any of the filtering combinations is reduced by up to 7dB when compared to the CNR of the conventional unfiltered system. For frequencies above 4.5MHz the CNR is increased. For example, at 6MHz the unfiltered system has a 33dB CNR. With the use of all three filters the CNR is increased by 7dB to 40dB. This is a relatively large increase in CNR, but still 5dB below the 45dB rule-of-thumb threshold. It is interesting to note that when the illumination path filter is used solo the CNR is increased at frequencies above 5MHz.

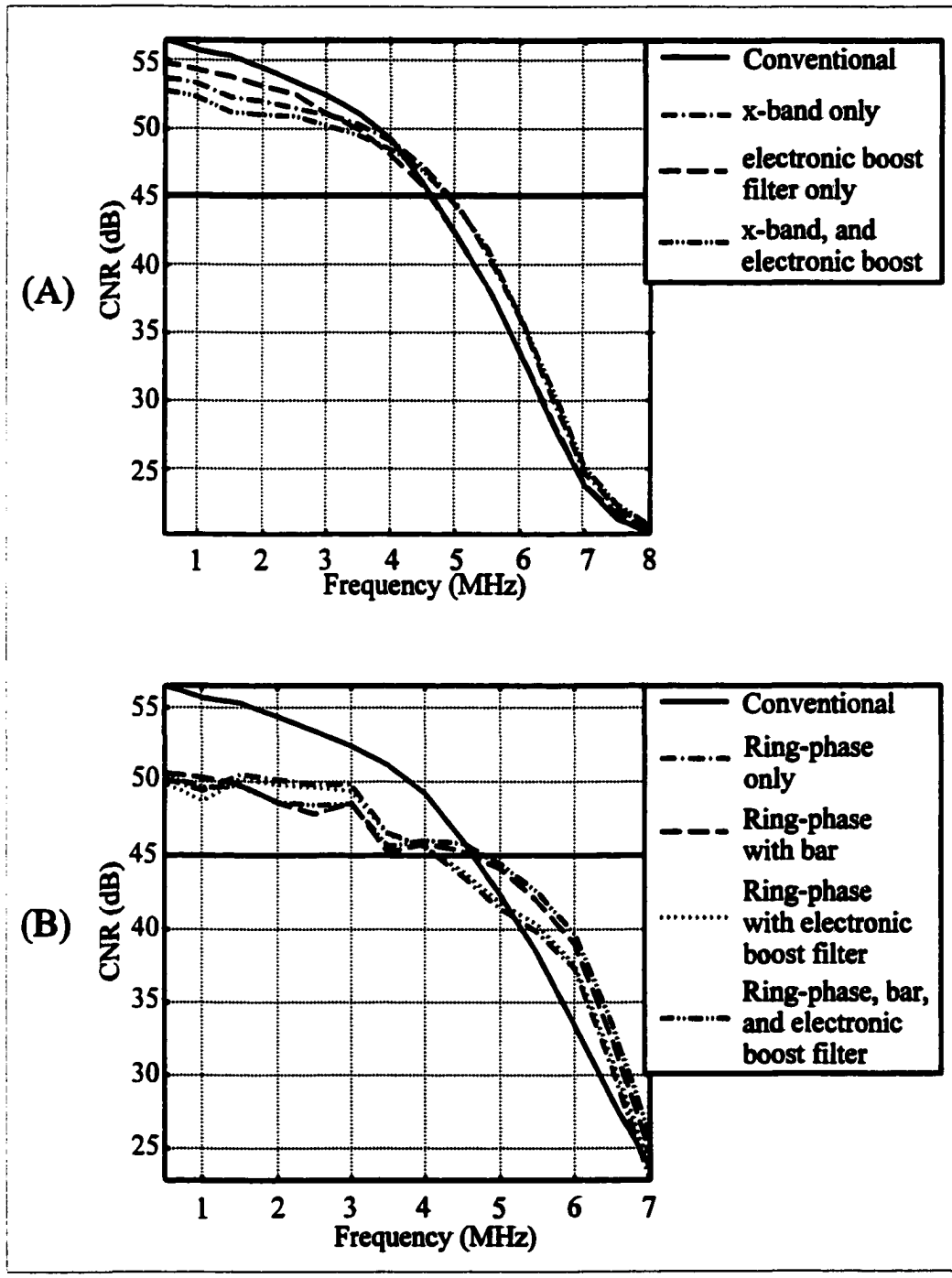

Figure 4.12. Carrier-to-noise ratio(CNR) for grooved media. (A) CNR for the unfiltered system, return-path optical filter, electronic boost filter, and combinations of the two. (B) CNR for the ring-phase illumination-path filter and combinations with the return-path filters.

4D.3.B - CNR with grooveless media

In Figure 4.13(a) measured CNR as a function of frequency for the return-path filtering schemes is shown for the grooveless media. The same trends are observed as for Figure 4.12(a). Figure 4.13(b) shows the measured CNR for the ring-phase illumination-path filter along with combinations with the different return-path filters. The same trends are observed as for Figure 4.12(b).

An increase in CNR is observed when the return-path optical filter is used. Qualitatively the reason is illustrated in the signal and power distributions shown in Figures 4.7 through 4.9. The increase in CNR is observed in the frequency band near NA/λ and above. The same trends are observed on grooveless media and on grooved media when the ring-phase illumination-path filter is used, specifically with respect to the decrease in CNR at low frequencies and the increase in CNR at high frequencies.

4D.3.C - Signal and noise power spectra

Some differences between simulated and measured data are now analyzed with signal and noise power spectra. The spectra are measured from single tone data patterns at 0.5MHz intervals. Measured spectra are analyzed for the unfiltered system and the ring-phase filtered system on grooveless and grooved media. The measured noise spectra for the written data tracks is also analyzed for the two media types.

Figure 4.14(a) shows the signal power and noise power spectra for experiments and simulations of the unfiltered and ring-phase filter source on grooveless media. In the simulation data it is observed that the ring-phase filtered source experiences as much as a

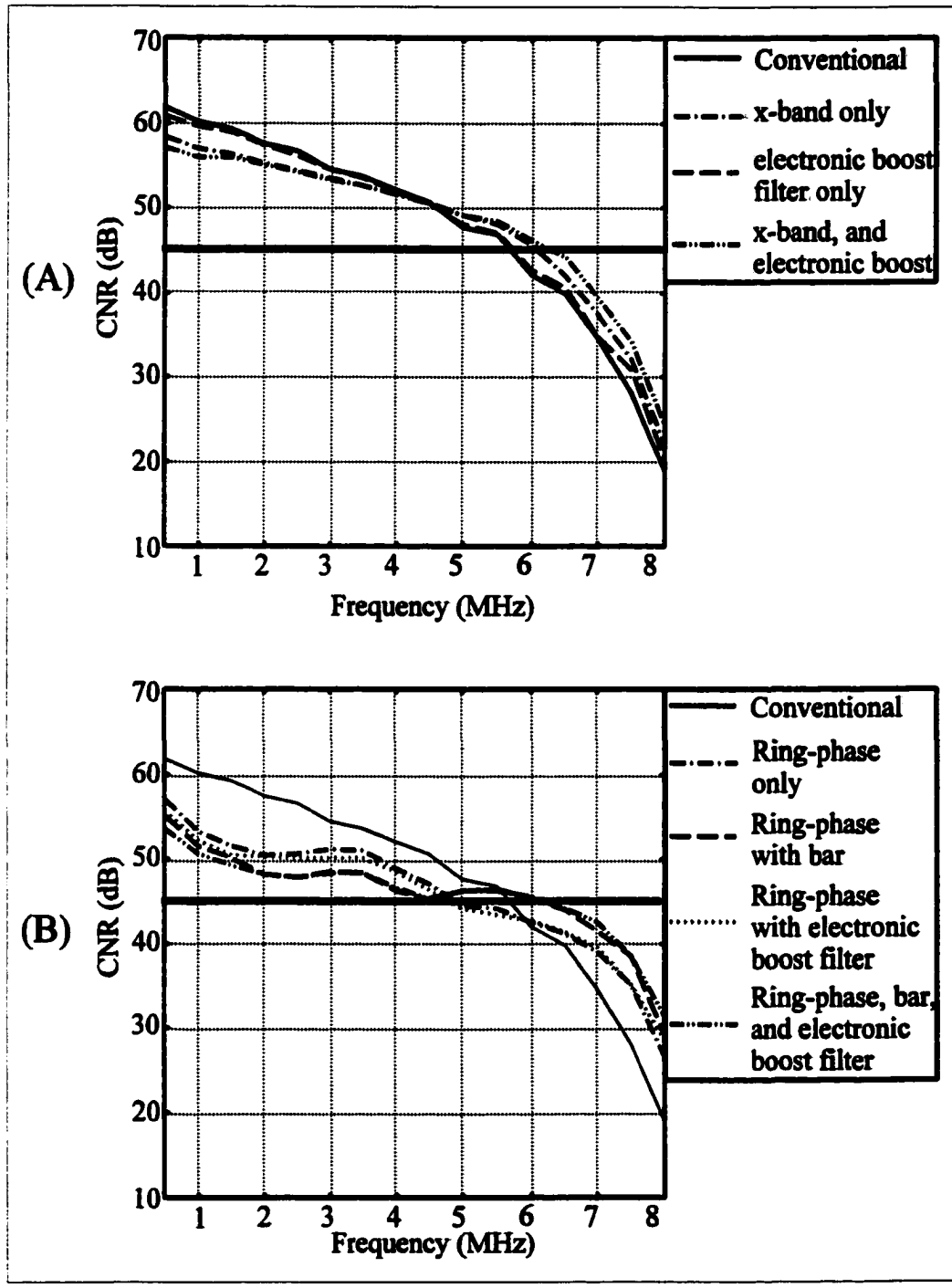

Figure 4.13. Carrier-to-noise ratio(CNR) for grooveless media. (A) CNR for the unfiltered system, return-path optical filter, electronic boost filter, and combination of the two. (B) CNR for the ring-phase illumination-path filter and combinations with the return-path filters.

10 dB loss in power at low frequencies compared to the unfiltered source. At high frequencies near 6MHz they become similar. When the input power level is increased so that the peak irradiance of the ring-phase filtered source is made equal to the peak irradiance of the unfiltered source, there is only a difference of 5dB at low frequencies, and there is more signal power in with the ring-phase filter above 6MHz.

The experimental ring-phase signal power spectra show the same trend as the simulation where there is reduced power at low frequencies and increased power at high frequencies compared to the unfiltered source. The experimental signal power spectra exhibit faster rolloff at high frequencies when compared to the simulation. The faster rolloff of the experimental spectra compared to the simulation can be due to aberrations present in the system (Wang, 1993). The faster rolloff of the experimental spectra compared to the simulation is also due to the difference in numerical aperture between the simulated system,

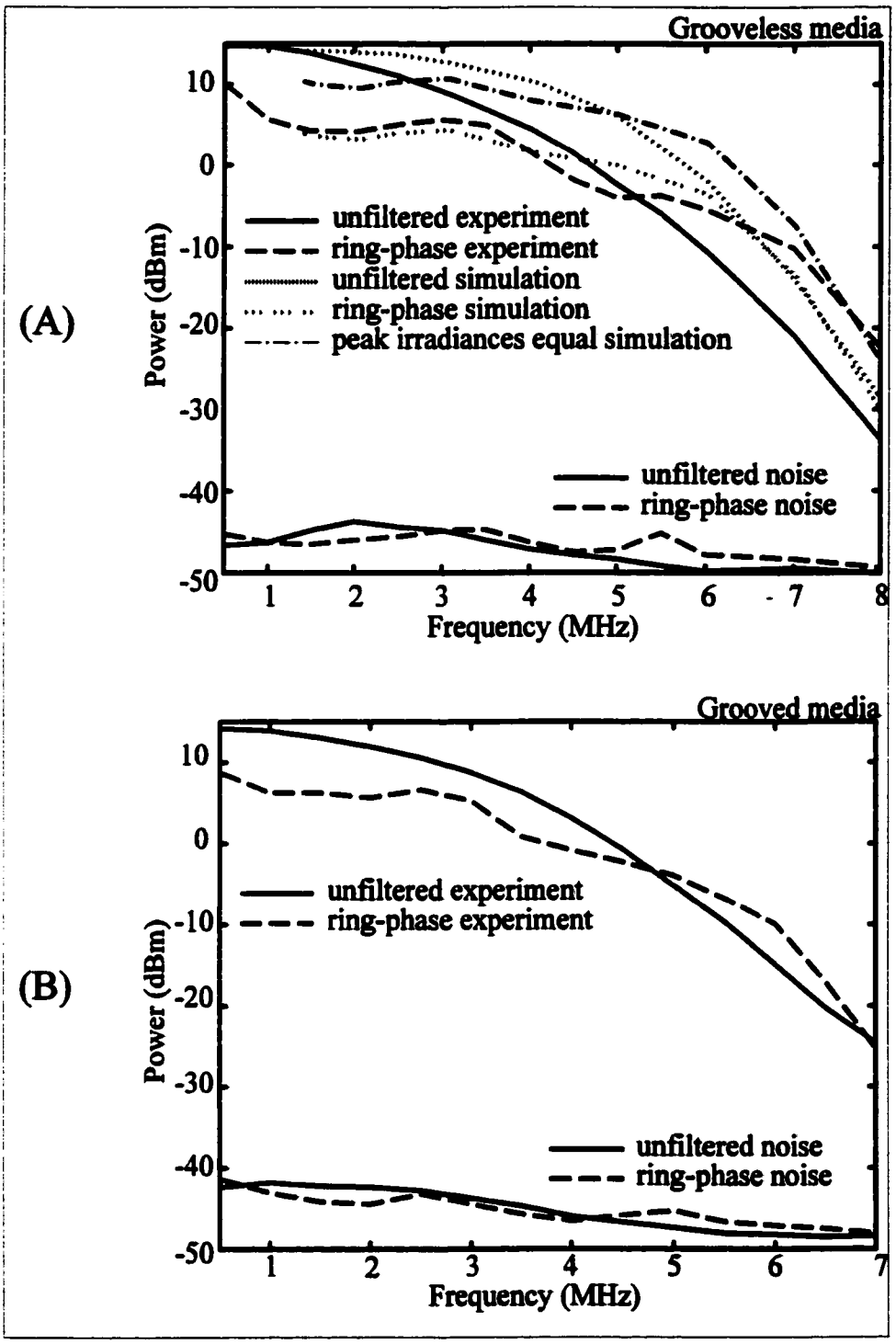

Figure 4.14. Signal and noise power spectra. (A) grooveless media, experimental and simulated signal power spectra and experimental noise power spectra of the written data track. (B) grooved media, experimental signal and noise power spectra of the written data track.

$NA_{simulated}$=0.55, and the experimental system $NA_{experimental}$=0.5.

Figure 4.14(b) shows the signal power and noise power spectra for experiments of the unfiltered and ring-phase filter source on grooved media. The experimental ring-phase signal power spectra show the same trend as observed in Figure 4.14(a), where there is reduced power at low frequencies and increased power at high frequencies for the ring-phase filtered compared to the unfiltered source. Another observation is that the signal power spectra on the grooved media are 1-2dB lower than the signal power spectra on the grooveless media.

Figure 4.14(a)&(b) also show the noise power spectra for the written data track. Comparison of the unfiltered written noise levels on the grooved media, Figure 4.14(b), to the unfiltered erased noise levels of Figure 4.6(a) indicates an increase in the noise floor of about 2dB. This result is due to an imperfect writing process. That is, an additional noise component that depends upon the data is introduced in writing. Writing noise arises from irregularities of the recorded data such as irregular mark shapes and poorly defined magnetic boundary transitions. Another observation is that on both the grooved and grooveless media the ring-phase filter written noise floor is below the unfiltered written noise floor at low frequencies and above the unfiltered written noise floor at high frequencies.

4D.3.D - CNR Summary

Both the illumination-path filters and the return-path filters, when used individually, are shown to increase the CNR of the high spatial frequencies. The best

overall experimental improvement in CNR is also achieved when the illumination-path and return-path filters are used together. The tradeoff for the high frequency improvement is that the illumination-path filters and the return-path filters are shown to decrease the CNR of the low spatial frequencies, with the largest reduction occurring when both filters are used together. A discrepancy between the measured and simulated signal power spectra is observed and is possibly caused by the difference between the numerical aperture of the simulated system $NA_{simulated}$=0.55, and the experimental system $NA_{experimental}$=0.5, and aberrations present in the experimental system. The noise power spectra is observed to increase for a written track of data compared to an erased track indicating a noise component that depends upon the written data.

4D.4 - Two-point response

The two-point response is measured using a long-mark, short-space, short-mark, short-space, long-mark sequence. The same worst-case scenario data pattern is shown in Figure 3.14. The long and short written mark sizes correspond to 1.65μm and 0.67μm, respectively.

Figure 4.15 shows the two-point response waveforms for the return-path filter combinations. Figure 4.15(a) shows the response for the conventional system. Figure 4.15(b) shows the response for the 18% x-band return path filter. Figure 4.15(c) shows the response for the electronic filter. Figure 4.15(d) shows the response for the combination of the two filters. It is clearly seen in Figure 4.15(d) that the best improvement in relative contrast occurs when all the filters are used together.

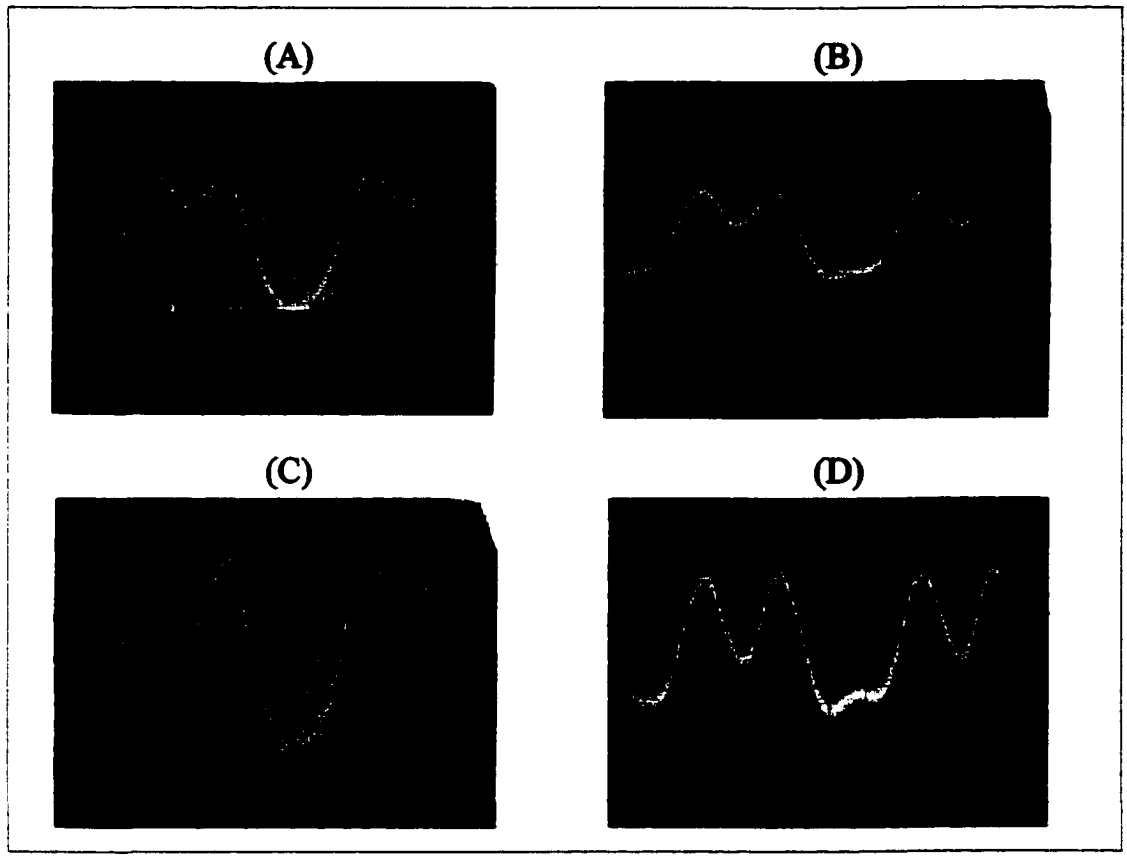

Figure 4.15. System two-point response for a worst-case scenario data pattern with long mark 1.65μm and short mark of 0.67μm. (A) conventional system (no filtering), 22% modulation, (B) return-path optical amplitude filter only, 43% modulation, (C) electronic boost filter only, 44% modulation, (D) combination of the two filters, 60% modulation.

4D.4.A - Two-point summary

The predictions and trends described in Chapter 3 on the influence of the different filtering techniques on the two-point response are verified experimentally. Both the return-path optical and electronic filters, when used individually, are shown to increase the relative contrast of the short mark. The best overall experimental improvement in the high frequency modulation of the signal is achieved when the return-path optical filter is

used with the electronic boost filter.

4D.5 - Jitter

Only the return-path optical amplitude filter and electronic boost filter are used in the jitter study. Jitter is measured using a Hewlett-Packard time interval analyzer(TIA). The TIA is setup to measure the pulsewidths of the data signals. For each pulsewidth the measured value is stored and then the histograms are generated from the data. The standard deviation of the jitter is then measured on the TIA and recorded.

The ability to write a pseudo-random data pattern would be an ideal way to analyze a specific data channel code, but this pattern was unavailable at the time of the experiments. Instead, the serial data generator is used to write a pattern of marks and spaces that correspond to the following four frequencies; 2.5MHz, 3MHz, 3.75MHz, and 5MHz.

Figure 4.16(a)-(d) show histogram outputs of the TIA for the unfiltered system, the return-path optical filter, the electronic boost filter, and the combination of the two filters. A qualitative visual inspection of the histograms shows that for the unfiltered system the histograms are not well separated. They are not well defined. They bleed into one another. The histograms improve with the optical filter, but they are still not well separated. With the electronic filter there is a definite visual improvement in the definition of the histograms. With both filters applied there is a dramatic improvement in the histogram definition compared with the unfiltered system.

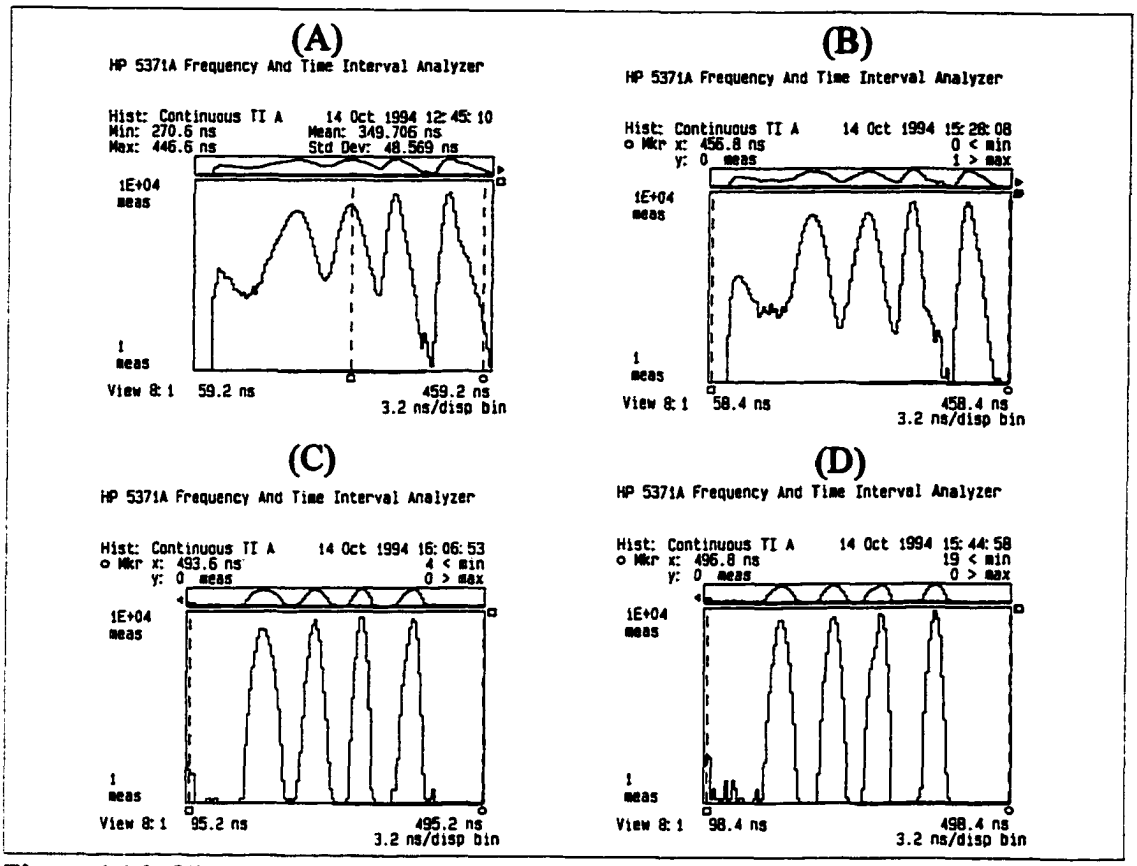

Figure 4.16. Histograms representing the transition location probability distribution associated with the threshold detection process. (A) conventional unfiltered system, (B) return-path optical amplitude filter, (C) electronic boost filter, (D) combination of the two filters in (B) and (C).

Figure 4.17 shows a bar chart of the measured system jitter as a function of frequency for the return-path filtering combinations. With either filtering technique used by itself the jitter σ is reduced from that of the unfiltered system. For instance, at 5MHz the return-path optical filter reduces the jitter σ from 12.1ns to 9.3ns and the electronic boost filter reduces the jitter σ from 12.1ns to 6.6ns. The optical filter is reducing jitter by reducing the noise in the data channel. The electronic filter reduces jitter by increasing the slope of the waveform. The electronic filter also amplifies the noise, but

the effect on the jitter is not as great as the slope increase effect described in Section 4C.2.

When the two filters are combined, the overall jitter is much lower than that of the unfiltered system, as shown by the significant decrease in σ at 5MHz from 12.1ns to 4.1ns. Another interesting feature to note is that the jitter at 2.5MHZ and 3MHz with electronic filtering is less than the combined filter jitter. However, at these frequencies the combined filter jitter is certainly tolerable. This effect can be understood by thinking

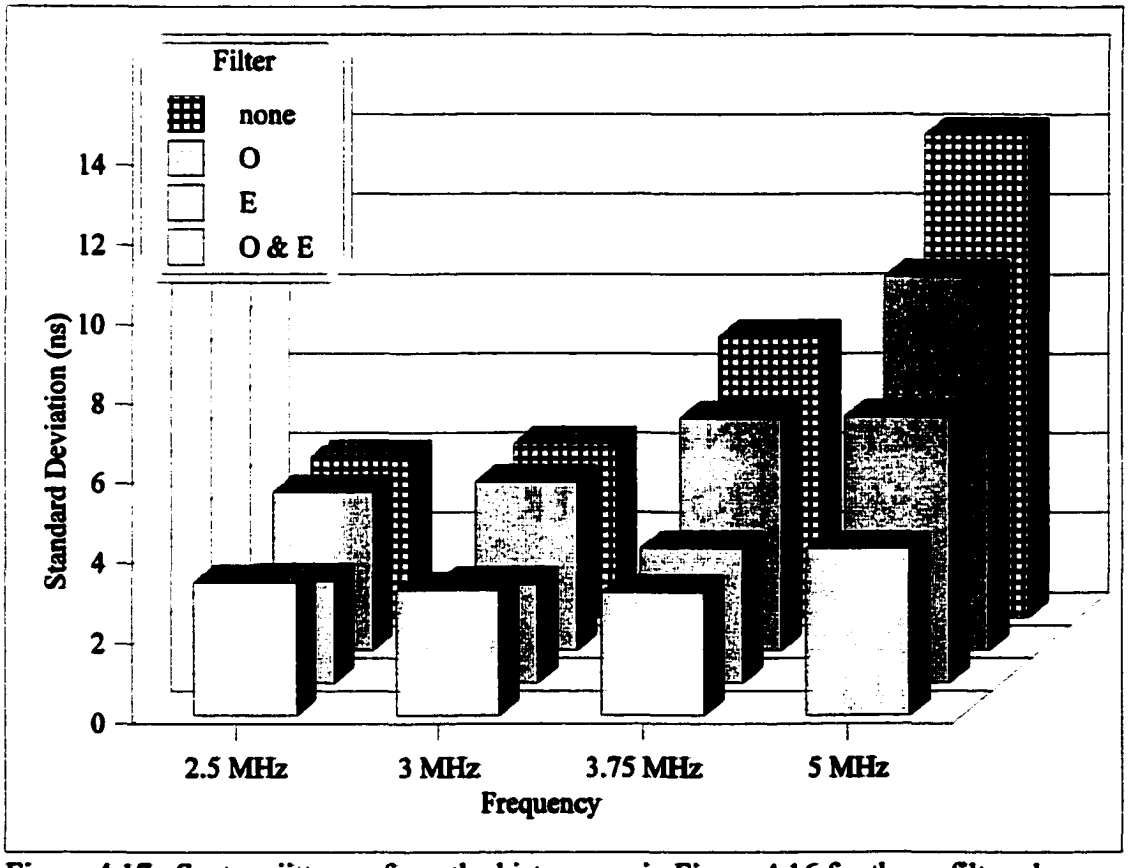

Figure 4.17. System jitter, σ, from the histograms in Figure 4.16 for the unfiltered system (none), return-path optical filter only (O), electronic boost filter only (E), and combination of the two filter (O & E).

about what is happening to the slope of the waveform for each filtering technique. The electronic filter is providing a nonlinear gain as a function of frequency and is increasing the slope of the waveform at every frequency, some more than others. The optical filter is reduces the amplitude of the low frequencies, so when the electronic filter is used together with the optical filter, the resulting amplitude is not as large as when the electronic filter is used alone. This amplitude effect is observed in the experimental two-point scans of Figure 4.15.

4E - Summary/conclusions

The signal and noise distributions are measured in the pupil of a magneto-optic data storage system and provide insight into the system performance. The signal distribution becomes bimodal as the spatial frequency of the data becomes small. This verifies that the data pattern acts like a collection of gratings. The noise distributions are observed to be a function of position in the pupil, as well as a function of temporal frequency when the disk is spinning. The spatial variation of the media noise is observed and shown to spread out in the pupil with increasing temporal frequency.

The pupil distributions of the signal and noise are shown to be significantly different. This leads to the design of return-path filters that not only partially equalize the system transfer function by reducing the low frequency amplitude, but also improve the CNR at high frequencies. The noise component in the CNR measurement is a narrow-band measurement within a 30kHz bandwidth. The SNR calculation based on an integrated noise component follows a similar pattern because the noise power is reduced

over the entire frequency range (Milster, 1996). In fact, the SNR is improved by as much as 7dB for certain frequency ranges.

The return-path optical filter can be applied to low contrast scanning optical microscopes in the following way: The highest increase in SNR will be observed when the object exhibits low contrast in a spatial frequency band near NA/λ and above. The return-path filters discussed so far are appropriate for a SNR increase in the direction of the scan. For many applications this is a significant improvement. In the direction perpendicular to the scan the filters will not produce the same increase in SNR. For two dimensional scanning the shape of the return-path filter should be modified to an opaque circle in the center of the pupil.

The measured CNR is shown to improve at high frequencies with the return-path optical filter and the ring-phase illumination-path filter. The ring-phase filter boosted CNR by as much as 5dB when used individually. The return-path optical filter boosted CNR by as much as 3dB when used individually. The largest increase in CNR, up to 8dB at high frequency, is observed when these two are used simultaneously. At low frequencies both filters are observed to reduce the CNR. The ring-phase filter is shown to decrease the CNR by as much as 7dB while the return-path filter decreased the CNR by 4dB at low frequencies.

Experiments confirm the simulations of Chapter 3 where significant improvement in system transfer function contrast at high frequencies is attained by application of optical and electronic filters described in Section 4A. Contrast improves when either of

the filtering techniques are used individually, but the largest increase in contrast arises when the filters are used simultaneously.

The two-point response of the system is examined for the return-path optical filter and the electronic boost filter. The experiment agrees with the simulation that shows the relative contrast of the short mark improving when either technique is used individually and the largest increase occurring when the filter are used simultaneously.

The system jitter for the return-path optical filter and the electronic boost filter is examined. The experiment shows reduced jitter when either filter is used by itself. The largest reduction occurs when the filters are used simultaneously.

The filtering techniques investigated are shown to perform best at high frequencies when used together. They are also shown to degrade performance at the low frequencies. The tradeoff is improved high frequency performance at the expense of low frequency performance. Just how much low frequency degradation is tolerable should be identified for a given system in order to justify the high frequency improvement.

CHAPTER 5 - A SINGLE MODE HIGH-POWER VERTICAL CAVITY SURFACE EMITTING LASER

Rather than using an amplitude filter in the illumination-path to narrow the central core of the focused spot, a high performance Vertical Cavity Surface Emitting Laser (VCSEL) may be used (Milster, 1998). The new VCSEL, developed by Motorola, has the property of emitting in a very high spatial mode and basically looks like a ring. The VCSEL spatial mode structure is very different from the traditional low order TE_{00} mode of edge emitting laser diodes. Thus, this VCSEL can be thought of as an amplitude filtered source that has the advantage of no additional superresolving components added to the system.

Traditionally, VCSELs have not been a design choice for applications that require a spatially and temporally stable high-power laser diode. There are stable single-mode VCSELs available, but they are low-power <2mW. The high-power VCSELS that are available, ~300mW, are multi spatial and temporal mode, and the spatial mode structure changes with injection current. This new VCSEL produces a single stable radial Hermite-Gaussian high-power mode (Milster, 1998).

There are some advantages and disadvantages of using this source in a data storage system. Some of the advantages are a low threshold current, manufacturability of two-dimensional arrays, and a circular output beam. The low threshold current is desirable because of low power consumption. The ability to produce two-dimensional arrays adds to the possibility of multiple-beam recording. The circular output beam

eliminates the anamorphic prism pair required for circularization of the traditional edge emitting laser diodes. The main disadvantage is the multi-mode spatial distribution of this device that requires the use of a phase mask if the laser is to be used in point focus applications such as data storage or scanning optical microscopes.

Section 5A introduces the properties of the new VCSEL. A description of VCSEL structure is presented. Output power characteristics under pulsed and CW operation are studied. The output irradiance distribution is also presented.

In Section 5B the stability of the output mode is investigated as a function of injection current. The mode measurement system is described and results presented.

In Section 5C a theoretical description of the preferred lasing mode in a center etched VCSEL is presented from the work of Darek Burak and Rolf Binder. The dependence of the preferred lasing mode on the radius of the center etched well is shown.

In Section 5D the measurement and modification of the optical properties of the VCSEL is presented. The phase relation between the adjacent lobes of this lasing mode are simulated and verified experimentally. A phase mask for the VCSEL is proposed for point focus applications.

In Section 5E the use of the VCSEL in a data storage system is discussed. Issues relating to the location of the phase mask in the system are discussed. An intermediate optical system, based on axicons to modify the obscuration ratio of the VCSEL, is described.

5A - Introduction of VCSEL

Various approaches have been attempted to increase the single mode output power of VCSELs (Oh, 1997) (Michalzik, 1997) (Wu, 1993). These approaches have the common characteristic of trying to increase the output power in the fundamental mode. Increasing the VCSEL size to increase the output power results in multi-mode operation, and therefore the predominant limitation on single mode output power has been the limitation imposed by the small size of the device. Increasing the size of the VCSEL reduces the difference in threshold gain for each mode which leads to the multimode operation that is observed in 'larger' (>25μm) VCSEL devices as the current is increased above threshold (Kuchta, 1994).

The device reviewed here describes a change in the structure of the VCSEL that leads to single high-order mode operation. Motorola introduced a structural element into a VCSEL resulting in the device operating in single stable high-order mode (Milster, 1998). The VCSEL structure has a relatively large diameter and produces significant optical power (Claisse, 1997).

5A.1 - VCSEL fabrication Motorola etched a small well in the top mirror of the VCSEL to achieve a single high-order mode lasing. The well has a smaller diameter than the emitting area, so an effective circular loss region is created in the center of the cavity. The loss region produces higher differential loss for low-order modes, so only high-order modes are above lasing threshold.

The results from a 55μm diameter device, $\lambda = 772$nm, are discussed in this section. To fabricate this VCSEL, Motorola first grew epitaxial material on an n+GaAs

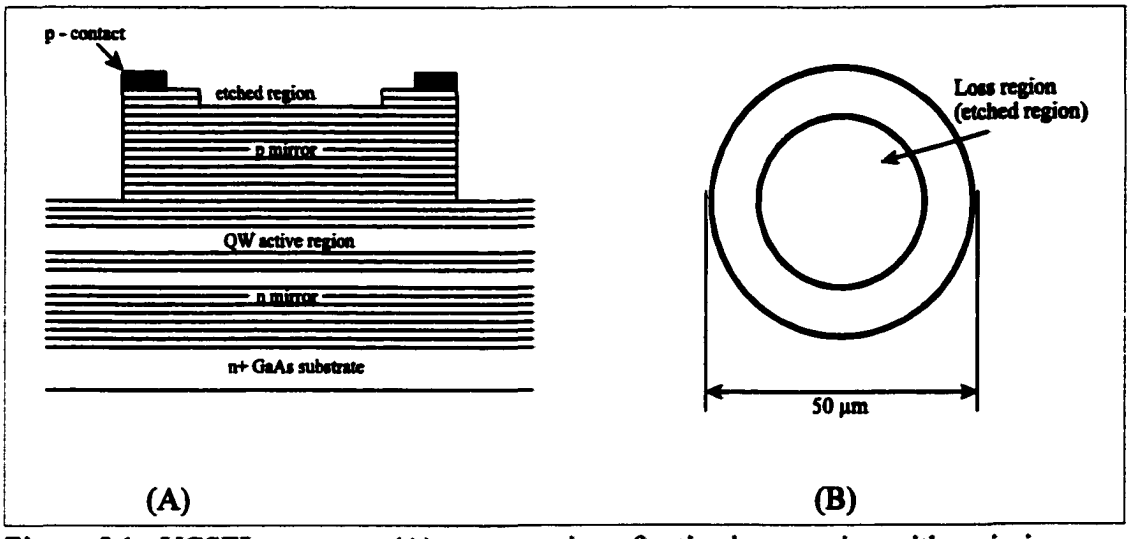

Figure 5.1. VCSEL structure, (A) cross-section of active layer region with emission aperture etched, (B) top view of the laser facet. Etched region reduces the p-mirror reflectivity.

substrate that consisted of 40 $Al_{0.95}GaAs/Al_{0.95}GaAs$ λ/2 n-doped mirrors, a four-quantum-well active region of 100Å $Al_{0.1}GaAs$ wells and 100Å $Al_{0.4}GaAs$ barriers and 25 $Al_{0.95}GaAs/Al_{0.95}GaAs$ λ/2 p-doped mirrors. Then ridge waveguide VCSELs were fabricated using the process detailed by Jiang (Jiang, 1997). Next, a circular region is etched within the emission aperture of the diode, as illustrated in Figure 5.1(a). This reduces the p-mirror reflectivity. Figure 5.1(a) shows a cross section side view of the VCSEL. Figure 5.1(b) shows a top view of the VCSEL. Devices of varying ridge, aperture and etch diameter were fabricated and tested. Results for a 55μm ridge diameter device, with 49μm aperture and center etch region of 30μm diameter is presented in this section.

5A.2 - VCSEL output characteristics

Although significant output power is achieved under pulsed operation, > 40mW at

80 mA injection current, the cw output power is limited by heating in the device to a maximum of 8mW at 40mA. The threshold current density is 630A/cm^2 pulsed operation, and 715A/cm^2 cw. The slope efficiency is 0.5mW/mA pulsed and 0.3mW/mA cw. Figure 5.2 shows the PI curve for a typical device under pulsed and cw operation.

Figure 5.3 shows a CCD image of the VCSEL output. This image remains stable

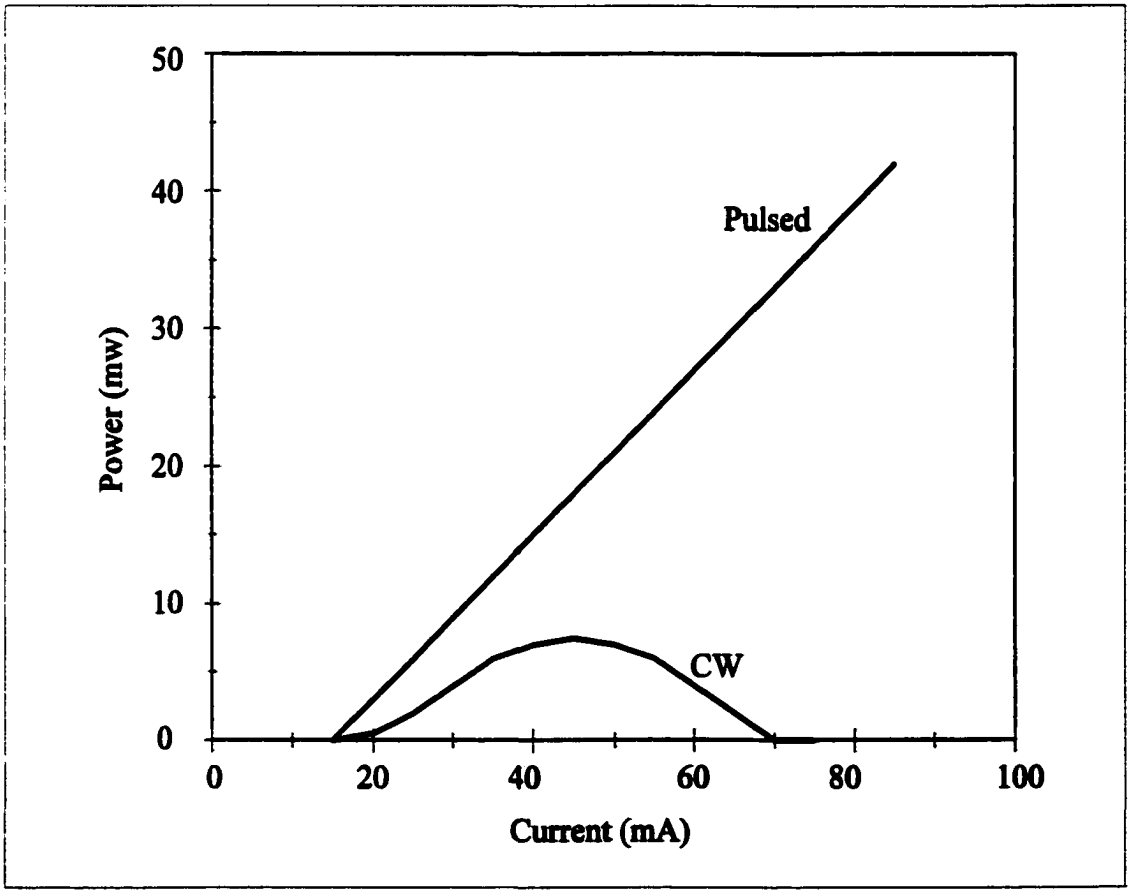

Figure 5.2. VCSEL output power as a function of injection current under pulsed and CW operation.

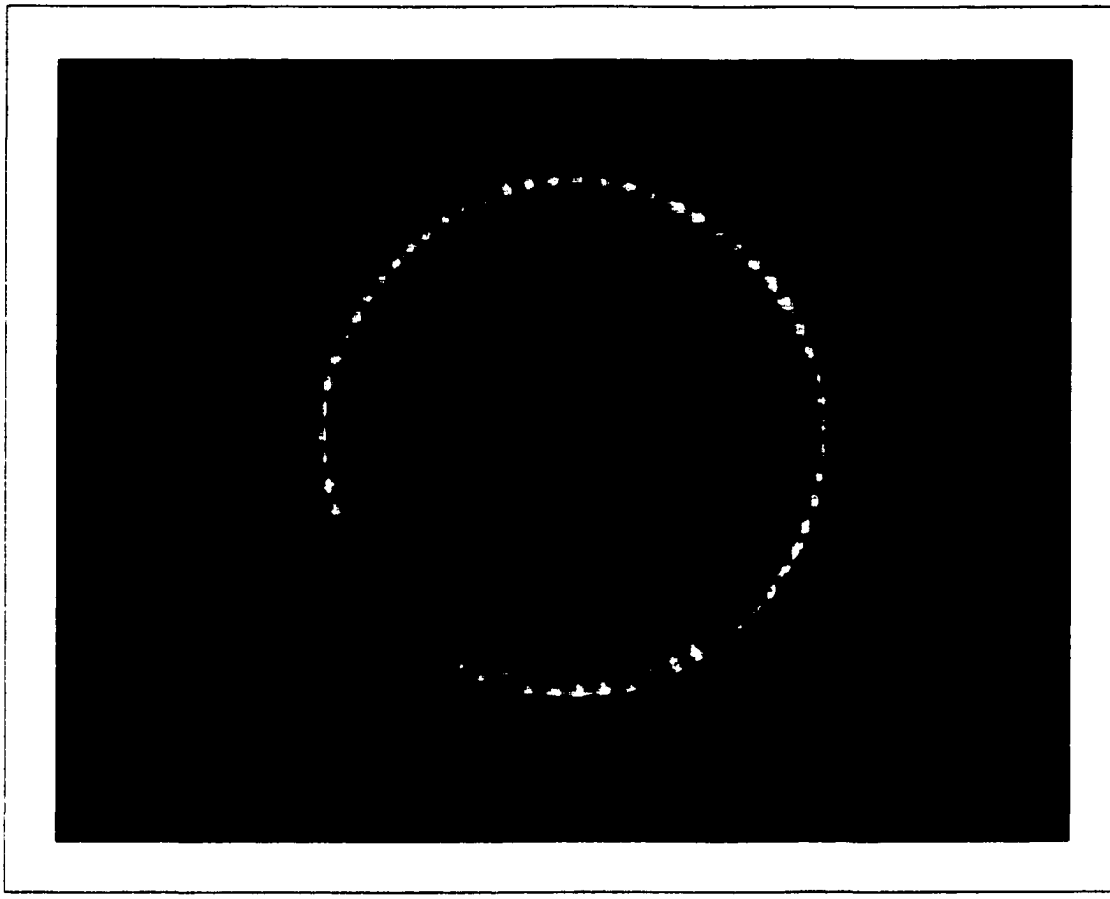

Figure 5.3. CCD image of 55μm VCSEL with etched aperture. The lobes that make up this distribution are clearly seen in this image.

under both pulsed and cw operation. The azimuthal and radial structure of the ring mode is stable versus injection current. The results were found to be repeatable after aging the diode several months.

5B - Mode stability

The temporal mode behavior of the VCSEL as a function of position on the emitting facet and injection current are studied. The stability of the mode structure is investigated as a function of injection current.

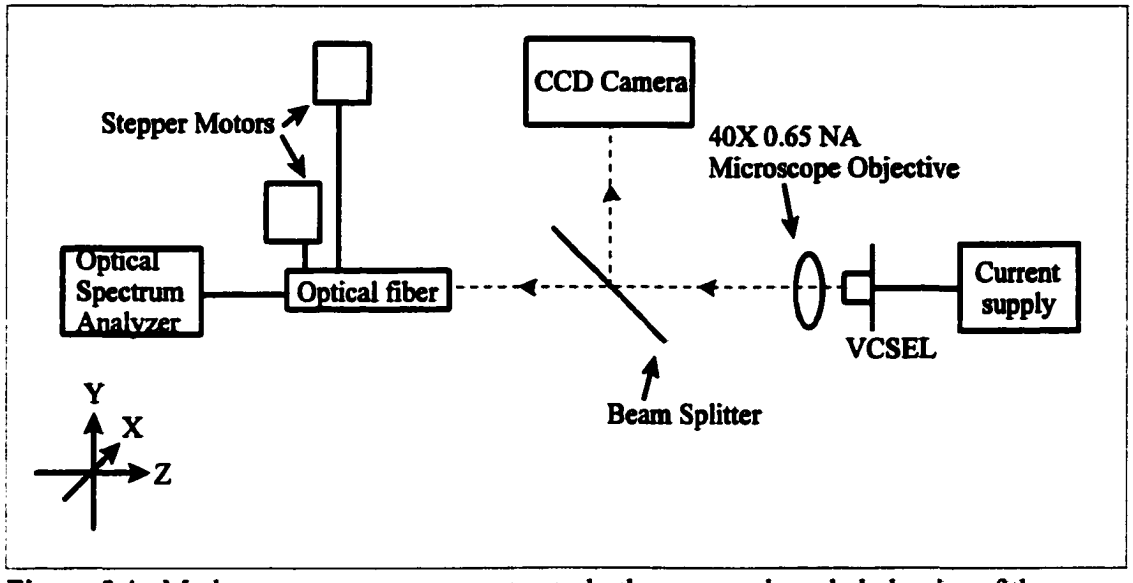

Figure 5.4. Mode measurement system to study the temporal mode behavior of the VCSEL as a function of position on the emitting facet and injection current.

An experimental system that is used to study the VCSEL mode structure is shown in Figure 5.4. The mode measurement system consists of a VCSEL, a current supply, a microscope objective, an optical fiber whose position is controlled by stepper motors, and a Hewlett-Packard Optical Spectrum Analyzer, as shown in Figure 5.4. The 40X microscope objective images the 50μm laser facet to a 2mm image at the scan plane. The current supply, stepper motors, and spectrum analyzer are controlled using LabView through a computer interface. The optical fiber is connected to the spectrum analyzer and scans the 2mm image, providing information on how the modes are distributed across the facet. Figure 5.5 shows how the temporal modes behave spatially across the emitting facet for injection currents of 17mA and 39mA. The dominant modes are distributed around the outside edge of the facet and are spatially and temporally stable. No significant changes are observed in the mode structure as current is increased, as observed

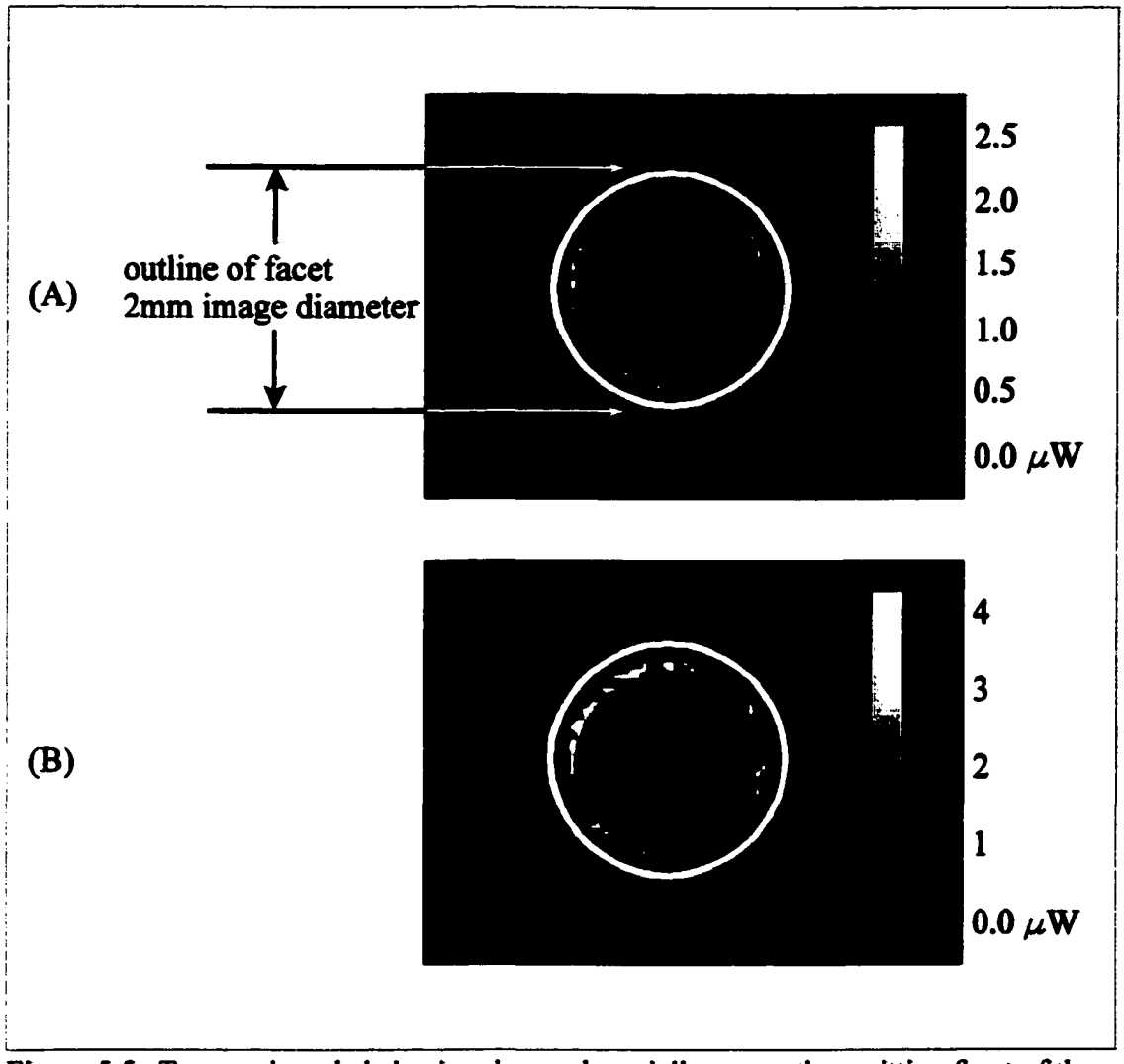

Figure 5.5. Temporal mode behavior observed spatially across the emitting facet of the VCSEL for (A) a current of 17mA, wavelength λ=771.7nm and (B) a current of 39mA and wavelength λ=771.8nm. There is no change in mode structure as current increases, but there is a small wavelength increase that corresponds to red shifting that is commonly observed in laser diodes.

in the mode distributions shown in Figure 5.5. A 0.1nm shift in wavelength is observed as the current increases. This wavelength increase corresponds to red shifting due to thermal heating that is commonly observed in laser diodes. The mode structure is observed around 771.7nm. Spectrum analyzer traces in surrounding wavelength regions

do not indicate any other lasing modes in the spectrum, and the optical power in the surrounding regions is insignificant compared to the lasing mode.

5C - Theoretical description of preferred lasing mode in center etched VCSEL

The following description is an outline of the theory presented by Burak and Binder (Burak and Binder, 1998). A simple theory, based on modal loss discrimination mechanism in VCSELs with slightly perturbed mirrors, is used to explain the preferred lasing mode in VCSEL structures using a central etched well. In is shown theoretically that selective etching of DBR mirrors in VCSEL structures can indeed lead to single mode lasing (Burak and Binder, 1998). It is assumed that the loss of the cavity with an etched well is described by an effective cavity loss, which combines the cavity losses of two simple radially uniform cavities. The effective cavity loss for a given hybrid mode $HE^{(M,L)}$ is calculated as

$$\gamma_{eff}^{(M,L)} = \frac{\int_A dA\ \gamma(r)\ Re[\boldsymbol{E}^{(M,L)} \times \boldsymbol{H}^{(M,L)*}] \cdot \hat{z}}{\int_A dA\ Re[\boldsymbol{E}^{(M,L)} \times \boldsymbol{H}^{(M,L)*}] \cdot \hat{z}} \quad , \quad (5\text{-}1)$$

where A is the transverse cross-section of the device, and $\mathbf{E}^{(M,L)}$ and $\mathbf{H}^{(M,L)}$ are electric and magnetic field vectors, respectively evaluated in the center of the active region, and M and L are the azimuthal and radial mode orders, respectively. The r-dependent cavity loss $\gamma(r)$ is defined as a step function

$$\gamma(r) = \begin{cases} \gamma_{N1}, & \text{for } r \le R_W \\ \gamma_{N2}, & \text{for } r \ge R_W \end{cases} \quad , \quad (5\text{-}2)$$

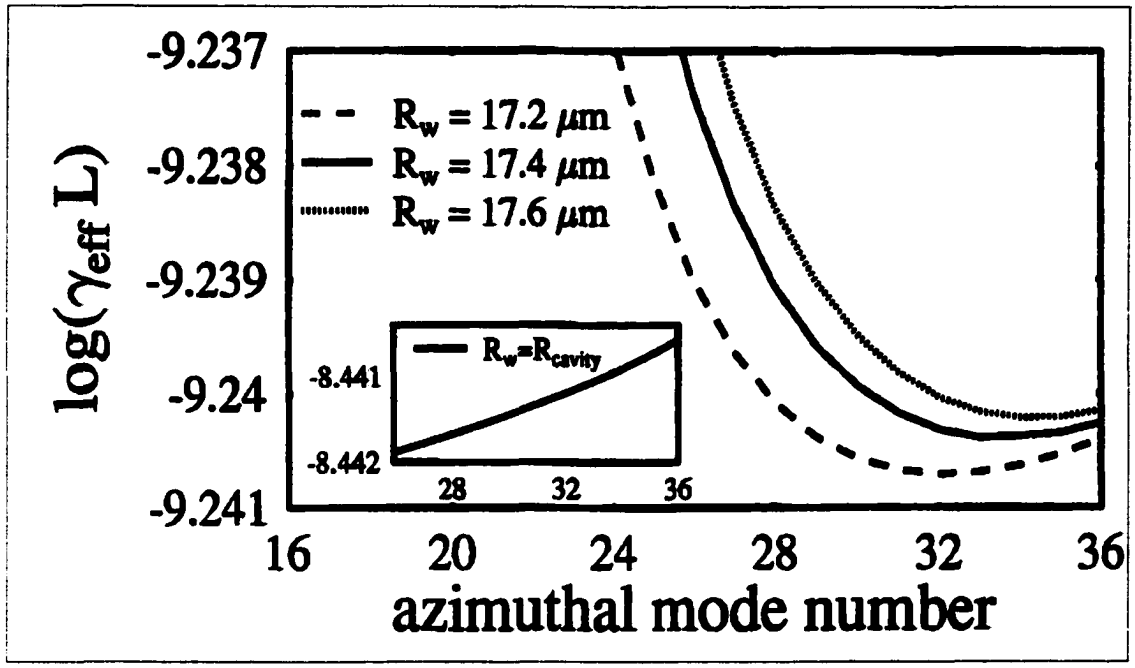

Figure 5.6. Dimensionless cavity loss γ_{eff} as a function of mode order for inner radii values : R_w 17.2μm, R_w=17.4μm, R_w=17.6μm. Inset: Normal ordering of cavity loss values calculated for a cavity without the center etched well on the top mirror.

where γ_{N1} [γ_{N2}]is the loss of the corresponding uniform cavity with the number of pairs in the top mirror given by $N_1 = 25$ [$N_2 = 28$], and R_w denotes a radius of the etched well. Note that in Eq. (5-1) the quantity $\gamma_{eff}^{(M,L)}$ is an averaged cavity loss with the weighting factor given by an amount of power optically confined in a part of a cavity characterized by loss $\gamma(r)$.

The cavity loss γ for each radially uniform cavity is calculated separately. This approach allows the calculation of the full 3D vectorial eigenmode profiles together with cavity losses and resonant wavelengths (Burak, 1997).

The experimental result in Figure 5.3 indicates that for the cavity configuration under consideration, only the $HE^{(31,1)}$ mode is lasing. A ring structure with $M_L = 64$

multiple lobes corresponding to $M=M_L/2 - 1 = 31$ lasing hybrid mode is observed.

The calculations assume that the effective diameter of the cavity is equal to the aperture diameter. In Figure 5.6 the results of cavity loss calculations for three different inner radii of a three-layer-pair-deep etched well are shown. Without the etched well, the cavity loss is shown to increase as the eigenmode number increases. That is, $\gamma^{M-2} < \gamma^{M-1} < \gamma^{M}$, where M is the azimuthal mode number, (see inset in Figure 5.6). With the etched well, reversal of the cavity loss values occurs, that is $...>\gamma^{M-2} > \gamma^{M-1} > \gamma^{M}$.....as shown in Figure 5.6. However, for modes of higher order than *m*, normal ordering of cavity losses is observed, that is $\gamma^{M} < \gamma^{M+1} <$ ..... Thus, the hybrid mode $HE^{(M,1)}$ has the lowest cavity loss and has the highest probability of lasing. This is clearly seen in Figure 5.6, where for the radius of the well $R_W = 17.4\mu m$ the hybrid mode $HE^{(31,1)}$ has a lowest cavity loss. It is shown that by changing R_W one can indeed select the lasing mode. Thus, for $R_W = 17.2\mu m$ and $R_W = 17.6\mu m$ the smallest cavity loss is for $HE^{(30,1)}$ and $HE^{(32,1)}$ modes, respectively.

5D - Measurement and modification of the optical properties

Optical properties of the mode structure and how to convert the higher-order mode into a distribution that can be focused to a point are investigated. Experimental results are compared with simulations. Simulations are performed with Optiscan (Milster, 1997). Optical properties of the mode produced by this new type of high-power VCSEL are determined by verifying the phase relation between the adjacent lobes and determining focused spot properties. The sensitivities of the focused spot to phase errors

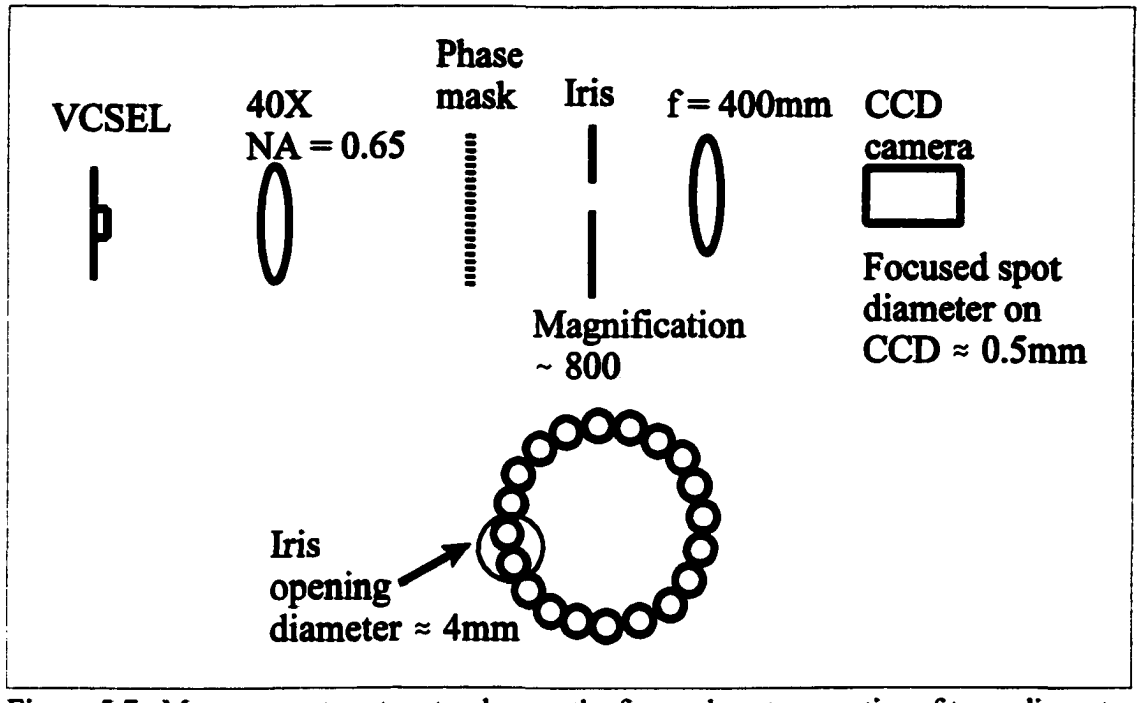

Figure 5.7. Measurement system to observe the focused spot properties of two adjacent lobes, of Figure 5.3, when they are in phase and out of phase.

in the phase mask is simulated. The focused spot sensitivities to amplitude variations are also studied.

5D.1 - Focused spot properties of two adjacent lobes

According to theory, each adjacent lobe of this higher order radial Hermite-Gaussian mode is 180° out of phase with the adjacent lobe. One aspect of the experiment is to investigate two adjacent lobes and verify that they are 180° out of phase. This is done by investigating focused spot properties of two adjacent lobes in a simple optical system when the two lobes are in phase and when they are out of phase. A mask is constructed to bring the two lobes in phase. The phase mask is a simple step etched to a depth of 0.839μm using an ion mill. The depth of the phase mask is toleranced by

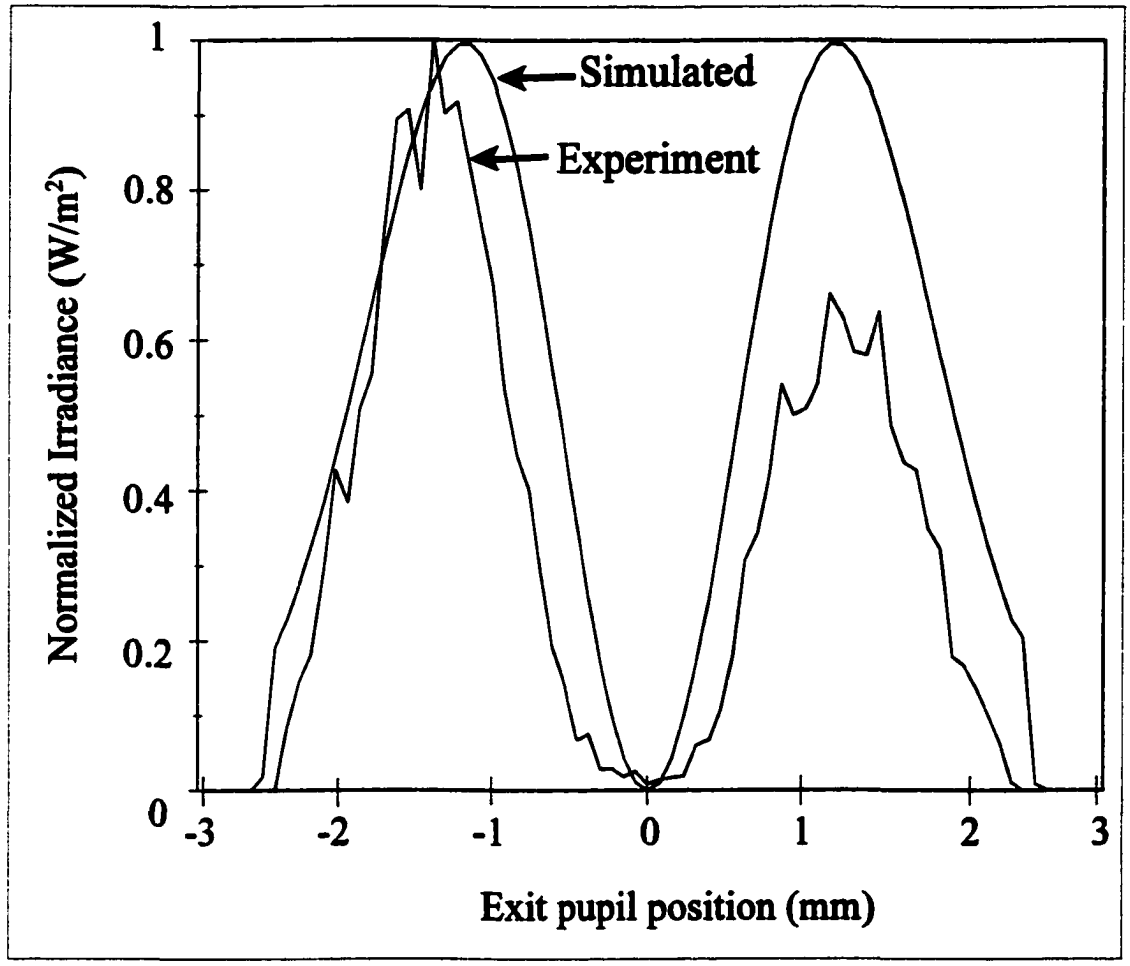

Figure 5.8. Profiles of the simulated Hermite-Gaussian TE_{10} distribution and the measured two lobes.

observing the focused spot properties in a simulation. The phase mask used in the experiment is measured and found to have a depth of 0.86μm, which is only in error by 2.5% compared to the desired depth of 0.84μm.

First, the source is imaged to a plane with a magnification of 800 so that the outer diameter of the ring is 4cm, and two adjacent lobes are 4mm across as shown in Figure 5.7. By using an iris, two adjacent lobes are selected to fill the entrance pupil of a lens. The phase mask and a lens are placed next to the iris. Then, properties of the focused

spot are observed on a CCD camera.

The Optiscan simulation consists of the source, phase mask, lens, and observation plane. The first source is a 2-lobe, Hermite-Gaussian TE_{10} distribution. An experimentally measured source distribution is also used in the simulation that is obtained using the CCD camera. Profiles of the experimental and simulated source distribution are shown in Figure 5.8. The phase mask changes the phase of one lobe by 180° relative to

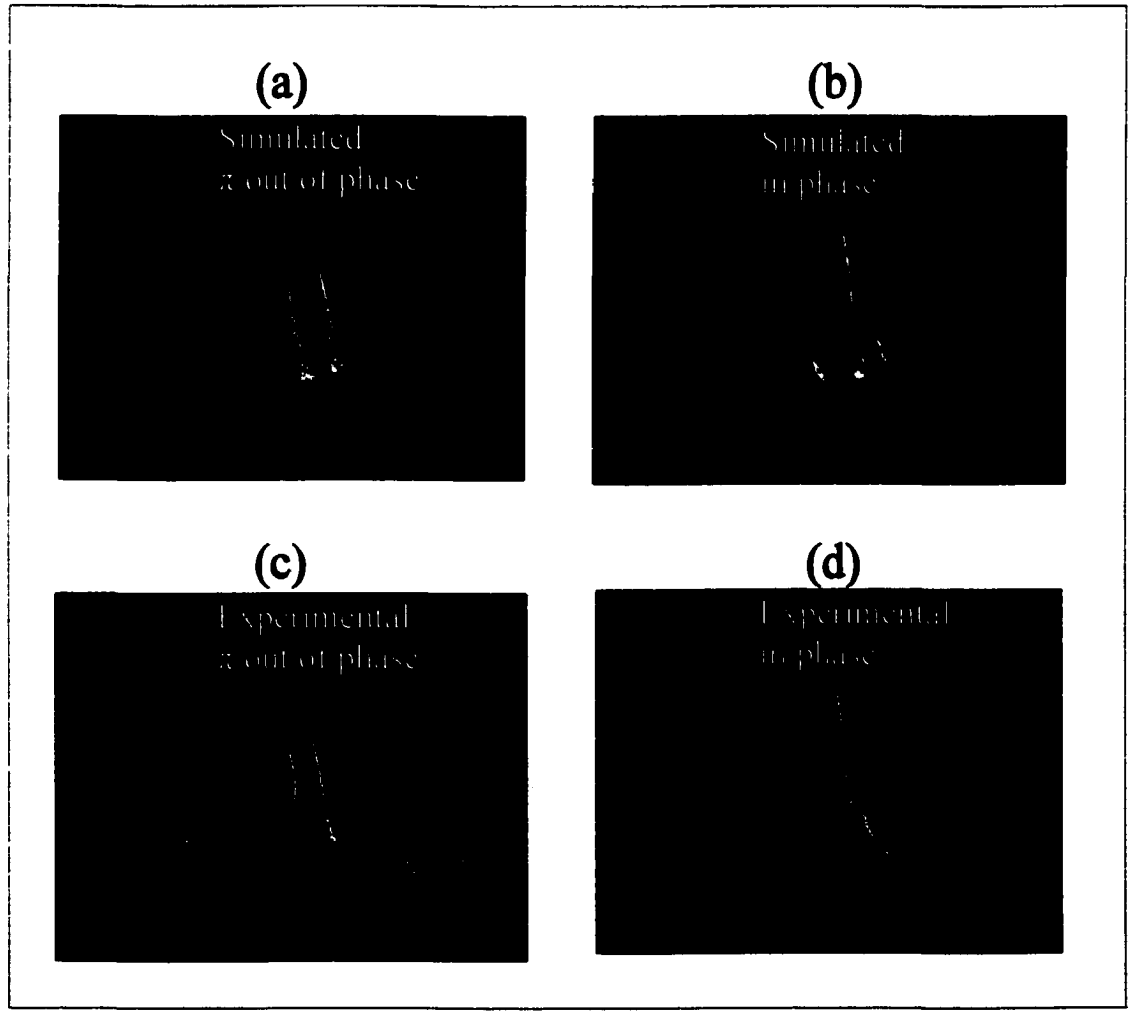

Figure 5.9. Focused spot distributions for 2 lobe pupil distribution, with the 2 lobes in phase and out of phase. Simulated results (a) and (b), experimental results (c) and (d).

the adjacent lobe. The lens is a Zeemax paraxial lens with a focal length of 3.89mm, entrance and exit pupil diameters of 5mm, and a numerical aperture of 0.55. The observation plane is the back focal plane of the lens.

Figure 5.9 shows the experimental and simulated Hermite-Gaussian TE_{10} focused spot distributions for the two-lobe pupil distribution when $\varphi = 180°$ and when $\varphi = 0°$. The simulated distributions show that the focused spot has a two-lobe distribution when $\varphi = 180°$, Figure 5.9(a), and becomes a strong central lobe with small side lobes when $\varphi = 0°$, Figure 5.9(b). The experimental distributions closely follow the simulation results, as shown in Figure 5.9(c)&(d). Both the experiment and the simulation show that the on-axis peak irradiance is higher when $\varphi = 0°$ than when $\varphi = 180°$. These results follow from the central ordinate theorem of Fourier optics (Gaskill, 1978).

The experimental in-phase focused spot distribution has slightly larger side lobes than is predicted by the simulation with the Hermite-Gaussian TE_{10}. Using the ratio of the peak side lobe irradiance to the on-axis peak irradiance of the focused spot as a figure of merit, a ratio of 0.25 is observed experimentally, and a ratio of 0.16 is observed for the simulated Hermite-Gaussian TE_{10} source. To resolve this difference, the experimental two-lobe source distribution is used as input into the simulation, which results in a calculated ratio of 0.28 that agrees very well with experimental results. This result implies that the experimental two-lobe source is not exactly a Hermite-Gaussian TE_{10} distribution, but more closely follows a cosine distribution (Burak, 1998).

5D.2 - focused spot sensitivities to amplitude and phase variations

From Figure 5.3 it is observed that every adjacent lobe does not have exactly the same irradiance value. In order to see if this has an effect on the focused spot, the Hermite-Gaussian TE_{10} source with unequal amplitudes in the two lobes when $\varphi = 0°$ is simulated. The focused spot is observed to be very insensitive to amplitude differences. An amplitude difference of 30% has the effect of changing the peak side-lobe ratio described in section 5D.1A by only 1.5%. The observation in Figure 5.9(c) can be explained by the fact that each lobe that makes up this VCSEL distribution is slightly

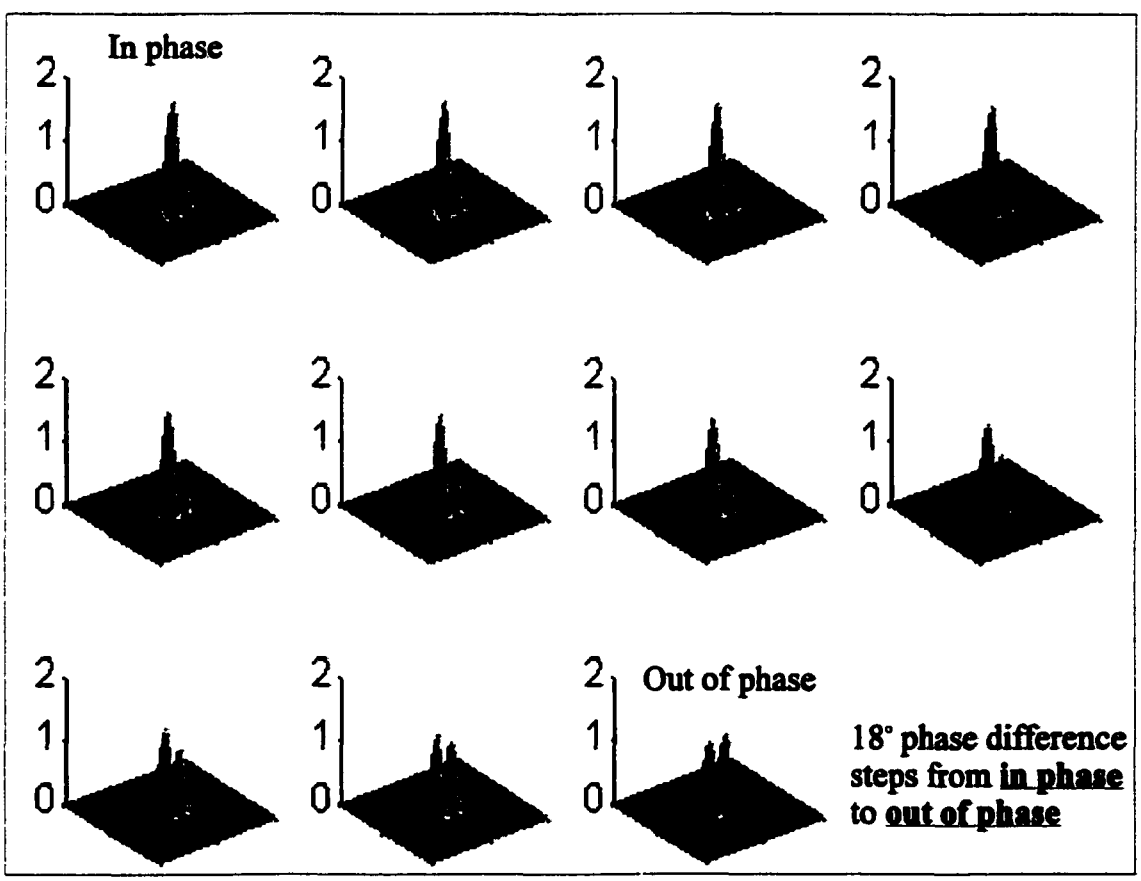

Figure 5.10. Focused spot distribution for different phase differences between the two lobes in the pupil of the objective lens. Starting out in the upper left with the two lobes in phase, $\varphi=0°$, and then working from left to right and down in 18° phase steps, $\Delta\varphi=18°$, until the two lobes are out of phase, $\varphi=180°$

different in amplitude so that when two adjacent lobes, with $\varphi = 180°$, are focused the two-lobe focused spot also has unequal amplitudes.

The effect of varying the phase φ between 0° and 180° when the lobes have equal amplitudes is investigated. Figure 5.10 shows the focused spot properties when the phase relation between the two lobes are changed. The focused spot starts out with the two lobes in phase and then each successive focused spot has $\Delta\varphi$ of 18° until the last picture where the out of phase condition $\varphi = 180°$ is reached. It is observed that as φ increases, a side lobe in the focused spot begins to grow at the expense of the central lobe, which experiences a peak reduction. When φ went from 0° to -180° it is observed that the opposite side lobe grows. This phase mismatch simulation shows that a phase difference of about 18° can be tolerated without significantly affecting the focused spot properties.

In order to make this VCSEL mode usable in an application that requires a tightly focused spot, a phase mask is necessary that brings the lobes in phase with each other. If this source is reimaged or used in the pupil of an optical system without a phase mask, a ring-like irradiance distribution in the focus plane is observed because of its self-similar Fourier transform property, as shown in Figure 5.11(a). This would not be useful for applications that require a point focus. If this source is reimaged or used in the pupil of an optical system with a phase mask, a point focus is observed, as shown in Figure 5.11(b).

The phase mask could be realized by depositing material of the appropriate thickness on every other lobe directly on the laser facet itself, or a separate element could

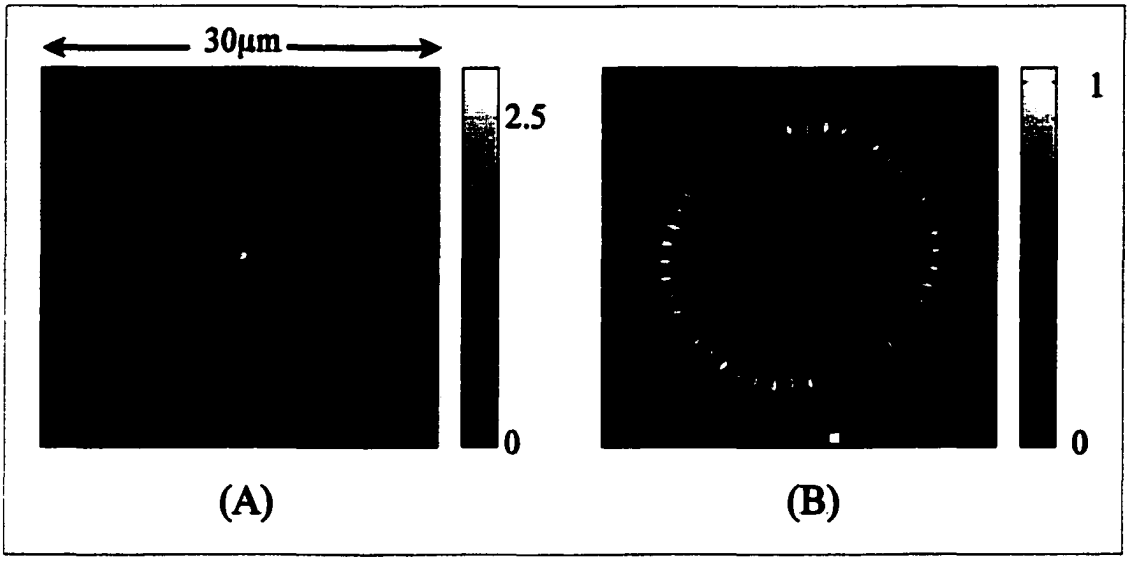

Figure 5.11. Simulation of the focused spot of the VCSEL source with the adjacent lobes in phase (A) and out of phase (B). When the adjacent lobes are in phase a nice tight focused spot is observed. When the adjacent lobes are out of phase the focused spot is similar to the source distribution.

be made that is placed downstream in an image plane of the laser. Simulations and experiments indicate that this VCSEL may be useful in systems that require a point focus, such as data storage, if a phase mask is used.

5E - issues concerning use of VCSEL in a data storage system

One concern of the VCSEL is the propagation of the light emitted from the front facet to a location downstream. Figure 5.12(a)&(b) show the irradiance distribution of a 50μm diameter VCSEL after propagating a distance of 100μm from the facet, with the adjacent lobes out of phase and with the adjacent lobes in phase. When the adjacent lobes are out of phase the propagated irradiance distribution, Figure 5.12(a), spreads out quickly and maintains the multiple lobe circular symmetry. When the adjacent lobes are

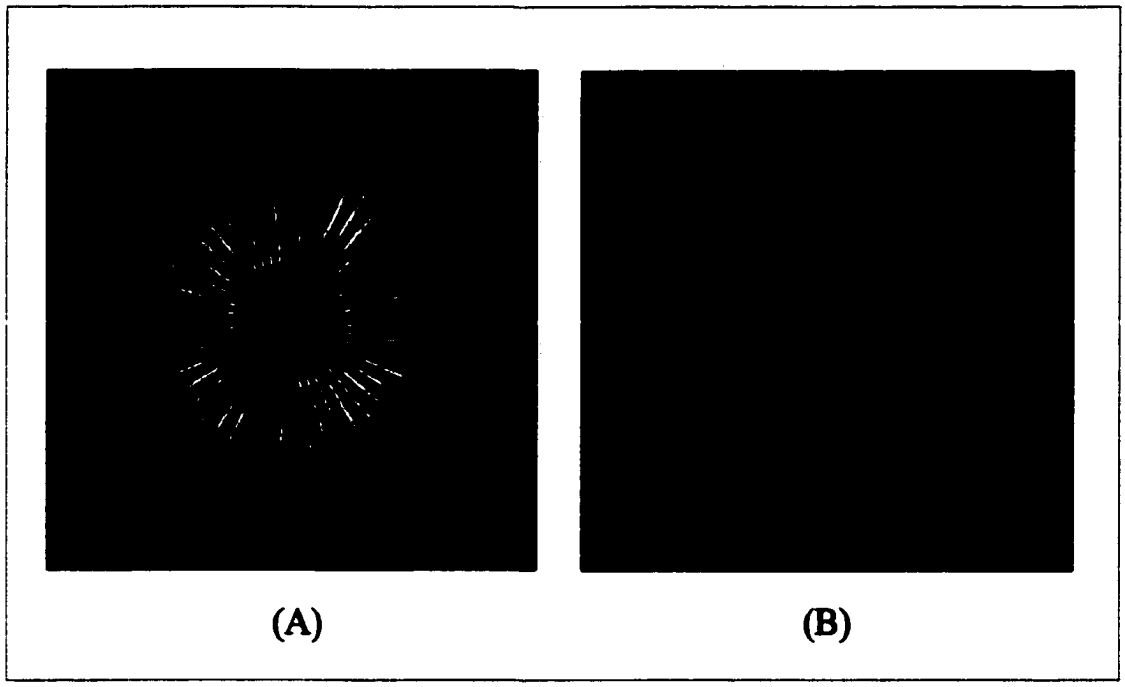

Figure 5.12. Irradiance distribution of VCSEL after propagating a distance of 100μm with the adjacent lobes out of phase, (A), and in phase, (B).

in phase the propagated irradiance distribution, Figure 5.12(b), turns into a J_0 Bessel beam that is sometimes referred to as a diffractionless beam in literature (Herman, 1991). Whether or not the phase mask is on the laser emission facet or etched in a glass slide and placed downstream in the optical system, a relay system should be used to image the ring into the exit pupil of the data storage objective lens.

Another concern is the high obscuration ratio, $\varepsilon>0.9$, of this source. The simulations in Chapter 3 section 3D.1A.B show the effects this ε has on the properties of the focused spot. The tradeoff of the reduced central core is the lower on-axis irradiance and increased sidelobe levels. The obscuration ratio of this source can be modified by a pair of optical elements called axicons (McLeod, 1954). Figure 5.13 shows a cross

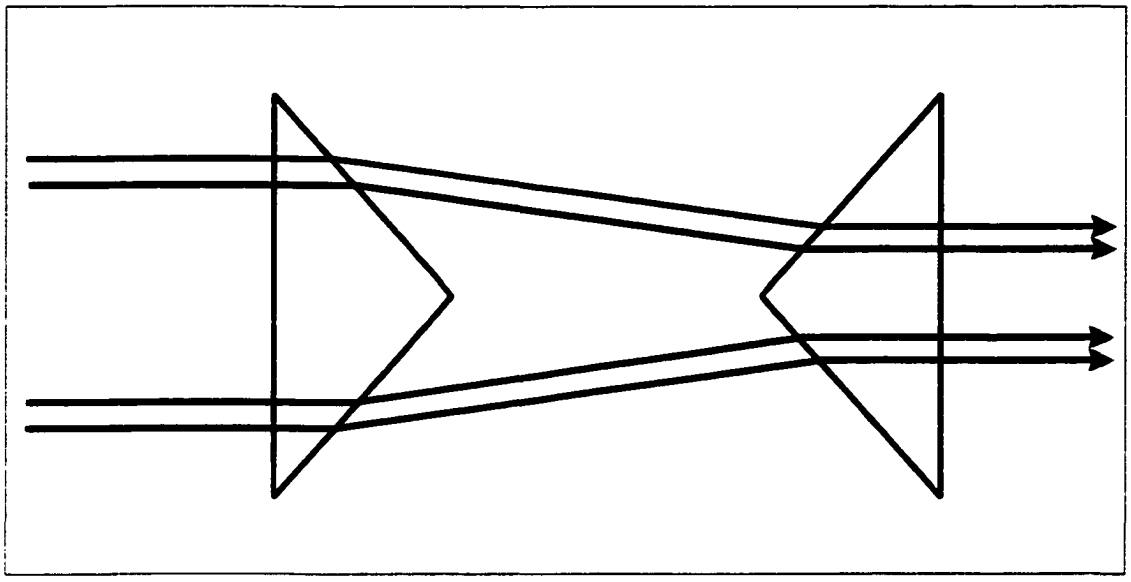

Figure 5.13. Cross section view of rotationally symmetric axicon pair. Illustrating how the obscuration ratio is changed.

sectional view of rotationally symmetric axicons. The second axicon planarizes the wavefront.

A simulation to change the obscuration ratio properties of the VCSEL distribution using an axicon is presented. The VCSEL source distribution, with the adjacent lobes in phase, is reimaged a plane with a magnification of 100. The distribution is now 5mm, which is the approximate size to fill a data storage objective lens. The distribution is then used as input into an axicon, and the light distribution for different propagation distances is observed for changing obscuration properties. Figure 5.14 shows the changing obscuration properties of the light distribution as it propagates. The obscuration ε is observed to decrease as the propagation distance decreases. Note that the propagation distances are rather large for a practical system, ranging in value from 45cm-75cm. This large range of distances can be overcome by starting with a smaller diameter reimaged

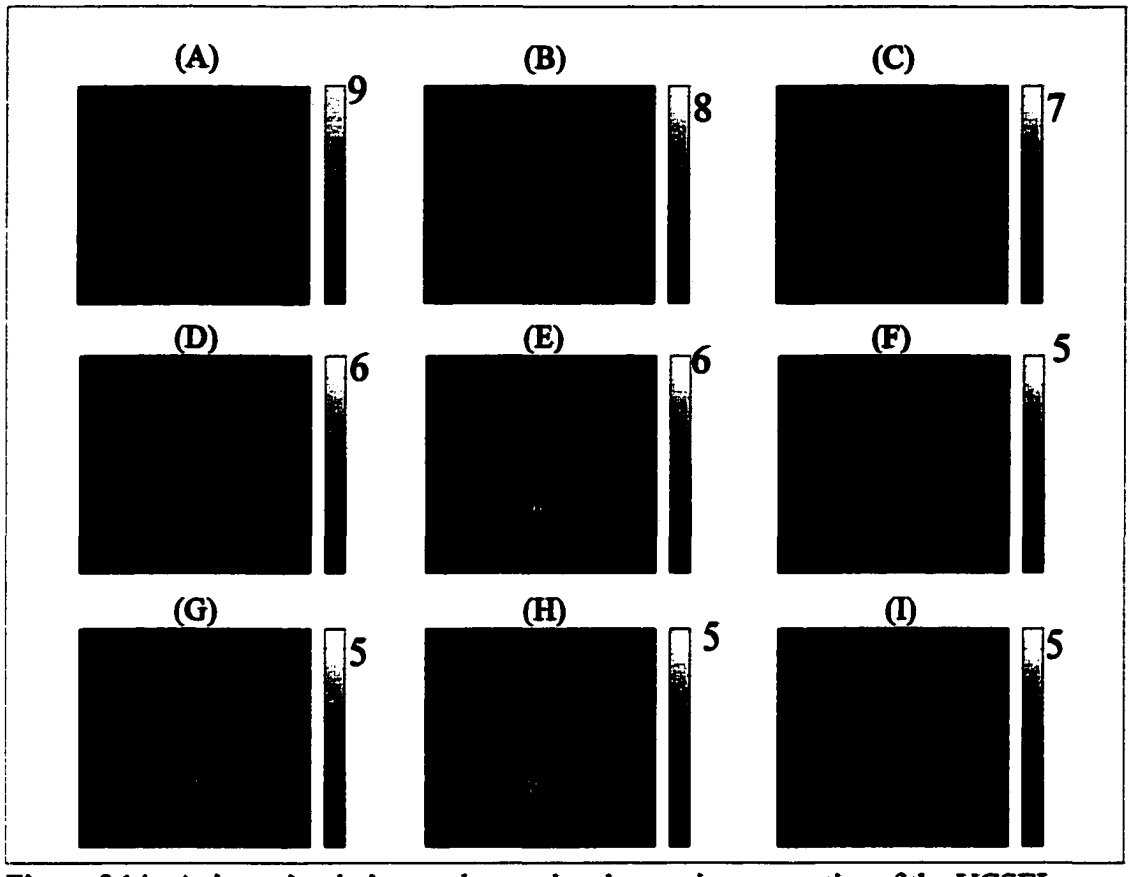

Figure 5.14. Axicon simulation to change the obscuration properties of the VCSEL distribution. Starting out with the distribution of the laser emission facet imaged to a plane with an image diameter of 5mm,(A). Then propagating a distance 40cm from the image plane. (C)-(I) are propagation steps of 5cm. The total propagation from (B)-(I) is 40cm -75cm.

source and optimized axicons. Axicons could be implemented as diffractive optical elements to keep the illumination-path as short as possible.

5F - summary

A new VCSEL structure is reviewed. The output power characteristics under pulsed and CW operation are observed. The output irradiance distribution is shown to follow a high spatial mode and basically looks like a centrally obscured source with

ε>0.9. The stability of the output mode is investigated as a function of injection current and shown to be temporally and spatially stable.

A theoretical description of the preferred lasing mode in a center etched VCSEL is reviewed (Burak and Binder, 1998). The dependence of the preferred lasing mode on the radius of the center etched well is shown.

The phase relation between the adjacent lobes of this lasing mode are simulated and verified experimentally. A phase mask for the VCSEL is proposed for point focus applications. Variations of the phase depth of up to 18° is shown to have only a small effect on the properties of the focused spot. Also the amplitude variations on the individual lobes that make up the distribution in Figure 5.3 have only a small effect on the focused spot.

Issues relating to the location of the phase mask in the system are discussed. The high obscuration ratio of the beam can be changed with a simple pair of axicons, which can be diffractive elements. If the VCSEL is used in a data storage system where the recording layer was insensitive to any heat generated by large sidelobes, such as the phase change medium in Section 3D.1.C, then the axicon pair to change the obscuration ratio may not be necessary. However, the phase mask is necessary for any point focus application of this source.

CHAPTER 6 - SUMMARY/CONCLUSIONS, FUTURE WORK

The signal and noise distributions in the pupil of a data storage system are shown to follow different spatial distributions in the pupil. The noise distribution is shown to be concentrated in the central portion of the pupil. The signal distribution is shown to be concentrated in the central portion of the pupil for low frequencies, and toward the edge of the pupil at high frequencies. This confirms that the data pattern acts as a collection of gratings. The different spatial distributions of the signal and the noise in the pupil allow the design of return-path optical filters that not only alter the system transfer function properties, but also modify the signal-to-noise ratio of the system.

The results for this magneto-optic data storage system are applicable to other optical disk storage systems such as those with phase change materials as their recording layer. The signal distributions will follow similar spatial patterns in the pupil. The noise should also follow similar distributions in the pupil.

6A - Summary/conclusions

Definitions of resolution and superresolution were reviewed. It is found that superresolution means different things to different disciplines. Even Oceanography has a definition of superresolution, "superresolution (oceanography) - separation of tides into components of different frequencies, without taking measurements for the full extent of the longest period component"(Parker, 1989). Perhaps the most vague definition is given by Lohmann "superresolution - better than normal "(Lohmann, 1983). Then one is left to ask what is normal? Chapter 2 clarified the definitions of superresolution pertaining to

optical systems. The first definition of superresolution is to increase the transmission of higher spatial frequencies. This definition is sometimes referred to as ultraresolution (Wilson and Sheppard, 1984). The second definition of superresolution is to restore lost frequency information beyond the system cutoff frequency. The image processing routines of superresolution definition #2 do have the potential for use in a data storage system. The non-iterative algorithms would be the least time consuming of the routines. This could be accomplished by knowing the properties of the object, and also knowing the properties of the system. The object information could be utilized in a non-iterative image processing routine on a digital signal processor(DSP) that reads in the unresolved waveform from the data channel in some prescribed blocks of data. Then the DSP performs the algorithm on the data and outputs the resolved data to the user. The third definition of superresolution is space-bandwidth product adaptation. These definitions are discussed in detail in Chapter 2.

In Chapter 3 diffraction modeling used to simulate a magneto-optic data storage system is described. The simulated performance of a magneto-optic data storage system is presented. Then superresolution components were modeled and their effect on the performance of the system is demonstrated. The system transfer function is partially equalized with the application of optical and electronic filters. The best overall equalization occurs when the optical and electronic filters are used simultaneously. The return-path optical filter accomplished this by attenuating the low frequencies relative to the high frequencies. The illumination-path ring-phase filter accomplishes equalization

by attenuating the low frequencies and boosting the high frequencies. The electronic boost filter accomplished this by providing higher gain at the high frequencies relative to the low frequencies.

In chapter 4 the experimental performance of a specific magneto-optic data storage system is presented. The effects of noise on the resultant images were observed. Also the specific superresolving filters investigated improved system performance as predicted in the simulations of Chapter 3. The signal and noise power distributions are mapped out as a function of position in the pupil. The concept of the data pattern acting as a collection of gratings is verified experimentally. The performance improvements at the high frequencies is shown to be traded off for low frequency degradation, but the low frequencies can usually tolerate some degradation. The return-path optical filter attenuated the low frequencies, but did increase CNR at high frequencies.

In Chapter 5 a new vertical cavity surface emitting laser (VCSEL) is introduced that has a special property. The irradiance distribution of this VCSEL follows a ring like distribution. It can be thought of as an amplitude filtered illumination-path source. With the addition of a phase mask this source can be used in a scanning optical microscope or a data storage system.

6B - Future work

As new optical disk data storage systems develop, the superresolution techniques of optical and electronic filtering will continue to enhance performance of the system, and aid in the realization of high density drives. One continuation of this work is to further

develop the understanding of the noise. Noise needs to be understood more fully in order to be able to design better noise cancellation or noise reduction techniques that allow the designer to control the signal-to-noise ratio.

While reading the work of Mendlovic and Lohmann, who defined Superresolution definition #3 (Mendlovic, Lohmann, 1997,1998), the following question arose; What happens to the light scattered by the high spatial frequency data pattern that does not get collected by the objective lens?

Bearing in mind the idea that the data pattern is collection of gratings, the diffracted orders from the focused spot reflecting off the data pattern are observed at the objective lens. From this picture the diffracted orders from the high frequencies no longer overlap the zero order as much and are only being collected by the objective lens at the edge of the pupil. The majority of the light from the diffracted order being scattered outside the pupil.

Are there any optical systems that can adapt the signal to the system? By adaption it is meant that the light that is scattered outside the pupil is brought back into the pupil by some auxiliary optical system. One such system used by Mendlovic and Lohmann is a simple prism. Figure 6.1(a) shows a picture of a data pattern acting as a high frequency grating where the ± 1 diffracted orders are not collected by the objective lens, only the zero order is collected. As a consequence of no overlapping area of the zero order with the ±1 orders there is no modulation in the data signal for this frequency because it is outside the bandwidth of the system transfer function. Figure 6.1(b) shows

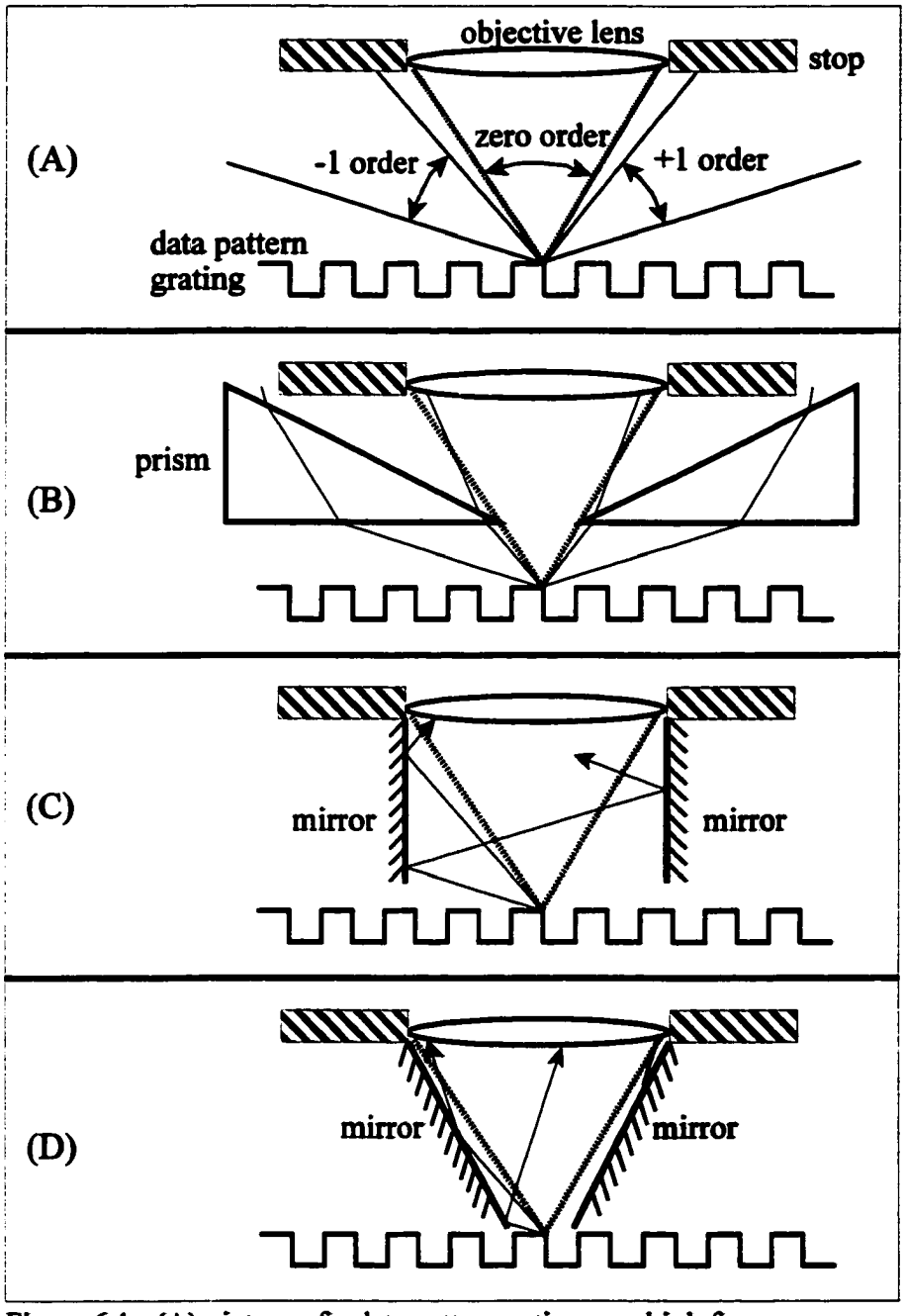

Figure 6.1. (A) picture of a data pattern acting as a high frequency grating where the ±1 diffracted orders are not collected by the objective lens, only the zero order is collected. (B) two prisms used to bend some of the ±1 orders back into the pupil. (C) two mirrors used to bend the ±1 orders back into the pupil, showing only the -1 order for clarity. (D) two angled mirrors to bend the ±1 orders back into the pupil, showing only the -1 order.

how two prisms might be used to bend some of the high frequency light back into the pupil. Rather than using prisms, a mirror system could also be used. Figure 6.1(c) and (d) show two possible mirror systems. The mirror system in Figure 6.1(c) makes the diffracted order look like an off axis source to the objective lens. The mirror system in Figure 6.1(d) just tilts the mirrors so the diffracted order still looks like an off axis source, but not as severely off axis as in Figure 6.1(c). The consequence of looking like an off axis source is additional aberration added to the wavefront of the diffracted order which may wash out the phase variation due to the data itself. If these adaptive systems work, they have the potential to partially equalize the system transfer function by boosting the high frequency response rather than attenuating the low frequencies. These adaptive systems may even extend the cutoff frequency of the system, in the scan direction only, if the light is detectable.

Each definition of superresolution shows the possibility of enhancing the quality of optical data storage systems leading to the possibility of increased data capacity. If given the time and money the techniques explored in this dissertation would enhance the performance of present optical storage technologies, and those of the future.

REFERENCES

Ando, H., T. Yokota, and K. Tanoue, "Optical head with phase-shifting apodizer," Jpn. J. Appl. Phys. **32**, No. 11B 5269-5276 (1993).

Ando, H., "Phase-shifting apodizer of three or more portions," Jpn. J. Appl. Phys., **31**, No. 2B, (1992).

Bastiaans, M.J., "The Wigner function applied to optical signals and systems," Optics Comm., **25**, No. 1, (1978).

Born, M. and Wolf, E., "Principles of Optics," (Pergamon Press, 1980).

Burak, D., R. Binder, "Electromagnetic characterization of vertical-cavity-surface-emitting lasers based on a vectorial eigenmode calculation," Appl. Phys. Lett., **72**, No. 8, p. 891, (1998).

Call, D. E., B. I. Finkelstein, "Dependence of laser-feedback noise on optical-path-length," Proc. SPIE, **1078**, p. 272-275, (1989).

Claisse, P., W. B. Jiang, P. Kiely, B. Galle, B. Koose, Motorola internal communication, (1997).

Classen, T.A.C.M., and Mecklenbräuker, W.F.G., "The Wigner distribution - a tool for time-frequency signal analysis part1, part2, part3," Philips J. Res., **35** (1980).

Cutrona, L. J., W. E. Vivian, E. N. Leith, and G. O. Hall, "A high-resolution radar combat-surveillance system," IRE Trans on Military Electronics, **Mil-5**, p. 127-131, (1961).

den Dekker, A.J. and A. van den Bos, "Resolution: a survey," J. Opt. Soc. Am. A, **14**, No. 3, p. 547-557. (1997)

Fienup, J. R., Kosek, M.R., and Stankwitz, H. C., "Application of superresolution algorithm to optical coherent imaging," Proc. SPIE, **2827**, p. 80-87 (1996).

Flagello, D. G., Milster, T. D., and Rosenbluth, A. E., "Theory of high-NA imaging in homogeneous thin films," J. Opt. Soc. Am., **13**, No. 1, (1996).

Frieden, B. R., "On arbitrarily perfect imagery with a finite aperture," Optica Acta, **16**, No. 6, (1969).

REFERENCES– *Continued*

Froehlich, F. F., M. S. Wang, T. D. Milster, "Technique for simultaneous alignment and collimation of a laser diode in an optical data storage head," Applied Optics, **30**, No. 31, p. 4481, (1991).

Gaskill, J. D., "*Linear Systems Fourier Transforms and Optics*," (John Wiley and Sons, 1978), pp. 71-74, 456

Gerchberg,R. W., "Super-resolution through error energy reduction," Optica Acta, **21**, No. 9, p. 709-720 (1974).

Goodman, J. W., "*Introduction to Fourier Optics*," (McGraw-Hill, 1968).

Harvey, J. E., "Fourier treatment of near-field scalar diffraction theory," Am J. Phys., **47**, No. 11, (1979).

Haskal, H. M., "Laser recording with truncated Gaussian beams," Applied Optics, **18**, No. 13, p 2143-2146, (1979).

Hegedus, Zoltan S., "Annular pupil arrays application to confocal scanning," Optica Acta, **32**, No. 7, p. 815 -826 (1985).

Herman, R. M., T. A. Wiggins, "Production and uses of diffractionless beams," J. Opt. Soc. Am. A., **8**, No. 6, p. 932-942, (1991).

Hirota, K. Ohbayashi, G., "Reliability of the phase change optical disk," Jpn. J. Appl. Phys., **36**, No. 10, p. 6398-6402, (1997).

Howe, D. G., " The nature of intrinsic error rates in high-density digital optical recording," Proc. SPIE, **421**, p. 31, (1983).

Jacquinot, P. and B. Roizen-Dossier, in Progress in Optics, E. Wolf , ed. (North-Holland, Amsterdam, 1964), **3**, Chap. 2, p.31. (1964).

Jiang, W. B., P. Claisse, C. Gaw, P. Kiely, B. Lawrence, M. Lebby, M. Roll, Proc. 47th ECTC, San Jose, p. 368, (1997).

Lohman, A. W., "Some thoughts on superresolution," in Proceedings of Workshop on Limits of passive imaging, C. Aleksoff, ed. [R. Guenther (ARO), Raleigh, NC., 1983], p. 37-43.

REFERENCES– *Continued*

Loze, M. K., Wright, C. D., "Temperature distributions in semi-infinite and finite-thickness media as a result of absorption of laser light," Applied Optics, **36**, No. 2, p. 494-507, (1997).

Mahajan, V. N., "Uniform versus Gaussian beams: a comparison of the effects of diffraction, obscuration, and aberrations," J. Opt. Soc. Am. A., **3**, No. 4 (1986).

Marinero, E. E., Arnett, P. C., McDaniel, T. W., Call, D. E., Finkelstein, B. I., and Jacquette, G. A., "Light intensity modulation direct overwrite on 130mm 2X MO media," Proc. SPIE, **2514**, p.390-400., (1995).

Mansuripur, M., "*The Physical Principles of Magneto-Optical Recording*," (Cambridge University Press, London,1995).

Mansuripur, M., G. A. N. Connell, J. W. Goodman, "Signal and noise in magneto-optical readout," J. Appl. Phys., **53**, No. 6, p. 4485-4494, (1982).

Mansuripur, M., Connell, G. A. N., "Laser-induced local heating of moving multilayer media," Applied Optics, **22**, No. 5, p. 666-670, (1983).

Marchant, A., "*Optical Recording*," (Addison-Wesley, 1990)

McLeod, J. H., "The Axicon : a new type of optical element," J. Opt. Soc. Am., **44**, No. 8, p.592-597, (1954).

Meinel, A. B., M. P. Meinel, and N. J. Woolf, "Multiple aperture telescope diffraction images," Applied Optics and Optical Engineering vol. IX, R. R. Shannon and J. C. Wyant ed., (Academic Press), ch. 5, (1983).

Mendlovic D., and Lohman, A.W., "Space-bandwidth product adaptation and its application to superresolution: fundamentals," J. Opt. Soc. Am. A., **14**, No. 3, p. 558, (1997)

Mendlovic, D., Lohman, A.W., and Zalevsky, Z., "Space-bandwidth product adaptation and its application to superresolution: examples," J. Opt. Soc. Am. A., **14**, No. 3, p. 563, (1997).

Michalzik, R., R. Jager, B. Weigel, M. Grabherr, C. Jung, G. Reiner, K. J. Ebling, paper MB3, IEEE/LEOS Summer Topical Meetings, Aug. (1997).

REFERENCES– *Continued*

Milster, T. D. and. Curtis, C. H., "Analysis of superresolution in magneto-optic data storage devices," Applied Optics, **31**, No. 29, p. 6272-6279 (1992).

Milster, T. D., E. P. Walker, "Mechanism for improving the signal-to-noise ratio in scanning optical microscopes," Opt. Lett., **21**, No. 16, p. 1304-1306, (1996).

Milster, T. D., "A user-friendly diffraction modeling program," SPIE Optical Data Storage meeting conference digest, P1, p. 60, April (1997).

Milster, T., Jiang, W., Walker, E., Burak, D., Claisse, P., Kelly, P., Binder, R., "A single-mode high-power vertical cavity surface emitting laser," Appl. Phys. Lett., **72**, No. 26, p.3425-3427., (1998).

Oh., T. H., D. L. Huffaker, M. R. MacDaniel, D. G. Deppe, paper WC3, IEEE/LEOS Summer Topical Meetings, Aug. 1997.

Parker, "*Dictionary of Scientific and Technical Terms*, 4th ed.," (McGraw-Hill, 1989).

Peyghambarian, N., Koch, S. W., and Mysyrowicz, A. "*Introduction to Semiconductor Optics*," (Prentice Hall, 1993).

Sales, Tasso R. M. and G. Michael Morris, "Fundamental limits of optical superresolution," Opt. Lett., **22**, No. 9 p. 582-584. (1997).

Seigman, A. E., "*Lasers*" (Univerity Science Books,1986).

Smith, W. J., "*Modern Optical Engineering*," (McGraw-Hill, 1990).

Strand, T. C., and H Werlich, "Aberration limits for annular Gaussian beams," AO, **33**, No. 16, (1994).

Tanabe, T., "Superresolution readout system with electrical equalization for optical disks," Applied Optics, **34**, No. 29, p. 6769-6774 (1995).

Walker, E. P. and T. D. Milster, "High-frequency enhancement of magneto-optic data storage signals by optical and electronic filtering," Opt. Lett. **20**, No. 17, 1815-1817 (1995).

REFERENCES– *Continued*

Walsh, David O., and Nielsen-Delany, Pamela A., "Direct method for superresolution," J. Opt. Soc. Am A., **11**, No. 2, p. 572-579 (1994).

Wang, Mark Shi, "Differential Wax-Wane Focus Servo," Phd. Dissertation, Optical Sciences Center, University of Arizona (1993).

Weyl, H., Ann Phys., **60**, 481 (1919).

Wigner, E., "On the quantum correction for thermodynamic equilibrium," Phys. Rev., **40**, (1932).

Wilson, T. and Sheppard C., "*Theory and Practice of Scanning Optical Microscopy*," (Academic Press, 1984), chs. 3, 6.

Wilson, T., Hewlett, S. J., "Superresolution in confocal scanning microscopy," Opt. Lett., **16**, 14, p. 1062-1064, (1991).

Wright, C. D., "Private Communication," (1998).

Wright, C. D. M. K. Loze, P. W. Nutter, 'A Matlab based read/write model for magneto-optic recording," Proc. SPIE, **3109**, p. 196-204, (1997).

Wu., Y. A., C. J. Chang-Hasnain, R. Nabiev, Electron. Lett., **29**, No. 20, (1993).

Yamanaka, Y., Hirose, Y., Fujii, H., Kubota, K., "High density recording by superresolution in an optical disk memory system," Applied Optics, **29**, No. 20, (1990).